# An Investigation of the Corrosion Behaviour of a Range of Engineering Materials in Marine Environments

Vol. I

A Thesis

Submitted in Fulfilment of the Requirements for the Degree of Doctor of Philosophy (Ph.D.)

by Anne Neville

Department of Mechanical Engineering,
University of Glasgow,
September 1995

*Dedicated to the memory of my Grandpa*

# Summary

This work represents an investigation of the corrosion behaviour of primarily high-grade alloys in marine environments. A range of marine conditions of varying severity has been considered and their effect on the electrochemical corrosion characteristics assessed. The study has utilised a range of electrochemical monitoring techniques, light and scanning electron microscopy and other surface techniques to assess the extent and morphology of corrosion attack under certain conditions.

Principal components of the study include the effect of elevated temperature (up to 60°C) on corrosion initiation and propagation in static and high velocity impinging seawater. In addition, the effect of micro and macro fouling has been assessed using immersion tests and a hydrodynamic model. Continuation of the biological effects on corrosion looked at the effect of the presence and activity of Sulphate Reducing Bacteria (SRB) on corrosion mechanisms. Correlations between accelerated laboratory tests and the real time behaviour of materials have been successfully made. Methods to counteract fouling often include the use of biocides and, in this study, the effect of high levels of hypochlorite dosing has been investigated.

Mechanical and corrosion effects by liquid impact and by liquid-solid impact constitute a major part of this work and the use of electrochemical tests has enabled the proportions of weight loss on a given material attributed to corrosion, erosion and a synergistic factor to be elucidated. Several options exist to combat excessive deterioration due to mechanical wear. Two processes, shot-peening and laser irradiation, have been assessed primarily for corrosion resistance in a marine environment.

# Acknowledgements

There are several people who have have been responsible for making the time spent in the Department of Mechanical Engineering very enjoyable. I must express my most sincere thanks to Dr Trevor Hodgkiess for all his advice, support and friendship offered throughout the three year period. Also, my thanks go to Margaret and Susan for all the laughs in the office.

A significant part of the work was performed outwith the University laboratories and I would like to express my gratitude to Mr Len Phillips, Weir Pumps Ltd, Cathcart, for his advice and assistance. At the Weir Pumps Research Department, Alloa, my thanks are extended to Mr John Dallas for the use of test rigs and equipment and especially to Stewart Halbert for his technical help during experiments.

Thanks go to Jeremy Thomason, at UMBSM for all his help and advice on all things biological!

I would like to acknowledge M. Lionel Lemoine for the provision of laboratory facilities at the IFREMER laboratories, Brest and for his kind welcome. Also Chantal Compere and Eva L'hostis for their help and advice.

On a personal level, many thanks to my parents for their immense encouragement and financial help during the last three years and my undergraduate course. Also a special thank you to Mark, especially for carrying my gear back from France!

# Contents

**Chapter Eight - A Study of the Effect of Micro and Macro-Fouling on the Short and Long Term Corrosion Behaviour of High-Grade Alloys**

# List of Figures

## Chapter 1



## Chapter 2

## Chapter 3

## Chapter 4

## Chapter 5

## Chapter 6

## Chapter 7

## Chapter 8

## Chapter 9

# List of Tables

## Chapter 9

# Chapter 1

## Introduction, Materials and Theory of Corrosion

Material selection as a discipline involves consideration of numerous factors which dictate the performance of an engineering system. In the first instance, mechanical requirements such as strength, toughness and ductility must be defined. Selection must then focus on the performance of potential materials from the viewpoint of material degradation due to interaction with the environment, in most aqueous systems, the main limitation being that of corrosion behaviour.

The adverse effects of corrosion are evident in a range of industrial sectors encompassing processing of corrosive inorganic acids (e.g. sulphuric and phosphoric), pulp and paper industry and production of food and beverages. Material selection can account for up to 7% of capital costs and 20% of maintenance costs in a pulp and paper processing plant [1]. However, undoubtedly the most severe and costly failures due to corrosion, often in conjunction with erosion, occur in seawater handling systems of which oil and gas production represents a significant proportion. Other major applications involve desalination operations in which seawater of varying ionic strength and temperature is handled and materials in the different stages of the process are chosen to reflect this. Since seawater is often the most readily available source of water, it is heavily employed within condenser cooling systems in coastal power plants.

Offshore applications utilise vast amounts of seawater in firewater systems, as cooling water, for ballast piping and for injection into wells to enhance the recovery of oil [2]. All these applications require process piping, pumping equipment and water storage vessels, which handle seawater at varying temperatures, velocities, pressures and salinity. Hence the scope for deterioration due to the interaction of the material with the electrolytic seawater, which can contain corrosive gases ($CO_2$ and $H_2S$) and be loaded with solid particles, is immense.

Major offshore operators world-wide continue to discover and exploit new oil and gas reserves thus laying down the challenge to material producers and selectors. Increasingly fields are discovered in deeper ocean locations where incidences of well-souring are increased and higher temperatures and pressures are encountered as illustrated by the deep reservoir (4000m) of the Embla project in the Norwegian Greater Ekfisk field [3]. The economic pressures to increase output are manifested in the need for rotodynamic machinery to operate at higher velocities, pipelines to handle larger volumes of fluid and systems to operate with minimum downtime.

One major offshore operator estimated that it's output will increase by 2% per year well into the next century utilising existing fields and in addition, new exploration regions in the Gulf of Mexico, Colombia and West of Shetland [4]. Preliminary approval has been obtained to develop the Natuna field in the South China Sea [5] which, if successful, will signal the largest offshore concentration of gas producing facilities in the world.

On average, 6000 tons of structural steel can be required for construction of a multi-well platform [2]. Equipment space and weight are at a premium on the platform and as an incentive to reduce topside weight, it was recently estimated [6] that a reduction in one ton of top weight will allow three tons to be saved in the supporting structure. Thus there is a genuine need to utilise materials which can offer this weight saving yet not compromise the corrosion resistance and mechanical properties.

Material selection which addresses concerns about performance and maintenance and also economic factors concerning the initial capital expenditure represents a formidable task. It must begin from an understanding of the performance limitations of currently available materials .

The work described herein is a broad based study of the corrosion behaviour of stainless steels, related high-grade Ni-base and Co-base alloys, lower grade steels and cast irons currently utilised in corrosive environments. The emphasis is on marine applications and in particular marine pumping systems within which some of the most severe physico-chemical and mechanical conditions are encountered.

The study initially assesses the effect of increased temperature on the electrochemical processes and mechanisms of corrosion attack in static seawater and progresses to focus on the effect of elevated temperature in the presence of a high velocity impinging seawater flow. Industrial applications often require systems to handle a working fluid containing entrained solids whether they are wood chips in the paper and pulp industry or sand particles in recovered fluids from the sea-bed. An impinging jet containing suspended solids was therefore used to simulate and assess the effect of repeated particle bombardment in a liquid stream.

In an attempt to improve the resistance of conventional metal surfaces to deterioration by the effects of wear in conjunction with corrosion, material processes have been developed which either involve changing the surface layer composition and morphology or adding a wear resistant layer. In this study, the corrosion resistance of

shot-peened and laser-treated surfaces has been investigated and assessed in conjunction with mechanical and microscopical observations.

Industrial marine environments can impose severe mechanical and physical constraints on components due to high velocity flows inducing shear stresses and impinging particles causing enhanced wear damage but in addition, the biological organisms can significantly increase the aggressive nature of the environment. Part of this project involved immersion tests in natural seawater to assess the changes in electrochemical characteristics of materials once a biofilm had become conditioned on the surface. In conjunction to the study of marine aerobic bacteria and organisms present in aerated seawater, a laboratory culture of anaerobic sulphate-reducing bacteria was sustained to simulate the aggressive conditions of high dissolved hydrogen sulphide content encountered in 'sour' oilfield locations.

As a final topic, the effect of dosing seawater with the biocidal hypochlorite ion in the form of sodium hypochlorite was investigated. Concentrations of 0-1ppm of free chlorine are normally used which has been shown [7] to effectively reduce microfouling but significantly higher concentrations of 500-600ppm can be encountered in distribution tanks, pipes and pumps at the dosing point of the system. It is the higher concentration which is of interest in this study.

Using a comprehensive experimental approach based on electrochemical and microscopical techniques, this work has identified mechanisms of corrosion deterioration and related this information to the fundamental electrochemical corrosion processes occurring in conditions of practical engineering importance.

On account of the diversity of the topics included in this study, each component (as summarised above) is contained in entirety (i.e. literature review, results and discussion) in separate chapters, followed by a general discussion/conclusion chapter. The remainder of this first chapter comprises some general comments on material selection in marine engineering followed by a description of the materials investigated in this work.

## Material Selection for Marine Applications

The selection of material for a particular marine application can, in theory, be made by one of two approaches. An initial low cost system utilising carbon steel or cast iron components can be adopted where maintenance costs will inevitably be higher or alternatively, higher grade alloys can be selected requiring less maintenance but significantly increased initial capital outlay [8]. In practice however, the selection process is a compromise between these two options. The trend in the major oil and gas and desalination industries is moving towards larger initial expenditure, aiming for dependable long-term performance with reduced maintenance [2]. Hence conventional materials such as carbon steel and cast iron, used extensively in construction of piping and water handling systems which require large scale maintenance and application of corrosion protection are increasingly replaced by cupro-nickel, stainless steel, nickel-base alloys and in some cases titanium. As an example, the Al-Jubail desalination plant in Saudi Arabia, built in the mid-1980's used 20,000 tonnes of stainless steel and 40,000 tonnes of cupro-nickel.

Failure of higher-alloyed materials still occur and as such, material limitations in many circumstances have been defined and are therefore well documented. The main limitation on copper alloys is their poor resistance to attack by corrosion in flowing seawater, illustrated by the design velocity data given below [8].

| Material | Design Velocity |
|---|---|
| Copper | 0.75m/s |
| Aluminium brass | 2.5m/s |
| 90/10 Copper Nickel | 3m/s |
| 70/30 Copper Nickel | 3.5m/s |

At velocities above the design velocity, the protective corrosion product layer, which in static conditions, confers protection against general corrosion, is removed by imposed shear stresses thus significantly increasing the corrosion rate.

Stainless steels and nickel-base alloys are finding increased application in piping systems, taking advantage of their improved resistance to erosion-corrosion and ability to withstand much higher velocities. Hence the potential exists to reduce pipe diameters and ultimately material costs compared to a copper or cupro-nickel system. The corrosion performance of stainless steels and nickel-base alloys is dictated by the

resistance to localised deterioration in chloride media [9,10,11] with standard austenitic stainless steels of the type UNS S31603 being prone to crevice attack in seawater [9].

Employment of high-grade alloys in components subject to the joint effects of corrosion and wear have, in many industrial applications, meant that frequent replacement of worn parts is necessary. Application of cermet coatings is being considered for valve seats, wear rings and in bearings where the mechanical properties of high-grade alloys can be exploited while enhancing wear resistance.

Stainless steels

Stainless steels are by definition ferrous alloys containing at least 11-12% chromium and in addition, varying amounts of other alloying elements, principally Ni, Mo and N.

Stainless steels resist corrosion chiefly because they are passive. This results principally from the fact that the passive state of Cr is very stable in many media [12]. As a major alloying element of stainless steels, Cr can transmit this characteristic to other metals with which it is alloyed [13]. Passivity is due to the formation of a protective layer on the surface of the metal. This layer has been studied by several workers and it is generally agreed that it is of the order of 15-30Å thick [14]. Although it is known to consist of mainly Cr and O (as $Cr_2O_3$) the form and exact composition of the layer is still ambiguous. Evidence of Fe, W and N in the passive layer has been reported in the literature [15,16] while authors postulate that Mo exists only in a certain potential range hence has a transitory presence during a critical stage of the film production [17].

The importance of the protective film existing on stainless steel in the passive state is its ability to act as a barrier to general charge transfer between the metal and its aqueous environment. Hence it can effectively prevent corrosion on a general scale.

Types of Stainless Steel

Although stainless steels have been commercially available since around 1914 [13], the composition of stainless steels are continually under development with the ultimate goal to achieve a material with good corrosion resistance without compromising mechanical properties. Significant refinement of fabrication processes was achieved in the late 1970's with the birth of argon-carbon-decarburization (AOD) which enabled strict control of alloy composition [18,19].

Classification of stainless steels is normally based on the metallurgical structure, namely, ferritic, austenitic, martensitic and duplex [20]. In addition, other classifications have been adopted to define post treatment processes such as precipitation hardening. There has been a modern tendency to label some of the newly developed stainless steels with enhanced corrosion resistance (by virtue of their higher alloying contents) as 'superduplex' and 'superaustenitic'.

The role of alloying elements in determining the metallurgical structure of a metal and its resistance to corrosion attack in certain environments is very complex. To increase the localised corrosion resistance of a material, the alloying elements must be in solid solution [11]. Although Cr is crucial in forming a protective barrier to charge transfer, its presence at high levels is limited by the formation of the intermetallic sigma phase [16] which can reduce the material ductility. Although Mo has been shown to improve the material resistance to localised corrosion attack, the mechanisms by which this is achieved are not well understood [16]. It is believed that the benefits of Mo are enhanced when in the presence of N [11,16,21,22] and Cr [17,23].

The interaction between alloying elements extends to synergistic effects being identified between Mn and N, Cr and N and Mo and N since the ferrite formers Cr, Mn and Mo all increase the solubility of N [24].

Austenitic/Superaustenitic

The AISI 300 series of stainless steels of which UNS S31600 and UNS S31603 (316L) are the materials under study here, represents a standard grade of austenitic stainless steel which are by far the largest tonnage in use in marine environments [25]. UNS S31600 and UNS S31603 (316L) are variations of the general purpose 304 grade in which Mo has been added to improve corrosion resistance. The 'L' signifies a reduction in carbon from the UNS S31600 grade which improves resistance to intergranular corrosion caused by precipitation of carbides during welding or casting.

The 6% Mo superaustenitic stainless steels evolved from the standard austenitic grades, the main variation to the composition being the addition of N. As an austenitic stabiliser, the N is effective in reducing the required amount of Ni and is therefore an economical choice. N is also beneficial in improving strength of the material as illustrated by the 50% increase in strength of the superaustenitic grades.[26].

Duplex/Superduplex

As early as the 1930's it was discovered that putting ferrite into austenite increased a material's resistance to sensitisation [16] and this signalled the creation of what are commonly called duplex stainless steels. Although duplex can be used to describe austenitic/martensitic or ferritic/martensitic stainless steels [27] the term is generally applied to ferritic/austenitic stainless steels with a balance of 50% of each phase.

Typically duplex stainless steels have a higher strength/weight ratio than austenitic stainless steels which attracts their use, especially in offshore applications [6,28]. First-generation duplex stainless steels were used in Sweden and Finland in the 1930's but the impetus for development emerged during the initial Ni shortages of the 1950's and subsequently in the late 1960's and 1970s. Problems due to lack of retention of mechanical properties (loss of ductility etc.) and corrosion resistance after a weld cycle were addressed through addition of N as an economic austenitic former [19]. This retained the phase balance after welding, hence enhanced the mechanical and corrosion properties and signalled the development of second generation duplex stainless steels of which the superduplex stainless steels form one category.

**Materials Investigated in this Programme**

The composition of the duplex and austenitic stainless steels, cobalt and nickel-base alloys included in this work are included in Tables 1.1-1.3 to follow.

| | Cr | Mo | Ni | C | Mn | Si | P | N | Cu | S |
|---|---|---|---|---|---|---|---|---|---|---|
| SAF 2205 | 21.56 | 3.5 | 5.5 | 0.026 | 1.33 | 0.58 | 0.03 | 0.17 | | <0.01 |
| UNS S32760 | 24.61 | 4.04 | 8.42 | 0.025 | 0.86 | 0.61 | 0.03 | 0.22 | 0.88 | <0.01 |
| 25Cr Duplex | 25.71 | 2.82 | 7.92 | 0.02 | 0.76 | 0.51 | 0.02 | 0.16 | 0.2 | <0.01 |
| UNS S31603 | 17.04 | 2.76 | 11.61 | 0.02 | 1.47 | 0.38 | 0.03 | | | <0.01 |
| UNS S31254 | 19.68 | 6.41 | 17.93 | 0.02 | 0.45 | 0.37 | 0.02 | | 0.74 | <0.01 |

Table 1.1. Compositions of stainless steels under investigation

Cobalt-base alloys

| | Cr | W | C | Ni | Mo | Si |
|---|---|---|---|---|---|---|
| Ultimet | 24.1 | 1.74 | | 8.04 | 5.6 | 0.17 |
| Stellite | 28.09 | 4.96 | 0.9 | | | |

Table 1.2. Composition of Cobalt-base alloys

Nickel-base alloys

| | Cr | W | Nb | Ni | Mo | Fe |
|---|---|---|---|---|---|---|
| Inconel 625 | 20.11 | | 3.2 | 61.69 | 8.4 | |

Table 1.3. Composition of Nickel-base alloys

Cast iron

A flake graphite cast iron, Grade 250 with composition 3.27%C, 0.91%Mn, 1.79%Si, <0.005%Mg and <0.01%P was included in the liquid and liquid-solid erosion test programme (See chapters 4 and 5)

Carbon-manganese steel

C-Mn steel was examined as an example of a material displaying active corrosion characteristics in seawater. This steel conformed to BS4360 Grade 50D with composition 0.19%C, 0.7%Mn, Fe balance.

**Theory of Corrosion**

The principles of corrosion are most effectively described in terms of electrochemical thermodynamics. Aqueous corrosion takes place via a series of reactions involving electron transfer and metallic species. For each reaction involving a transfer of electrons, there exists what is defined as an equilibrium potential and this represents one of the most important concepts in electrochemical corrosion.

The equilibrium electrode potential $E_o$ for a particular chemical reaction in an aqueous environment is calculated from the Nernst equation which for a reaction

$$M^{n+} + ne \rightarrow M$$

is written as

$$E_o = E^o_o + \frac{RT}{nF} \ln\left[\frac{a_{M^{n+}}}{a_M}\right]$$

where R is the general gas constant, F is Faraday's constant and T is the temperature in °K.

In aqueous corrosion there are two types of reaction which can occur at an electrode surface : anodic or cathodic. An anodic reaction, or oxidation reaction involves, on a metallic electrode, the dissolution of metal to form metal ions and electrons such as the dissolution of iron

$$Fe \rightarrow Fe^{2+} + 2e.$$

In contrast, a cathodic or reduction reaction involves the consumption of electrons which balances the production of electrons from the anodic reaction. On any electrode, the rate of consumption and release of electrons must be equal. Cathodic reactions in aqueous solutions are dependent on the environmental conditions. Common reactions encountered in neutral solutions are

$$O_2 + 2(H_2O) + 4e \rightarrow 4(OH)^-$$ (Oxygen-reduction)

and

$$2(H_2O) + 2e \rightarrow H_2 + 2OH^-$$ (Water reduction)

while in acidic conditions,

$$2H^+ + 2e \rightarrow H_2$$ (Hydrogen ion reduction)

is more prominent.

The mixed potential theory, applied to a metallic substrate in an aqueous solution, states that any metal which is immersed in an aqueous solution will adopt an electrode potential denoted E, the value of which is determined by the anodic and cathodic reactions at the electrode surface. This introduces a triad of conditions which express the first principle of electrochemical thermodynamics [29]. For an oxidation reaction to take place (release of electrons) at an electrode, the mixed potential E must exceed the equilibrium electrode potential for that reaction. Secondly for a reduction reaction (consumption of electrons) to occur, then E must be more electronegative than $E_o$. On an electrode whose potential represents this equilibrium value, a reaction cannot take place by either oxidation or reduction.

On a freely corroding specimen the anodic and cathodic charge transfer must be equal to maintain electrical neutrality and the potential exhibited is the mixed potential $E_{corr}$.

At $E_{corr}$, the corrosion current $I_{corr}$ can be used to determine the corrosion rate by Faraday's Law of Electrolysis which relates charge transfer to the rate of metal dissolution [29]. $I_{corr}$ can not be measured directly since the anodic and cathodic reactions are occurring at discrete sites on the electrode and it is impossible to insert an ammeter within the micro electrical circuit. Electrochemical techniques exist to enable the measurement of $I_{corr}$ by extrapolation. An electrochemical cell is set up as in Fig. 1.1 in which the potential of the working electrode (the corroding metal) is measured against the reference electrode (normally calomel or Ag/AgCl). The inert auxiliary electrode (normally platinum) forms an electrical circuit for current to flow between itself and the working electrode.

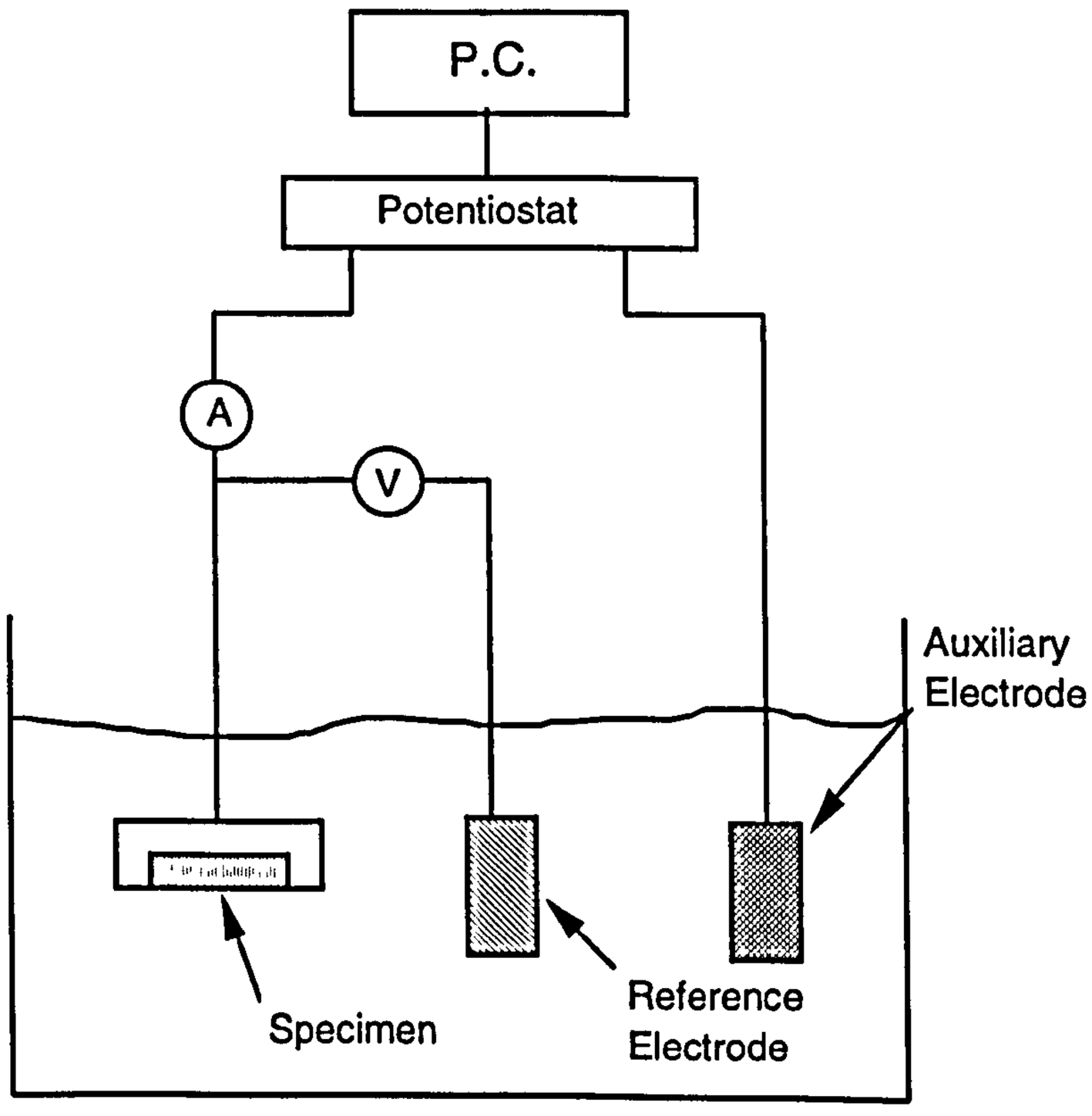


Fig. 1.1. Electrochemical cell

The potential of the working electrode is then shifted in the anodic direction (positive with respect to $E_{corr}$) or cathodic direction (negative with respect to $E_{corr}$) and the potential-current relationship is plotted. A system of anodic and cathodic polarisation curves is created which follow a Tafel relationship away from $E_{corr}$ as shown in Fig. 1.2. On extrapolation of the linear E-log I portions of the plots, the corrosion current can be established.

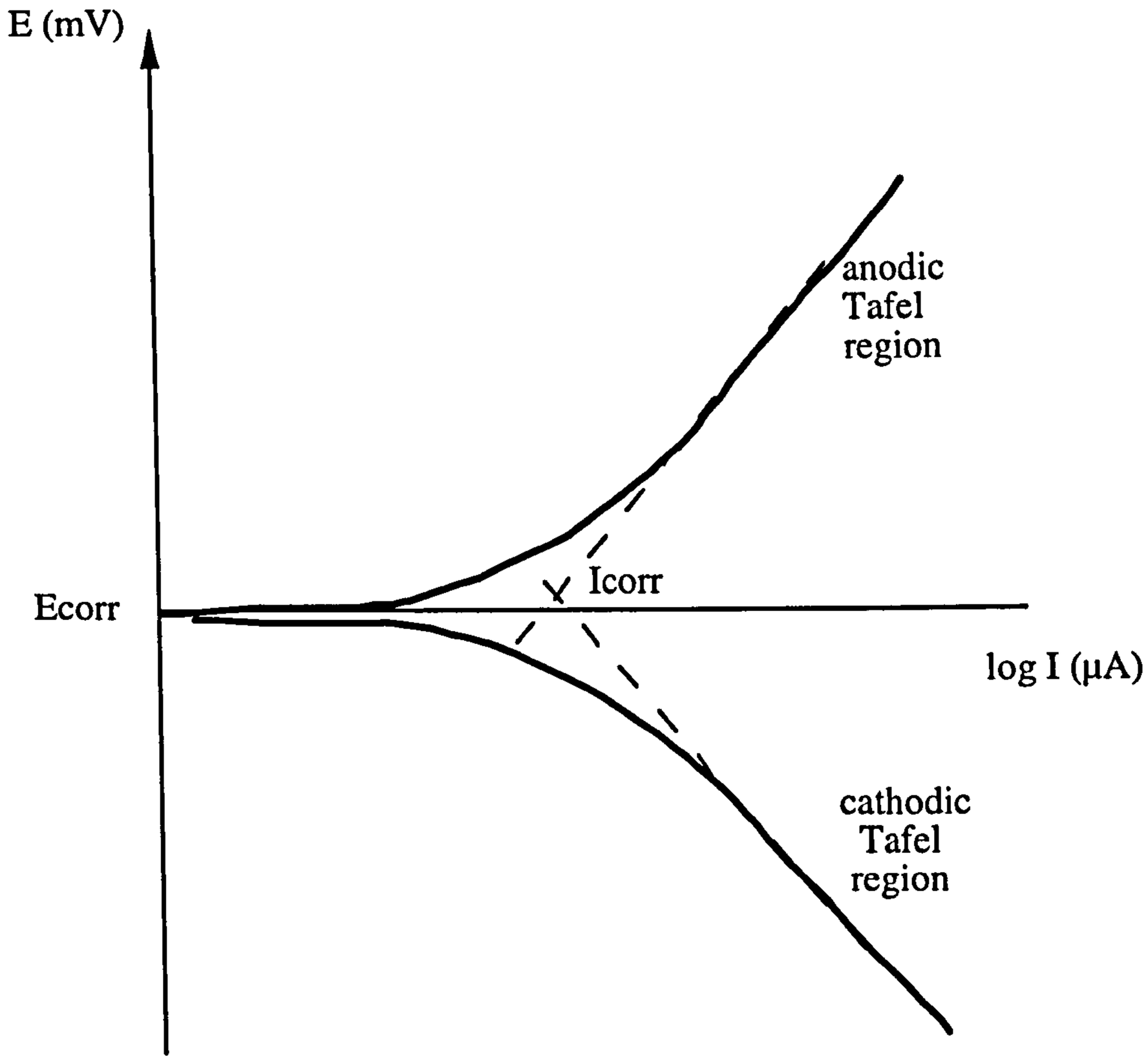


Fig. 1.2. Tafel regions away from $E_{corr}$ and extrapolation to $I_{corr}$

Corrosion monitoring through establishment of $I_{corr}$ can be achieved via linear polarisation techniques developed by Stern and Geary [30] in which a step difference in electrode potential $\Delta E$ is applied to the working electrode in the electrochemical cell and $I_{corr}$ is calculated from

$$I_{corr} = \frac{BI}{\Delta E}$$

where

$$B = \frac{1}{2.3\frac{(b_a + b_c)}{b_a b_c}}$$

and $b_a$ and $b_c$ are Tafel constants in mV/decade for the anodic and cathodic reactions respectively.

Calculation of a corrosion rate by Tafel extrapolation or linear polarisation is only of use in situations where a component is corroding uniformly and a rate of metal loss can be determined for use in design predictions.

Electrochemical reactions do not always follow Tafel kinetics: oxygen reduction is a particular example of a reaction which progresses controlled by effects other than activation effects due to overpotential. Oxygen reduction can follow Tafel kinetics initially but because the mobility of oxygen molecules in an aqueous environment is relatively slow, the rate of consumption can exceed the mass transfer and lead to a depletion of reactants at the surface. Concentration polarisation effects are represented in cathodic polarisation by a reduction in the reaction rate as in Fig. 1.3.

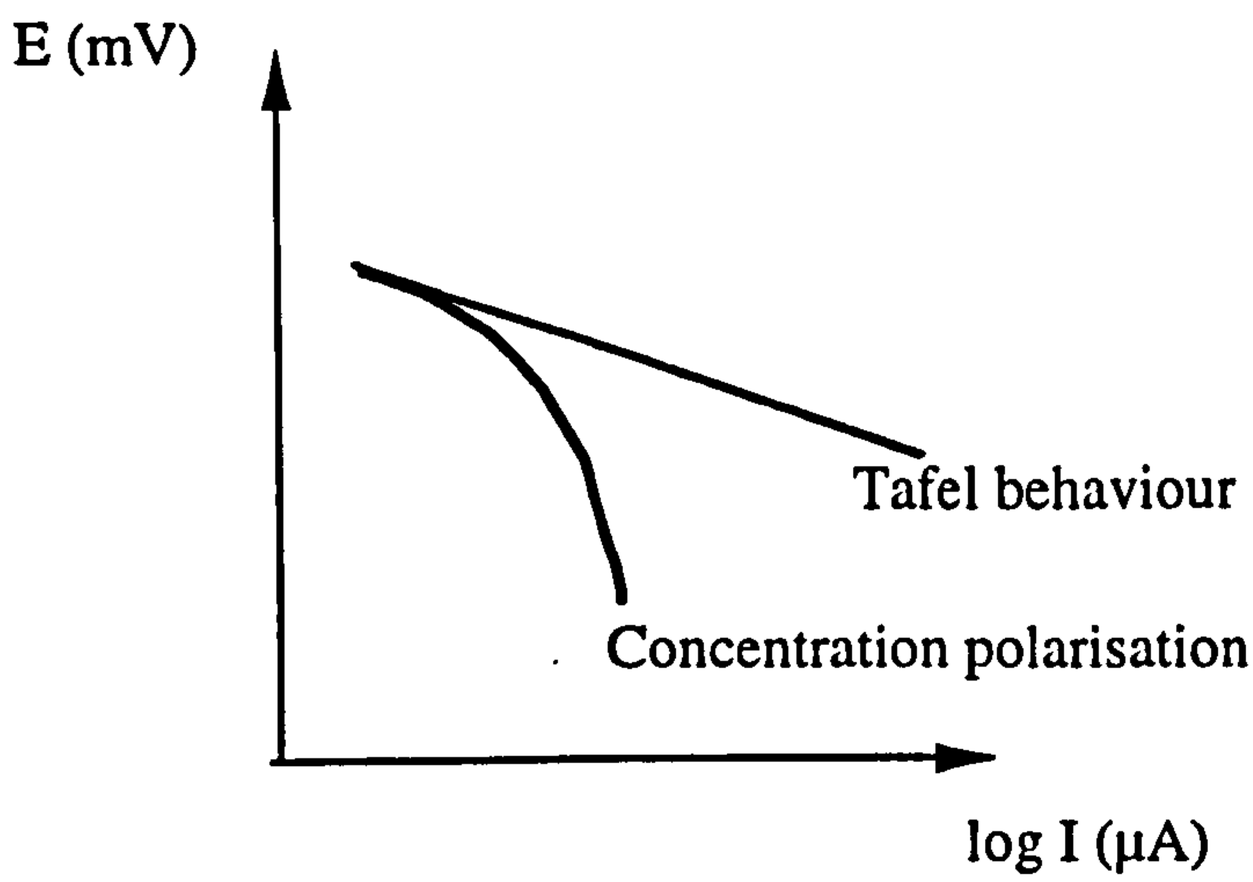


Fig. 1.3. Concentration polarisation effects slow down the cathodic reaction

Passivity

Passivity describes the situation where a metal surface does not readily corrode over its entire surface. Stainless steels exhibit passivity in a range of environments due to a thin adherent film of high electrical resistance. The nature of the passive film on stainless steel, known to be rich in $Cr_2O_3$ has formed the basis of many studies.

Passive behaviour is manifested electrochemically in an anodic polarisation plot of the type shown in Fig. 1.4. Small anodic currents are registered in the potential region between the active-passive transition and a point where the current increases rapidly. The increase in current can be attributed to transpassive dissolution or to localised corrosion.

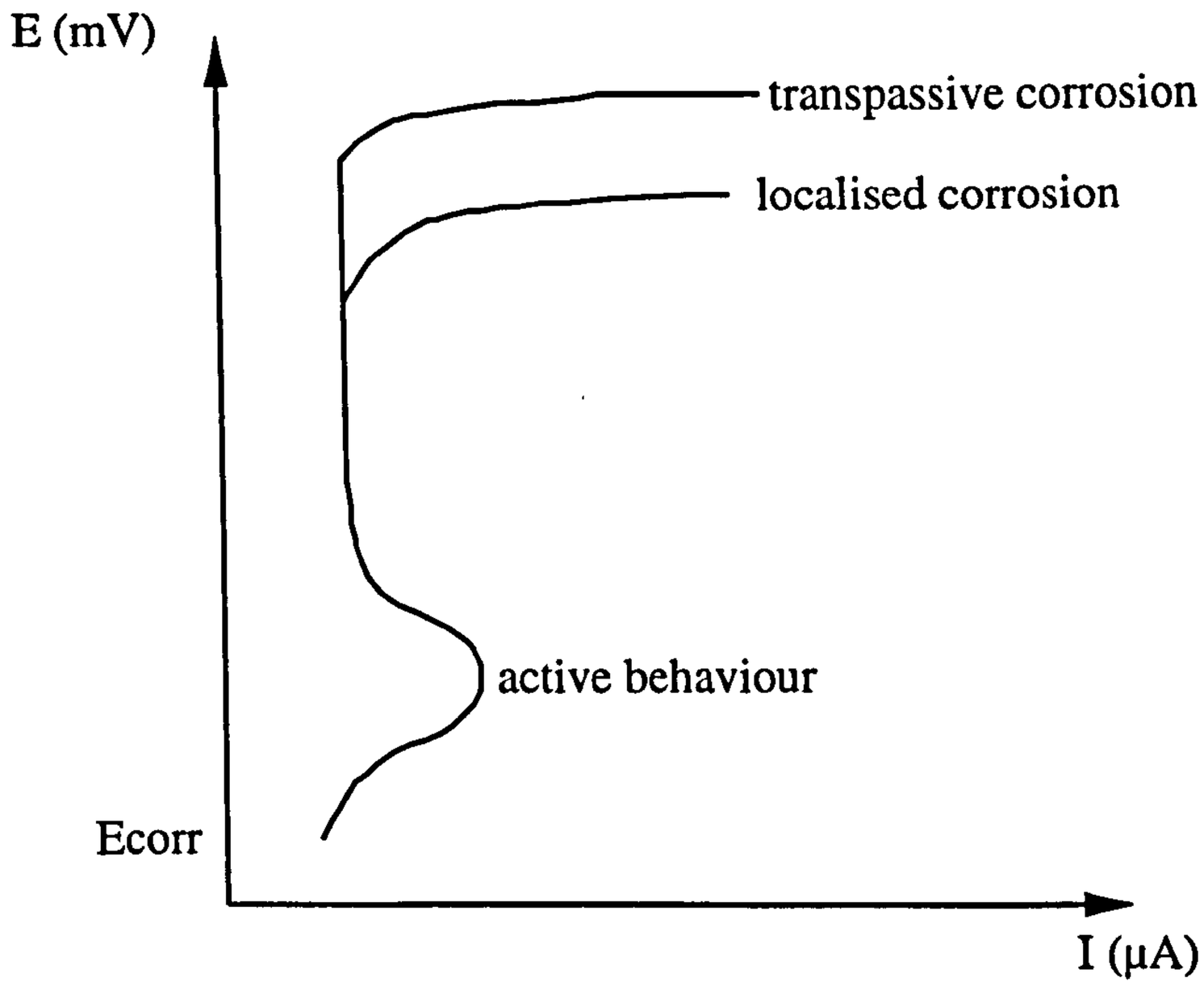


Fig. 1.4. Electrochemical representation of passive behaviour

Localised Corrosion

Localised attack is the most insidious form of corrosion attack since relatively low corrosion currents, concentrated in microscopic areas lead to high rates of local metal loss. Pitting attack is a form of attack which initiates on a free surface due to imperfections of the passive film at non-metallic inclusions or where local loss of integrity occurs.

Crevice corrosion, another form of localised attack, is initiated primarily due to environmental factors which can be local depletion of oxygen under a deposit, high chloride content or local drop in pH. Mechanisms of crevice corrosion and pitting corrosion propagation are similar in that larger cathodic currents (due to the larger cathodic area) outside the pit provide the coupling reaction to stimulate high rates of metal dissolution within the pit. The build up of corrosion products at the mouth of a corroding pit facilitates the separation of the anodic site from the aerated cathodic site to set up an occluded cell represented schematically in Fig. 1.5.

Less common forms of localised attack are grain boundary or intergranular attack in which the areas susceptible to attack are the grain boundaries or regions adjacent. The causative mechanism is partitioning of elements to leave local compositional variations.

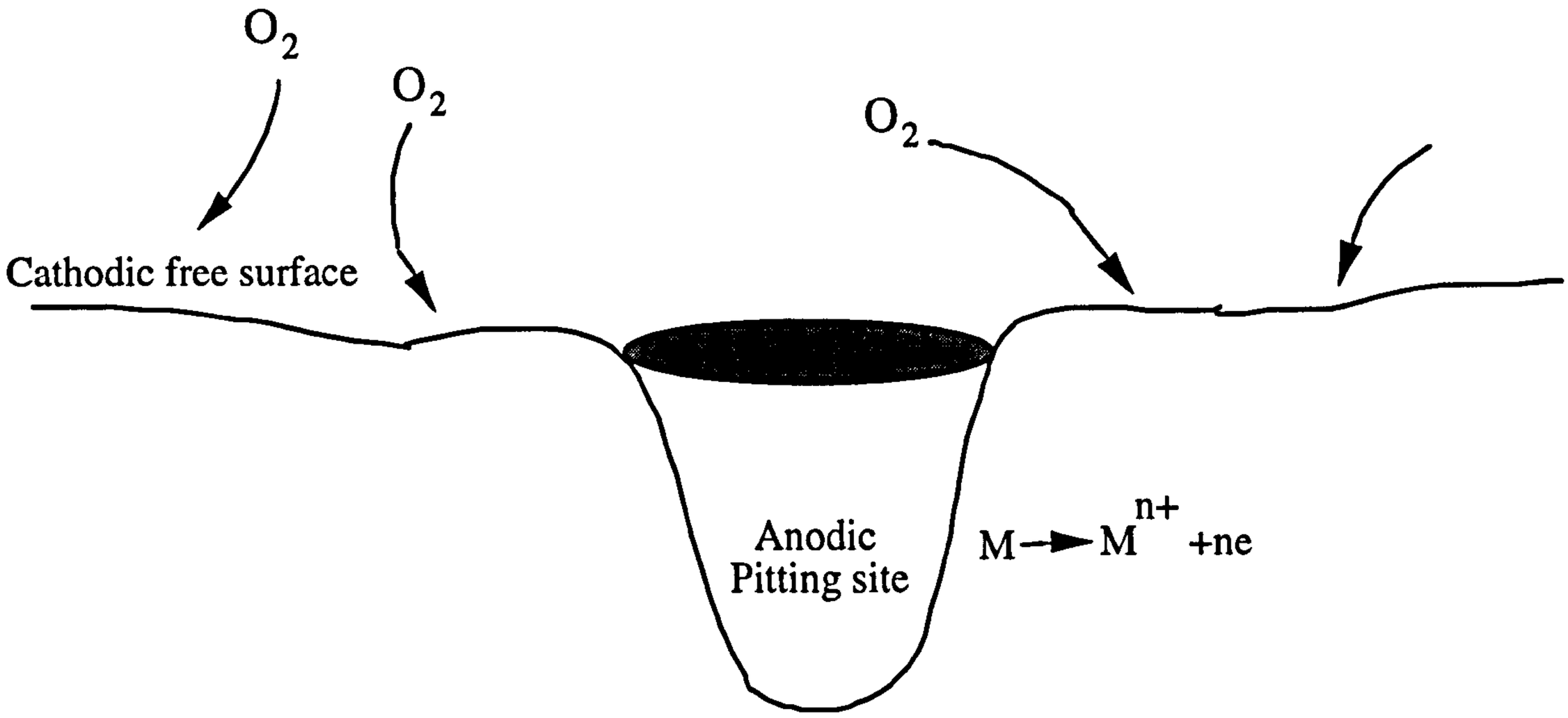


Fig. 1.5. Site of localised corrosion where larger cathodic area stimulates the local rate of metal dissolution in the pit

## References

1. A. I. Asphahani, Corrosion resistance of high performance alloys, *Mater. Perf.*, December 1980

2. C. M. Schillmoller, M. R. Jasner, High performance alloys for offshore process piping, *Mater. Perf.*, January 1984

3. S. T. Mohagen, 25Cr duplex stainless steel, *Stainless Steel Europe*, Vol 6, 10, December 1994

4. Anon. BP exploration reviews progress, *Stainless Steel Europe*, Vol 6, 9, November 1994

5. Anon, Multi-billion project ready to go, *Stainless Steel Europe*, Vol 6, 2, March 1994

6. C. M. Schillmoller, High performance alloys : How they are used offshore, *World Oil*, July 1988

7. G. Ventura, E. Traverso, A. Mollica, Effect of NaClO biocide additions in natural seawater on stainless steel corrosion resistance, *Corrosion*, Vol. 45, No. 4, 1989

8. B. Todd, Corrosion and materials selection in seawater systems, *I. Mech. E. Publication*, C76/79, 1979

9. G. E. Moller, The successful use of austenitic stainless steels in seawater, *Society of Petroleum Engineering Journal*, April 1977

10. J. W. Oldfield. Test techniques for pitting and crevice corrosion resistance of stainless steels and nickel-base alloys in chloride-containing environments, *International Materials Reviews*, Vol. 32, No. 3, 1987

11. A. J. Sedriks. New stainless steels for seawater service, *Corrosion*, Vol. 45, No. 6, 1989

12. M. Pourbaix, Atlas of electrochemical equilibria in aqueous solutions, Pergamon, Cebelcor, 1966

13. J. D. Redmond, K. H. Miska, The basics of stainless steels, *Chemical Engineering*, October 1982

14. C. Compere, P. Jaffre, D. Festy, Ageing of 316L stainless steel in natural seawater. Statistical study of the relationship between open circuit potential, exposure time and pitting potential, CORROSION, NACE 1995

15. A. J. Sedriks, Effects of alloy composition and microstructure on the passivity of stainless steels, *Corrosion*, Vol. 42, No. 7, 1986

16. C. V. Roscoe, K. J. Gradwell, The history and development of duplex stainless steels "All that glisters is not gold", *Presented at the International Conference on Duplex Stainless Steels*, The Hague, October 1986

17. J. N. Wanklyn, The role of Mo in the crevice corrosion of stainless steels, *Corros. Sci.*, Vol. 21., No. 3, p211-225, 1981

18. P. Lovand, Super stainless steels, *Stainless Steel Europe*, Vol. 5, No. 5, November 1993

19. R. M. Davison, J. D. Redmond, Practical guide to using duplex stainless steels, *NiDI Technical Series No. 10 044*, January 1990

20. G. L. Masters, Crevice corrosion of austenitic and duplex stainless steels in seawater, *PhD Thesis*, Cranfield University, 1993

21. A. H. Tuthill, Guidelines for the use of copper alloys in seawater, *Mater. Perf.* September 1987

22. Y. C. Lu, M. B. Ives, C. R. Clyton, Synergism of alloying elements and pitting corrosion of stainless steels, *Corros. Sci.*, Vol. 35, Nos. 1-4, 89-96, 1993

23. M. Renner, U. Heubner, M. B. Rockel, E. Wallis, Temperature as a pitting and crevice corrosion criterion in the $FeCl_3$ test, *Werkstoffe und Korrosion*, 37, 183-190, 1986

24. H. Berns, High nitrogen stainless steels, *Stainless Steel Europe*, Vol. 6, No. 3, April 1994

25. A. H. Tuthill, Usage and performance of nickel-containing stainless steels in both saline and natural waters and brines, *Mater. Perf.*, July 1988

26. R. M. Davison, J. D. Redmond, Practical guide to using 6Mo austenitic stainless steels, *NiDI Technical Series No. 10 032*, December 1988

27. S. Jana, Effect of heat input on the HAZ properties of two duplex stainless steels, *Journal of Materials Processing and Technology*, 33 (1992) 247-261

28. J. Glover, Recent developments in corrosion resistant metallic alloys for construction of seawater pumps, *Mater. Perf.*, July 1988

29. L. L. Shreir, *Corrosion*, Vol. 1, George Newnes, London, 1963

30. M. Stern, A. L. Geary, Electrochemical polarization, *J. Electrochem. Soc.*, 1957, Vol. 104, No. 1, 56-62

# Chapter 2

# An Investigation of the Effect of Temperature on the Corrosion Behaviour of High-Grade Alloys in Seawater

## Introduction

In this chapter, the effect of temperature on the electrochemical characteristics and mechanisms of corrosion is investigated. A series of potentiodynamic tests were conducted in seawater in the temperature range 18°C - 60°C. Anodic polarisation test results were used to compare the susceptibility of each material to attack and the effect of elevated temperature on the passivity characteristics. These data were compared to those existing in the literature for the determination of a critical pitting temperature or a critical crevice temperature.

The work was then extended to focus on the effect on the electrochemical characteristics and corrosion mechanisms at a range of temperatures from ambient to 90°C in concentrated brine solution. Only three materials were considered because the research was conducted primarily to solve a specific engineering application to which the four materials were viable options. Details of the application are given later.

The kinetics of the predominant cathodic reaction (oxygen-reduction) and the hydrogen-production reaction were studied using potentiodynamic cathodic polarisation scans. The chapter discusses mechanistic changes in the localised corrosion processes and relates this to the observed electrochemistry. The applicability of Pitting Resistance Equivalent (PRE) and related empirical formulae is discussed.

## Literature Review

Localised corrosion resistance of stainless steels is generally accepted as the main parameter which limits their suitability for seawater service [1,2]. Thus, continual alloy development is aimed at improving a material's resistance to in particular crevice and pitting corrosion which constitute the most common forms of localised attack. As was said previously, the terms pitting and crevice corrosion are often used interchangeably since workers have established that the chemical mechanisms are similar, however the initiation conditions are somewhat different. Crevice corrosion occurs within the crevices formed by for example rivets, bolts and valve seats whereas pitting corrosion initiates on an open surface.

Although localised forms of corrosion lead to much smaller weight losses than general corrosion, they represent particularly severe types of attack, the consequences of which can be significant loss of mechanical properties or perforation of sealed vessels or pipes. Figure 2.1 shows severe crevice corrosion of a stainless steel bolt (UNS S31603) which formed a crevice with a wooden beam in the splash zone of the sea and after 3 years in service was severely attacked by localised corrosion.

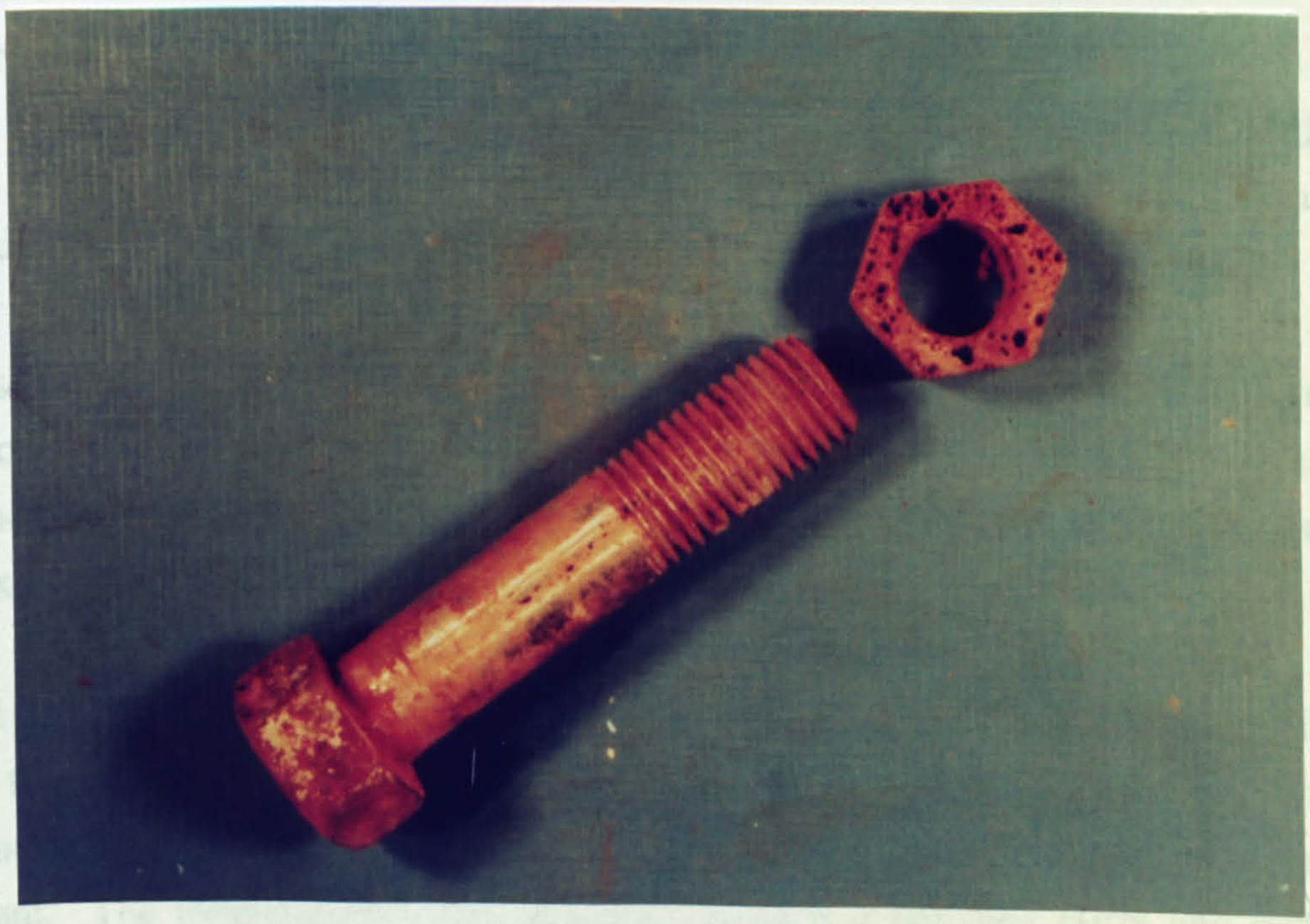

Fig. 2.1. Crevice corrosion on a stainless steel bolt after 3 years in the splash zone

It has been recognised that initiation and propagation of localised forms of attack are enhanced in static seawater [3-6] - the presence of moving seawater can in some

circumstances prevent the creation of an occluded cell to initiate localised attack and by the supply of oxygen to promote passivity [7]. During periods of maintenance or plant shutdown in seawater handling systems, pumps and piping are often flushed with a low Total Dissolved Solids (TDS) fluid to reduce the probability of attack initiation.

Selection of stainless steels for seawater applications is often achieved by reference to empirical formulae such as the PRE (Pitting Resistance Equivalent) or "Wirksumme" [8] which are derived from field data of materials in service. PRE expressions are based on the knowledge that alloying elements which are important for resistance to pitting attack are Cr, Mo and N. Several authors have attempted to quantify the relative influence of each element by developing formulae of the type :

$$\mathbf{PRE_N = X\%Mo + Y\%Cr + Z\%N}$$

where a higher $PRE_N$ denotes better pitting resistance [9]. X, Y and Z are assigned different values according to the importance of each element. Early formulae included Cr and Mo only since the importance of N was at that time not realised [8]. Different workers have developed formulae where values of X are normally 1, but values of Y range from 3-3.3 and for N are more diverse between 12.8 and 30.

A $PRE_N$ of no less than 38 is predicted [10] to be required to eliminate problems due to crevice attack in ambient temperature seawater whereas more generally according to Roscoe et al. [11], localised corrosion can be deterred in oxygenated seawater by employing stainless steel with $PRE_N > 40$.

Expressions analogous to the PREs do not exist for high grade alloys such as the nickel-base Inconel types or for Cobalt based alloys such as the Stellite group. However since the principal alloying elements are Cr, Mo and N, it may be assumed in some cases that these expressions could equally be applicable.

Natural seawater temperatures and salinities are very different world-wide and for this reason the electrochemical corrosion behaviour of high-grade alloys in seawater at different temperatures and the effect of temperature on the mechanisms of attack are important. The temperature in the northern North Sea between 60°N and 62°N was found to vary annually from a minimum of 8°C to a maximum of 13°C [8], whereas in the China sea it can be in excess of 30°C. Similarly the salinity in the Arabian Gulf can be up to 50,000ppm in contrast to the dilute water of 28,000ppm in the Clyde Estuary. However, much more extensive variations in seawater temperatures and TDS are

encountered in industrial seawater handling systems - in desalination processes, in oilfield applications, heat exchangers in power generation plants as examples.

Desalination by Reverse Osmosis (RO) is carried out within the temperature range 18°C-35°C [12] with brine concentrations of up to 50% more than the seawater feed [13]. Typical upper brine temperatures of 120°C are encountered in the Multistage Flash (MSF) process and chloride content of the concentrated brines can reach 45,000-50,000ppm [14]. UNS S31603 type stainless steel has been shown to suffer pitting, crevice and intergranular corrosion under conditions in the flash chambers of such plant [14].

Condenser tubing in seawater-cooled nuclear power plants was traditionally fabricated from copper-base alloys but service experience has shown inadequate corrosion resistance and therefore corrosion resistant high-grade alloys are being investigated [15]. Cooling water characteristics can vary from brackish waters of approximately 3000ppm chloride content at a temperature of 50°C to typical North Sea water with chloride content of 15,000ppm-17,000ppm.

Production equipment in oilfield applications can be required to handle fluids of varying corrosivities. In addition to the level of dissolved gases and suspended solids which constitute an aggressive media, the temperature of 'produced water' can be in excess of 90°C and have a TDS four times greater than that of normal seawater. Hence the corrosivity of a fluid is dependent on a number of interdependent variables.

Corrosion of carbon steels in high temperature water has been studied by several authors [16,17]. The corrosion rate has been shown to increase by approximately 50% between the winter temperature of 7°C and to the summer temperature of 27-29°C [18]. It has been recognised that dissolved oxygen accelerates corrosion in high temperature water. Since solubility of oxygen decreases as the temperature increases, several authors have tried to identify a level of oxygen at which corrosion stops but to date none has been found. However, it is generally agreed that at elevated temperatures the corrosion rate of carbon steel reduces due to the reduced oxygen content to stimulate the cathodic process.

Temperature increase in saline or non-saline waters affects the structure and composition of the oxide formed on carbon steel [19] and thus influences the rate of corrosion. Potter and Mann [20] showed a double layered oxide to exist on carbon steel with an inner layer of compact magnetite and a more loosely adherent outer layer of well developed magnetite crystals. However Bloom et al. [21] showed the formation of

a single layered magnetite and proposed a mechanism by which pores or gaps in the oxide are blocked by migrating $O^{2-}$ or $Fe^{2+}$ ions.

Stainless steels and related alloys corrode in seawater predominantly by localised corrosion mechanisms and it was shown by Hodgkiess and co-workers [4] that at ambient temperature the level of dissolved oxygen in seawater plays a crucial role in determining the corrosivity of two 300 series stainless steels [4,5]. However, the effects of temperature on the mechanisms and rate of localised corrosion initiation and propagation are not well documented. It has been shown that increased temperature increases the susceptibility of stainless steels to localised corrosion initiation but propagation rates can be lower at higher temperature [22]. The net effect of these conflicting tendencies presents a complex interaction of kinetic mechanisms.

Saricimen et al. [14] recognised that the observed decrease in the passive range of UNS S31603 at 60°C compared to 25°C is due to the solution being more corrosive at 60°C owing to increased reaction kinetics. They postulated that the higher temperature stabilised a passive film with different structural characteristics than that formed at the lower temperature. The thermodynamics of hydrolysis reactions between the ions of the alloying elements such as Fe, Cr, Mo and Ni at elevated temperature are assumed to change as was shown [3-6,23] and the normally non-crystalline hydrated oxides such as M-OH and M-OOH tend to become more crystalline. The mechanisms by which the form of the passive film affects the localised corrosion initiation and propagation is not fully understood.

Several workers have investigated the corrosion resistance of passive alloys using the Critical Pitting Temperature (CPT) and Critical Crevice Temperature (CCT) criteria. The CPT encompasses several definitions which depend on the experimental method used. Determination can involve use of electrochemical techniques or can be via simple immersion tests. In either test, the CPT is effectively a ranking parameter which can be useful in comparing the susceptibility to localised corrosion of different types and grades of material.

Immersion techniques to determine CPT and CCT are normally variants of the ASTM G48 $FeCl_3$ test in which specimens are immersed for different lengths of time and the weight loss due to corrosion measured. As early as 1938, a method for determining the relative susceptibility to pitting of stainless steels in 10%$FeCl_3.6H_2O$ solution was reported [24]. Instead of weight loss, temperature is the ranking parameter in CPT and CCT tests [1]. Immersion in 10% $FeCl_3$ at temperatures progressively increased from ambient temperature followed by microscopical examination allows a temperature to be

defined, above which crevice or pitting attack occurs. The specimen arrangement differs whether CPT or CCT is being determined - the normal arrangement for CCT being that used by Dundas et al. and other workers [1,25] where a rubber band forms a crevice when wrapped around two Teflon cylinders placed on the major faces of the sheet specimen.

An alternative method of determining CCT and CPT is using potentiostatic control within an electrochemical cell. The specimen is held at a fixed potential versus the Saturated Calomel Electrode (SCE) and the temperature progressively increased at a predetermined rate. The CPT or CCT is defined as the minimum temperature to cause a rapid increase in current flow signifying pitting or crevice corrosion. The CCT or CPT is therefore dependent on the holding potential and on the rate of temperature increase. Oldfield suggested that this technique, although suitable as a means of ranking materials qualitatively is of only limited use in predicting actual service performance since the same sample is used at progressively elevated temperatures. Thus changes will occur in the crevice solutions and it may well be that initiation actually occurs at a lower temperature than the defined CCT or CPT [1].

Potentiodynamic anodic polarisation scans have been utilised to develop data on the CPT of superferritic stainless steels [26] where a significant lowering of the pitting potential is indicative of the critical pitting temperature. Determining the CPT by electrochemical techniques presents problems in specimen preparation since electrical connection must be achieved in the absence of a crevice.

Qvarfort [27] developed the electrochemical Avesta cell to measure CPT which eliminated crevice corrosion and in this work described the very sharp transition between transpassive corrosion and pitting corrosion. A series of potentiodynamic polarisation tests were performed at small temperature intervals. The pitting potential as a function of temperature was recorded.

In the transpassive region, the pitting potential varies very little with temperature - pitting corrosion is signalled by a drastic decrease in pitting potential over a small (1°C) change in temperature. The CPT was therefore formally defined as the maximum temperature at which only transpassive corrosion occurs.

Mathematical correlations between the CPT and the $PRE_N$ and the CCT and the $PRE_N$ have been developed by linear regression and from experimental data from various sources [9,24]. In 10%$FeCl_3$, M. Renner et al. [24] developed the formulae

$$\mathbf{CPT\ (°C) = 2.5\%Cr + 7.6\%Mo + 31.9\%N - 41}$$

and

$$\mathbf{CCT\ (°C) = 3.2\%Cr + 7.6\%Mo + 10.5\%N - 81}$$

which illustrate a higher weight influence of Cr and a lower importance attributed of N in resisting crevice corrosion at elevated temperature. Reference to the work of Streicher [28] implies that perhaps a Cu factor should be included in formulae of the type above since it has been shown to promote the growth of pits but retard pit initiation. Similar correlations of the type CPT = A + b PRE, where A and b are constants, have been developed and are summarised in [9].

Several workers have deduced CPT and CCT values for high-grade alloys and generally the agreement is that the CCT value is consistently lower than the CPT value for a particular alloy.

A. Garner [29] showed that the CPT increases with Mo content of the alloy and quoted values of 87°C and 9°C for the CPT of UNS S31254 and UNS S31603 respectively in 10%$FeCl_3$. Roscoe et al. [11] studied the CPT and CCT of stainless steels in seawater and recorded values of CPT and CCT as listed in Table 2.1.

| | **CPT** | **CCT** |
|---|---|---|
| UNS S32760 | >100°C | 78°C |
| SAF 2205 | 51°C | 34°C |
| UNS S31254 | 83°C | 62°C |
| 25Cr Duplex | 58°C | 38°C |
| UNS S31603 | 18°C | 11°C |

Table 2.1. Experimentally determined CPT and CCT values

J. Chance et al. [30] illustrated that N has a beneficial effect in increasing the CPT up to a level of 0.2-0.3% above which no improvement is recorded.

Nickel base alloys have been studied [24] and the CPT and CCT values >85°C were recorded for Inconel 625 in 10%$FeCl_3$ and importantly it was observed that Cr-free Ni-Mo alloys did not resist pitting in 10%$FeCl_3$ thus indicating that Mo is beneficial in the presence of Cr.

It is widely accepted that halide ions are particularly aggressive to the passive film formed on stainless steels and related alloys. Chloride ions have been shown to be the species responsible for localised breakdown of the passive film [31] due to their ability to replace water molecules in undeveloped parts of the hydrated oxide film and form soluble metal chloride complexes which are easily removed to achieve film breakdown. However, the relation between bulk chloride concentration and localised corrosion resistance has been shown to be complex [27]. It has been shown [32-34] that the pitting potential determined by potentiodynamic tests is proportional to the logarithm of the chloride content.

**Experimental Methods**

Electrochemical Monitoring

The experimental techniques utilised in this programme to monitor the electrochemical behaviour of the materials consisted of DC potentiodynamic and potentiostatic tests. Specimens with an electrical connecting wire were embedded in a non-conducting resin and the exposed face (10mm x 10mm) subsequently ground to a 600-grit finish. A number of samples were further polished using 1μm-diamond paste to facilitate microscopic examination after corrosion tests. Potentiodynamic tests were carried out using a computer-controlled potentiostat which was programmed to shift the specimen potential relative to a reference Saturated Calomel Electrode (SCE) from its free corrosion potential ($E_{corr}$) at a rate of 15 mV/min in either the anodic or the cathodic direction. The same scan rate was used in all potentiodynamic tests reported in this thesis. The current in the cell corresponding to each potential was recorded automatically. A platinum-spade auxiliary electrode was employed. The experimental set-up, incorporating the electrochemical cell was previously described in chapter 1 and shown in Fig. 1.1. For each temperature , three replicate tests were performed for each material in the anodic polarisation section and two in the cathodic polarisation section.

Experiments were carried out in a solution of 35,000 TDS of "Instant Ocean", a product containing all the ionic constituents of sea water. Anodic polarisation scans were carried out on each material at a range of temperatures between 18°C and 60°C. For the materials showing passive behaviour in static sea water, on increasing the potential from the free-corrosion value $E_{corr}$ in an anodic polarisation scan, low currents are recorded until a potential, $E_b$, is reached. $E_b$ represents the potential at which the current starts to rise significantly over a small shift in potential indicating a loss of passivity or film breakdown. $E_b$ is labelled the "breakdown" or "damaging" potential,

rather than the pitting potential used by several authors, to emphasise that mechanisms other than pitting can induce the loss of passivity. The current corresponding to the breakdown potential is denoted $I_b$ (the breakdown current). Each anodic polarisation scan was reversed once the current reached 500μA and the current $I_{max}$ represents the maximum current attained should the current not begin to fall immediately after scan reversal. $E_r$ is called the repassivation potential and represents the potential at which the current falls to the small values recorded during the forward scan. These parameters are shown schematically in Fig. 2.2 for a material exhibiting passive behaviour.

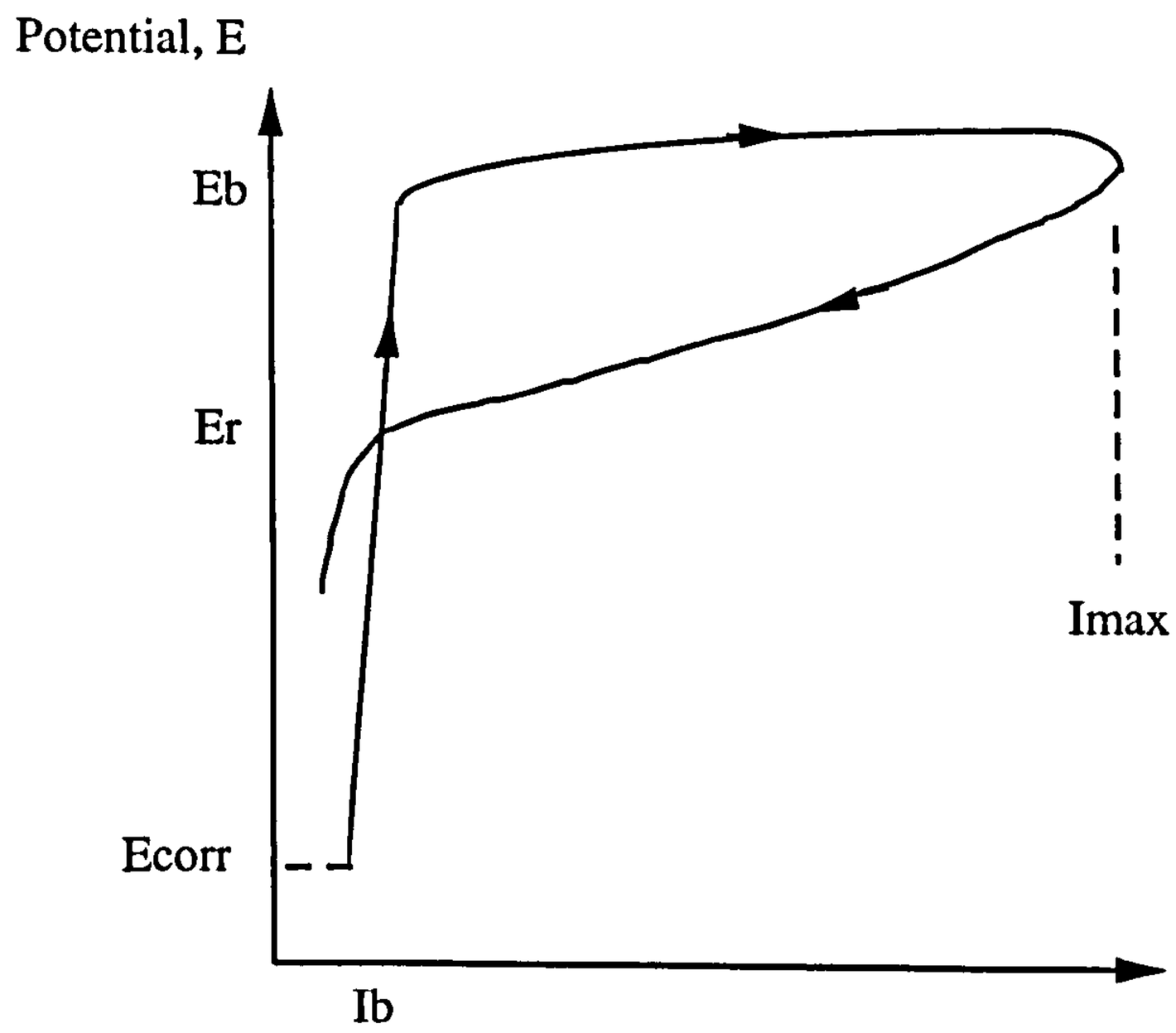


Fig. 2.2 Anodic polarisation of a 'passive' material and the important electrochemical parameters

Cathodic scans were carried out on all materials at 18°C and 50°C under static conditions. The cathodic polarisation curve in aerated seawater is normally plotted on a semi-log scale and is of the form illustrated in Fig. 2.3. The initial reaction - oxygen reduction - proceeds until a limiting current density is achieved and at that point the rate of oxygen transport to the electrode surface is not sufficient to maintain a steady activation controlled reaction rate and hence the reaction becomes diffusion controlled. When the electrode potential becomes sufficiently negative, an alternative reaction - hydrogen production/evolution - can occur and is not under diffusion control. As such, the reaction in the hydrogen production region follows Tafel kinetics until very high currents are achieved.

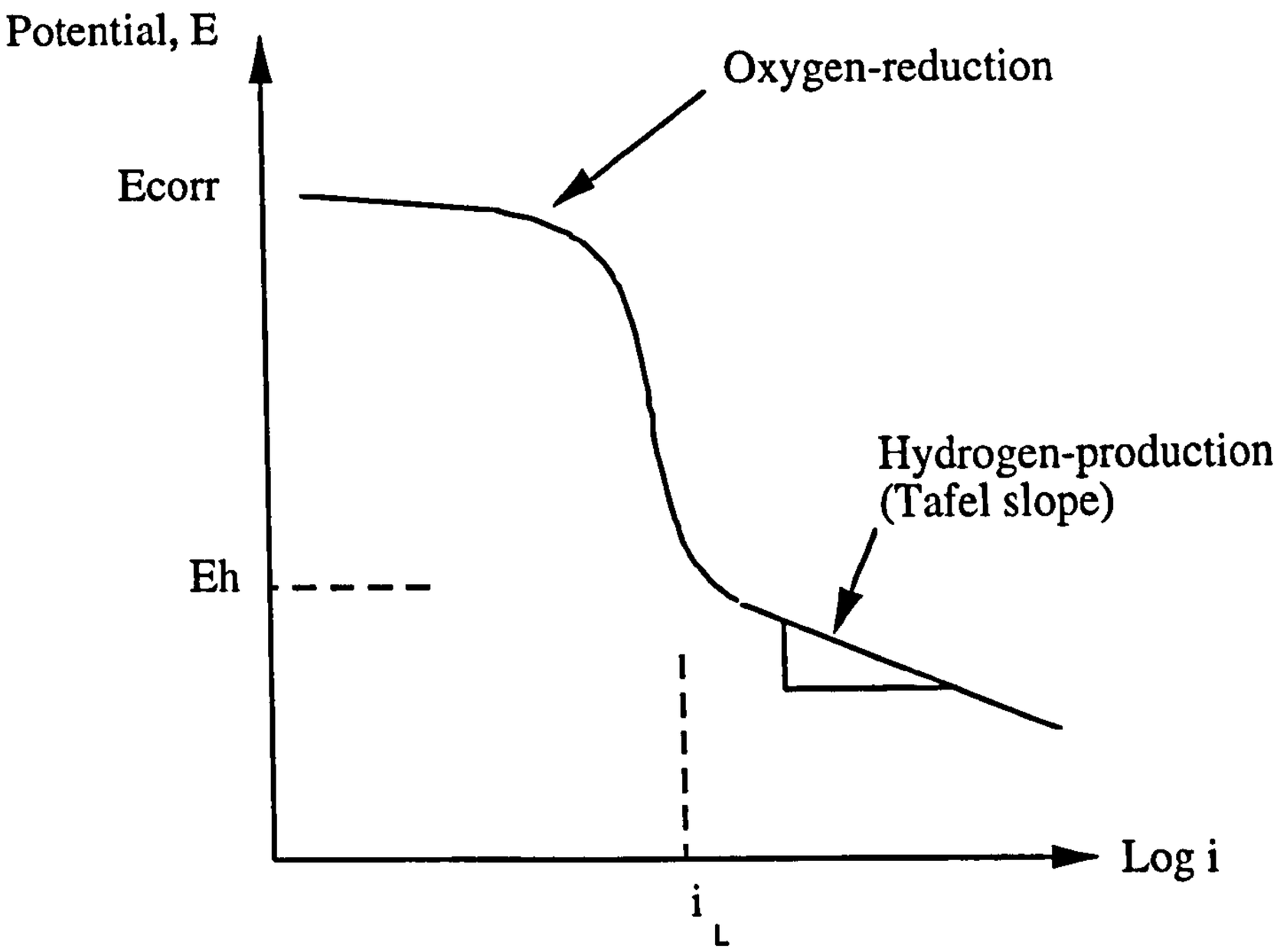


Fig. 2.3. Schematic representation of a cathodic polarisation curve in aerated seawater

Static tests were conducted with the specimen and the two electrodes in a water bath at the appropriate temperature. At temperatures above 50°C the reference electrode was connected to the electrochemical cell via an agar salt bridge since the stability of saturated calomel electrodes at elevated temperature is doubtful. For both the anodic and the cathodic polarisation experiments, the specimens were exposed to the experimental conditions for 4 hours before polarisation scans began.

Specimen Examination and Analysis

On conclusion of the electrochemical tests the specimens were removed from the water bath, rinsed in distilled water and air dried.

Microscopic analysis involved both light and scanning-electron facilities. The objective of this examination was to characterise the type and extent of attack which facilitated the observed rapid rise in current at potential $E_b$. After, each anodic polarisation test details of the relevant types of attack were recorded, such as the extent (if any) of crevice attack at the metal/resin interface, the maximum pit depth, the approximate number of pit initiation sites, pit position and morphology and the general surface appearance. Energy-dispersive Electron Probe Micro-Analysis (EPMA) facilities available on a Leica Cambridge, Stereoscan 360 Scanning Electron Microscope (SEM) were used and all analyses were subject to atomic number, absorption and fluorescence (ZAF) corrections.

**Results - Anodic Potentiodynamic Tests**

Static tests in ambient temperature sea water clearly demonstrated (Fig 2.4) the superiority of the duplexes, super-duplex and the superaustenitic stainless steel over UNS S31603 and also over the nickel-base and cobalt-base alloys in resisting passive-film breakdown (i.e. higher $E_b$ values) and this enhanced corrosion resistance of the higher-alloyed stainless steels is in accordance with much other previous research conducted at ambient temperature.

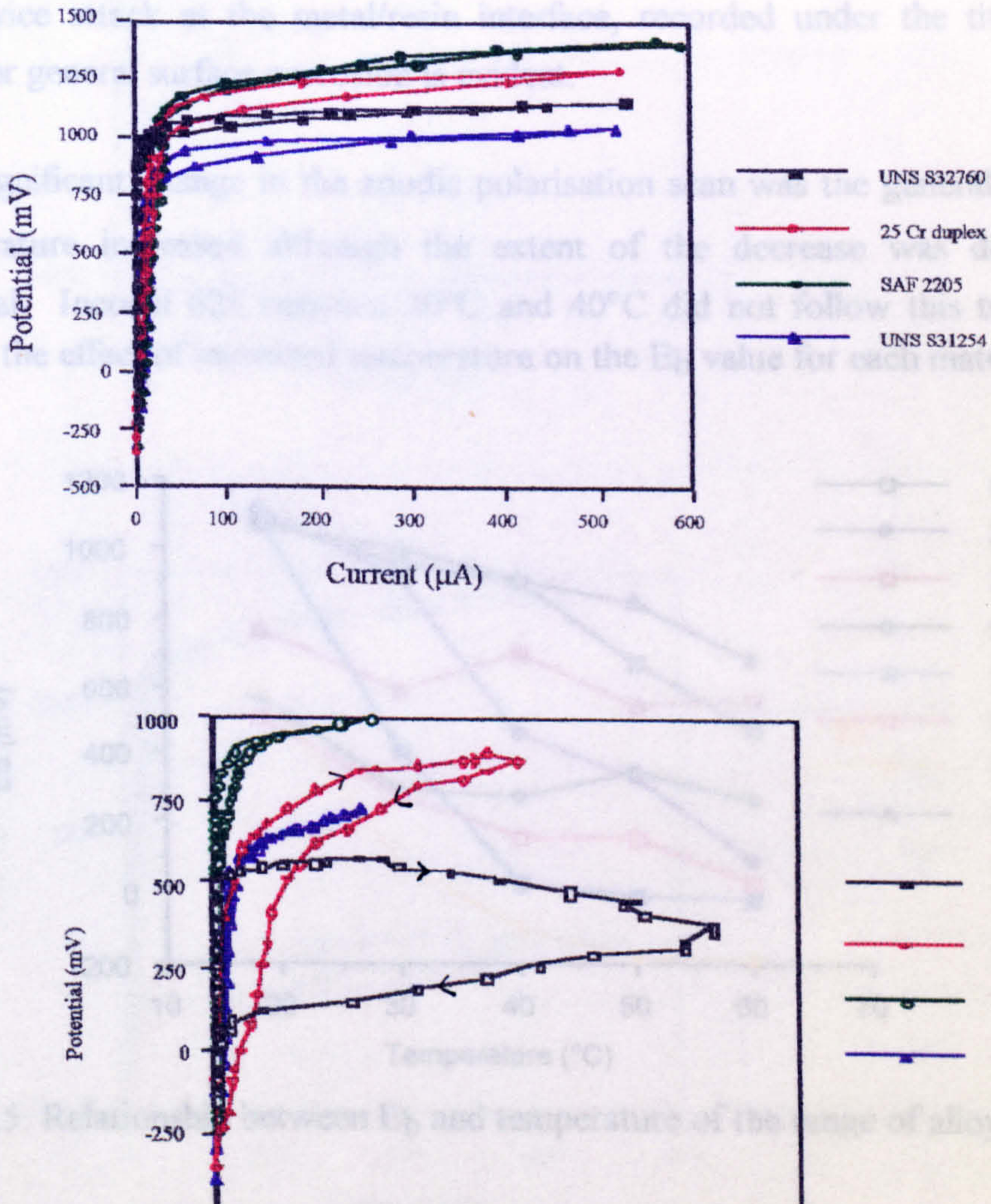


Fig. 2.4. Anodic polarisation at 18°C in static seawater (a) Superduplex, superaustenitic and duplex stainless steels and (b) cobalt-base alloys, Inconel 625 and austenitic UNS S31603 stainless steel

Although it was not possible to reasonably distinguish between the corrosion resistance of the top four alloys using the electrochemical parameter, $E_b$, some differentiation was

possible from the results of the microscopic examination of anodically polarised specimens (Table 2.2). This revealed that the extent of crevice and pitting attack on the superduplex and superaustenitic alloys was noticeably less than on the other two duplex stainless steels.

Distinct differences in all the anodic electrochemical parameters ($E_{corr}$, $E_b$, $I_{max}$, $E_r$, $I_b$) were observed as tests were carried out at temperatures increased above ambient (18°C). The details of all such changes are given in Tables 2.3-2.6. Quantification of the attack at each temperature is by measurement of the maximum pit depth (MPD), length of crevice attack at the metal/resin interface, recorded under the title "crevice" and whether general surface corrosion is evident.

One significant change in the anodic polarisation scan was the general fall in $E_b$ as the temperature increased although the extent of the decrease was dependent on the material. Inconel 625 between 30°C and 40°C did not follow this trend. Figure 2.5 shows the effect of increased temperature on the $E_b$ value for each material.

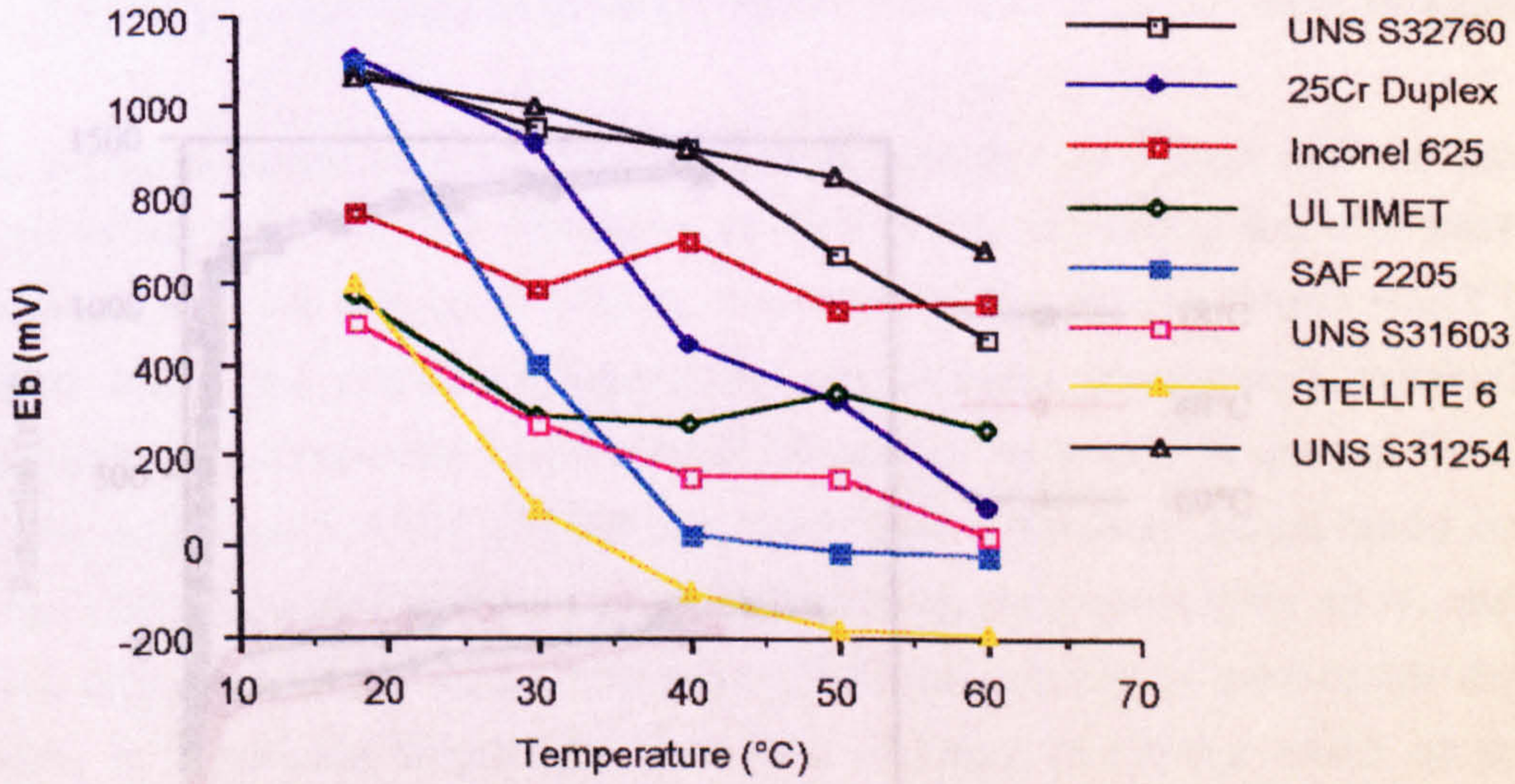


Fig. 2.5. Relationship between $E_b$ and temperature of the range of alloys

These values can be compared later to the results under conditions of liquid impingement. Inconel 625 proved to be the least affected by increased temperature and at the other extreme, the cobalt-based Stellite 6 showed a much more active $E_b$ at 60°C. Figure 2.6a shows the changing characteristics of the anodic polarisation curve, on increasing the temperature of the seawater, for the superaustenitic UNS S31254 stainless steel which exhibited good resistance to passivity breakdown. In contrast, Fig 2.6b shows the SAF 2205 duplex alloy which at 18°C exhibited behaviour comparable to the

superduplex stainless steel yet at 60°C exhibited only a very small passive potential range.

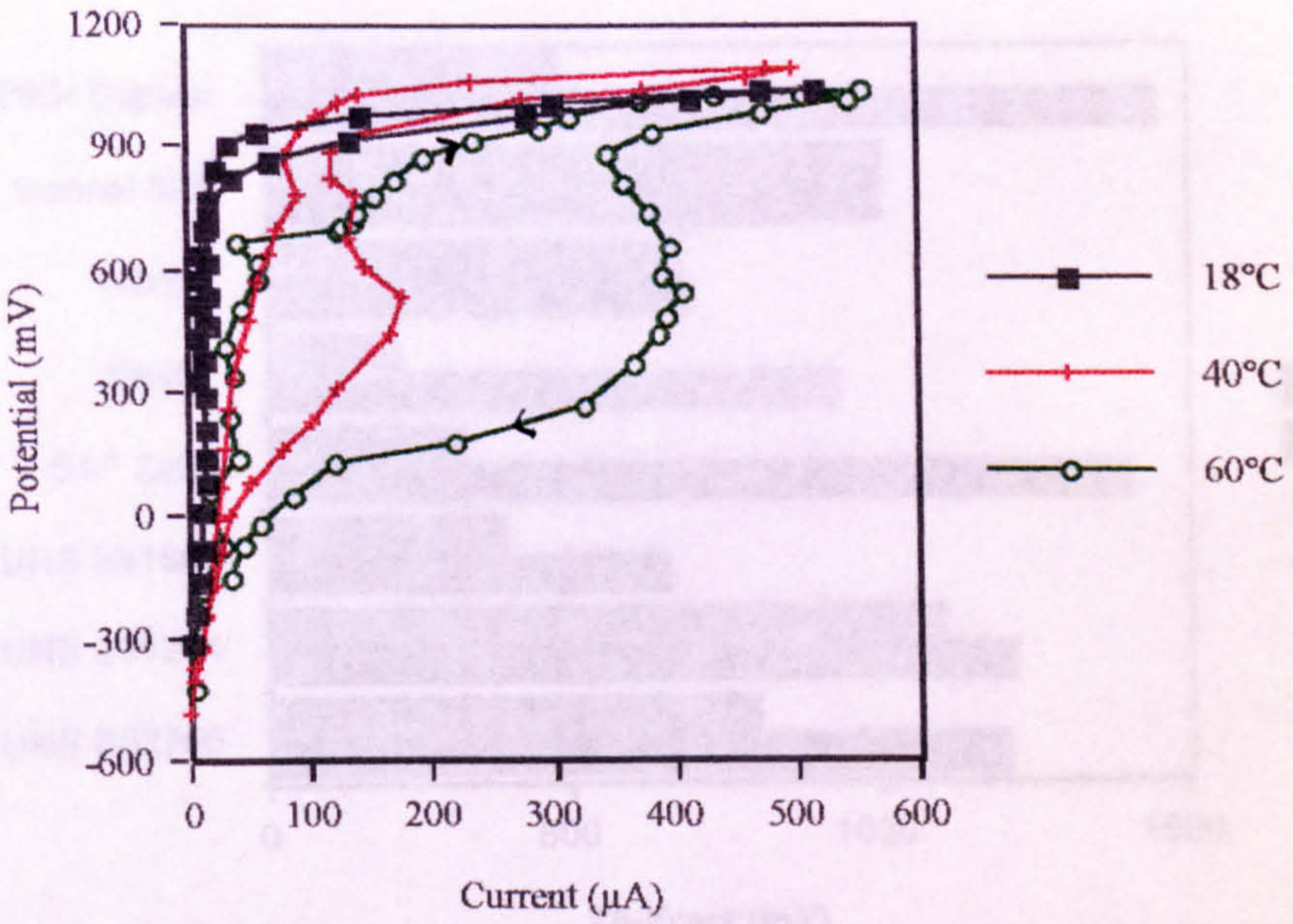


(a)

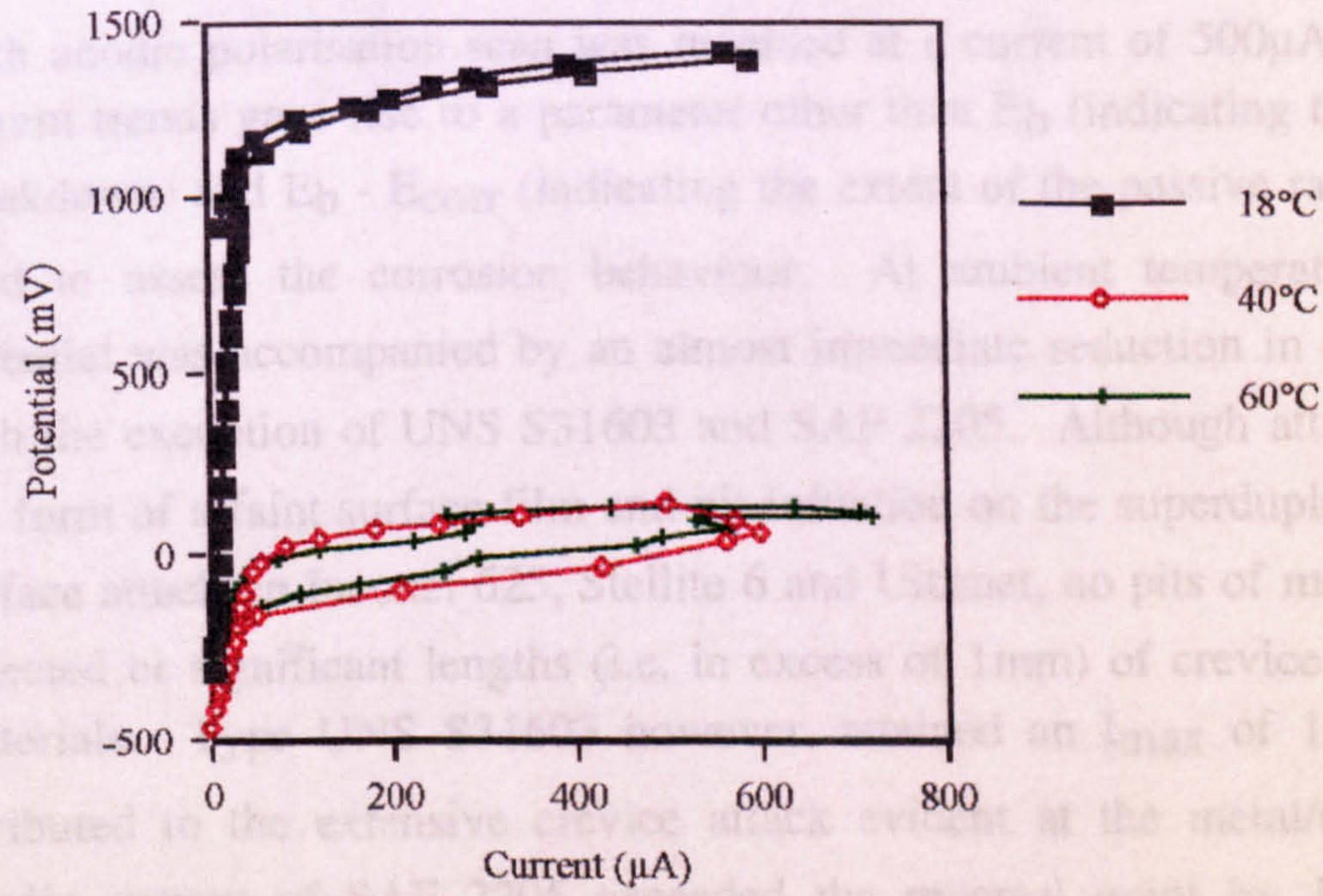


(b)

Fig. 2.6. Evolution of anodic polarisation curve of (a) Superaustenitic UNS S31254 alloy and (b) SAF 2205 duplex alloy

The parameter $E_b$ - $E_{corr}$ gives an indication of the potential range over which the material is in the passive state. As expected, the parameter is very much material dependent and for each stainless steel and Stellite 6, significant decreases were recorded as the temperature increased from 18°C to 60°C (Fig. 2.7). However, negligible changes

as the temperature increased from 18°C to 60°C (Fig. 2.7)for Inconel 625 and Ultimet indicated that the increased temperature did not significantly affect the passive range of these two materials.

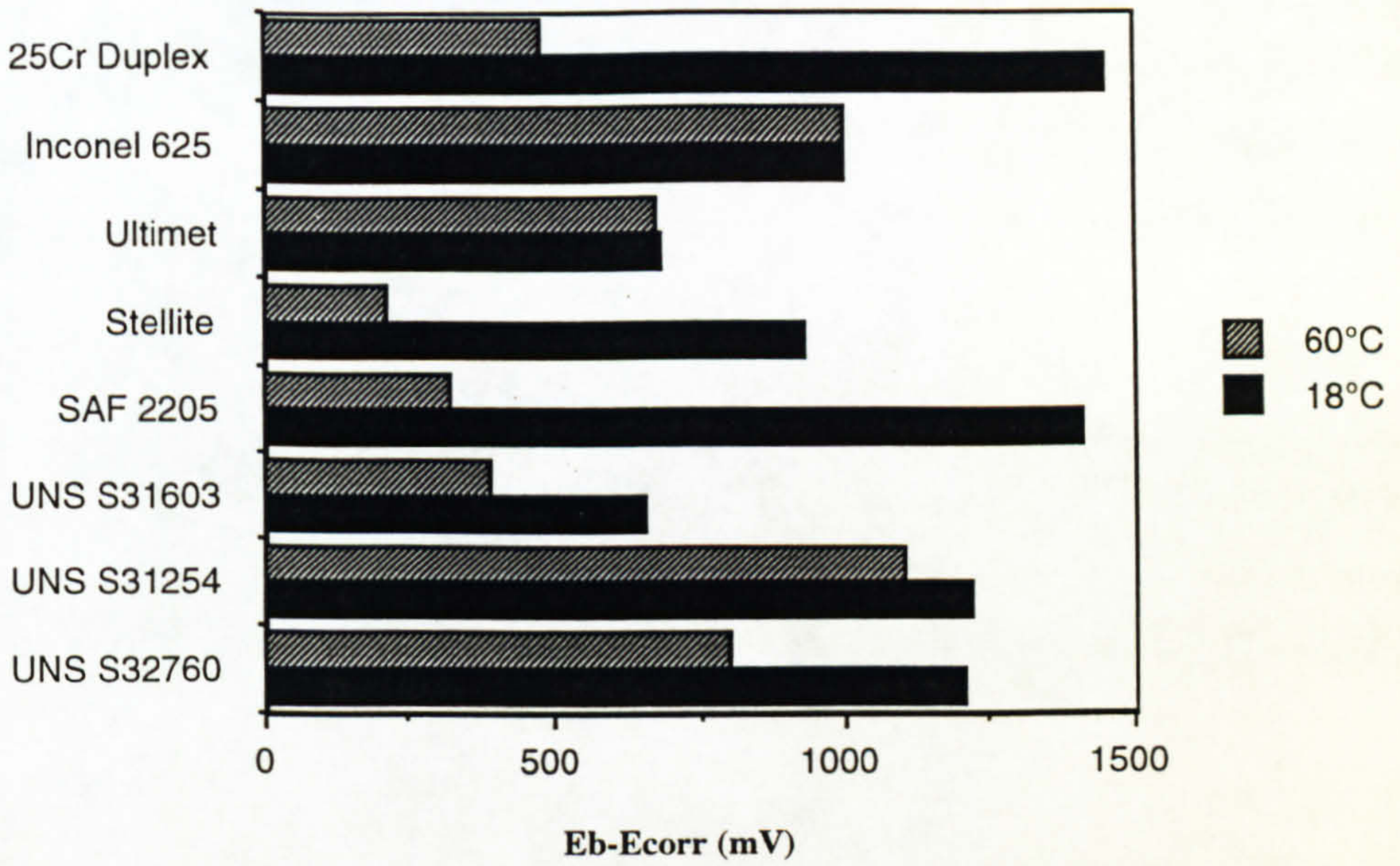


Fig 2.7. Change in $E_b$-$E_{corr}$ as the temperature is increased in the range 18°C-60°C

Each anodic polarisation scan was reversed at a current of 500μA and the subsequent current trends gave rise to a parameter other than $E_b$ (indicating the resistance to film breakdown) and $E_b$ - $E_{corr}$ (indicating the extent of the passive range) which could be used to assess the corrosion behaviour. At ambient temperature, reversal of the potential was accompanied by an almost immediate reduction in current for all alloys with the exception of UNS S31603 and SAF 2205. Although attack could be seen in the form of a faint surface film and pit initiation on the superduplex alloy, and general surface attack on Inconel 625, Stellite 6 and Ultimet, no pits of measurable depth were detected or significant lengths (i.e. in excess of 1mm) of crevice attack on these four materials. Type UNS S31603 however, attained an $I_{max}$ of 1600μA and this was attributed to the extensive crevice attack evident at the metal/resin interface. The anodic current of SAF 2205 exceeded the reversal point by 120μA which further suggested its inferior behaviour to the other duplex stainless steels and the superaustenitic material at ambient temperature, not indicated by $E_b$. At the moderately raised temperature of 30°C, Stellite 6 in addition to UNS S31603 and SAF 2205 exhibited a continued current increase immediately the scan was reversed. Interestingly, UNS S31603, Stellite 6 and SAF 2205 also suffered the largest decreases in $E_b$ over the same temperature range.

Inconel 625 and Ultimet exhibited $I_{max}$ currents equivalent to the reversal current over the entire, 18°C-60°C, range. The behaviour of the superaustenitic was also good in this respect up to 60°C but UNS S31603 was poor at ambient temperature and above. The other materials exhibited relatively high values of $I_{max}$ at various temperatures above ambient with the superduplex exhibiting the good behaviour similar to Inconel 625 up to and including 40°C but at 50°C attained an $I_{max}$ value of 4700μA and this relatively high anodic current could be explained by the greater extent of crevice attack (40mm of metal/resin interface) and depth of pitting attack (maximum pit depth 26μm).

At 60°C, only Inconel 625 and Ultimet had an $I_{max}$ value equivalent to the reversal current of 500μA and in addition, over the entire temperature range no localised attack either in the form of pitting or crevice attack was observed on Inconel 625 and only pit initiation on a very minor scale on Ultimet. Figures 2.8 a, b, c, d and e illustrate the progressive changes in the anodic polarisation characteristics on the superduplex alloy as the temperature increased.

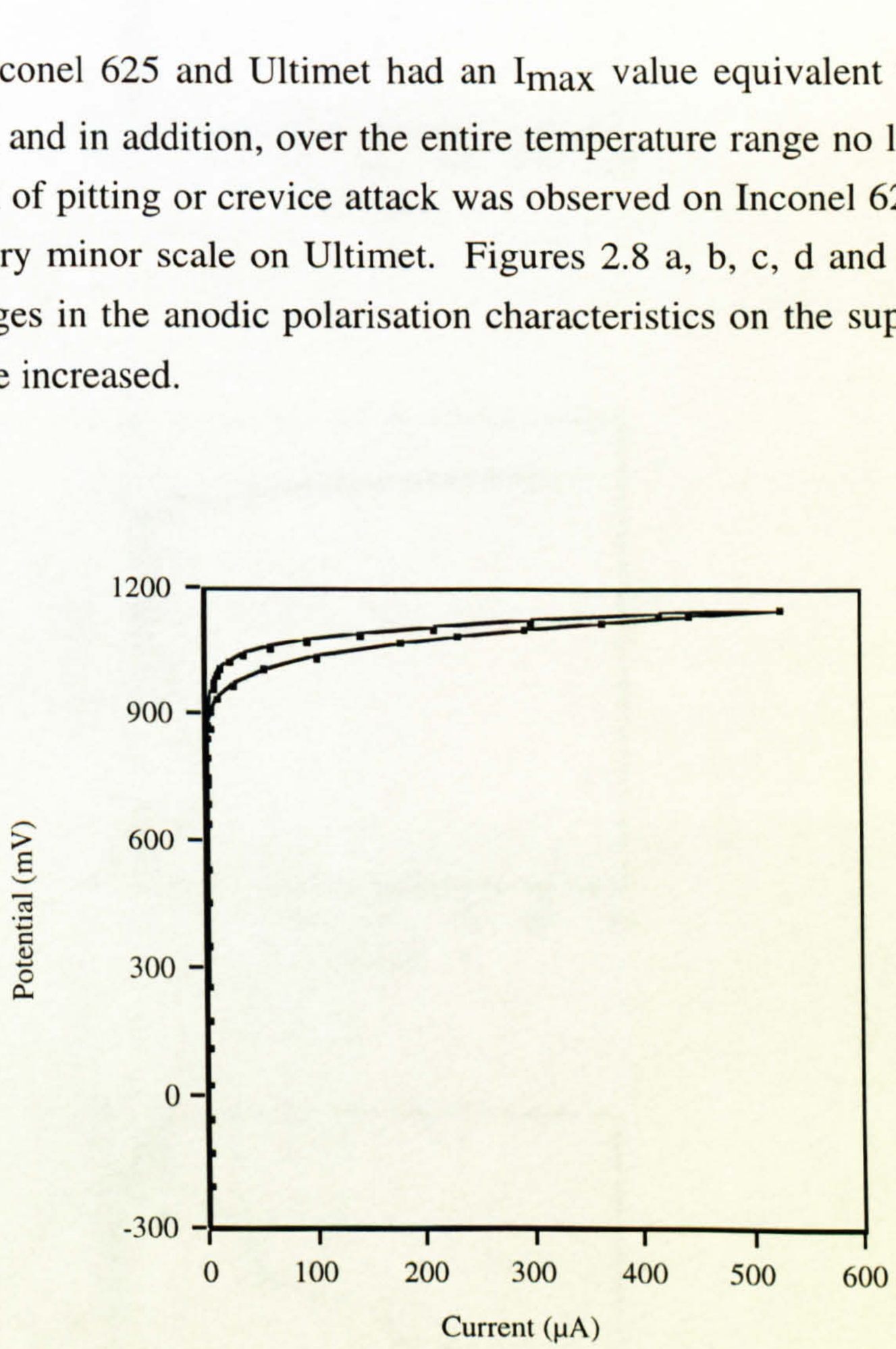


(a)

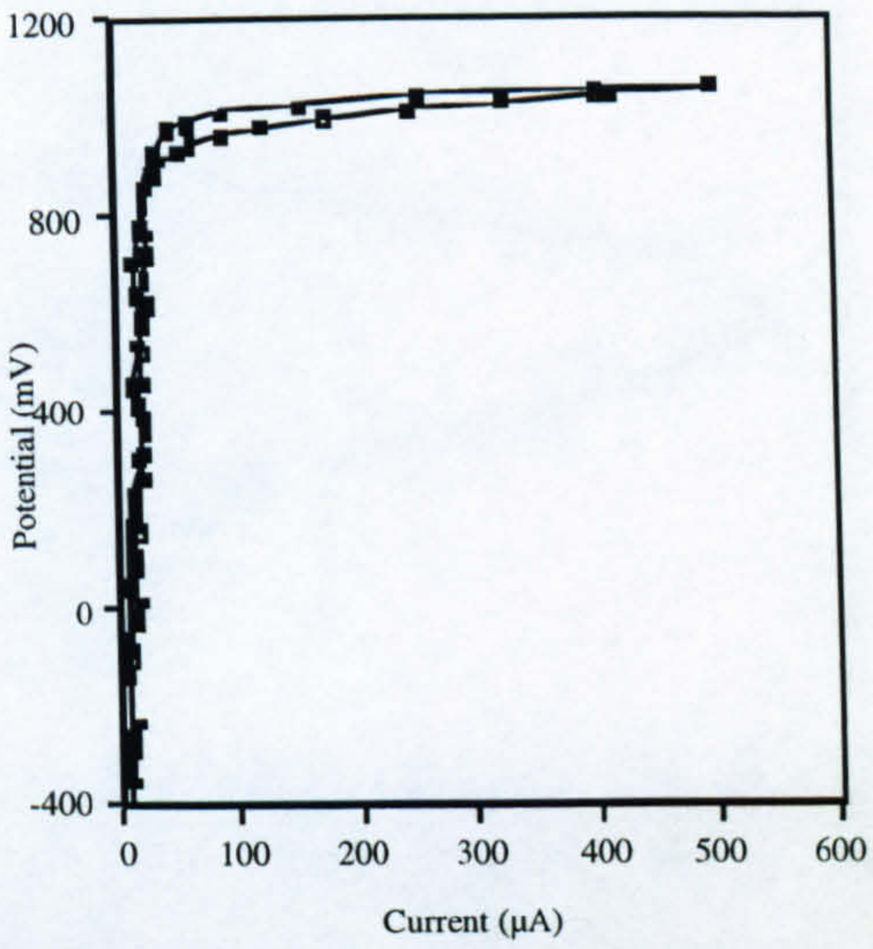
1200
800
400
0
-400
Potential (mV)
0
100
200
300
400
500
600
Current (μA)

(b)

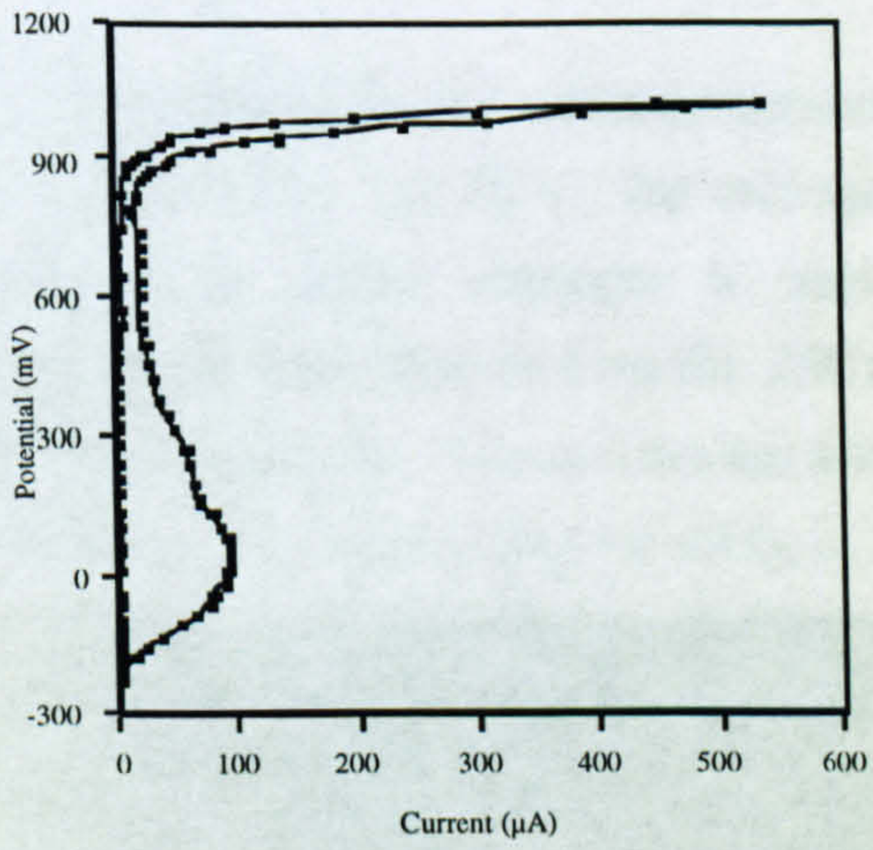
1200
900
600
300
0
-300
Potential (mV)
0
100
200
300
400
500
600
Current (μA)

(c)

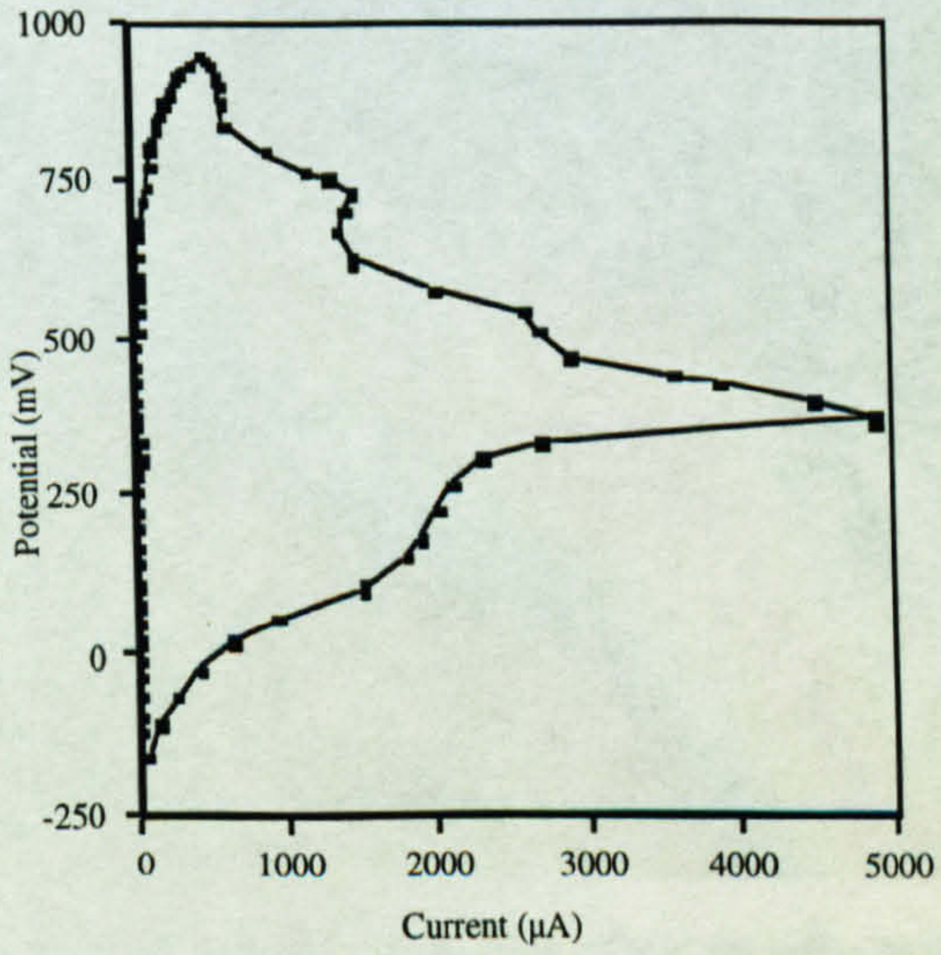
1000
750
500
250
0
-250
Potential (mV)
0
1000
2000
3000
4000
5000
Current (μA)

(d)

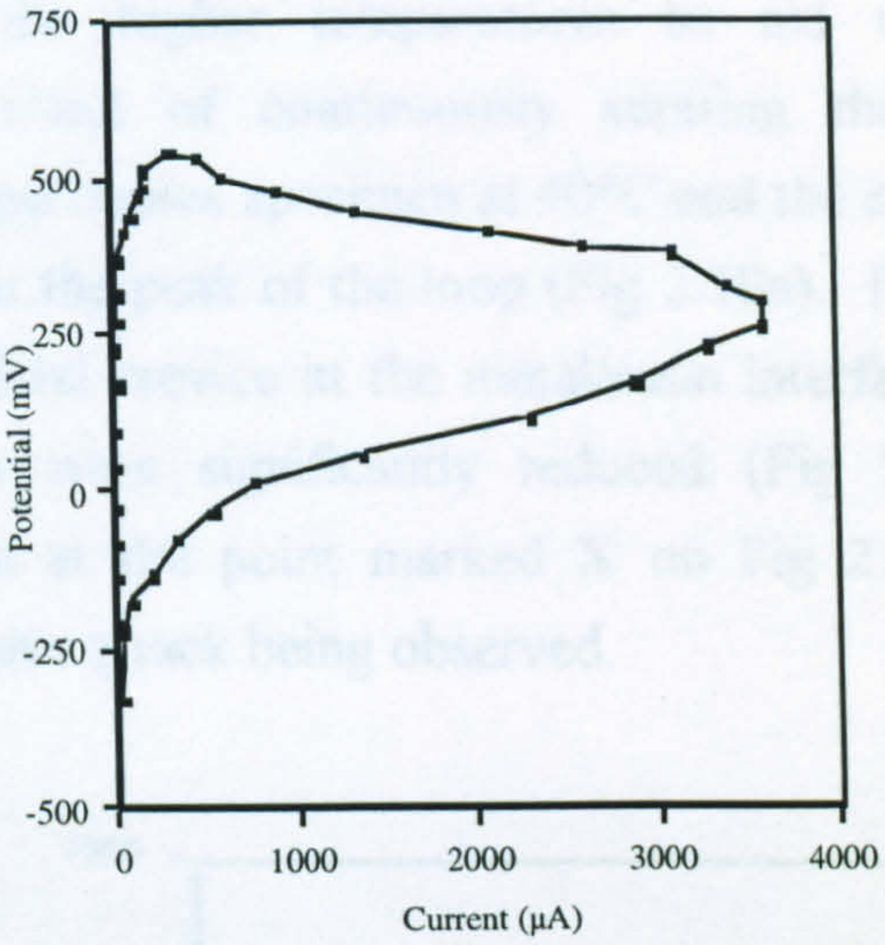


(e)

Fig. 2.8. Anodic polarisation in static seawater at (a) 18°C (b) 30°C (c) 40°C (d) 50°C and (e) 60°C

Very little change was observed in the electrochemical features or the microscopic analysis between 18°C and 30°C. At 40°C, the emergence of an "active" loop on the reversed scan indicated that initial attempts to repassivate were not completely successful. Similar behaviour was observed on the 25Cr duplex and the superaustenitic alloy at 30°C and 50°C respectively. Severe crevice attack was evident in the presence of this loop as illustrated for the superaustenitic alloy in Fig.2.9.

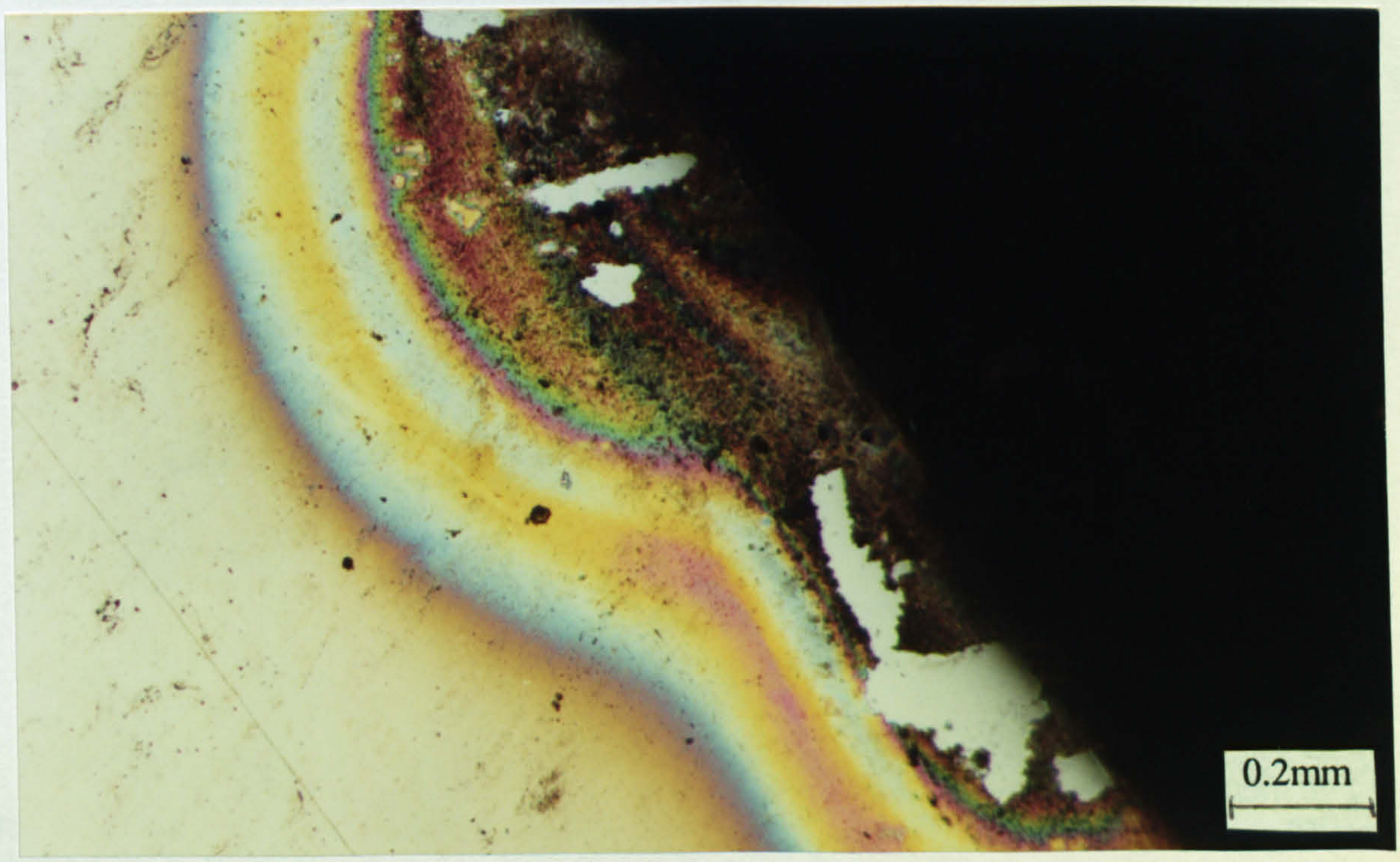


Fig. 2.9. Crevice attack on UNS S31254 after anodic polarisation at 50°C

The possibility that the observed active behaviour could be due to insufficient oxygen being available at the higher temperatures to aid complete repassivation was investigated. The effect of continuously aerating the sea water during anodic polarisation on the superduplex specimen at 40°C and the superaustenitic at 50°C was to increase the current at the peak of the loop (Fig 2.10a). However, when a varnish was used to seal the artificial crevice at the metal/resin interface, the severe crevice attack and the active loop were significantly reduced (Fig 2.10b). Also stopping the potentiodynamic scan at the point marked **X** on Fig 2.10a, before the active loop, resulted in less extensive attack being observed.

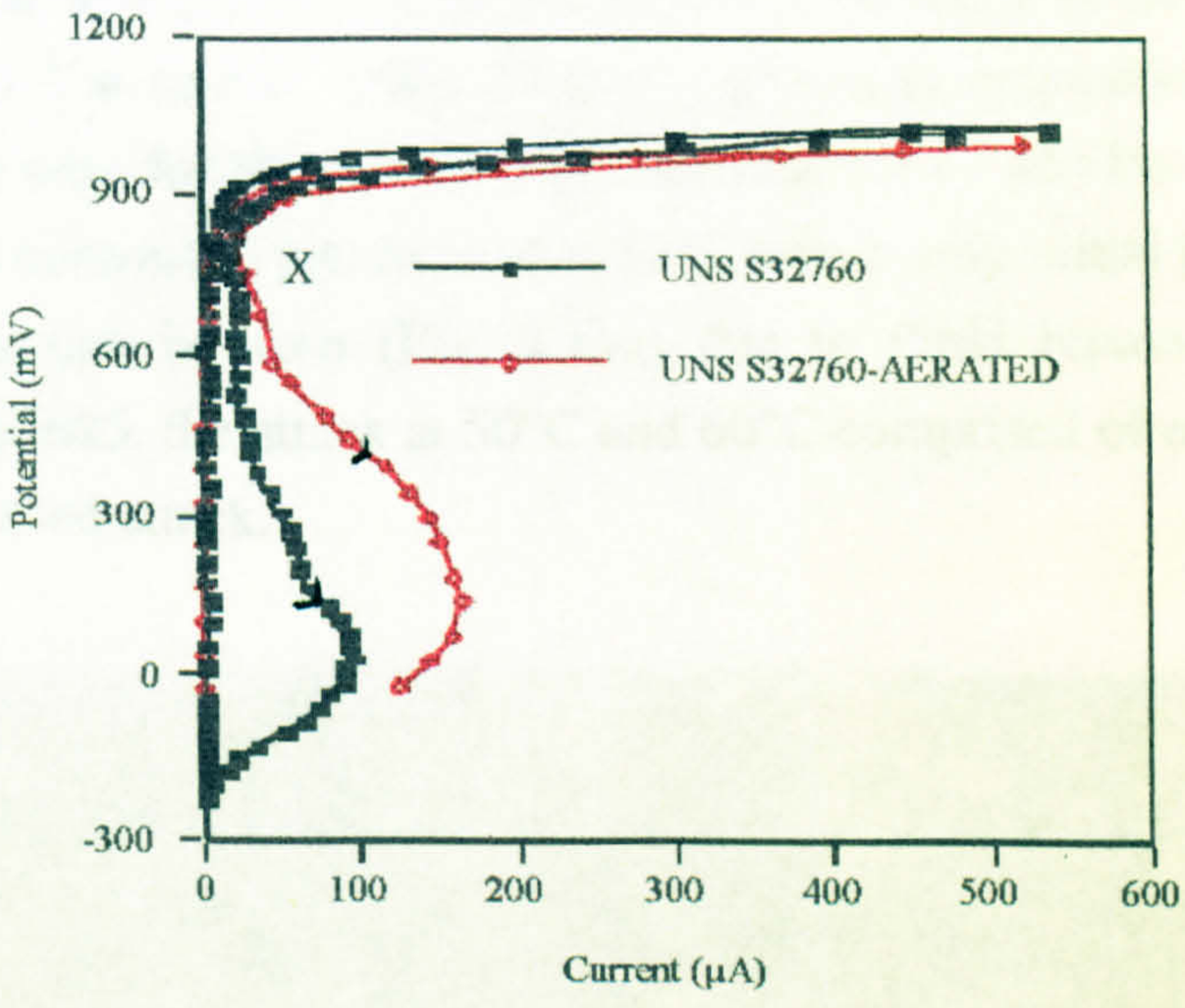


(a)

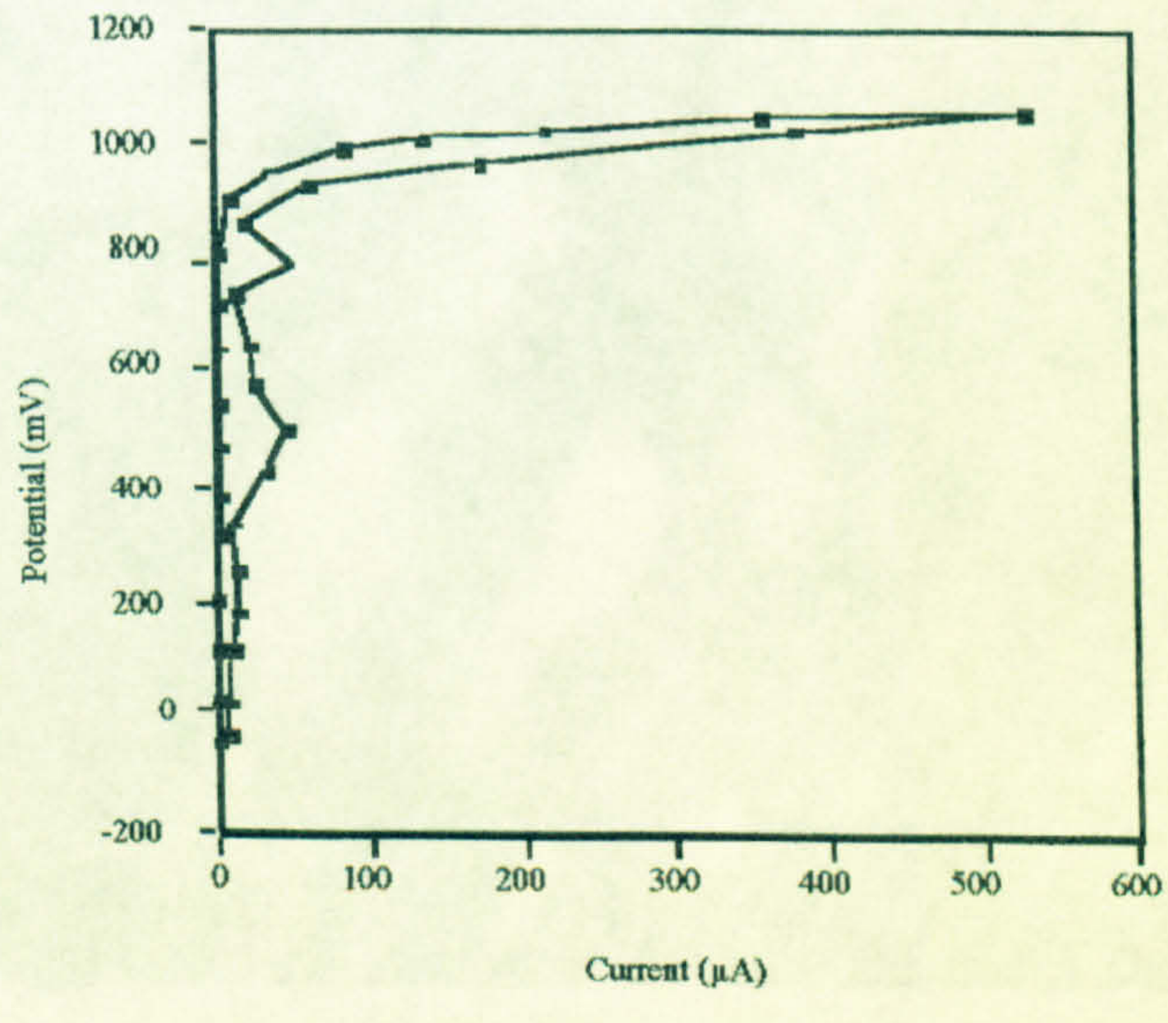


(b)

Fig 2.10. (a) Effect of aeration enhancing the active loop, (b) 'Lacomit' laquer eliminates the active loop

As shown in Figs. 2.8c and d, continued increase in temperature to 50°C meant that the superduplex alloy could no longer begin to repassivate and high currents were attained after the scan reversal. A fall in $I_{max}$ was recorded on increasing the temperature from 50°C to 60°C as shown in Figs 2.8d and e. Figure 2.11a shows a light micrograph of a fully developed pit on this material after anodic polarisation at 50°C. The grain structure can clearly be seen in the vicinity of the pit. The attack seems to be propagating via the grain boundaries, leaving individual grains protruding into the pit as can be seen more clearly in the SEM micrograph (Fig 2.11b) of a different region on the same superduplex specimen. Microanalysis via EDAX facilities on the SEM , yielded a higher Fe and Ni concentration on the grain (area 1 on Fig 2.11b) and higher Cr and Mo concentrations on the area adjacent to the grain (area 2 on Fig. 2.11b), confirming area 1 as austenite and area 2 as ferrite. Table 2.7 gives the exact compositions which indicate that the partitioning ratio for Mo and Ni is greater than for Cr and Fe. This large extent of propagation is in contrast to pits formed at 30°C where only initial film breakdown in the immediate area can be seen (Fig. 2.11c) due to rapid repassivation. With the exception of Inconel 625, the attack at 50°C and 60°C comprised of mixed mechanisms of general and localised attack.


(a)

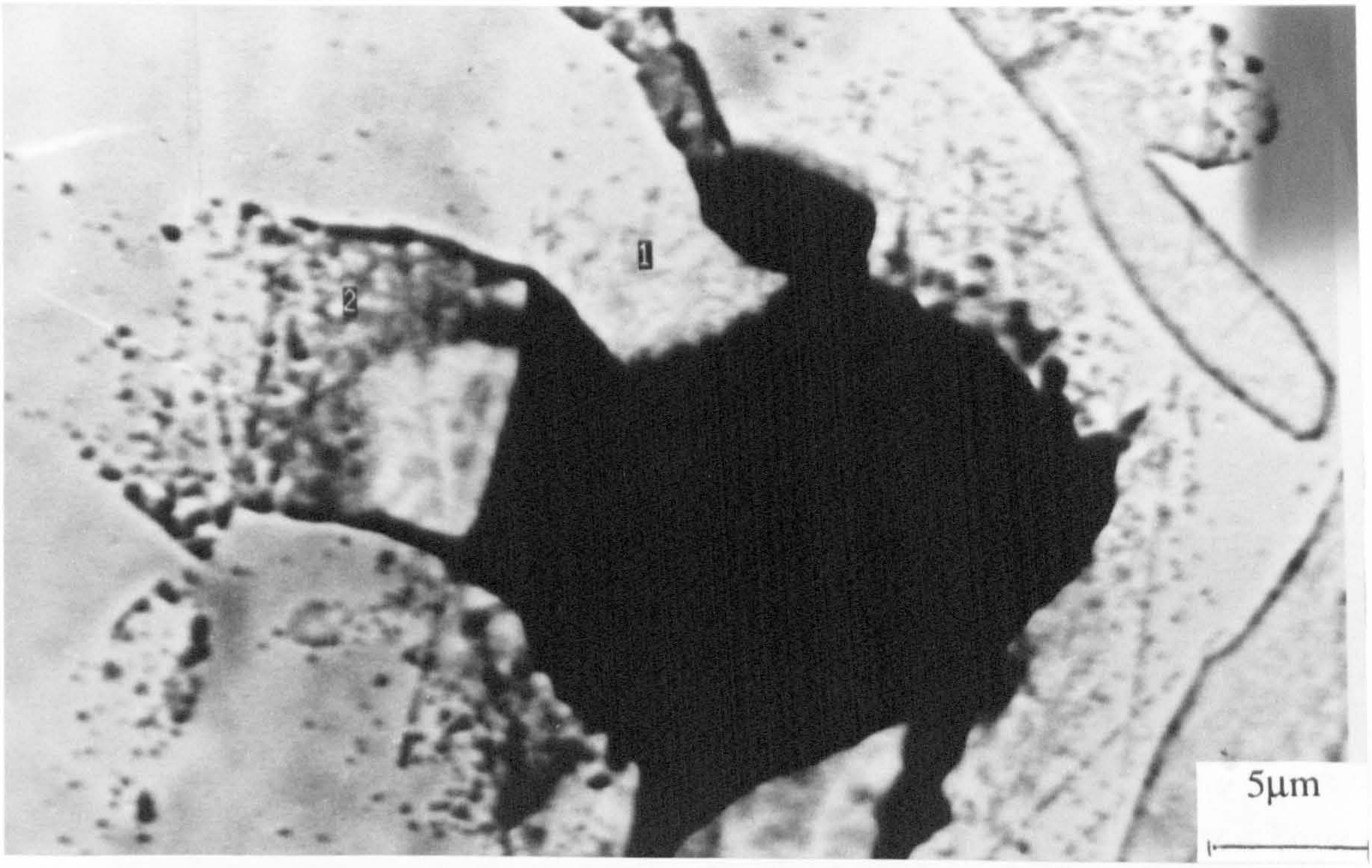


(b)

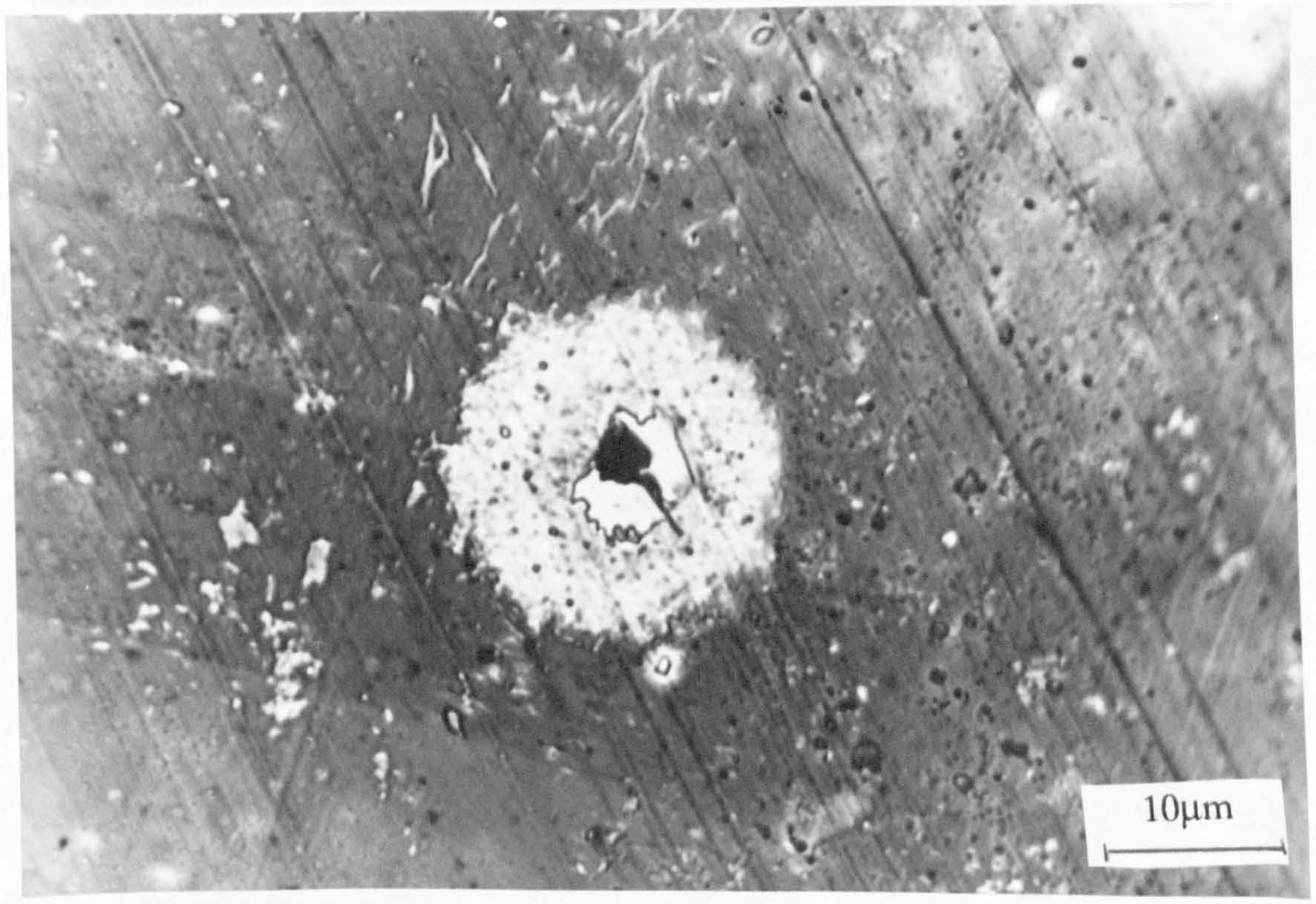


(c)

Fig. 2.11. Pitting on the superduplex UNS S32760 alloy at 50°C (a) light micrograph (b) SEM micrograph and (c) at 30°C light micrograph

As mentioned previously, Inconel 625 showed no signs of any crevice or pitting attack but instead a general thin coloured film (Fig 2.12a). General attack on the other materials at higher temperature was either in the form of a coloured surface film, as illustrated on the superduplex alloy UNS S32760 in Fig. 2.12b, which was discontinuous at areas of crevice and pitting attack or in the case of the duplex stainless steels (25Cr and SAF 2205) the coloured film enhanced the two-phase structure. Figure 2.13a illustrates the mixed attack after an anodic polarisation on the 25Cr duplex at 50°C. Pit initiation on an etched background can be seen, the coloured film tending to be enhanced on the ferritic phase (Fig 2.13b). Severe crevice attack on the same specimen was observed (Fig 2.14).

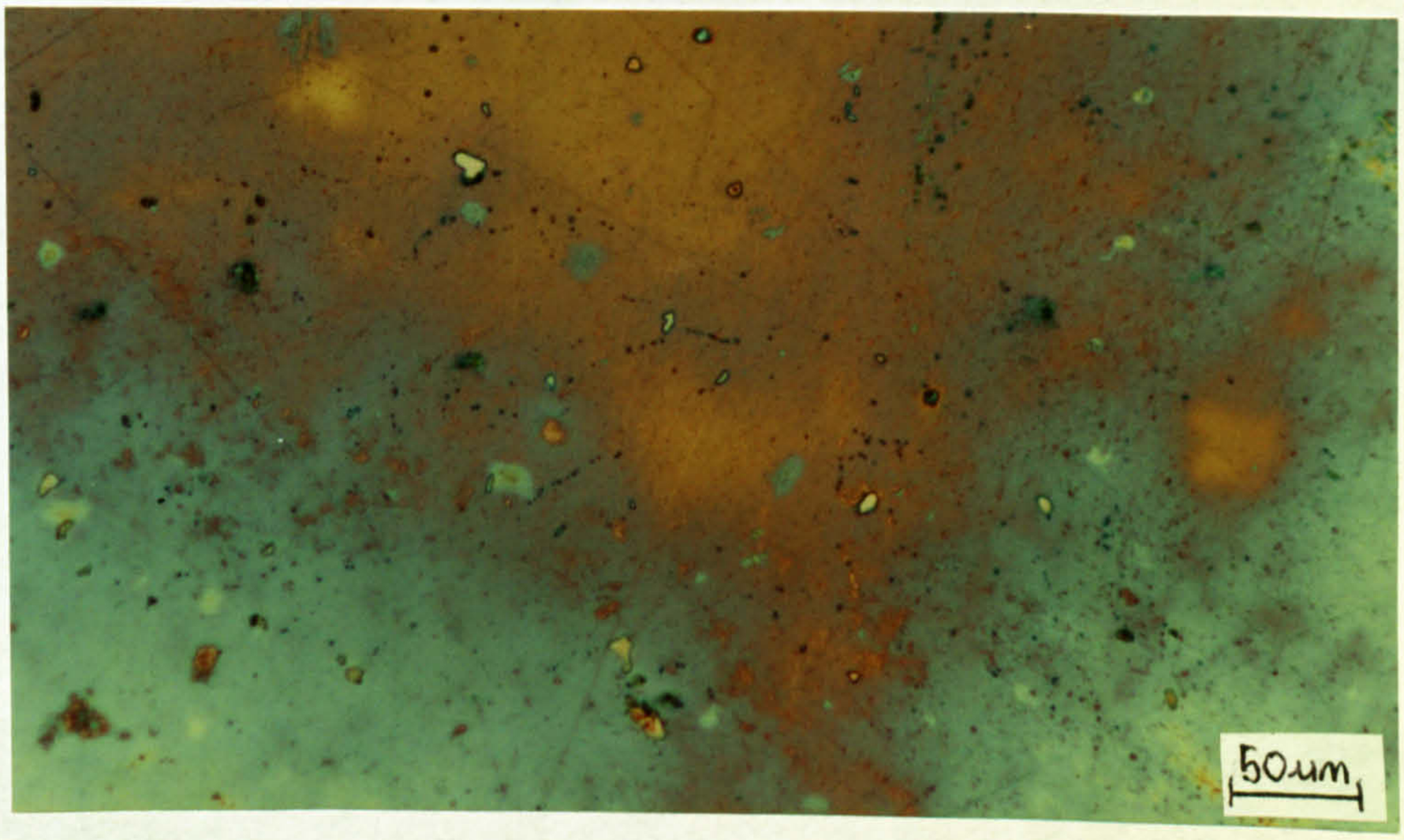


(a)

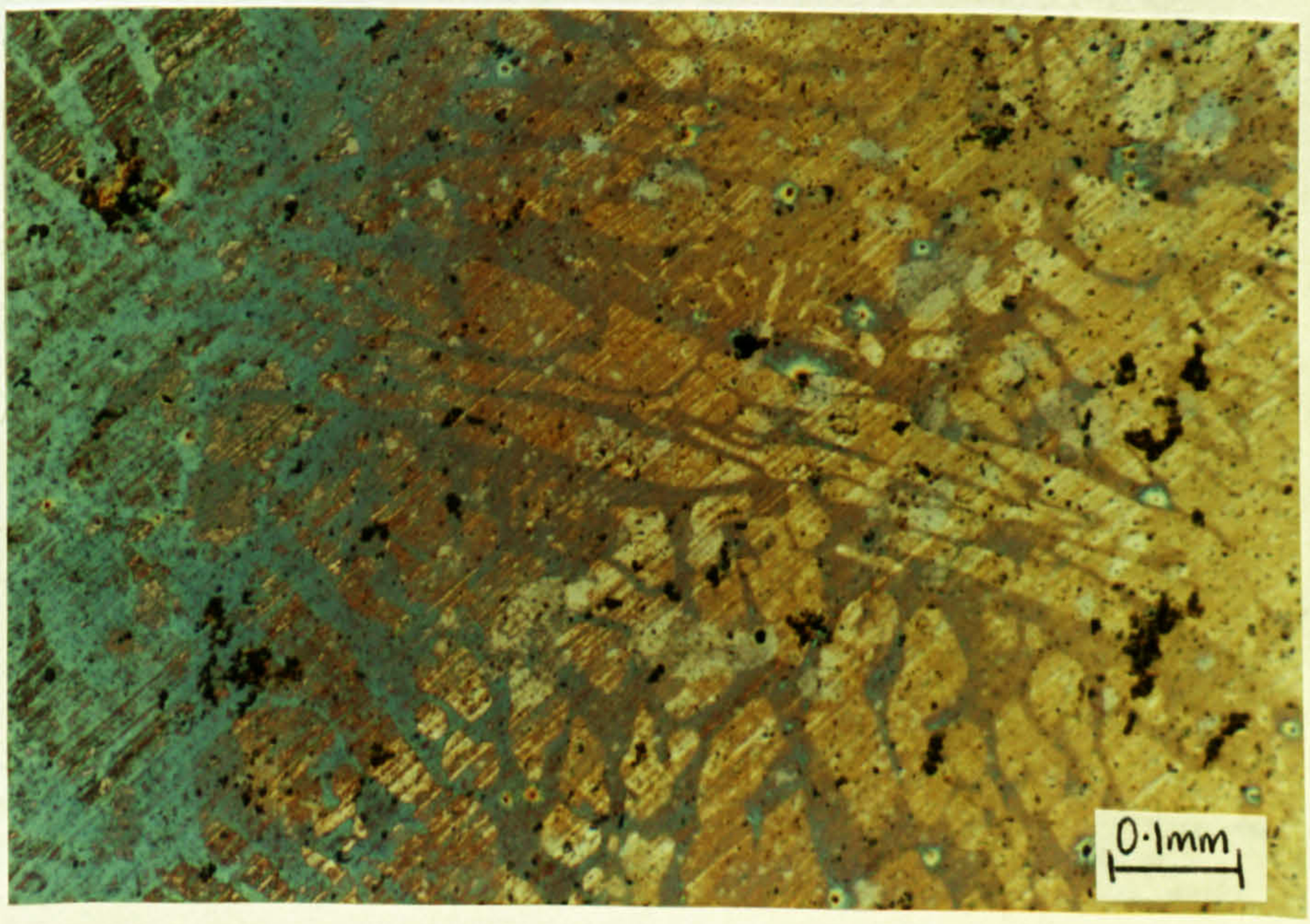


(b)

Fig. 2.12. Coloured film formed after anodic polarisation in 50°C seawater etching on (a) Inconel 625 and (b) UNS S32760

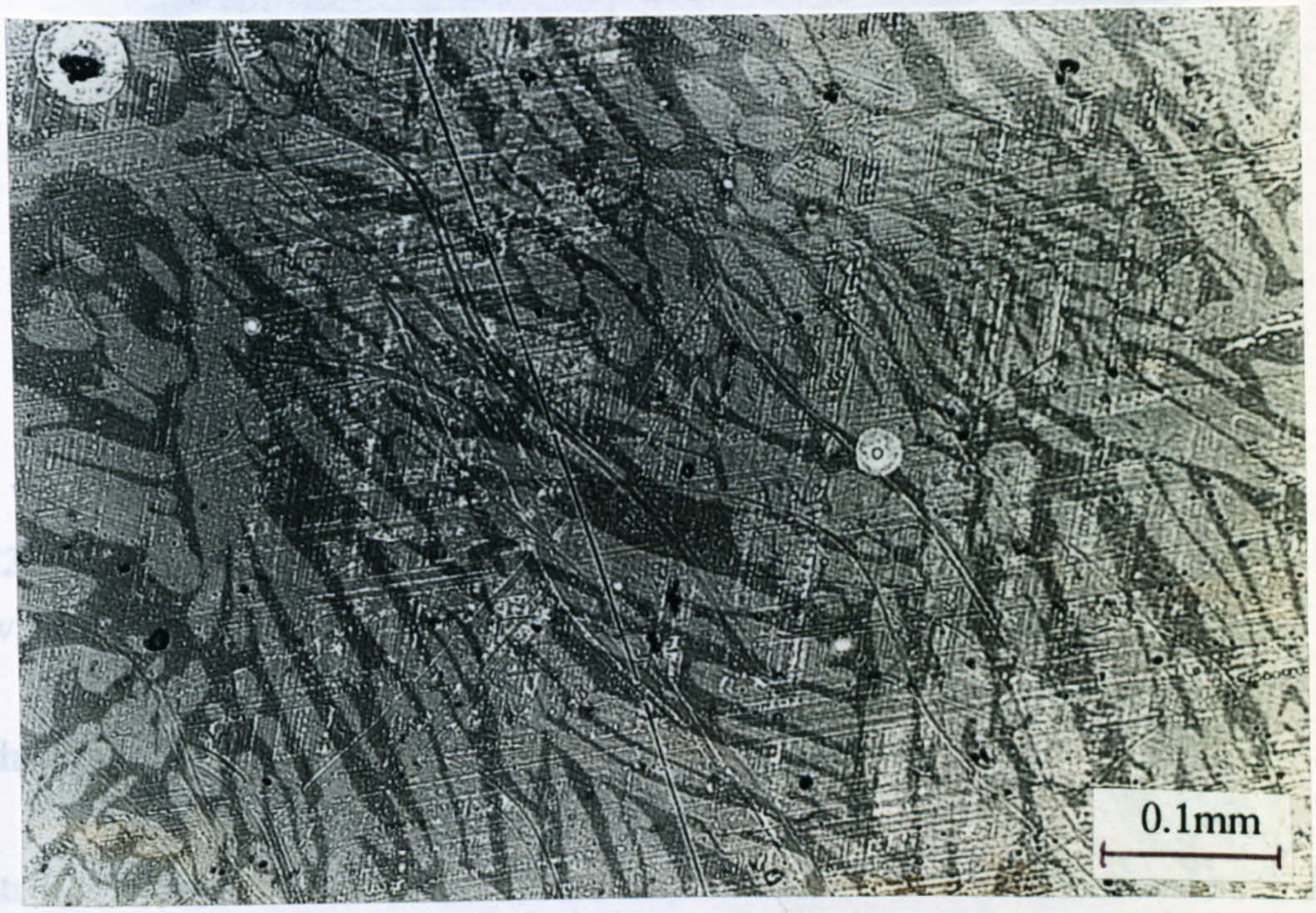


(a)

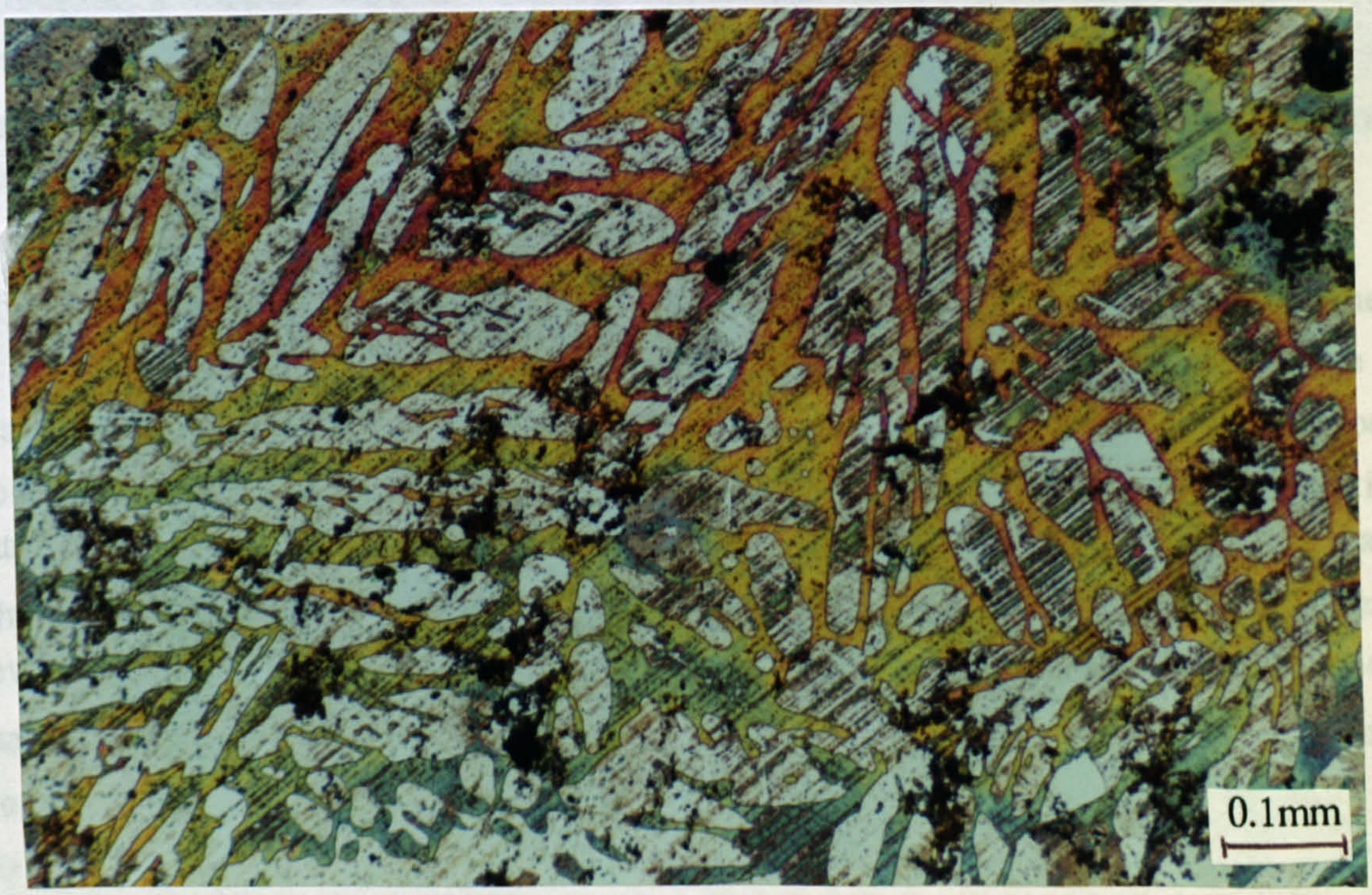


(b)

Fig 2.13. Mixed modes of attack on the 25Cr duplex stainless steel after anodic polarisation at 50°C (a) etching and pitting attack (b) coloured film predominant on the ferrite phase

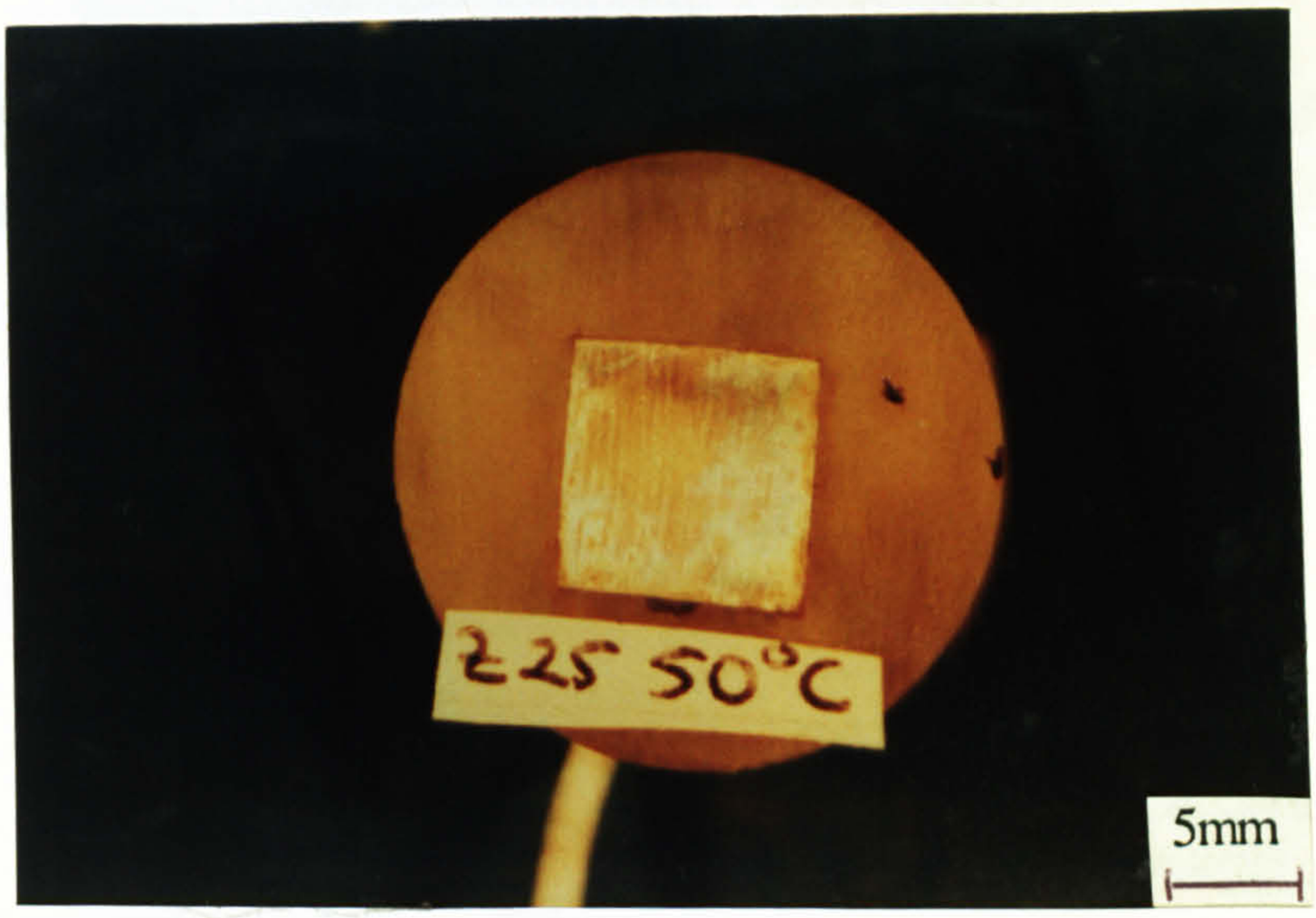


Fig 2.14. Crevice corrosion on the 25Cr duplex alloy after anodic polarisation in 50°C seawater

**Cathodic Polarisation Tests**

In static sea water, cathodic polarisation curves took on a complex form, resulting in very small currents (up to 1-2μA) until a potential attained values around -350 to -450mV, depending on the alloy. Thereafter, for the stainless steels, the E/log I relationship was linear (Tafel behaviour) for a small potential range prior to the current exhibiting a limiting value, $i_L$, but once the polarisation had decreased to sufficiently low values (around -1000mV or lower and denoted by $E_h$ in Tables 2.8 and 2.9), the cathodic currents increased to much higher values typical of hydrogen evolution kinetics. The parameter $E_h$ is shown for the 25Cr duplex in Fig. 2.15.

Figure 2.16 is presented with the intention of illustrating the important point that there is a significant difference in the cathodic polarisation characteristics on the range of materials studied. Although on the Co-base and Ni-base alloys there tended not to be a concentration polarisation controlled region although there were two distinct reaction rates before the onset of hydrogen evolution (i.e. in the potential region from $E_{corr}$ and $E_h$). This was also true on the stainless steels in that there appeared to be what was a severely polarised reaction at potentials modestly shifted from $E_{corr}$ which was manifested in very small currents being recorded. The second reaction on the stainless steels proceeded to attain a higher limiting current density. Work performed on rotating disk electrodes (reported in chapter 8) also inferred the occurrence of a two stage cathodic reaction in what would be commonly referred to as the oxygen-reduction region. The rotating disk accentuated the cathodic current such that two concentration polarisation regions on UNS S31603 could be more clearly identified (Fig. 2.17).

region. The rotating disk accentuated the cathodic current such that two concentration polarisation regions on UNS S31603 could be more clearly identified (Fig. 2.17).

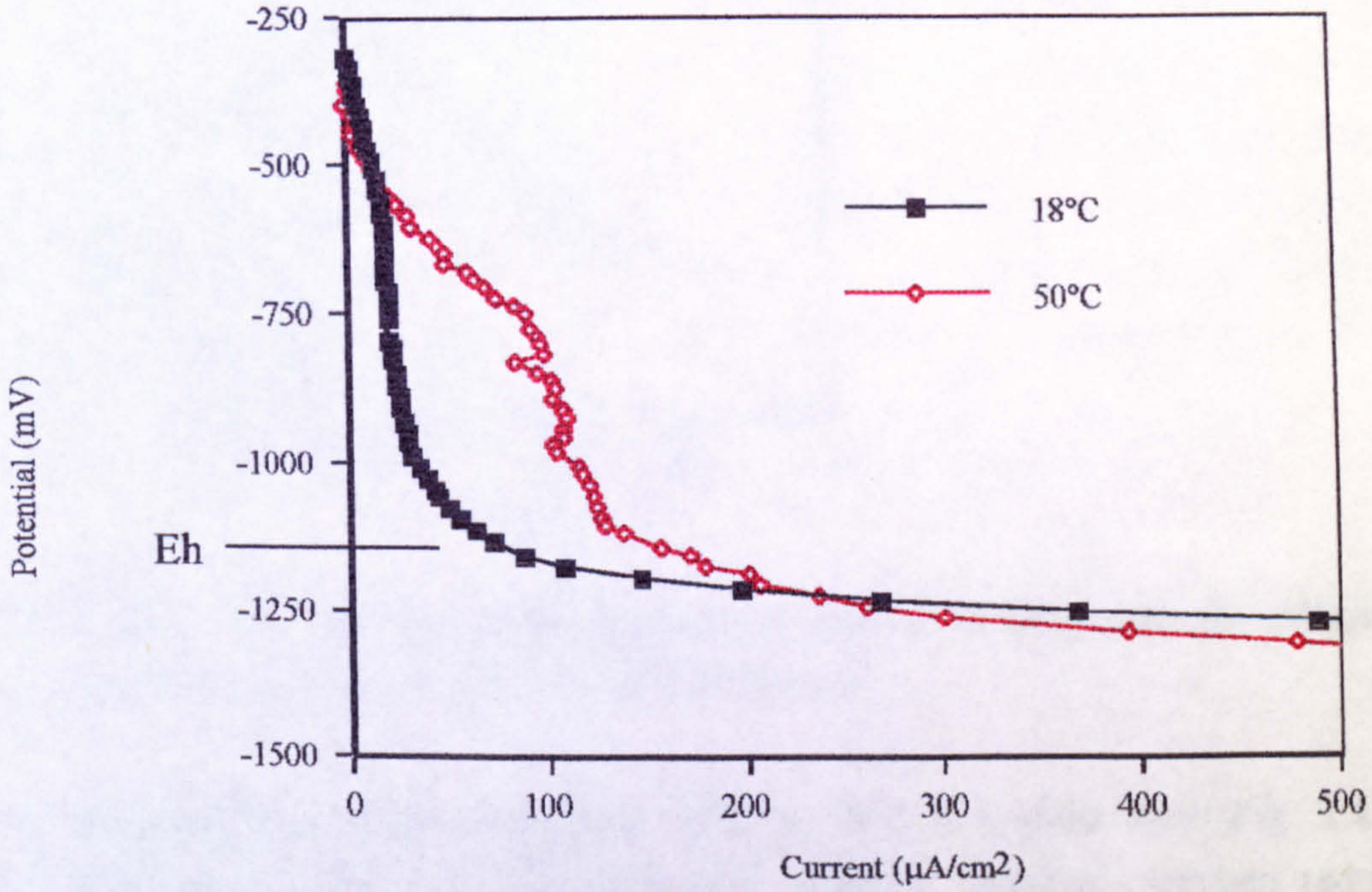


Fig. 2.15. Cathodic polarisation at 18°C and 50°C in static seawater on 25Cr duplex stainless steel

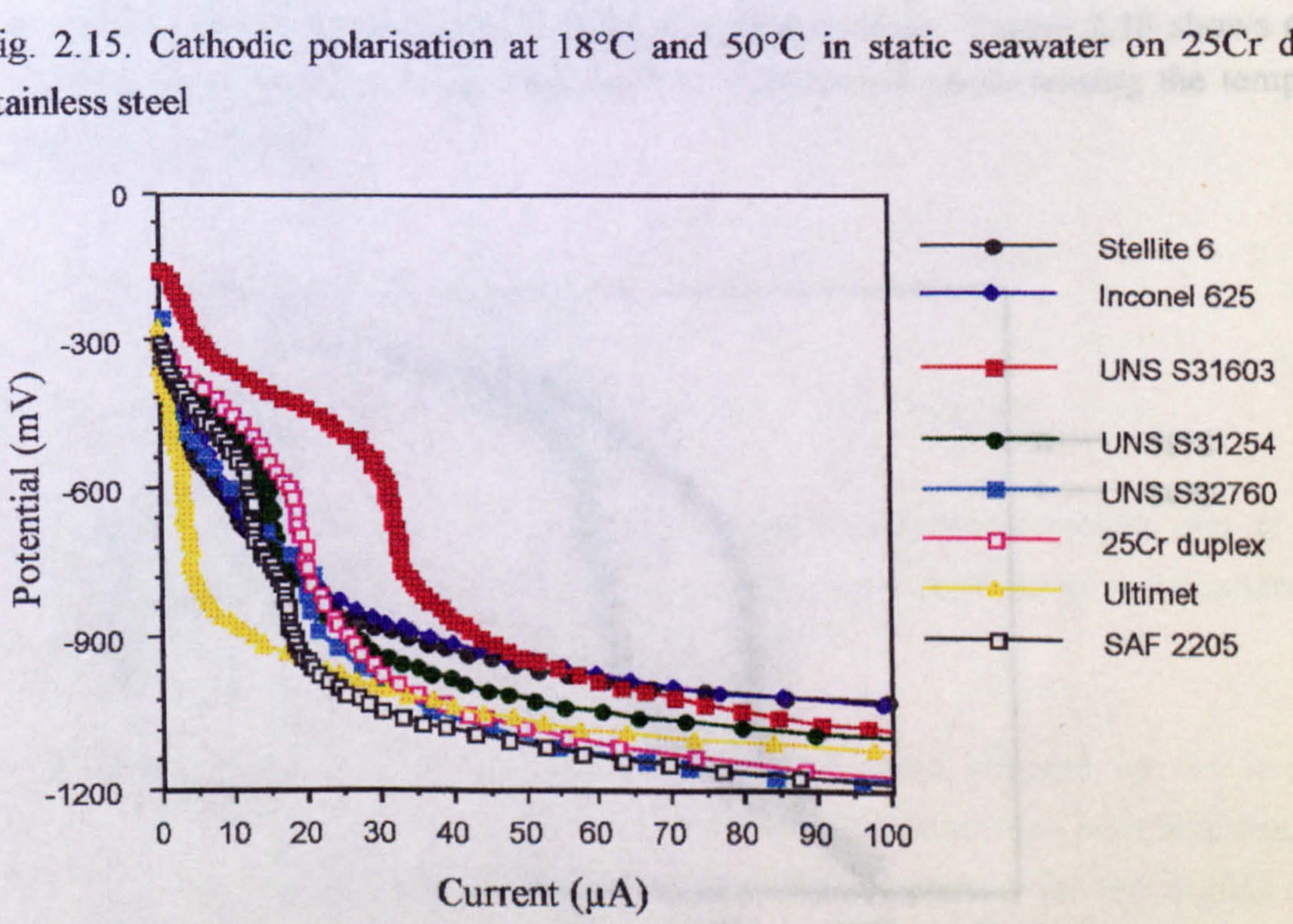


Fig. 2.16. Cathodic polarisation in static seawater at 18°C on the range of alloys in the study

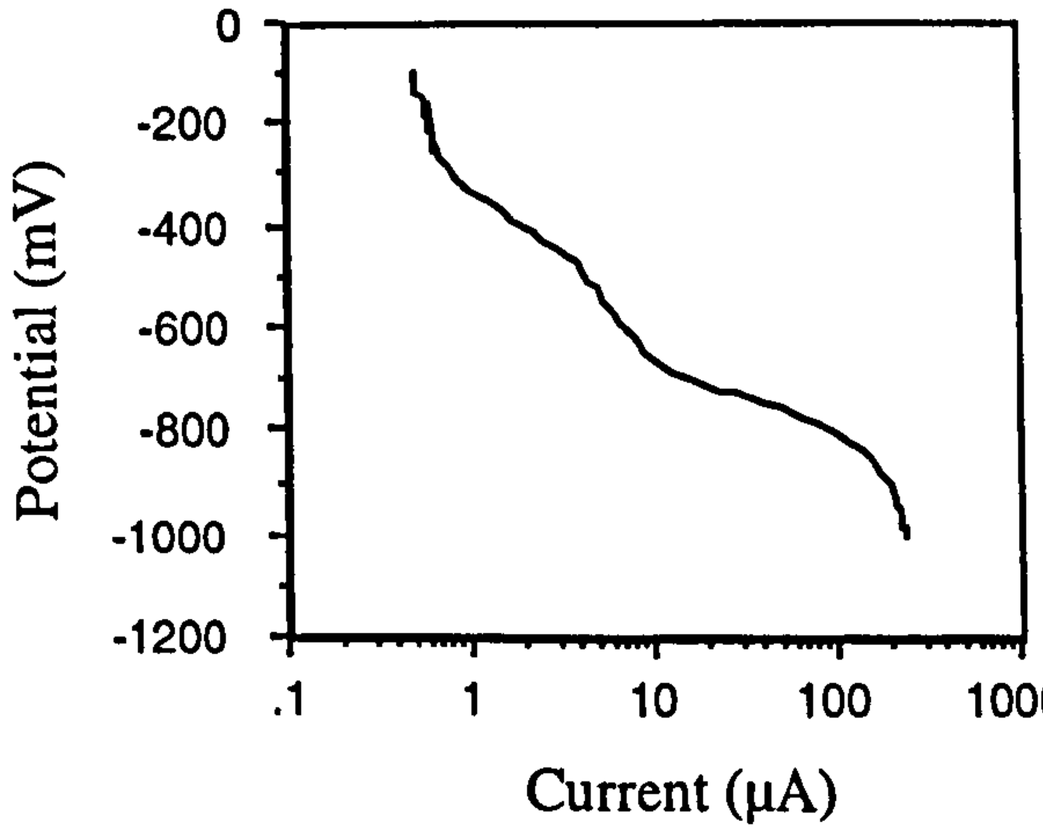


Fig. 2.17. Two concentration polarisation regions during cathodic polarisation on rotating disk electrode of UNS S31603 at 600rpm

On increasing the temperature from 18°C to 50°C it is clear from Fig. 2.15 that the limiting current density for the prominent cathodic reaction - oxygen reduction - is significantly increased and this was the case for all the stainless steels. On the stainless steels concentration polarisation effects were still evident. Figure 2.18 shows on SAF 2205, the increase of $i_L$ from 18μA/cm$^2$ to 120μA/cm$^2$ on increasing the temperature from 18°C to 50°C.

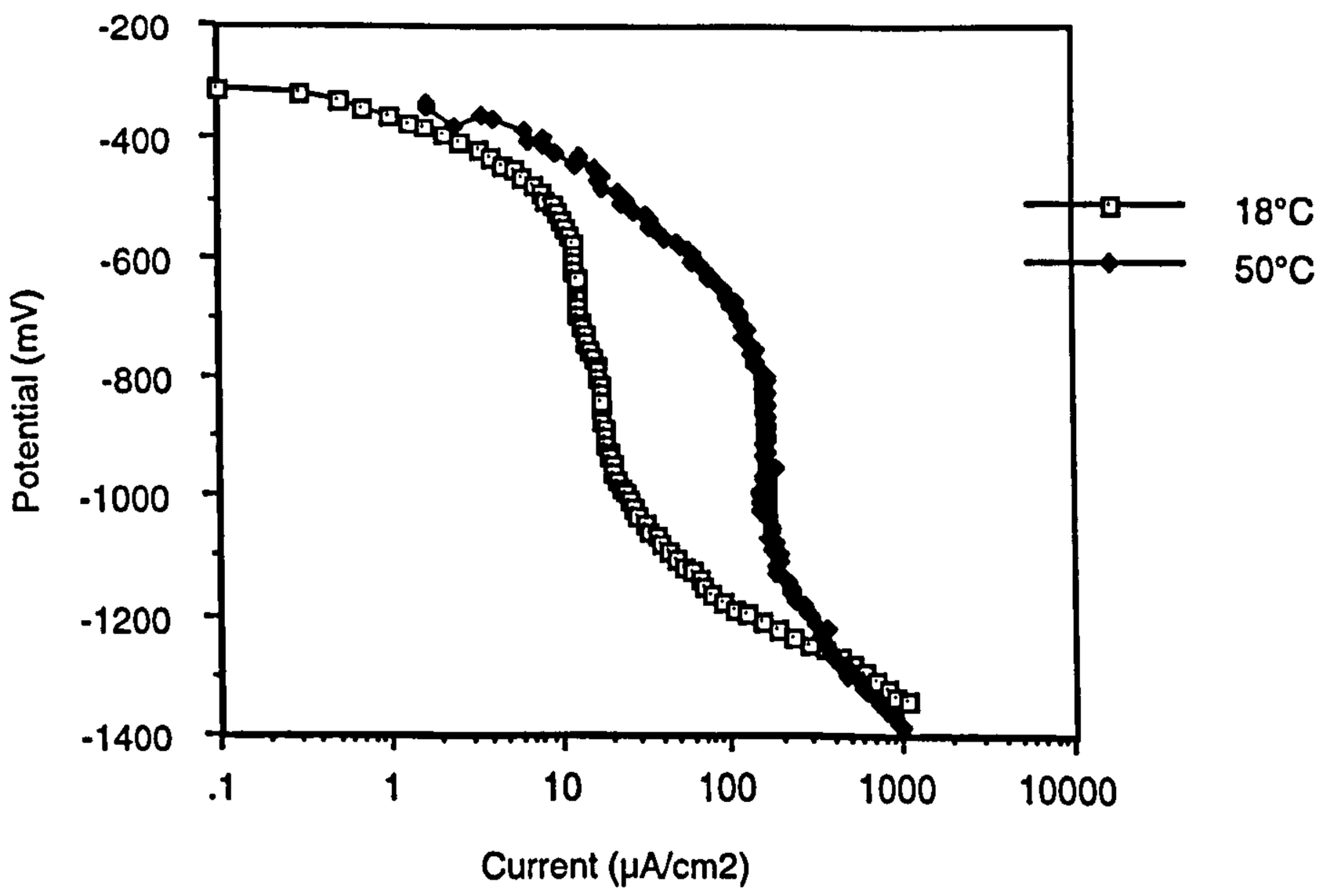


Fig. 2.18. Cathodic polarisation on SAF 2205 in static seawater

The cathodic reaction on the nickel and cobalt base alloys followed a somewhat different trend to the stainless steels at ambient temperature and this was also the case at

50°C. It can be seen in Fig. 2.19 for Inconel 625 at 18°C that although there is a change in reaction rate at low current values (approx. 5μA/cm$^2$) the cathodic reaction seems to follow Tafel kinetics in the region **a** and concentration polarisation effects are observed. At higher temperature, a similar effect is observed but with the Tafel region **x** commencing at a much higher current value of in excess of 100μA/cm$^2$. Region b at 18°C seems to signify the production of hydrogen but commences without severe concentration polarisation effects being observed. In region **y** at 50°C there is a slight change in gradient of the cathodic reaction, perhaps corresponding to the start of the hydrogen evolution reaction.

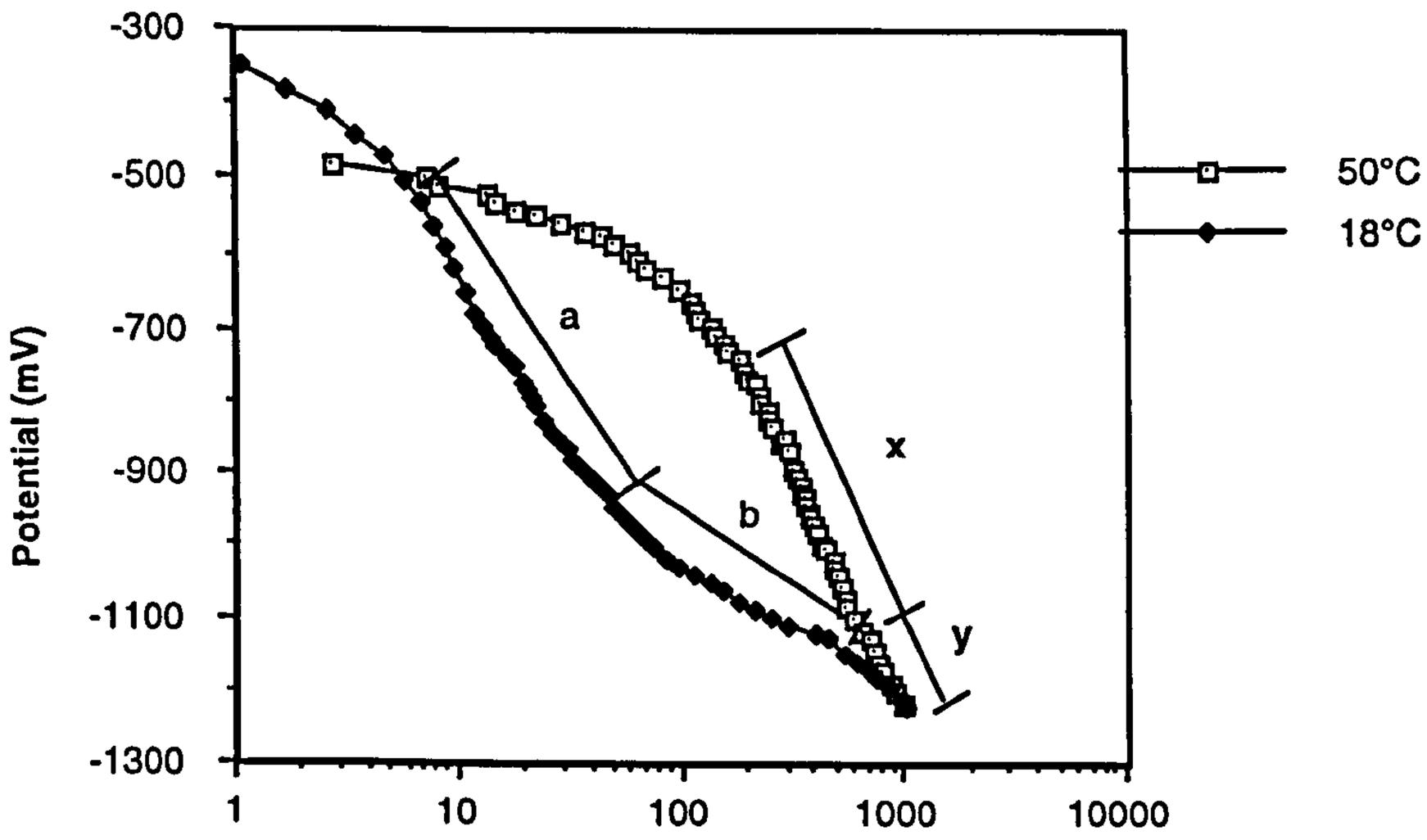


Fig. 2.19. Cathodic polarisation on Inconel 625 in static seawater

The behaviour of Stellite 6 was somewhat similar with the exception that at 50°C, a small area which resembled a limiting current density was observed at 100μA/cm$^2$ over a very short potential range of 100mV( Fig 2.20).

The kinetics of the hydrogen-production reaction were affected by the increase in temperature on all materials with the exception of the austenitic stainless steels (UNS S31254 and UNS S31603). The rate of reaction decreased for the duplex stainless steels, Inconel 625 and the cobalt-base alloys manifested in increasing Tafel slope gradients. In contrast, the increased temperature tended to increase the rate of $H^+$ reduction on the austenitics. The values of the Tafel slope are given in Table 2.8.

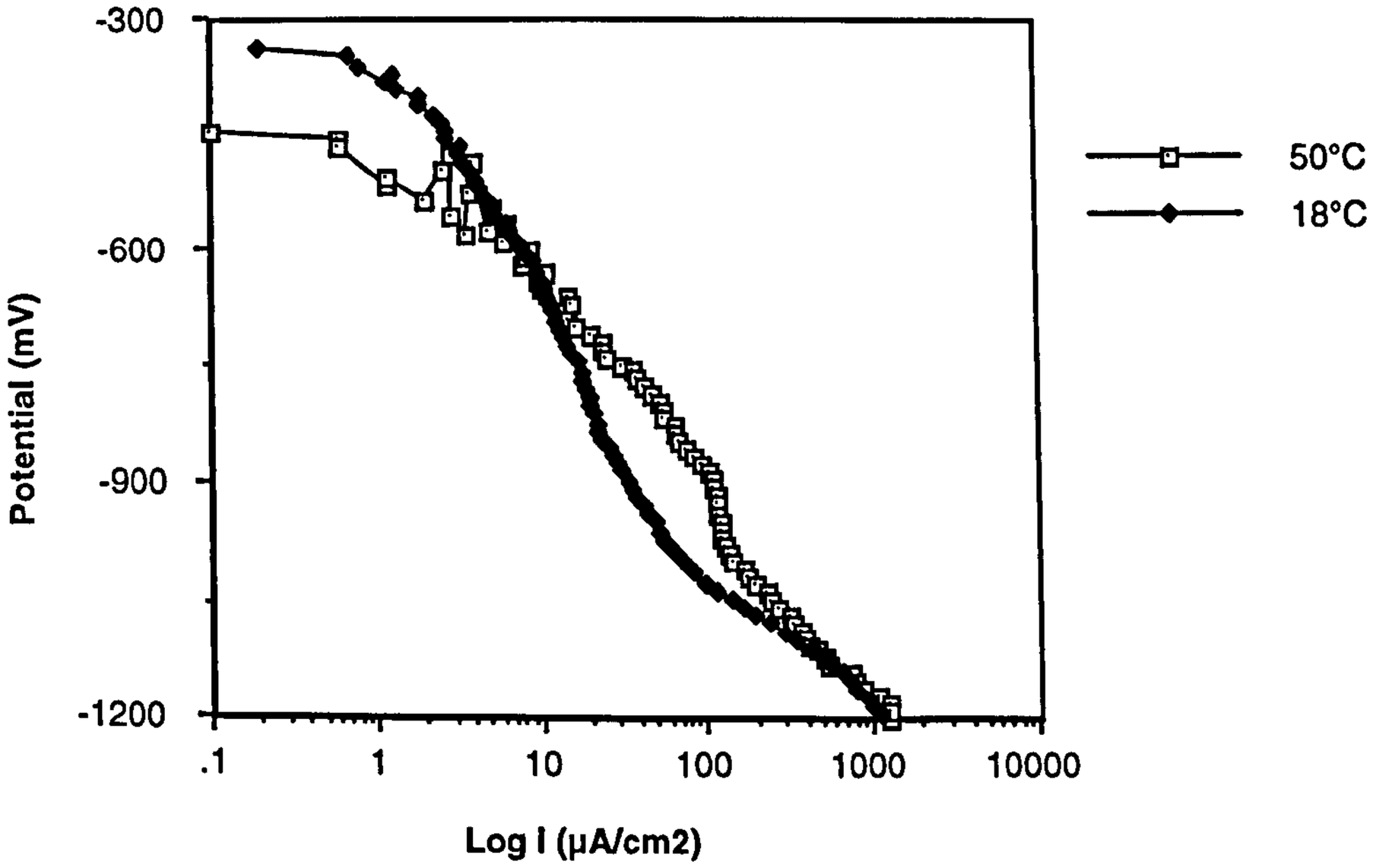


Fig. 2.20. Cathodic polarisation in static seawater on Stellite 6

| | Ecorr (mV) | Eb (mV) | Eb-Ecorr (mV) | Er (mV) | Ib (μA) | Imax (μA) | Types of Attack | MPD | Crevice |
|---|---|---|---|---|---|---|---|---|---|
| **UNS S32760** | -222 | 1083 | 1205 | 908 | 8 | 500 | P.i+C+G | | <1mm |
| **Inconel 625** | -238 | 763 | 1001 | imme.. | 80 | 500 | G | | |
| **SAF 2205** | -315 | 1095 | 1410 | 1035 | 30 | 620 | P+C+G | 6μm | 6-7mm |
| **25Cr Duplex** | -345 | 1105 | 1450 | -195 | 45 | 530 | P.i+C | 14μm | 3-4mm |
| **UNS S31603** | -155 | 505 | 660 | 2 | 2 | 1600 | C+G | | 8mm |
| **UNS S31254** | -156 | 1064 | 1220 | 934 | 40 | 520 | C+P.i. | | <1mm |
| **Ultimet** | -114 | 570 | 684 | Imme | 50 | 500 | P.i.+G | | |
| **Stellite 6** | -330 | 600 | 930 | -330. | 80 | 540 | G | | |

**Immed.**- Immediate repassivation **P**-pitting attack **C**-crevice attack

**P.i.**-Pit initiation

Table 2.2. Electrochemical parameters for anodic polarisation in static seawater at 18°C

| | Ecorr (mV) | Eb (mV) | Eb-Ecorr (mV) | Er (mV) | Ib (μA) | Imax (μA) | Types of Attack | MPD | Crevice |
|---|---|---|---|---|---|---|---|---|---|
| **UNS S32760** | -422 | 957 | 1379 | 888 | 40 | 500 | P. i+G | | |
| **Inconel 625** | -373 | 586 | 959 | Imme | 50 | 500 | G | | |
| **SAF 2205** | -402 | 417 | 819 | -293 | 60 | 940 | C+P | 15μm | <1mm |
| **25Cr Duplex** | -332 | 918 | 1250 | -237 | 130 | 500 | C+P | 8μm | 3mm |
| **UNS S31603** | -346 | 274 | 620 | -166 | 30 | 970 | C | | 25- |
| **UNS S31254** | -448 | 1002 | 1450 | 927 | 140 | 550 | G | | |
| **Ultimet** | -315 | 294 | 609 | Imme | 40 | 500 | G | | |
| **Stellite 6** | -362 | 88 | 450 | -312 | 80 | 900 | G+C | | 20mm |

Table 2.3. Electrochemical parameters for anodic polarisation in static seawater at 30°C

| | Ecorr (mV) | Eb (mV) | Eb-Ecorr (mV) | Er (mV) | Ib (μA) | Imax (μA) | Types of Attack | MPD | Crevice |
|---|---|---|---|---|---|---|---|---|---|
| **UNS S32760** | -247 | 903 | 1150 | -248 | 30 | 530 | P+C | 17μm | 12mm |
| **Inconel 625** | -407 | 693 | 1100 | 473 | 50 | 500 | G | | |
| **SAF 2205** | -467 | 30 | 497 | -197 | 70 | 600 | C | | 15- |
| **25Cr Duplex** | -301 | 460 | 761 | -100 | 80 | 3500 | G+P | 29μm | |
| **UNS S31603** | -393 | 156 | 549 | -274 | 190 | 540 | C+G | | 20- |
| **UNS S31254** | -485 | 904 | 1389 | -295 | 75 | 540 | C | | 40mm |
| **Ultimet** | -424 | 275 | 699 | Imme | 95 | 500 | G | | |
| **Stellite 6** | -352 | -102 | 250 | N.R. | 30 | 630 | G | | |

Table 2.4. Electrochemical parameters for anodic polarisation in static seawater at 40°C

| | Ecorr (mV) | Eb (mV) | Eb-Ecorr (mV) | Er (mV) | Ib (μA) | Imax (μA) | Types of Attack | MPD | Crevice |
|---|---|---|---|---|---|---|---|---|---|
| **UNS S32760** | -185 | 665 | 850 | -185 | 80 | 4700 | P+C+G | 26μm | 40mm |
| **Inconel 625** | -489 | 541 | 1030 | 531 | 200 | 530 | G | | |
| **SAF 2205** | -412 | -12 | 400 | -271 | 90 | 680 | P+C+G | 23μm | 6-7mm |
| **25Cr Duplex** | -311 | 329 | 640 | -231 | 100 | 1700 | P+C+G | 18μm | 40mm |
| **UNS S31603** | -365 | 155 | 520 | -215 | 50 | 1650 | P+C+G | 25μm | 10mm |
| **UNS S31254** | -167 | 843 | 1010 | 813 | 40 | 500 | C+P.i. | | 30mm |
| **Ultimet** | -222 | 350 | 572 | Imme | 100 | 500 | P.i.+G | | |
| **Stellite 6** | -359 | -179 | 180 | N.R. | 50 | 580 | G+C | | |

Table 2.5. Electrochemical parameters for anodic polarisation in static seawater at 50°C

| | Ecorr (mV) | Eb (mV) | Eb-Ecorr (mV) | Er (mV) | Ib (μA) | Imax (μA) | Types of Attack | MPD | Crevice |
|---|---|---|---|---|---|---|---|---|---|
| **UNS S32760** | -326 | 474 | 800 | -226 | 90 | 3400 | P+C+G | 19μm | 18mm |
| **Inconel 625** | -435 | 563 | 998 | 415 | 60 | 500 | G | | |
| **SAF 2205** | -334 | -14 | 320 | -184 | 50 | 730 | P+C+G | 10μm | 8-10mm |
| **25Cr Duplex** | -384 | 96 | 480 | -54 | 30 | 1600 | P+C+G | 18μm | 20-22mm |
| **UNS S31603** | -362 | 28 | 390 | -142 | 35 | 1400 | P+C+G | 21μm | 40mm |
| **UNS S31254** | -417 | 683 | 1100 | -217 | 25 | 550 | C+P.i. | | 6-8mm |
| **Ultimet** | -412 | 263 | 675 | Immed | 100 | 500 | P.i.+G | | |
| **Stellite 6** | -401 | -190 | 211 | N.R. | 90 | 590 | P+G+C | 11μm | 40mm |

Table 2.6. Electrochemical parameters for anodic polarisation in static seawater at 60°C

| | Cr | Mo | Fe | Ni |
|---|---|---|---|---|
| **Area 1** | 24.4 | 3.6 | 64 | 9.1 |
| **Area 2** | 27.8 | 5.7 | 59.6 | 6.4 |

Table. 2.7. Chemical analysis on superduplex alloy UNS S32760 in Fig. 2.11b

| | Ecorr(mV) | iL(μA/cm$^2$) | Eh(mV) | Tafel(hy-ev)(mV/decade) |
|---|---|---|---|---|
| **UNS** | -254 | 27 | -1203 | -120 |
| **Inconel** | -297 | - | -1138 | -130 |
| **SAF 2205** | -308 | 18 | -1158 | -150 |
| **25Cr** | -319 | 10 | -1040 | -140 |
| **UNS** | -155 | 30 | -1084 | -200 |
| **UNS** | -317 | 5 | -980 | -200 |
| **Ultimet** | -277 | - | -1076 | -270 |
| **Stellite 6** | -341 | - | -1000 | -240 |

Table 2.8. Electrochemical parameters for cathodic polarisation in static seawater at 18°C

| | Ecorr(mV) | iL(μA/cm$^2$) | Eh(mV) | Tafel(hy-ev)(mV/decade) |
|---|---|---|---|---|
| **UNS** | -276 | 75 | -1126 | -200 |
| **Inconel** | -364 | - | -1144 | -300 |
| **SAF 2205** | -337 | 120 | -1077 | -280 |
| **25Cr** | -360 | 110 | -1296 | -200 |
| **UNS** | -311 | 115 | -1089 | -210 |
| **UNS** | -269 | 100 | -1009 | -220 |
| **Ultimet** | -367 | - | -948 | -500 |
| **Stellite 6** | -450 | 120 | -1148 | -530 |

Table 2.9. Electrochemical parameters for cathodic polarisation in static seawater at 50°C

**Discussion - Anodic potentiodynamic tests**

This research was intended to be a comparative study of the corrosion behaviour of high-grade alloys, and to enable comparisons to be made, a range of electrochemical parameters and results from detailed microscopy had to be considered. Electrochemical potentiodynamic anodic polarisation scans provide a means of ranking materials according to their relative resistance to passivity breakdown and in this work, attempts were also made to correlate the electrochemical parameters to the extent of corrosion propagation. It might appear that where mixed mechanisms of attack are involved, there is an inherent difficulty in comparing the severity of corrosion attack from one material to another but in conjunction with evaluation of electrochemical parameters, this can be successfully achieved. In trying to encompass the range of both localised and general mechanisms, the study becomes more applicable to the behaviour of the materials in real service conditions.

Using the electrochemical parameter, $E_b$, as an indication of resistance to passivity breakdown, the material ranking table in Fig. 2.21 was constructed for the temperatures at the lower and upper limits of the study in static sea water. It should be noted that the same ranking is obtained if the parameter $E_b$-$E_{corr}$ is used. Shown also are the main mechanisms of attack observed on each material after polarisation. As mentioned previously, the electrochemical measurements demonstrated a clear superiority at 18°C between the duplex stainless steels and the superaustenitic alloy as a group over the Ni-based, Co-based and UNS S31603 alloys, but no conclusive distinctions were possible between the top four alloys. However, from the consideration of the extent of attack (Table 2.2), there is some justification for the ranking order shown in Fig. 2.21 for 18°C.

It was anticipated that increasing the severity of the test conditions (here increasing the temperature) would distinguish between the electrochemical characteristics of the previously inseparable materials. However, as shown in Fig. 2.21, the effect was not only to accomplish this but change the entire ranking order thus demonstrating the important point that increases in temperature do not affect all materials to the same extent.

## MATERIAL RANKING UNDER STATIC CONDITIONS

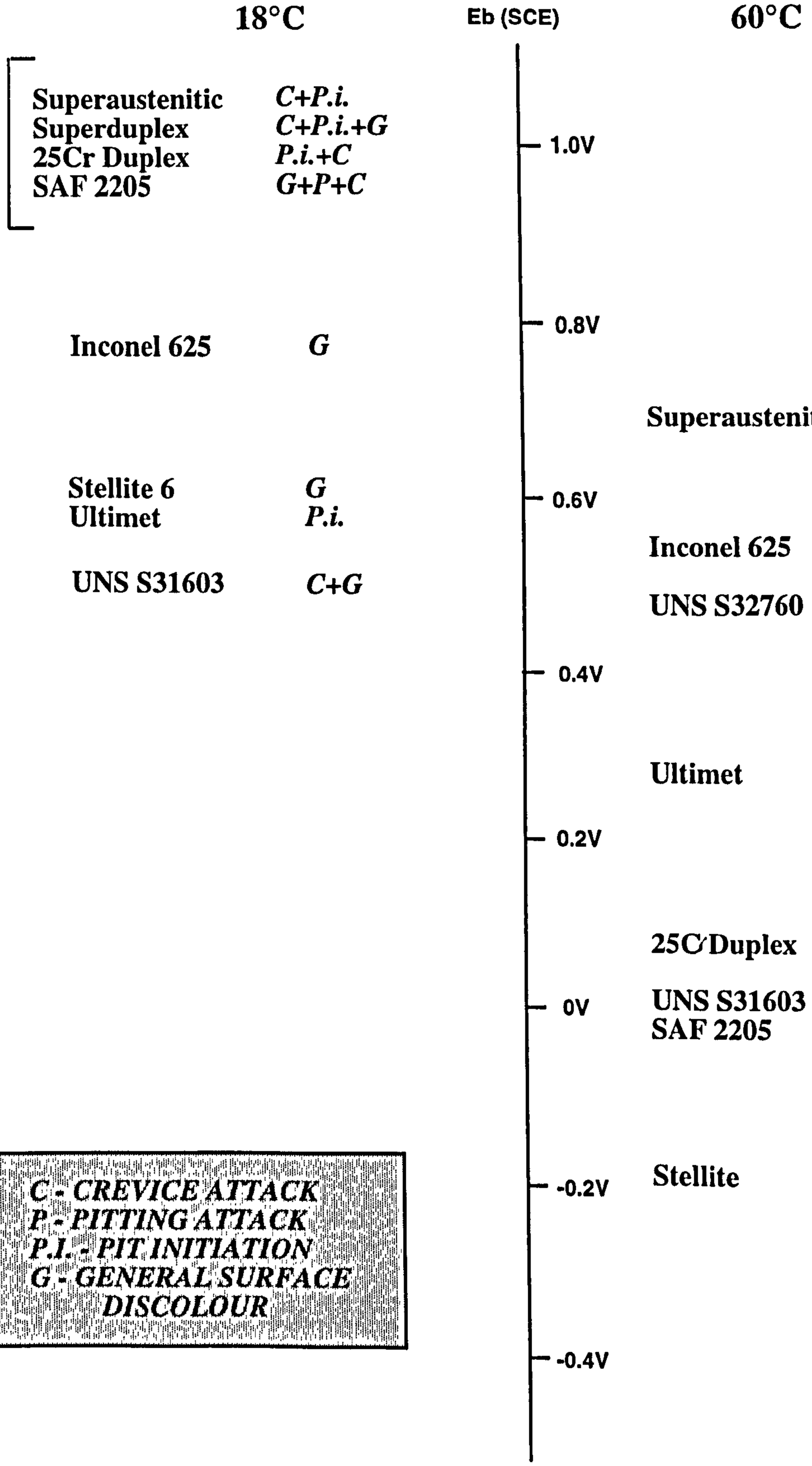


Fig. 2.21. Material ranking in static seawater

Interestingly, at 60°C, Inconel 625 which showed its good resistance to changes in passivity breakdown potential (denoted by the small decrease in $E_b$) resisted any form of localised attack and the only form of attack detected was a general surface discolour, thus confirming its previously reported good resistance to localised forms of attack [35]. The relatively poor electrochemical performance of, in particular, SAF 2205 and the 25Cr duplex alloy at elevated temperature was substantiated by the enhanced levels of localised attack in the form of pitting and crevice attack. Correlation between the maximum pit depth and the $I_{max}$ value was made in that, for any particular material, larger pit depths were detected as $I_{max}$ increased. It was concluded that $I_{max}$ was an inverse measure of the material's ability to repassivate and hence the extent of propagation once corrosion had initiated.

In halogen-containing environments, where stainless steels and related alloys have been shown, in the past, to be susceptible to localised attack [36], emphasis has been put on determining the relative influence of the alloying elements Cr, Mo and N in resisting localised attack. The general benefits of such alloying elements have indeed been demonstrated in this work. For instance, Inconel 625 was observed to be most superior in resisting pitting and severe crevice attack over the range of conditions studied. Also, only minor pitting attack was observed on the superaustenitic stainless steel and Ultimet. These influences of alloy chemistry on localised corrosion resistance have been encompassed in empirical formulae such as the "Pitting Resistance Equivalent" (PRE) %Cr+3.3%Mo+16%N [37,38]. Indeed it has become common for manufacturers and also users of such alloys to rely on such PRE values to rank materials. The PRE relation is focused especially on comparison of the behaviour of stainless steels and has seen much application in relation to corrosion resistance at ambient temperatures. Indeed the alloy ranking in Fig. 2.21 for static sea water at 18°C is essentially in line with the PRE predictions (especially if it is noted that pitting or crevice corrosion was not observed on the Inconel 625 material). However, it would appear that the PRE formula may be less reliable for other conditions. For instance, this study has demonstrated that, in static sea water, the temperature dependence of passive film breakdown differs between the various alloys. This feature, for example, appears to reverse the significantly higher corrosion resistance at ambient temperature of the SAF 2205 stainless steel compared to UNS S31603. Also, at temperatures in excess of 40°C, severe pitting attack on the superduplex stainless steel was detected yet the PRE value is comparable with both the superaustenitic and Ultimet. Moreover, the PRE formula does not appear to easily relate to the Co-based alloys - although the *general* benefit of higher Mo is reflected in the superior corrosion resistance of Ultimet compared to Stellite.

Prediction of the performance of high grade alloys at elevated temperature is normally achieved by means of parameters such as the critical pitting temperature (CPT) and the critical crevice temperature (CCT). The standard test method for determining CPT and CCT is normally the ASTM G48-76 using $FeCl_3$ solution. The most important alloying elements in determining localised corrosion resistance at higher temperatures are generally accepted to be Cr, Mo and N as for ambient temperature conditions. Hence empirical formulae for CPT and CCT have been developed[39] analogous to the PRE. As a tool for ranking the material performance of the duplex stainless steels, the CCT and CPT formulae are in agreement with the ranking attained experimentally in this study by electrochemical parameters. Figures 2.22 and 2.23 plot CPT and CCT as determined by the empirical formulae against $E_b$, determined in this work at 60°C. It can be seen that there is a general agreement that a higher predicted CPT and CCT value is normally associated with a higher $E_b$ value but there are irregularities in particular with reference to the cobalt-based alloys. The CPT and CCT formulae tend to suggest a higher ranking for the cobalt based alloys.

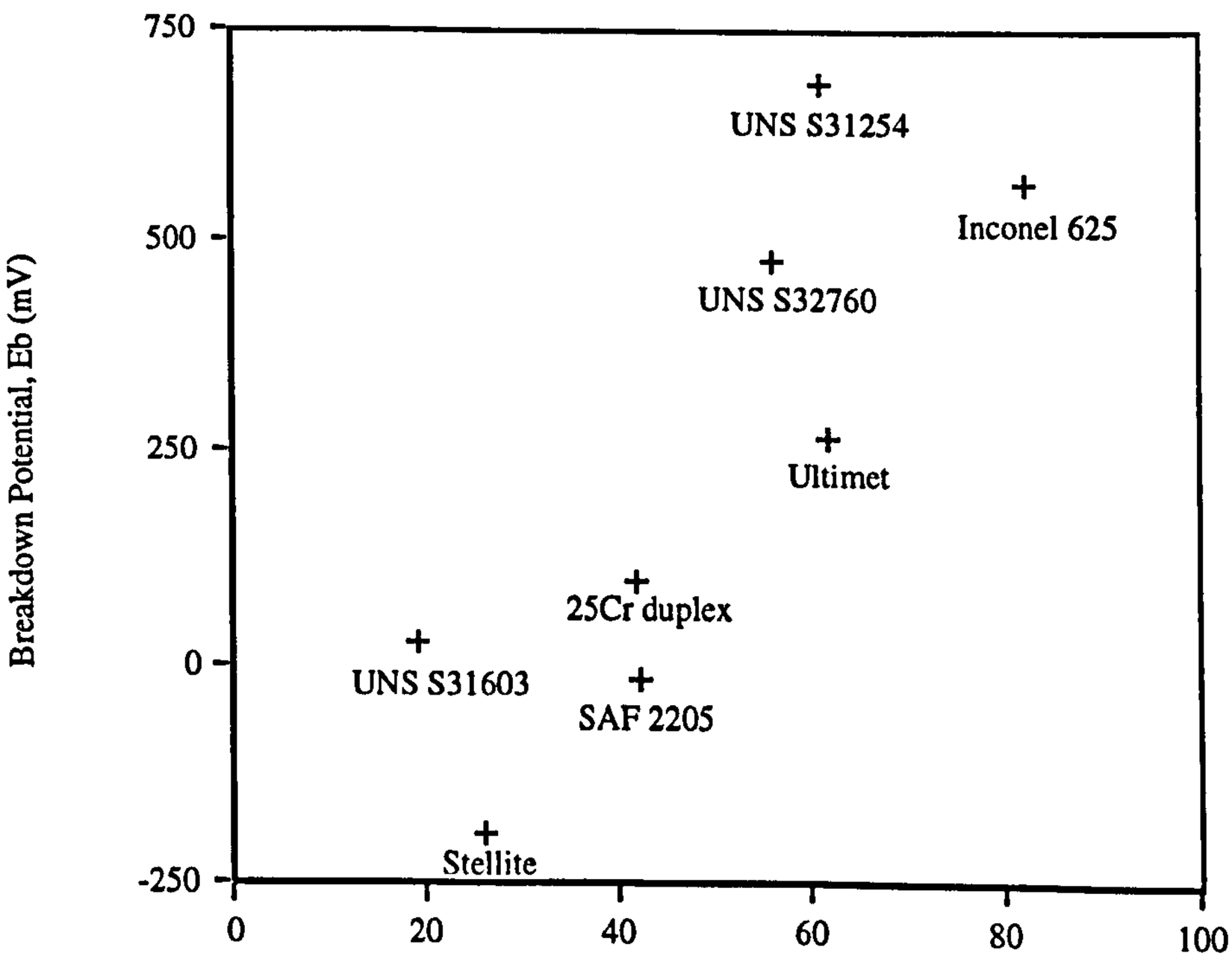


Fig. 2.22. CPT (from empirical formula) versus $E_b$ (determined experimentally) in static seawater at 60°C

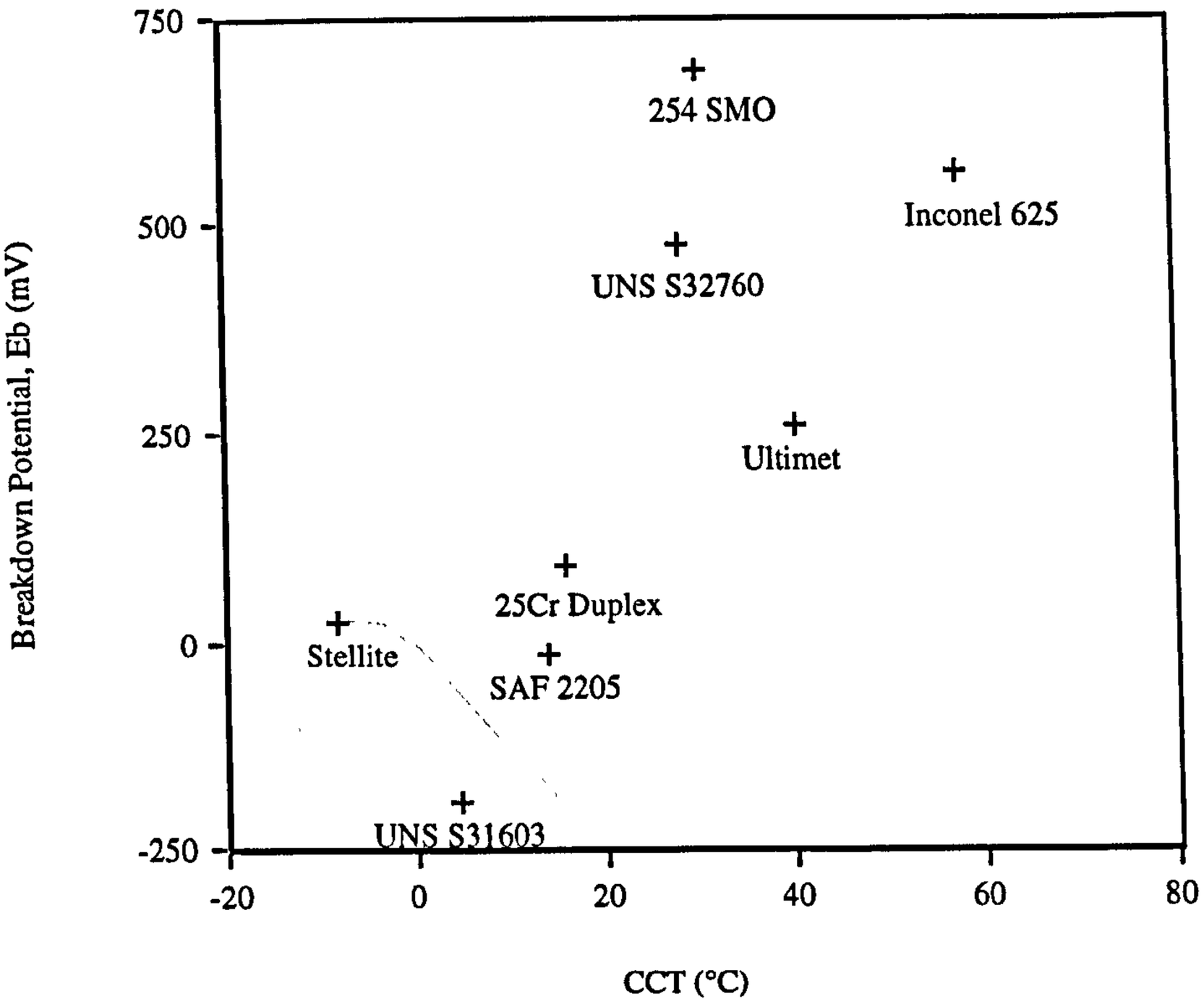


Fig. 2.23. CCT (from empirical formula) versus $E_b$ (determined experimentally) in static seawater at 60°C

The CCT and CPT formulae tend to underestimate the resistance of UNS S31603 at elevated temperature particularly with respect to SAF 2205 since, in this work, the SAF 2205 was shown to be marginally more susceptible to localised attack at elevated temperature than the UNS S31603 yet the CPT and CCT formulae predicted that the duplex alloy should be much more resistant. The results of this current study are supported in recently reported plant experience where the susceptibility of SAF 2205 in comparison to UNS S31603 has been demonstrated [40].

Since this work involves an investigation of mixed mechanisms of localised and general attack, the emphasis is not on determining a critical pitting or crevice temperature but on identifying a temperature above which the material susceptibility to attack increases, the mechanism of attack being identified by microscopical techniques. Results have shown that the critical breakdown temperature for the stainless steels, evaluated in this study, lie between the predicted CPT and CCT values. For the Stellite 6 the critical breakdown temperature was shown to be much lower than the predicted value. It is suggested that the Ultimet and Inconel 625 alloys did not reach their critical

temperature up to 60°C since substantial decreases in $E_b$ were not detected and this is in agreement with previous work [40]. Roscoe et al. [11] evaluated the CPT and CCT in seawater for the stainless steels already shown in Table 2.1. This work has shown consistently that UNS S32760 is susceptible to localised attack at temperature in excess of 40°C which is in contrast to that found by Roscoe et al. The estimation of the CPT and CCT for UNS S31254 seems to be in agreement with this study since at 60°C, very little localised attack was observed and a significant fall in $E_b$ was not evident.

In summary, where several mechanisms of attack can occur concurrently, the effect of Cr, Mo and N in resisting attack become very complex, particularly at elevated temperatures and as such a closer look at the behaviour via electrochemical parameters supported by microscopy may be more appropriate than the simple use of empirical formulae.

**Cathodic Polarisation**

Typically, in electrochemical pitting corrosion studies, the anodic reaction is investigated as it yields invaluable information on the mechanisms of attack which predominate under certain conditions. Also it allows materials to be ranked according to their resistance to passivity breakdown via accelerated test methods. However, since in an electrochemical cell the total cathodic current must equal that of the anodic reaction, the rate of cathodic activity can become the controlling factor in corrosion propagation once corrosion has initiated. Particularly in the severe conditions of elevated temperature, where the tendency for corrosion initiation has been shown to increase, the importance of the cathodic reaction progression is even greater. Since once corrosion has initiated a drop in potential is recorded, the cathodic characteristics in the potential region negative to the newly exposed $E_{corr}$ are of interest.

Another important aspect of the cathodic reaction kinetics is the ability of depolarisation to induce an ennoblement of the free corrosion potential. Several authors have reported ennoblement of $E_{corr}$ in natural, aerated sea water [41-47] and have postulated that where marine organisms are present, their respiratory activity increases the rate of oxygen reduction at the surface and the exchange current density for the oxygen-reduction cathodic reaction, hence noble values of $E_{corr}$ are recorded. Therefore there is an increased danger of initiating localised corrosion when depolarisation of the cathodic reaction for whatever reason pushes the free corrosion potential nearer to the breakdown potential.

The initial, low current behaviour upon commencing the cathodic polarisation scans may be due to the presence of an oxide on the surface of the material and could be, as Vetter explained [48], the reduction of the oxide (or chemisorption) layers. Alternatively, it may be associated with a two-stage oxygen-reduction reaction involving the formation of an intermediate product, possibly $H_2O_2$,

$$O_2 + 2H^+ + 2e \rightarrow H_2O_2$$

as suggested by others [48,49], followed by reduction of $H_2O_2$ via,

$$H_2O_2 + 2H^+ + 2e \rightarrow 2H_2O$$

which occurs at a higher overpotential and creates the second increase in reaction rate as shown by the second 'wave' in the rotating disk cathodic polarisation plot..

The composite cathodic reaction described above has been shown to be mass-transfer controlled [49], the limiting factor being the supply and replenishment of oxygen to the electrode surface. However, if oxygen concentration in the bulk solution was the only controlling factor for the extent of the reaction, $i_L$ would have been smaller at 50°C than at 18°C as the measured concentration of dissolved oxygen was shown to decrease (as expected) at elevated temperature. In relation to explaining the observed cathodic depolarisation of the oxygen-reduction reaction at elevated temperature in static conditions , the following factors may be relevant;

1) The effect of higher temperature on the mass transfer characteristics of dissolved-oxygen in sea water
2) The effect of higher temperatures on the equilibrium electrode potentials ($E_o$) of the cathodic reactions
3) The effect of higher temperature on the rate of $H_2O_2$-reduction while following Tafel kinetics

At 18°C in static sea water, there is a very short potential range where oxygen reduction proceeds and seems to be following a linear E-log i relation but once the current attains a few μA, concentration polarisation effects are apparent. It is evident from the progression of oxygen reduction at 50°C that, more important than the concentration of the reactant in the sea water, is it's rate of transport to the electrode surface, quantified by the diffusion coefficient which is known to increase with temperature. Hence it can be concluded that the increase of diffusion coefficient with temperature has implications for the progression and rate of oxygen reduction (whether by a single step or a two step

process) since more efficient replenishment of reactants at the substrate surface counteracts a lower bulk oxygen concentration due to decreased solubility. Thus at 50°C, the reaction could proceed to reach a limiting current in the order of 100μA/cm$^2$ before concentration polarisation effects were observed. Once the integrity of the passive alloys has been lost either locally or generally, a depolarised cathodic reaction at least partly can account for increased propagation rates which have been observed at elevated temperature.

The relatively rapid hydrogen production reaction, which occurs at more negative potentials does not have direct relevance to the propagation rates of corrosion in the aerated sea water conditions studied here. However, it does have implications for components of these materials which might come under the influence of cathodic protection systems because of possible problems due to hydrogen ingress into the substrate component. The Tafel slopes indicated that this reaction occurred faster on duplex stainless steels and Inconel 625 in static sea water. Although this reaction is well known to occur at widely different rates on different materials, these variations are perhaps a little surprising.

Increased temperature to 50°C resulted in an increased Tafel slope for the hydrogen-production reaction on the duplex stainless steels, Inconel 625 and the cobalt-based alloys signifying increased polarisation at elevated temperature. The dependence of the effect of temperature on material type is apparent with the hydrogen-production Tafel slope of the austenitic stainless steels not significantly affected by the increased temperature.

Although it is recognised that rates of propagation of pits and crevice corrosion are largely controlled by anode/cathode area ratios, these polarisation tests have indicated that an additional factor may be differences in cathodic polarisation characteristics between different alloys. Of greatest interest in this respect were the distinct cathodic characteristics exhibited by the cobalt and nickel -base alloys.

**General Materials Comparison**

What this study has illustrated is that for each material, in conditions of high temperature, accelerated test methods in conjunction with microscopic examination can define an envelope of conditions in which the material should perform satisfactorily.

One of the main implications from this study is the apparent reliability of the nickel-based Inconel 625 and the cobalt-based Ultimet in resisting localised attack and

maintaining passive behaviour in conditions where the stainless steels and other alloys have been shown to suffer enhanced attack.

In relation to the stainless steels, of course considerable work and practical experience has demonstrated the relatively poor resistance of type UNS S31603 steel to localised corrosion (especially crevice corrosion) at ambient temperature in saline environments and the benefits in these respects resulting from increasing the Cr, Mo and N contents of these alloys. This study has demonstrated that, under static conditions, the resistance to passivity breakdown of UNS S31603 (and also of the two duplex stainless steels, SAF 2205 and the 25Cr variety) is reduced by moderate increases in temperature from ambient. Moreover, the very substantial decrease in the passive range of Stellite 6 between 18°C and 30°C suggests that caution must be taken in utilising Stellite 6 in chloride-containing environments especially where temperatures are expected to exceed 18°C. The superaustenitic, superduplex, Inconel 625 and Ultimet alloys possess greater resistance to attack promoted by exposure to sea water at temperatures above ambient. However, on the superduplex alloy, the severity of localised pitting attack was shown to increase significantly at temperatures in excess of 40°C suggesting that, for applications where conditions would likely entail prolonged periods of exposure to stagnant sea water at elevated temperature, the superaustenitic, nickel-based Inconel 625 or Ultimet would be more effective in resisting localised attack.

**Conclusions**

This study has successfully demonstrated that elevated temperatures in the relatively small range (18°C-60°C) studied have significant effects on the electrochemical polarisation characteristics and also on the extent and mechanisms of attack observed. Important changes in the relative corrosion performance of the materials as the temperature increased were elucidated.

Under static conditions at elevated temperatures, evidence for accelerated loss of passivation was given by:-

- a lower resistance of each material to passivity breakdown, denoted by a lower breakdown potential, $E_b$
- a decrease in the potential range over which the materials were "passive" denoted by the parameter $E_b$-$E_{corr}$
- enhanced localised attack propagation as temperature increased

- changes in the relative corrosion performance of the materials as the temperature increased

Cathodic reaction kinetics were found to be dependent on material. Significant differences between stainless steels and Co and Ni-base alloys were observed. Depolarisation of the cathodic reaction as the temperature increased implied higher propagation rates would prevail in higher temperature seawater and this was consistent with microscopical observations.

Material selection for applications where elevated temperatures are to be encountered must take into consideration the effect on the temperature on the mechanisms of attack and the relative susceptibility at a particular temperature. Use of empirical formulae based on service experience at ambient temperature must be used with caution.

## References

1. J. W. Oldfield, Test techniques for pitting and crevice corrosion resistance of stainless steels and nickel-base alloys in chloride-containing environments, *International Materials Reviews*, 1987, Vol. 32, No. 3, pg153

2. A. J. Sedriks, New stainless steels for seawater service, *Corrosion*, Vol. 45, No. 6, June 1989

3. O. Olsson, B. Wallen, Experience with a high Mo stainless steel in saline environments, *Desalination*, 1983, Vol. 44, 241

4. T. Hodgkiess, A. Asimakopoulos, Studies of the localised-corrosion behaviour of some stainless steels, Incoloy 825 and Titanium in seawater, *Desalination*, 1981, Vol. 38, 247

5. T. Hodgkiess, W. T. Hanbury, M. H. Hejazian, Corrosion tests of a range of materials in three MSF plants, *Desalination*, 1983, Vol. 44, 223

6. B. Todd, Materials for multi-stage flash distillation plants, *Middle East Water Sewage J.*, Oct-Nov. 1977

7. A. H. Tuthill, Guidelines for the use of copper alloys in seawater, *Mater. Perf.*, September 1987

8. C. M. Schillmoller, M. R. Jasner, High performance alloys for offshore platform process piping, *Mater. Perf.*, January 1984

9. E. Alfonsson, R. Qvarfort, Investigation of the applicability of some PRE expressions for austenitic stainless steels, *Presented at the International Conference on Electrochemical Methods in Corrosion Research*, EMCR '91, July 1-4, 1991, Helsinki

10. T. J. Glover, Recent developments in corrosion resistant metallic alloys for construction of seawater pumps, *Mater. Perf.*, July 1988

11. C. V. Roscoe, K. J. Gradwell, The history and development of duplex stainless steels. 'All that glisters is not gold'. *Presented at the Duplex Stainless Steels Conference*, The Hague, October 1986

12. A. M. Hassan, A. U. Malik, Corrosion resistant materials for seawater RO plants, *Desalination*, Vol. 74, 1989, 157-170

13. J. A. Carew, M. Abdel-Jawad, A. Julka, Corrosion performance of selected stainless steels in brine for reverse osmosis desalination plants, *Brit. Corr. J.*, Vol. 29, No. 4, 1994, p275

14. H. Saricimen, Corrosion of 316L austenitic stainless steel under desalination plant conditions, *Brit. Corr. J.*, Vol. 29, 4, 1994

15. J. Ollson, Application of UNS S31254 (Avesta Sheffield 254 SMO) austenitic stainless steel in power plants, *NACE*, Cincinatti, Ohio, March 1991

16. W. E. Rutcher, R. K. Hart, Influence of oxygen on high temperature aqueous corrosion of iron, *Corrosion*, Vol. 19, 1963, p127

17. E. G. Brush, W. L. Pearl, Corrosion and corrosion product release in neutral feedwater, *Corrosion*, Vol. 28, 1972, p129

18. B. Todd, Corrosion and materials selection in seawater systems, *I. Mech. E. Publications*, 1979

19. K. Mabuchi, Y. Horii, H. Takahashi, M. Nagayama, Effect of dissolved oxygen on the corrosion behaviour of carbon steel in high temperature water, *Corrosion*, Vol. 47, No. 7, July 1991

A. J. Sedriks, Effects of alloy composition and microstructure on the passivity of stainless steels, *Corrosion*, Vol. 42, No. 7, 1986

20. E. C. Potter, G. M. W. Mann, *Proc. 1st Int. Congress on Metallic Corrosion*, 1961, p417

21. M. C. Bloom, G. N. Newport, W. A. Feaser, Steel corrosion mechanisms. The growth and breakdown of protective films in high-temperature aqueous systems : 15%NaOH at 316°C, *J. Electrochem. Soc.*, Vol. 111, 1964, p1343

22. A. P. Bond, M. J. Dundas, S. Eherot, M. Semchyshen, Stainless steels for seawater service, *Stainless steel '77*, Paper 15

23. J. Pleava, *Nyby Uddeholm Corrosion Control Information*, No. 1, Avesta Sandvik Tube, Sandvik Sweden, 1983

24. M. Renner, U. Heubner, M. B. Rockel, E. Wallis, Temperature as a pitting and crevice corrosion criterion in the $FeCl_3$ test, *Werkstoffe und Korrosion*, 37, 183-190, 1986

25. J. J. Dundas, A. P. Bond, Corrosion resistance of stainless steels in seawater, *Mater. Perf.*, October 1985

26. G. Moretti, G. Quartarone, A. Tassan, Pitting corrosion behaviour of superferritic stainless steels in waters containing chloride, *Werkstoffe und Korrosion*, Vol. 44, 24-30, 1993

27. R. Qvarfort, Critical pitting temperature measurements of stainless steels with an improved electrochemical method, *Corros. Sci.*, Vol. 29, No. 8, 987-993, 1989

28. M. S. Streicher, Development of pitting resistant Fe-Cr-Mo alloys, *Corrosion*, Vol. 30, No. 3, 1974

29. A. Garner, Material selection for bleached pulp washers, *Pulp Paper, Can.*, Dec 1981, 82, (12), T414

30. J. Chance, K.J. Gradwell, W. Coop, C. V. Roscoe, Structure property relation in a 25Cr-7Ni-2Mo duplex stainless steel casting alloy, *Duplex Stainless Steels Conference Proceedings*, ASM Metal/Materials Tech. Series, paper 8201-019, p771, 1982

31. M. Al-Arrayedh, B. Ericsson, M. Othani, Construction and operation of 46000m3/day reverse osmosis desalination plant, RA's ABU JAJUR, Bahrain, *Desalination*, 1985, Vol. 55, 39-342

32. R. C. Newman, E. M. Franz, *Proc. 9th Int. Congr. on Metallic Corrosion,* Toronto, Vol. 4, p373, 1984

33. N. Azzerri, F. Mancia, A. Tamba, Electrochemical predictions of corrosion behaviour of stainless steels in chloride-containing water, *Corros. Sci.*, 22, 675 (1982)

34. T. Suzuki, Y. Kitamura, Critical potential for growth of localised corrosion of stainless steels in chloride media, *Corrosion*, Vol. 28, 1, 1972

35. A. I. Asphahani, Corrosion resistance of high performance alloys, *Mater. Perf.* Dec. 1980, p33

38. A. J. Sedriks, *International Metals Review*, 27, 321 (1982)

39. T. J. Glover, Recent developments in corrosion resistant metallic alloys for the construcition of seawater pumps, *CORROSION/88*, Paper No.323, NACE, Houston

40. E. Alfonsson, R. Qvarfort, Investigation of the applicability of some PRE expressions for austenitic stainless steels., *Avesta Corrosion Management*, No.1, 1992

41. J. Nordström, J. Olsson, *Proceedings of the World Conference on Desalination and Water Treatment*, November 1993, Japan, Vol. 1, 577-584

42. V. Scotto, Di. R. Cintio, G. Marcenaro, The influence of marine aerobic microbial film on stainless steel corrosion behaviour, *Corros. Sci.* 25, 185, (1985)

43. P. Gallagher, R. E. Malpas, E. B. Shone, Corrosion of stainless steels in natural, transported and artificial seawaters, *Brit. Corros. J.*, 23, 4 (1988)

44. Wallen. B., Henrikson. S., Effect of chlorination on stainless steels in seawater, *Werkstoffe und Korrosion*, 40, 602-615 (1989)

45. V. Scotto, M. Beggiato, G. Marcenaro, R. Delleplane, Marine Corrosion of Stainless Steels: Chlorination and Microbial Effects, *European Federation of Corrosion Publications.*, No.10 (1990).

46. P. Gartland, Marine Corrosion of Stainless Steels: Chlorination and Microbial Effects, *European Federation of Corrosion Publications*, No.12 (1990).

47. P. Gallagher, A. Nieuwhof, R. J. M. Tausk, Marine Corrosion of Stainless Steels: Chlorination and Microbial Effects, *European Federation of Corrosion Publications*, No. 6 (1990).

48. K. J. Vetter, *Electrochemical Kinetics*, Academic Press, 1967, London

49. M. B. Ives, Y.C. Lu, J. L. Luo, Cathodic reactions involved in metallic corrosion in chlorinated saline environments, *Corros. Sci.* 32, 1, (1991)

# Chapter 3

# Material Selection for High Temperature and High Salinity Applications

## Introduction

As a continuation of the work reported in chapter 2, the results to be presented in this section focus on the behaviour of three materials in severe conditions of high temperature and concentrated brine. The series of tests, the results of which are reported here, were performed in relation to an engineering failure which occurred in an oilfield pumping application.

Industrial Situation

The conditions generated in offshore pumping conditions within the oil recovery process have been reported to cause failure to pump components in relatively short periods. Material selection to resist degradation in such conditions represents a formidable task.

In this particular application, the susceptible components consisted of impeller neck and eye wear rings, and the auxiliary sleeving on the pump shaft. The pump, situated on the oil platform, was subjected to produced water which had a salinity of almost four times that of normal seawater and was at a temperature of 90°C. The water chemical analysis is given below:

| | |
|---|---|
| Sodium | 700ppm |
| Potassium | 674ppm |
| Calcium | 6130ppm |
| Strontium | 340ppm |
| Magnesium | 827ppm |
| Barium | 2.9ppm |
| Iron | 1.1ppm |
| Chloride | 76000ppm |
| Sulphate | 589ppm |
| Bicarbonate | 201ppm |
| Carbonate | 0ppm |
| pH 6.7 | |

The wear rings were Stellite 6, the cobalt-base alloy and the auxiliary sleeving was a superduplex 25Cr/5Mo alloy, similar but not identical to, the superduplex UNS S32760 included in this programme.

In the first section of this work the mechanisms of failure of the real components and the results of the post-failure analysis will be reported. The study will then focus on reporting results of laboratory tests performed in simulated produced water conditions, the purpose of which is to determine the relative performance of selected alloys and discuss their applicability for this particular application. The main objective of the test programme was to ascertain the relative importance of seawater concentration and temperature in the deterioration of the tested materials.

## Experimental Methods

Experimental techniques used in this chapter are similar to those used in chapter 2. The tests, at three temperatures (18°C, 50°C and 90°C) were performed in static conditions, the only difference being that at each temperature, the effects of deaeration and increased seawater concentration were investigated. Deaeration was achieved by bubbling nitrogen through the solution for the duration of the test, with the exception of the 90°C tests, since it was assumed that due to the natural decreasing solubility of oxygen at elevated temperature, very low oxygen conditions would be achieved. The stability of the saturated calomel electrode is adversely affected at temperatures in excess of 50°C and as such, a salt bridge was used in the elevated temperature tests.

The materials under study in this chapter included Stellite 6, UNS S32760 superduplex stainless steel and the 25Cr duplex. Duplicate tests were performed at each temperature and for each salinity on specimens of 1cm$^2$ exposed surface area.

## Results

### Analysis of Pump Components After Service

Examination of the Stellite 6 wear ring revealed very severe pitting corrosion on the outer circumference. The extent of the pitting is clear from Fig. 3.1a which shows a low magnification view of the outer surface of a section of the wear ring. The pitting corrosion, shown more closely in Fig. 3.1b, was found to be the causative mechanism of loss of mechanical strength which led to eventual splitting of the wear ring in the axial direction while in service. The pitting depth illustrated in Fig. 3.2, from a radial cross section through one of the surface pits has clearly led to a significant loss of thickness in localised areas. It can be seen from Fig. 3.2 that there is a thin membrane of material over the mouth of the pit and that propagation seems to have been via a tunnelling mechanism under this membrane.

Closer examination of the wear ring surface using light and ultimately scanning-electron microscopy showed there to be overall surface attack which could be seen in an etching of the surface to reveal the dendritic cast structure of the Stellite 6 alloy. Figure 3.3 shows clearly the appearance of the Stellite 6 microstructure in which pitting attack could be found.

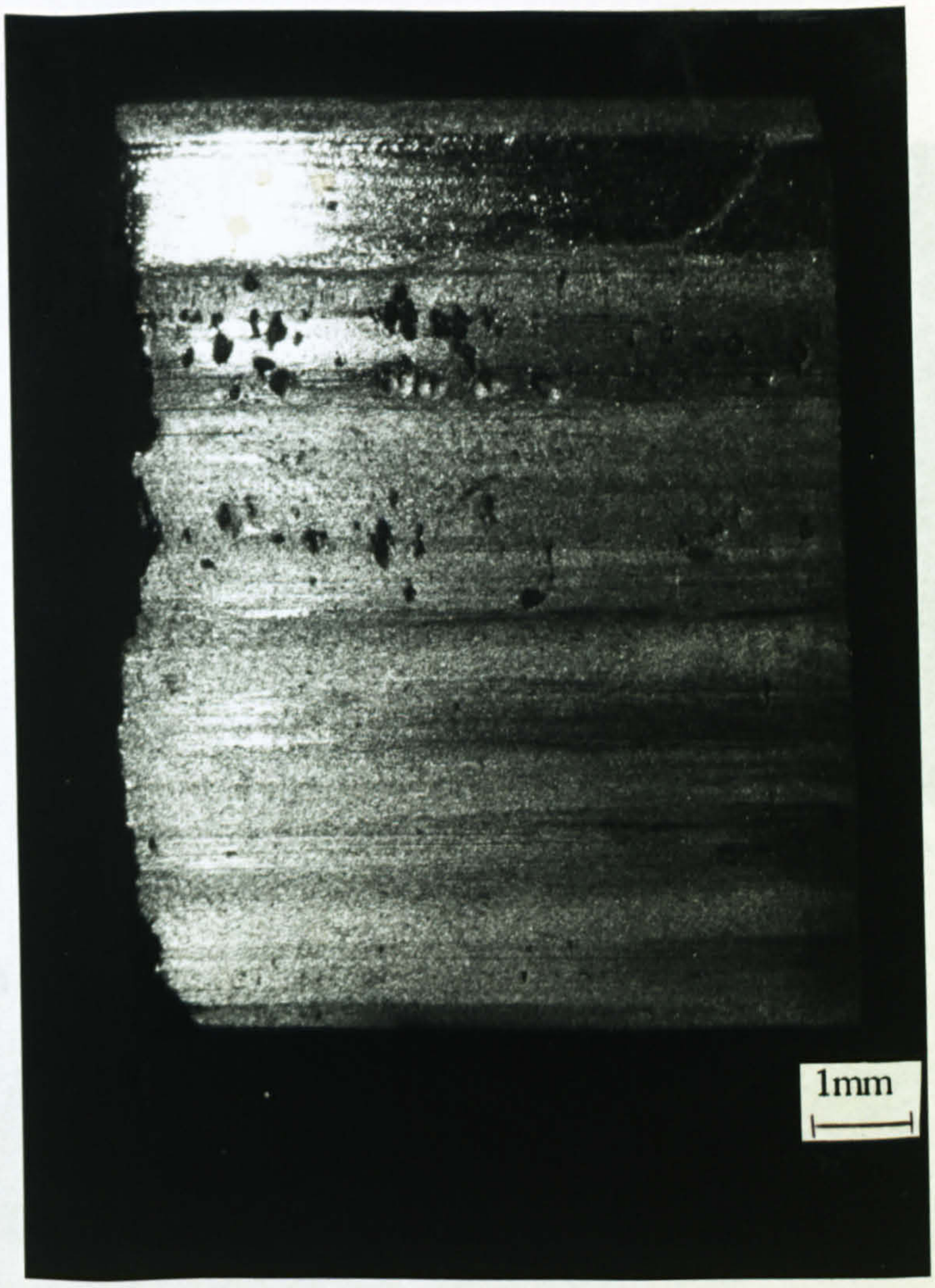


(a)


(b)

Fig. 3.1(a) Pitting on the outer surface of a Stellite 6 wear ring after exposure to seawater at 90°C and approximately four times the concentration of normal seawater and (b) closer view of pitting on the outer surface of the Stellite 6 wear ring

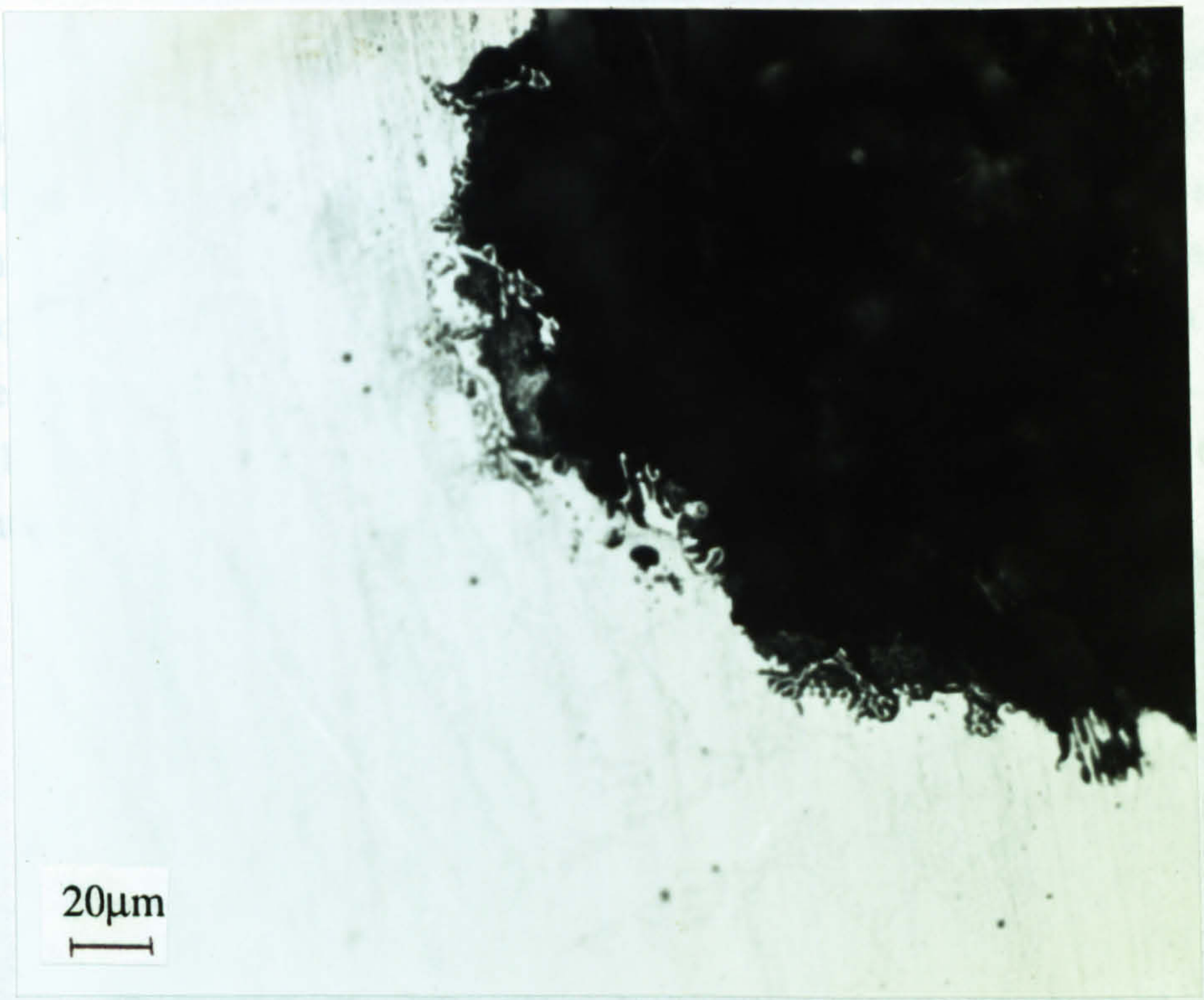


Fig. 3.2. Cross section through one of the pits on the Stellite 6 wear ring

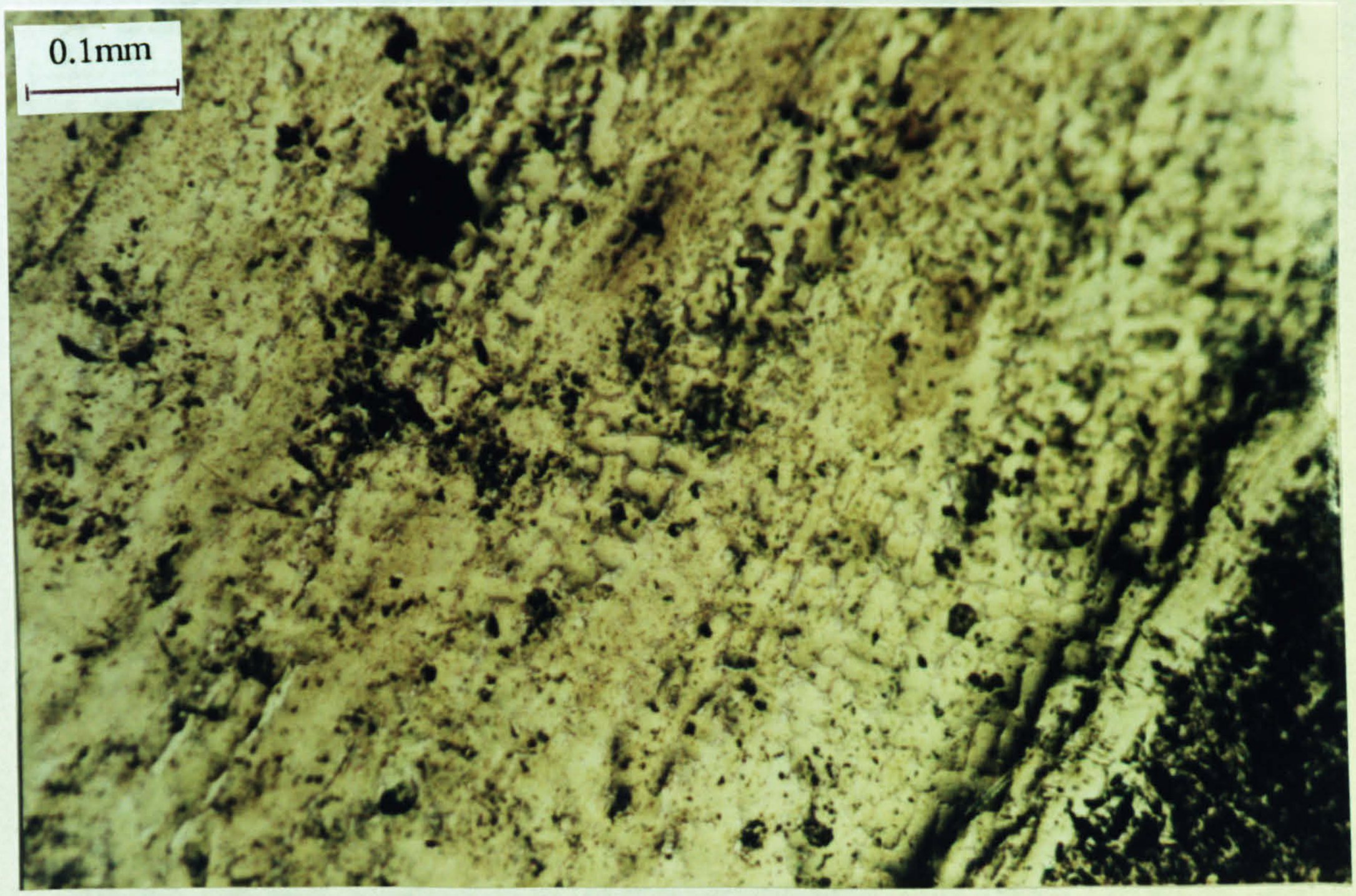


Fig. 3.3. General etching of the surface of the Stellite 6 wear ring

Within the extensive deterioration of the surface, as shown in the SEM micrograph (Fig. 3.4a), significant compositional differences were detected relating to the Cr distribution in the cast material. The composite structure consisted of two main phases: the matrix, which had a composition comparable to the standard composition of the Stellite 6 alloy and dentritic regions (the needle-like regions shown in Fig. 3.4b within one of the pits) the composition of which was rich in Cr and depleted in Co compared to the Stellite 6 bulk analysis. Figure 3.5 compares the main element concentrations (Cr and Co) for standard Stellite 6, the dendritic regions and the matrix.

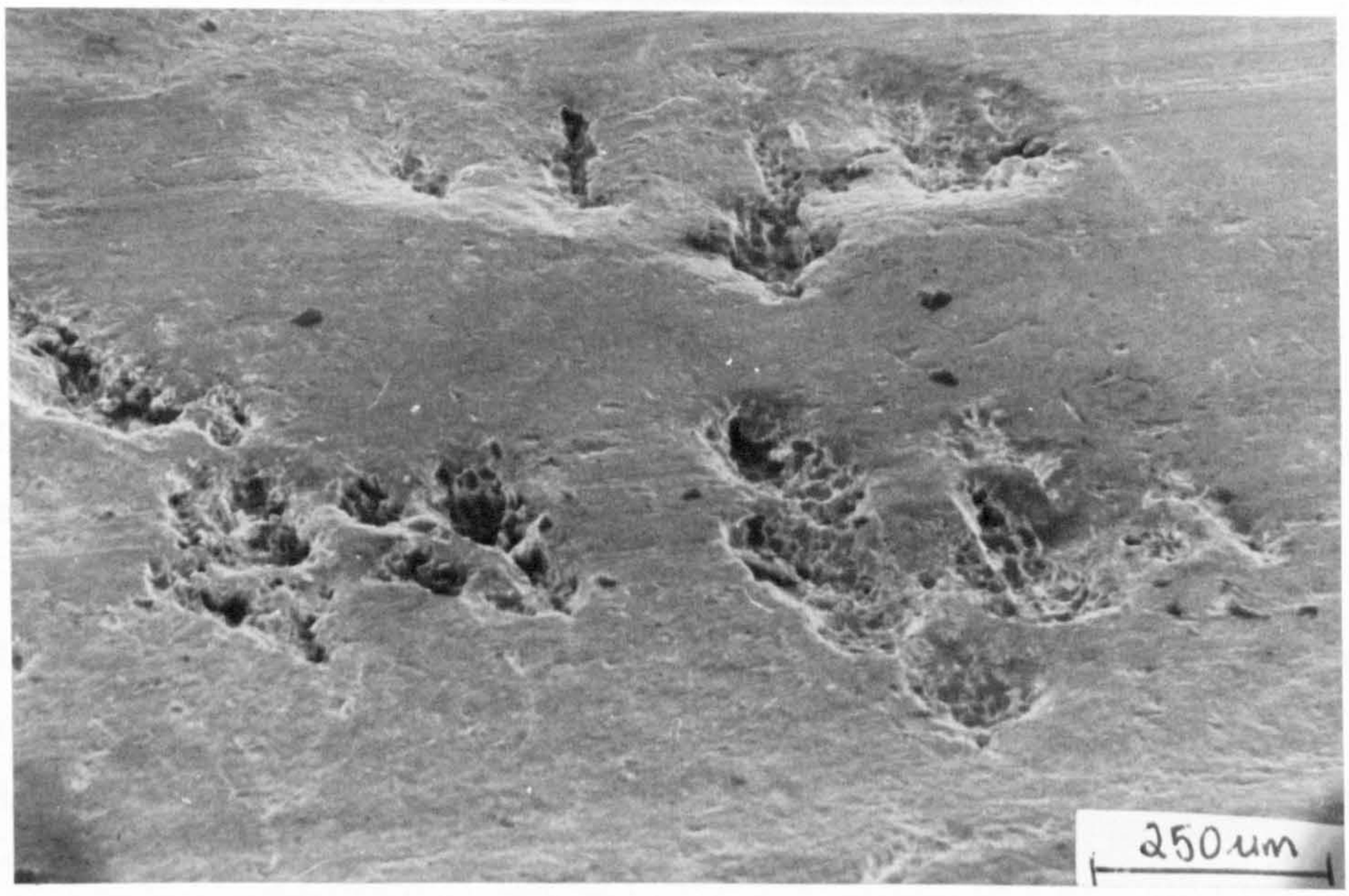


(a)

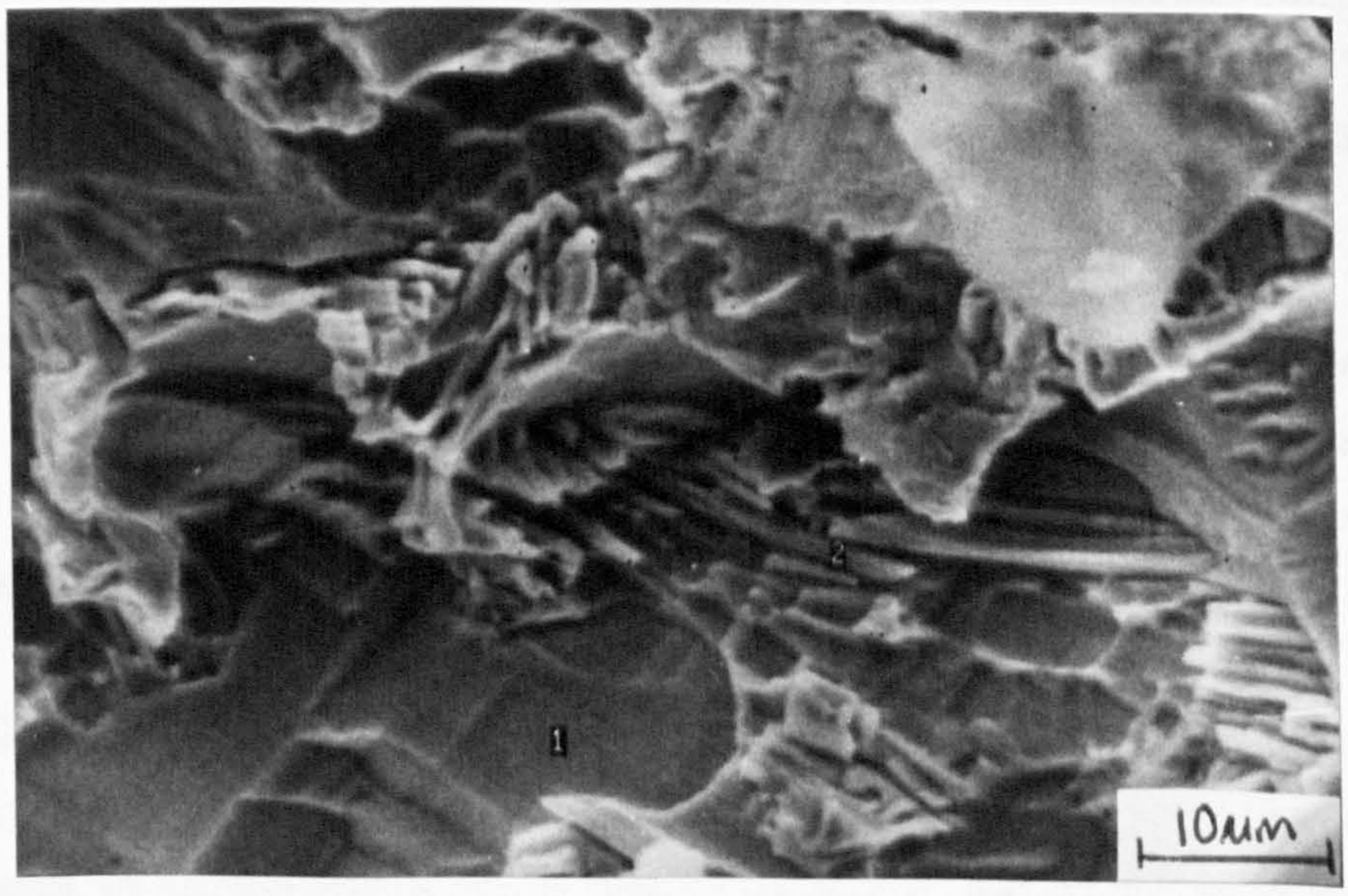


(b)

Fig. 3.4. (a) SEM micrograph of the extensive deterioration on the surface of Stellite 6 and (b) dendritic region within one of the pits, 1-needle-like dendrites, 2- matrix

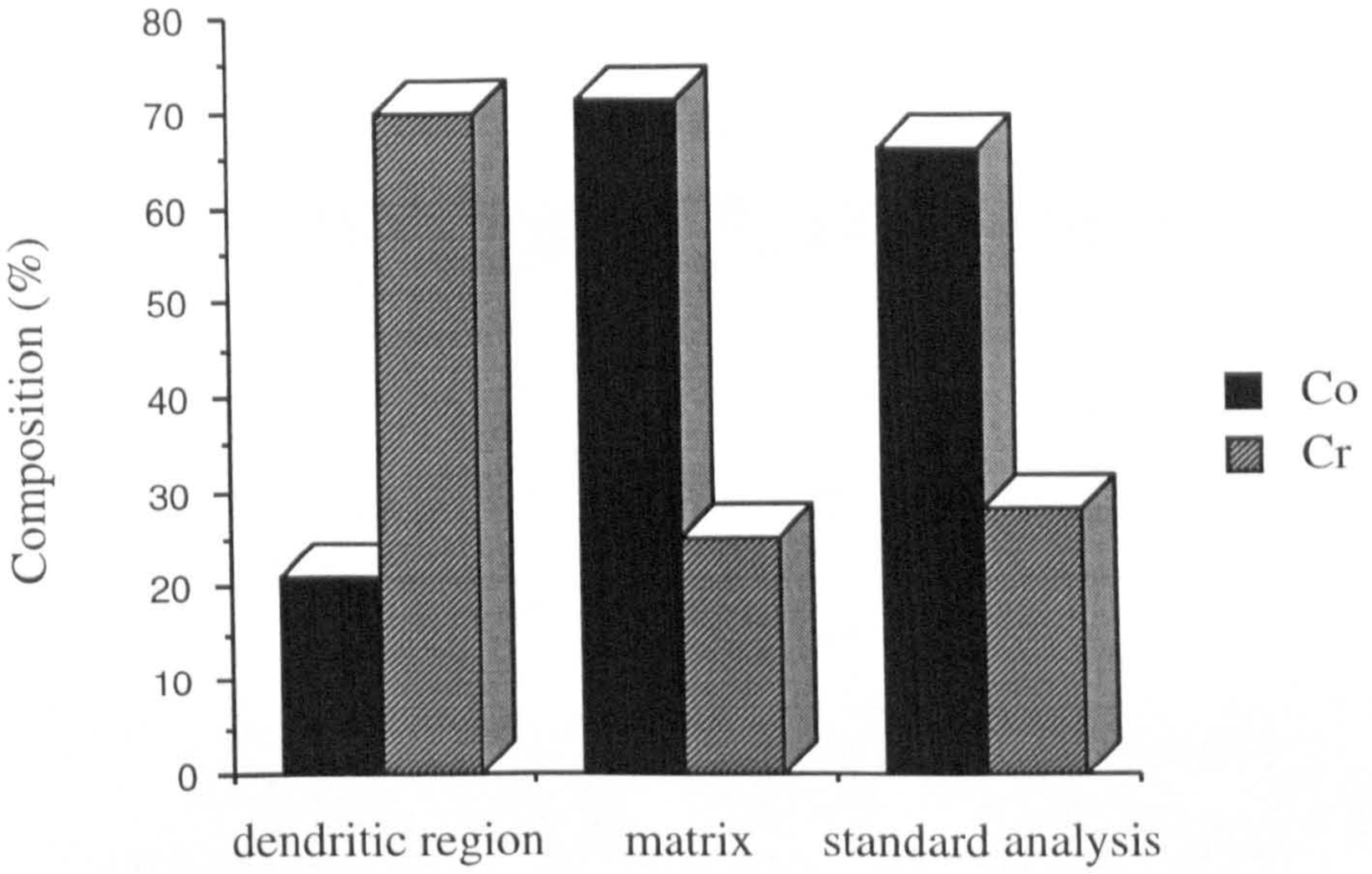


Fig. 3.5. Composition of Cr and Co within the pit on the Stellite 6 component compared to the standard analysis

From analyses within the pits on the surface of the component and on unattacked regions, it was found that the attack was via preferential dissolution of the lower-Cr matrix to leave a Cr-rich dendritic network. The remaining undissolved material would therefore be brittle, and as the failure suggested, have much reduced mechanical properties. It could therefore be possible that the partitioning of Cr to the dendrites caused an area of very much depleted Cr to form immediately adjacent to the dendrite thus inducing enhanced attack. However, no such regions were identified. Analysis on the unattacked regions revealed a composition of Cr not much greater than in the matrix wihin the pit.

The auxiliary sleeving has the purpose of protecting the shaft from degradation due to wear and corrosion. Under the same conditions which caused premature failure of the Stellite 6 wear ring, the auxiliary sleeving, fabricated from 25Cr/5Mo superduplex stainless steel, was found to have suffered severe attack.

The attack on the sleeving component (shown in Fig. 3.6) was found on the outer face which would have formed an interference fit with a wear ring. The most severe attack was found in the region shown by the arrow in Fig. 3.6. Attack was also found in other areas along the sleeving. The metal dissolution was manifested in what seemed to be pitted regions as in Fig. 3.7 and only on the most severely attacked regions was it clear that there had been selective attack on one of the duplex phases (Fig. 3.8). The two

phase structure was made apparent in addition by the coloured surface at the attacked areas (Fig. 3.9). EPMA confirmed that the ferrite (higher Cr and Mo) had preferentially dissolved as shown clearly in Fig. 3.10. The lighter areas in Fig. 3.10 represent the austenitic phase whilst the attacked ferrite is shown as the darker phase.

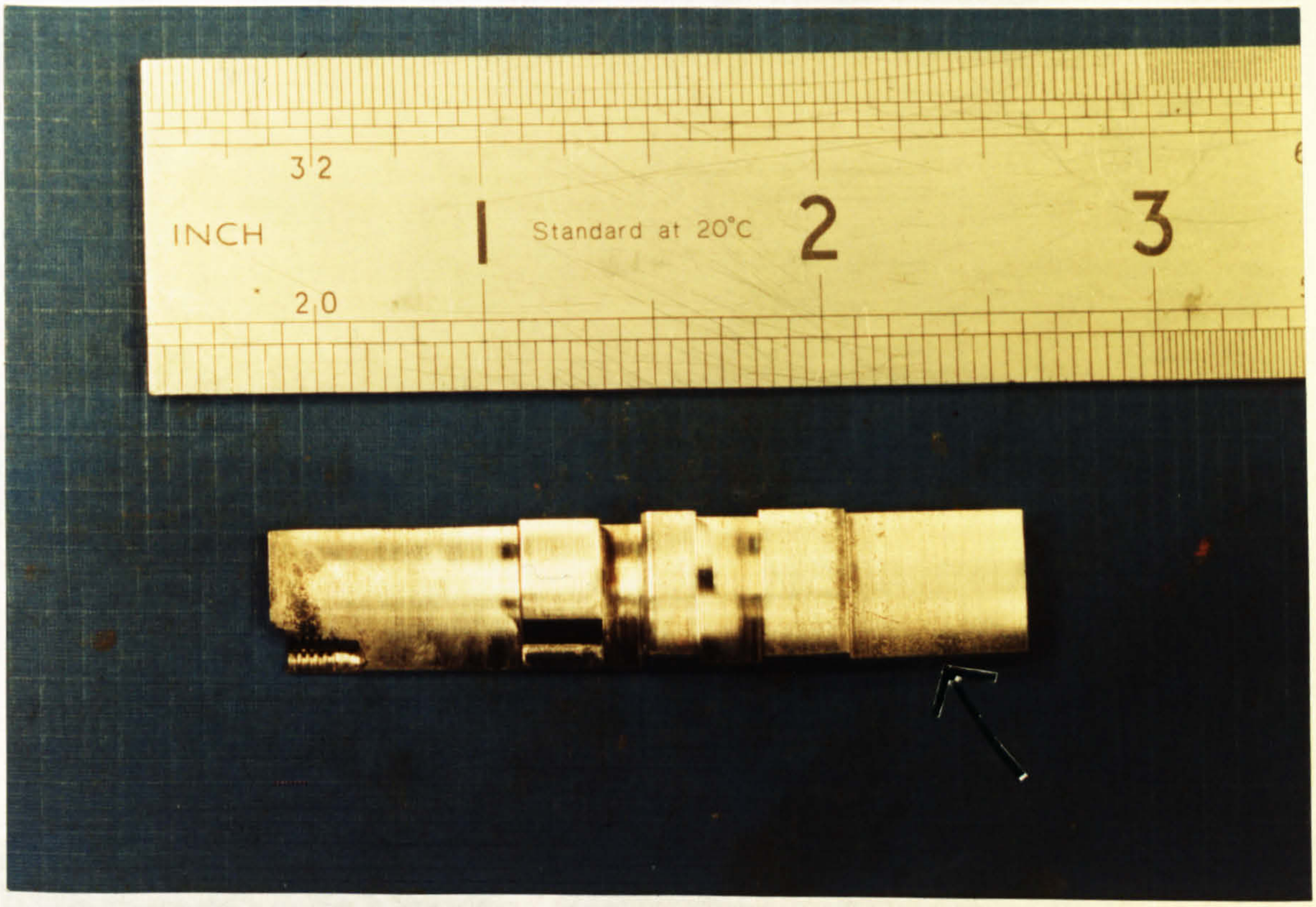


Fig. 3.6. Sleeving of 25Cr/5Mo superduplex stainless steel showing area of severe attack at the right hand side

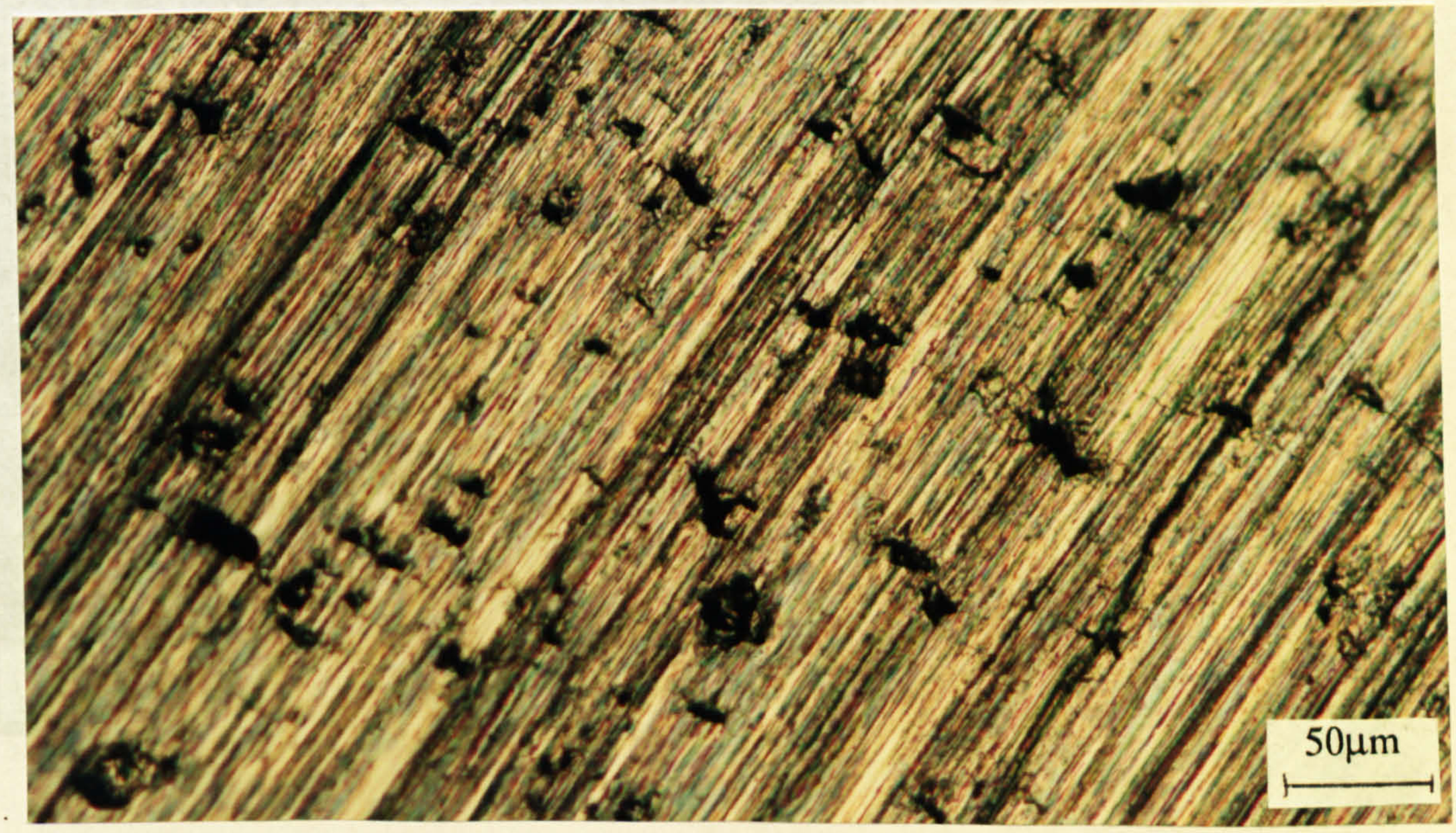


Fig. 3.7. Pitting initiated on the auxiliary sleeving

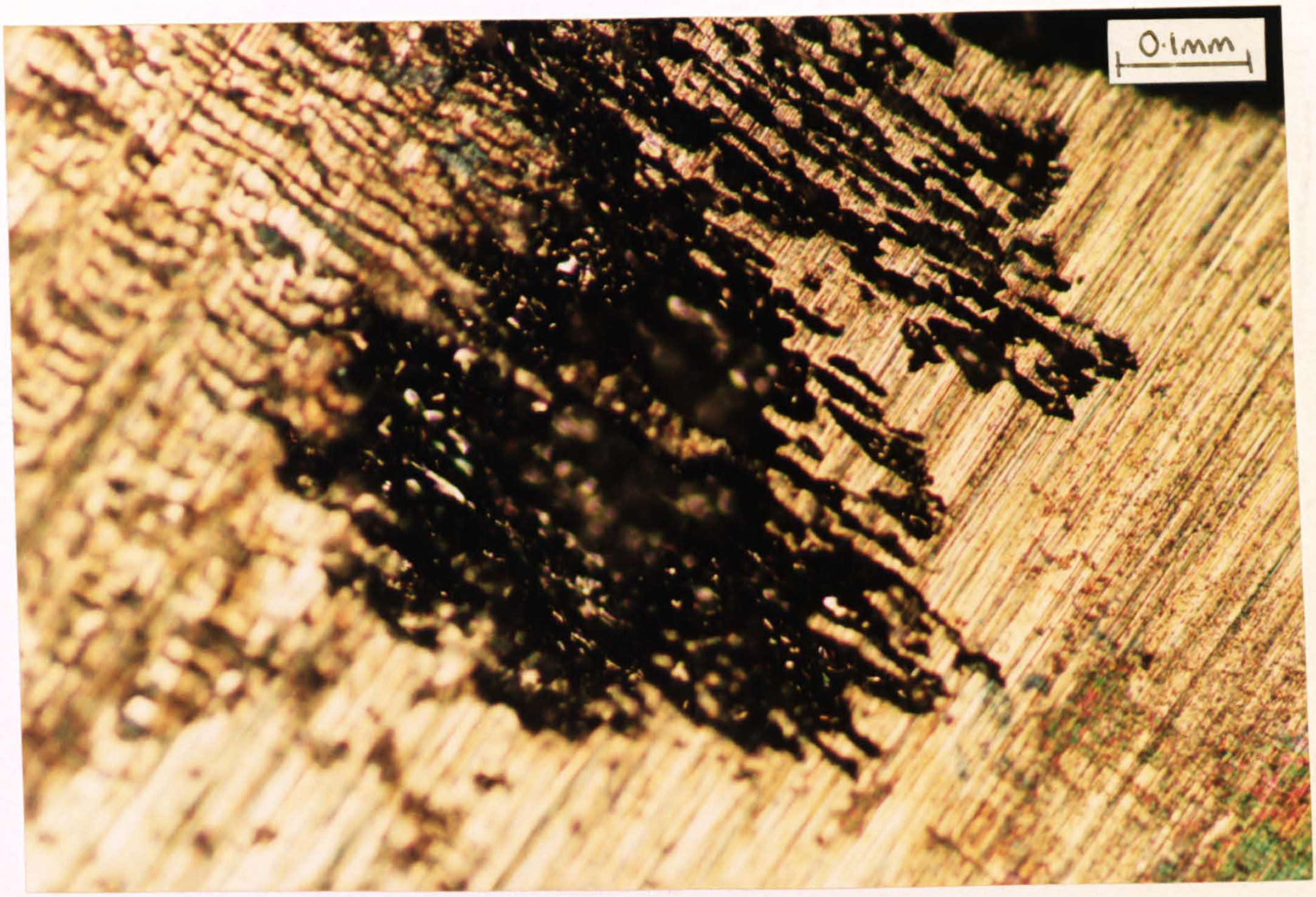


Fig. 3.8. Selective attack of one of the duplex phases on the sleeving component

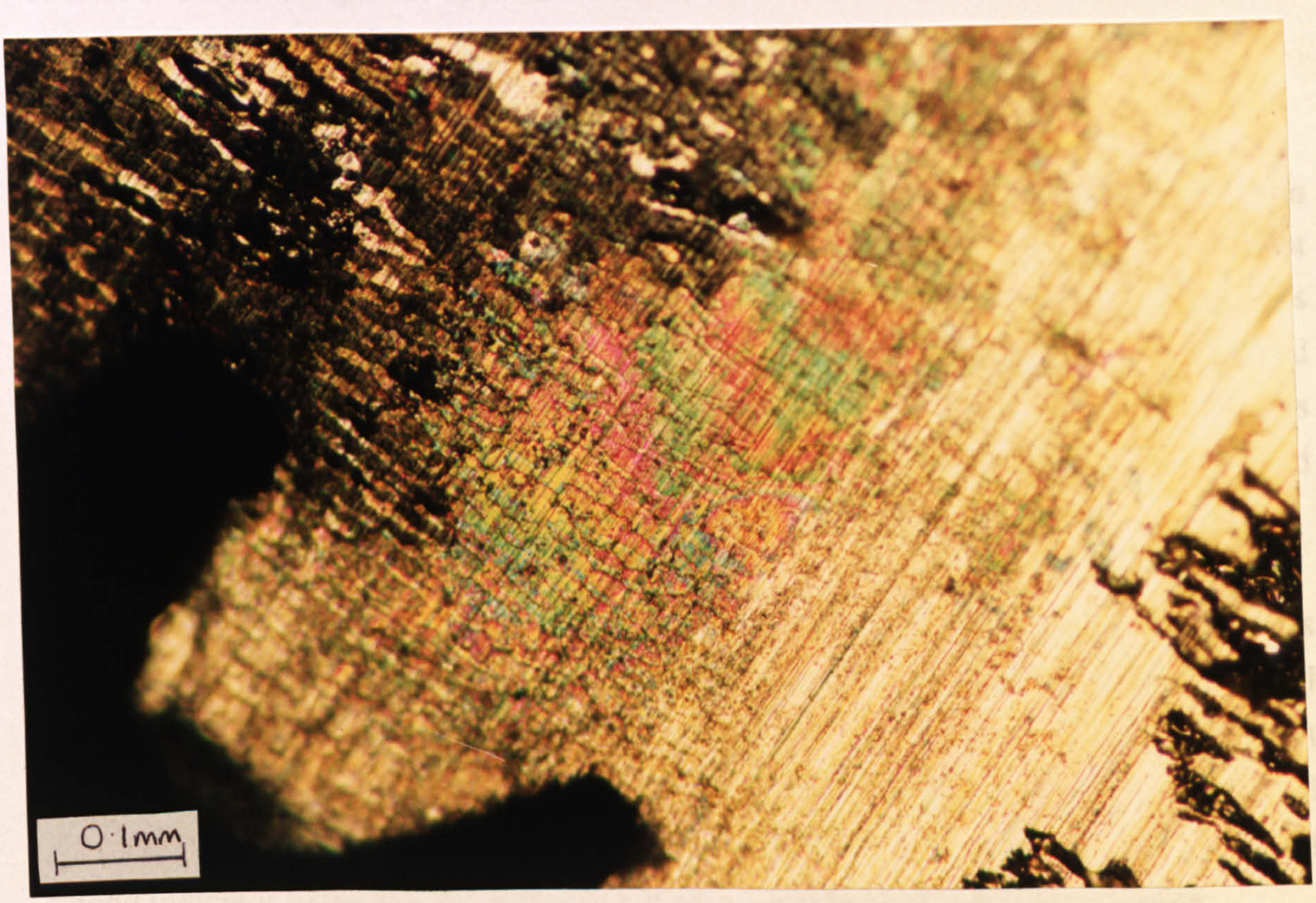


Fig. 3.9. Coloured surface of corroded area on the auxiliary sleeving showing the two phase structure

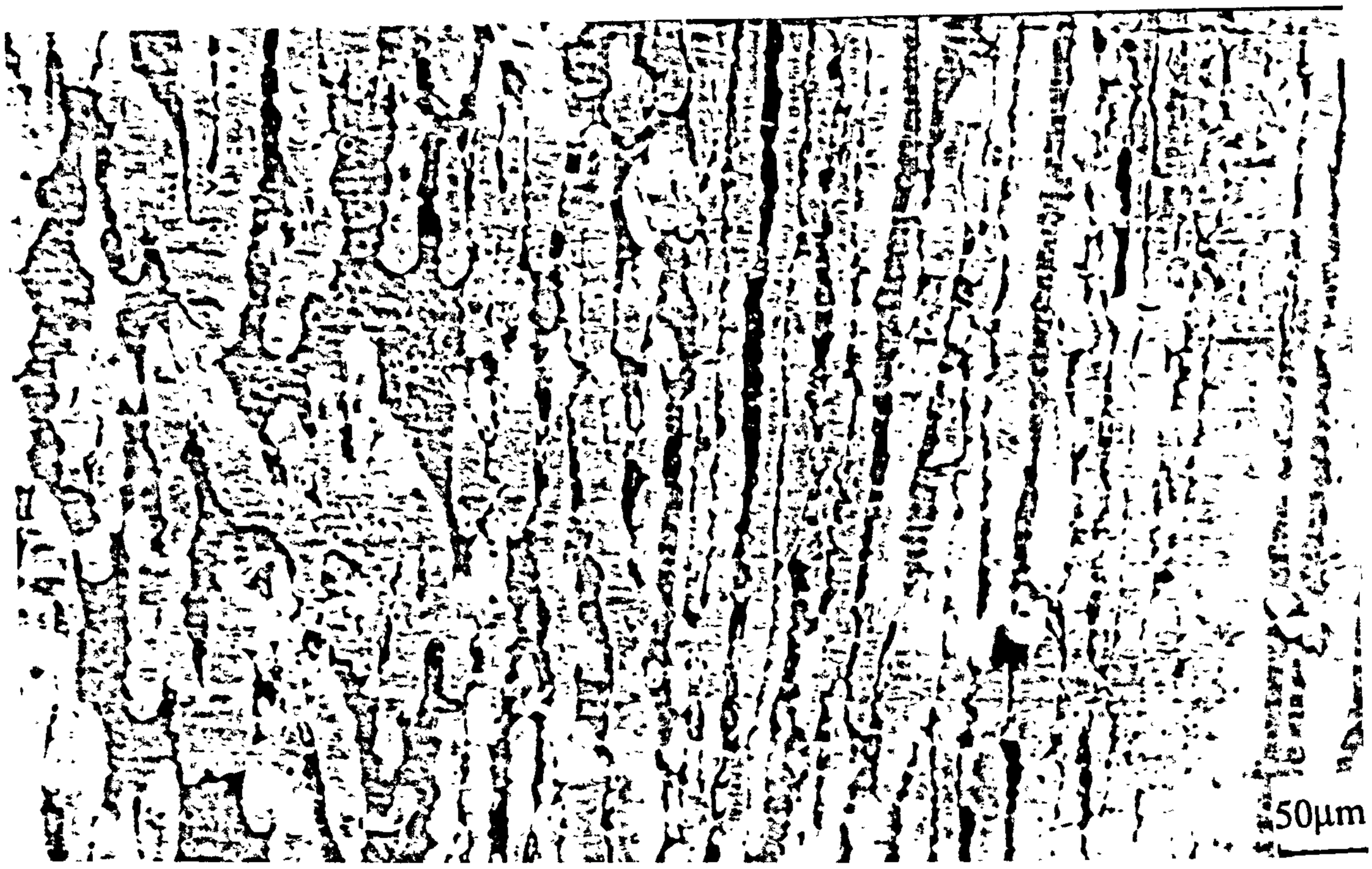


Fig. 3.10. Ferrite dissolution on the superduplex sleeving. Ferrite shown as the darker of the two phases. Ferritic phase analysis, 29%Cr, 4.8%Mo, 3.8%Ni, 1%Cu, 0.4%Si, 59.8%Fe. Austenitic phase, 22%Cr, 2.1%Mo, 7.35%Ni, 64.3%Fe, 1.5%Cu.

Laboratory Electrochemical Tests and Post-Test Microscopy

Work reported in chapter 2 demonstrated the superior resistance to passivity breakdown of the duplex and the superduplex stainless steels to the Stellite 6 alloy in seawater at ambient temperature. In addition, it was shown that on even the superduplex stainless steel, the effect of increased temperature alone was to increase the material susceptibility to localised corrosion and propagation. As such, the results of this chapter will demonstrate the relative effects of the seawater temperature, salinity and aeration on the corrosion characteristics of the three materials and the extent of attack.

The results in chapter 2 demonstrated that the effect of increased temperature alone was to significantly enhance the localised corrosion initiation and propagation for all materials. However, the key observation was that the extent was significantly different for each material and, as such, the ranking of the materials changed at elevated temperature. Hence, it was concluded that ambient temperature (18°C) behaviour is not a good indicator to predict the performance of a material at elevated temperature.

Effect of Increased Temperature Alone

As an extension of the work in chapter 2, this work has shown that at the increased temperature of 90°C, via electrochemical tests, that the resistance of the stainless steels is further reduced from the performance at 50°C manifested in a significant lowering of the parameter $E_b$ (Figs. 3.11a and b).

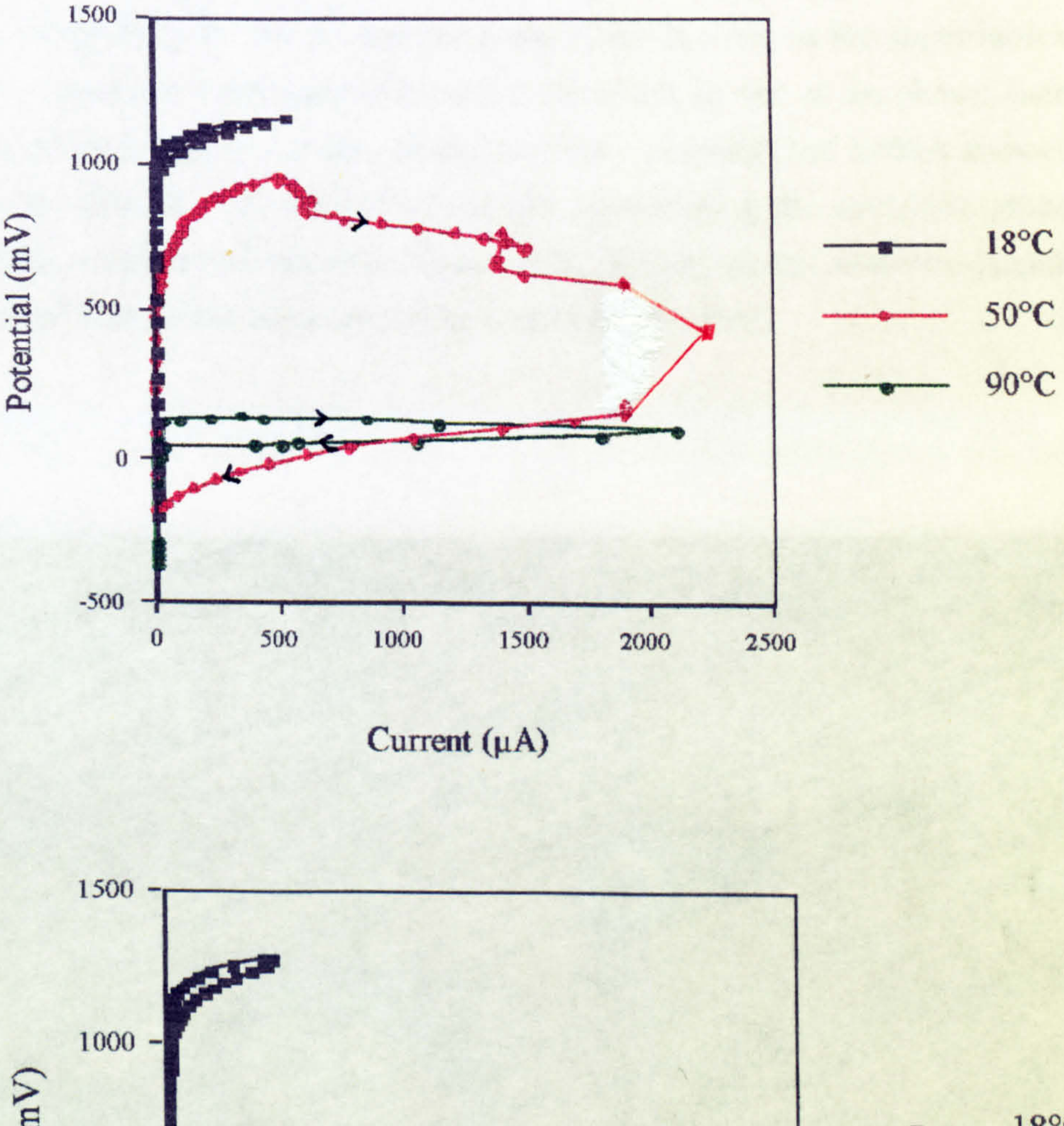


Fig. 3.11. Anodic polarisation of (a) the superduplex alloy and (b) 25Cr duplex at 18°C, 50°C and 90°C.

The electrochemical results were substantiated by the post-test examination which revealed extensive localised attack at 90°C on both materials and maximum pit depths of more than five times those measured at 50°C (136μm and 174μm for the superduplex and the 25Cr duplex respectively compared to 23μm and 26μm at 50°C). As observed at 50°C, and indeed on the actual failed sleeving, a coloured film was evident over the surface within which the surface was obviously etched (Fig. 3.12). The pitted sites, once corrosion products were removed, could be identified by a skeletal structure with a deep pitted region beneath. Figure 3.13 shows on the 25Cr duplex the thin layer of perforated material over the pit and the same effect is seen on the superduplex alloy in Fig. 3.14. Attempts were made to correlate the attack to one of the phases (and perhaps relate the attack to the attack seen on the auxiliary sleeving) but EPMA showed there to be attack on both phases, the lighter shadow representing the austenitic phase and the darker shadow the feritic phase in figure 3.15. Pitting on the austenite islands (lighter shadow) and also on the adjacent ferrite matrix can be seen.

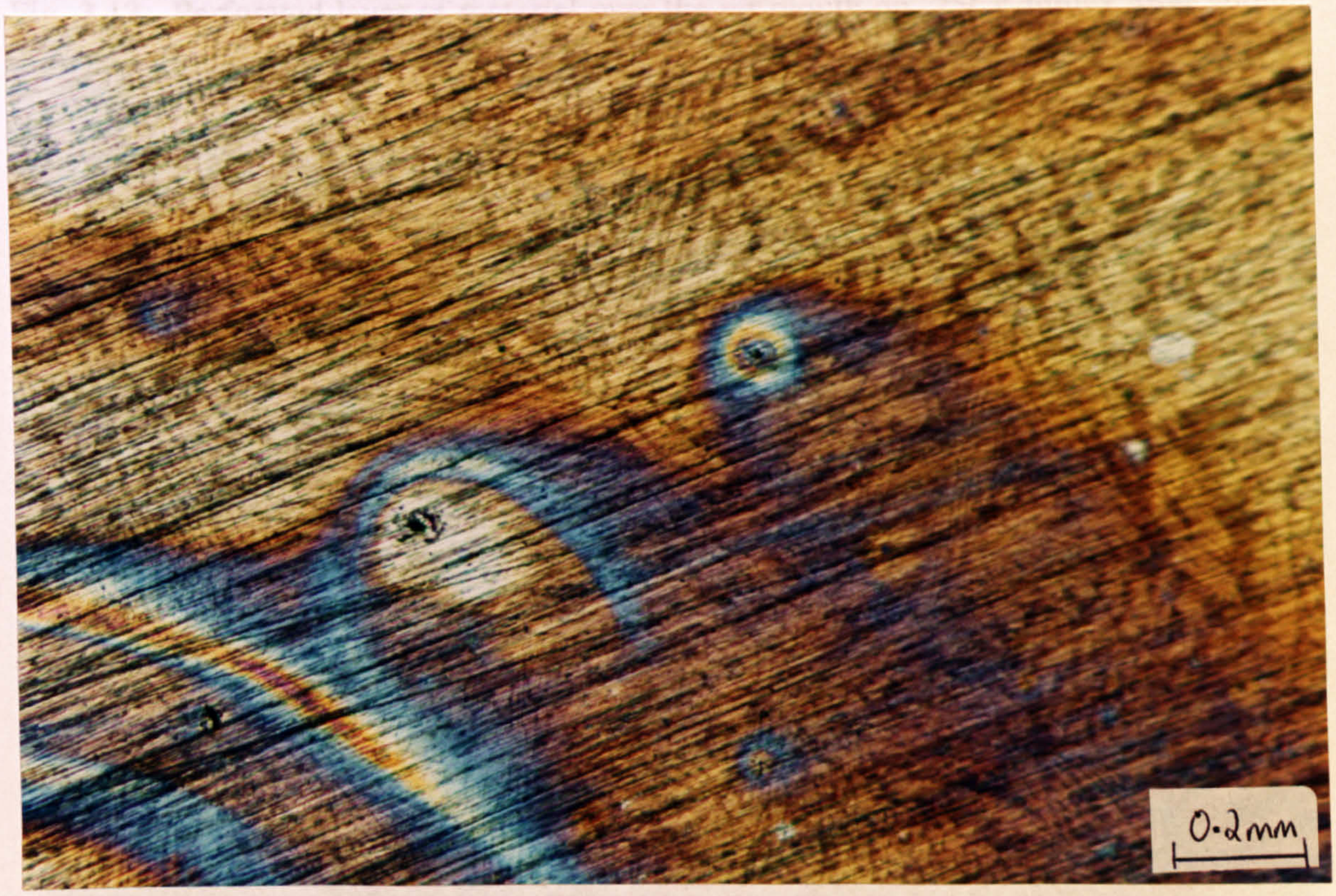


Fig. 3.12. Coloured surface on 25Cr duplex with pitted sites dispersed after anodic polarisation at 90°C. In addition, etching can be seen within the colour.

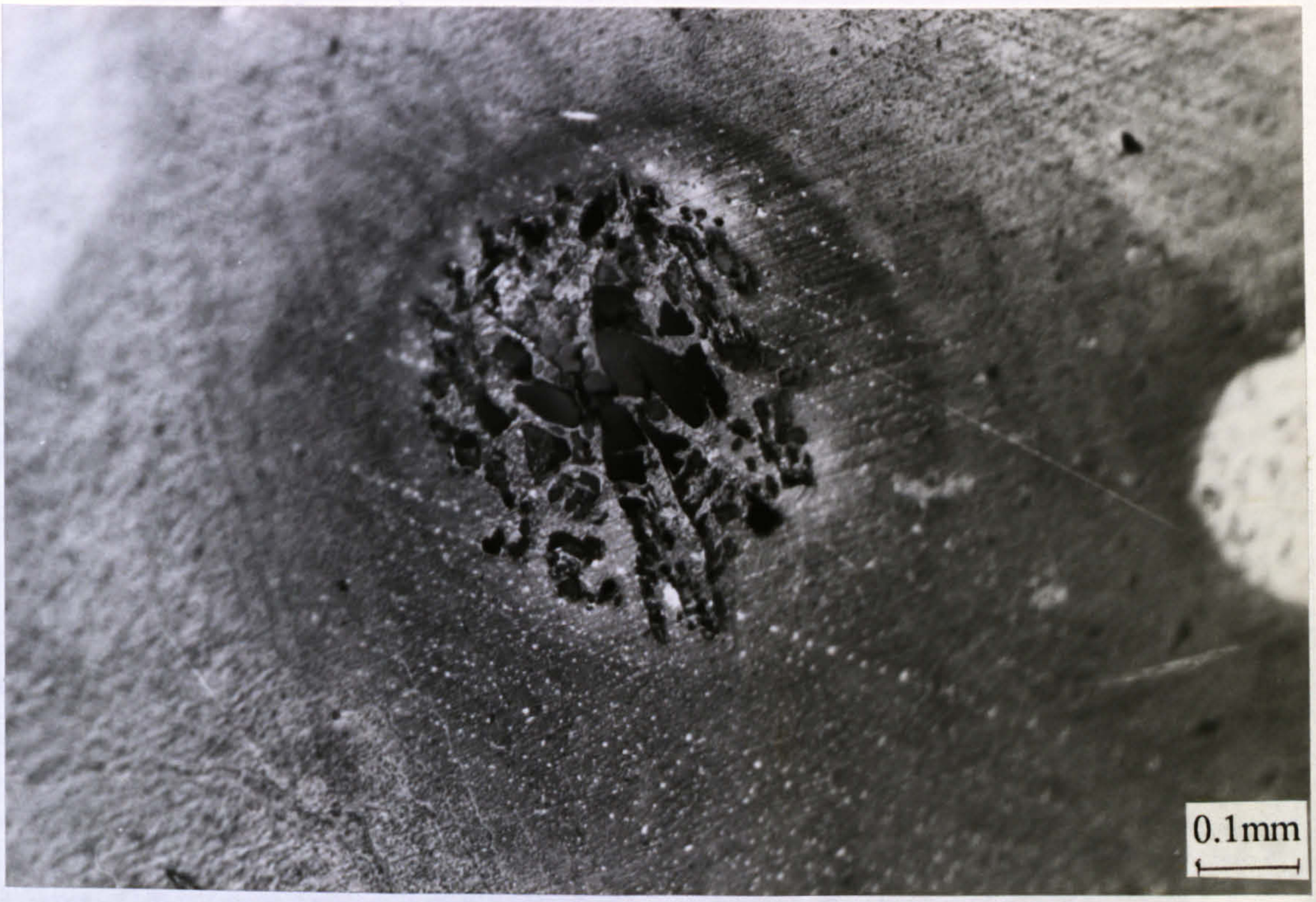


Fig. 3.13. Perforated layer of material over the pit mouth on 25Cr duplex after anodic polarisation at 90°C


Fig. 3.14. Pitting attack on UNS S32760 after anodic polarisation at 90°C

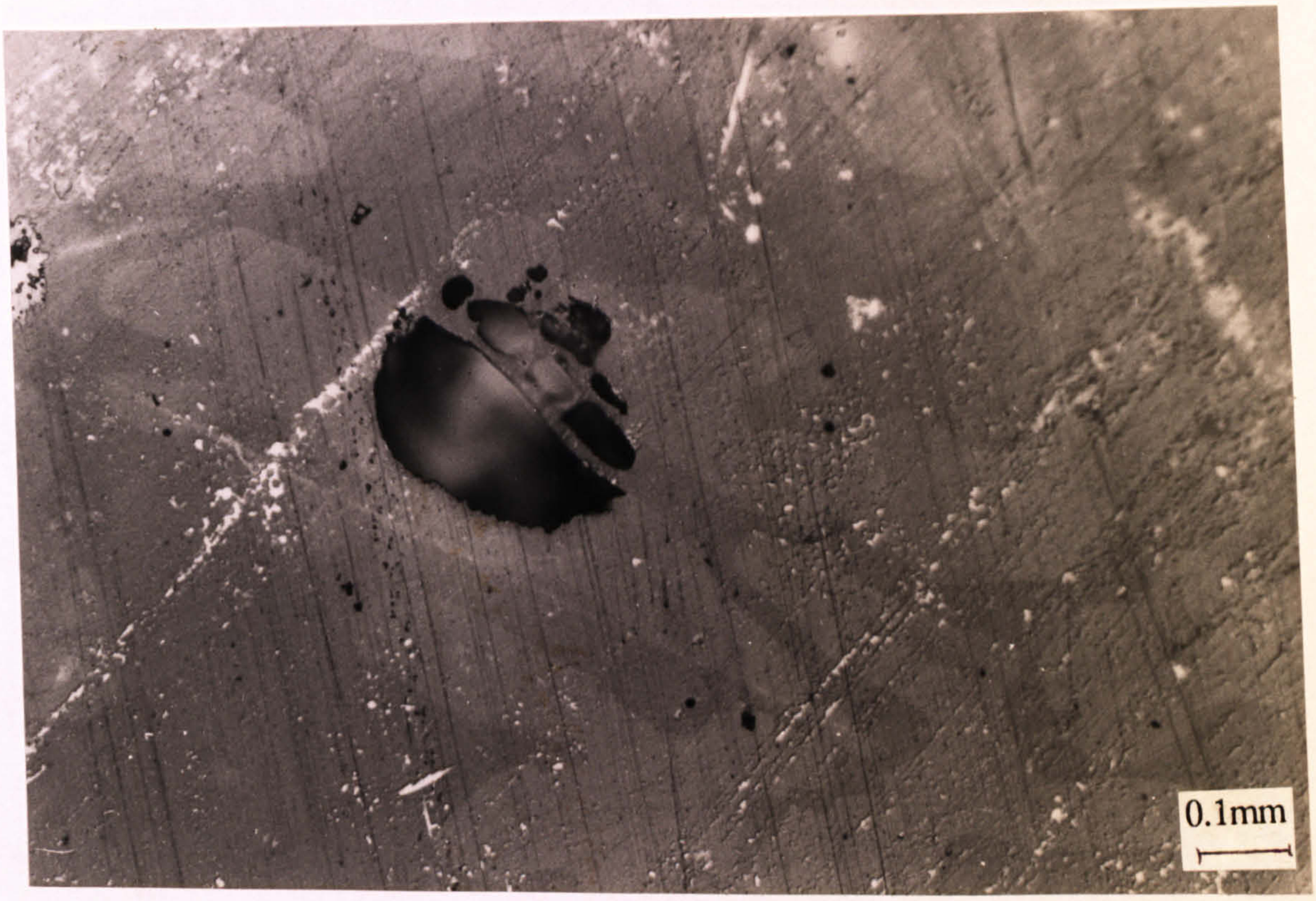


Fig. 3.15. Pitting attack on both phases of the duplex stainless steel after anodic polarisation at 90°C

In agreement with observations on the stainless steels, on Stellite 6, it can be seen that there is a significant lowering of $E_b$ on increasing the temperature from 18°C to 50°C (Fig. 3.16). However, on further increasing the temperature to 90°C, the effect was to actually cause a small ennoblement of $E_b$ which could possibly suggest less extensive attack at 90°C than at 50°C. However, it can be seen from the electrochemical polarisation scan that there are important features, other than $E_b$, which would contradict the implications from $E_b$. Most importantly, the current registered in the potential region immediately increased from $E_{corr}$ was an order of magnitude greater than observed at 50°C and although the currents were stable with increased potential for quite a significant potential range, they were not typical of what could be regarded as "passive" currents. In addition, at 90°C, there was an increase in $I_{max}$ after scan reversal.

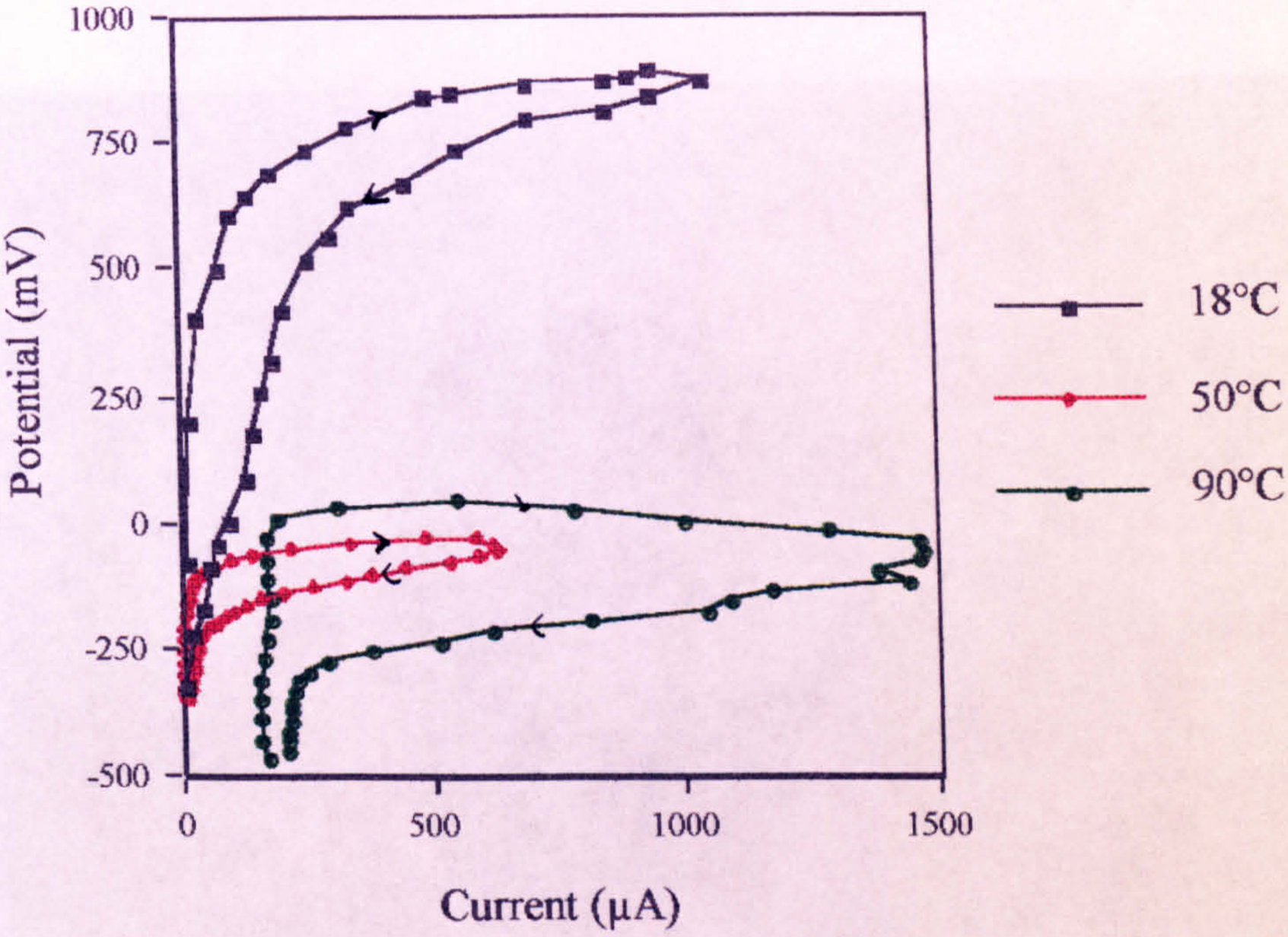


Fig. 3.16. Anodic polarisation on Stellite 6 as a function of temperature

Post-test examination revealed an interesting change of attack mechanisms as the temperature was increased to 90°C, compared to the mechanisms observed at 50°C. At 50°C Stellite 6 was shown to be prone to severe crevice attack and was also generally attacked in the form of an etching of the surface layer. At 90°C the general etching and crevice attack were still apparent but in addition, there was severe pitting, the form of which closely resembled the attack found on the Stellite 6 wear ring. Figures 3.17 and 3.18 show two pits in which, at the periphery of the pit, there is evidence of the same preferential attack of the lower Cr phase of the material. The attack can be compared to the attack in one of the pits found on the actual service components as shown previously in Fig. 3.2. The mechanism of attack was confirmed to be comparable to the service attack seen on the wear ring after SEM examination and in Fig. 3.19, which is a view of the structure of the material inside the pit, the dendritic phase, remaining after depletion of the matrix by preferential dissolution, can be seen.

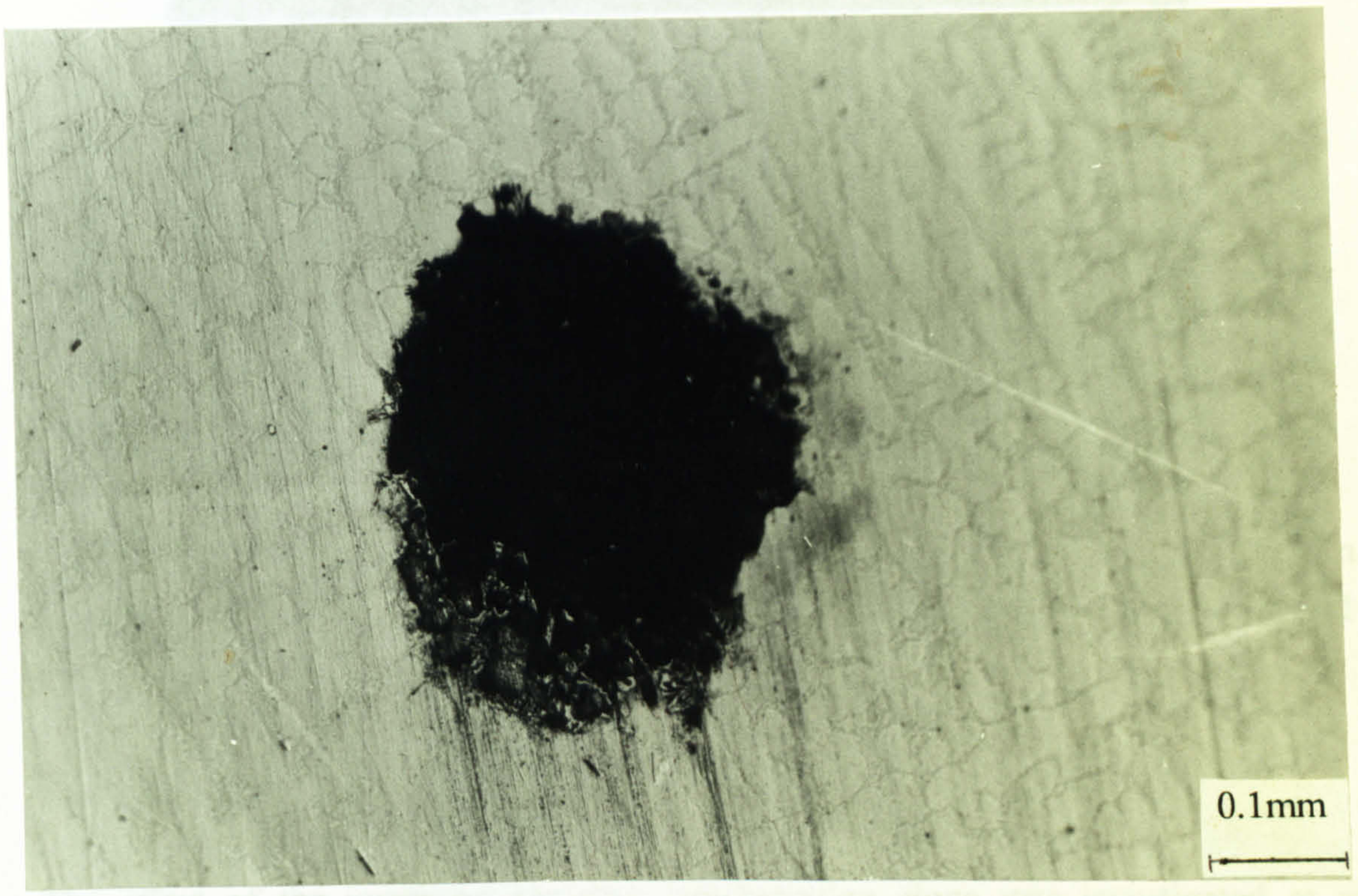


Fig. 3.17. Attack at a pitted site on Stellite 6 after anodic polarisation at 90°C

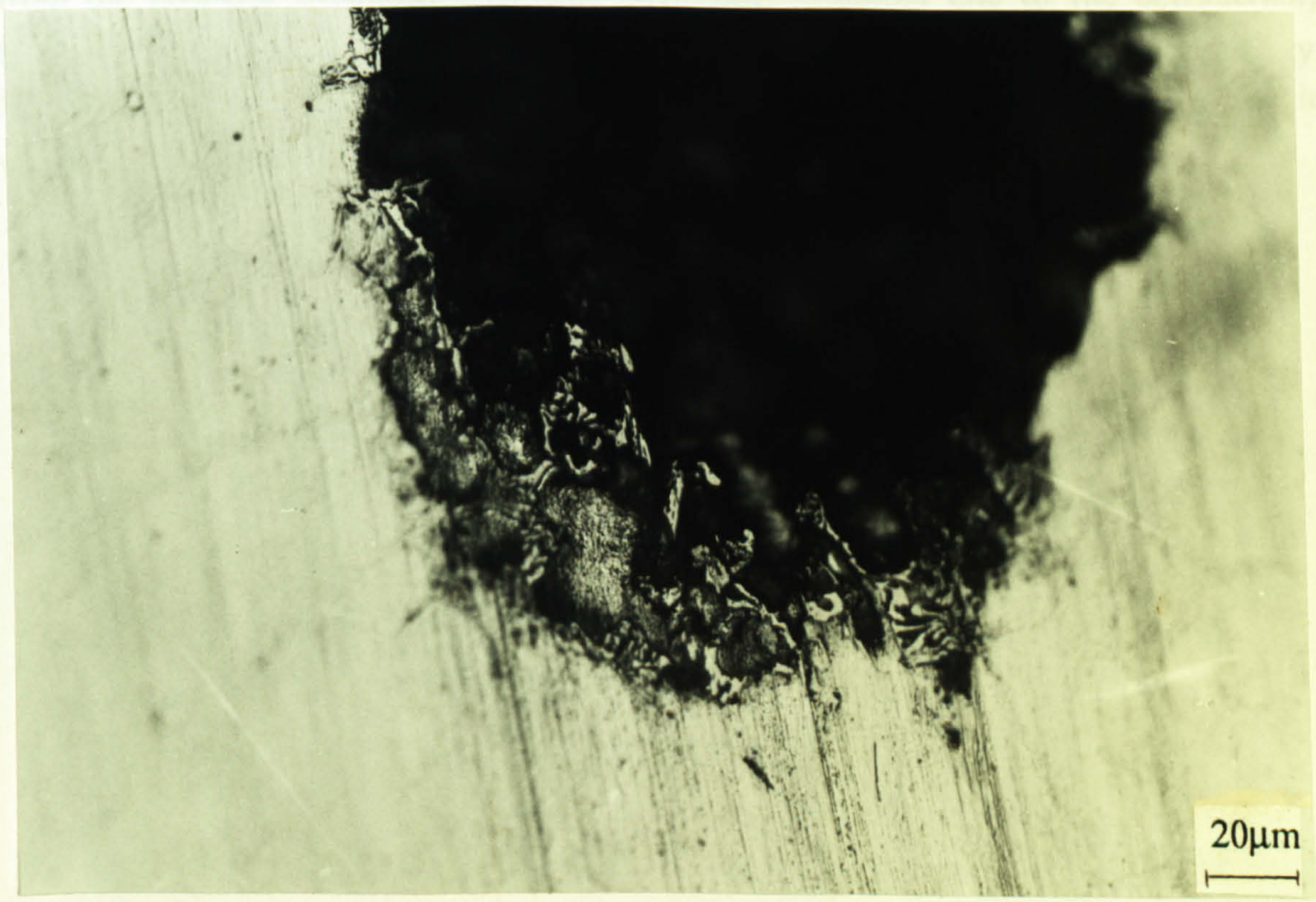


Fig. 3.18. Attack at a pitted site on Stellite 6 after anodic polarisation at 90°C

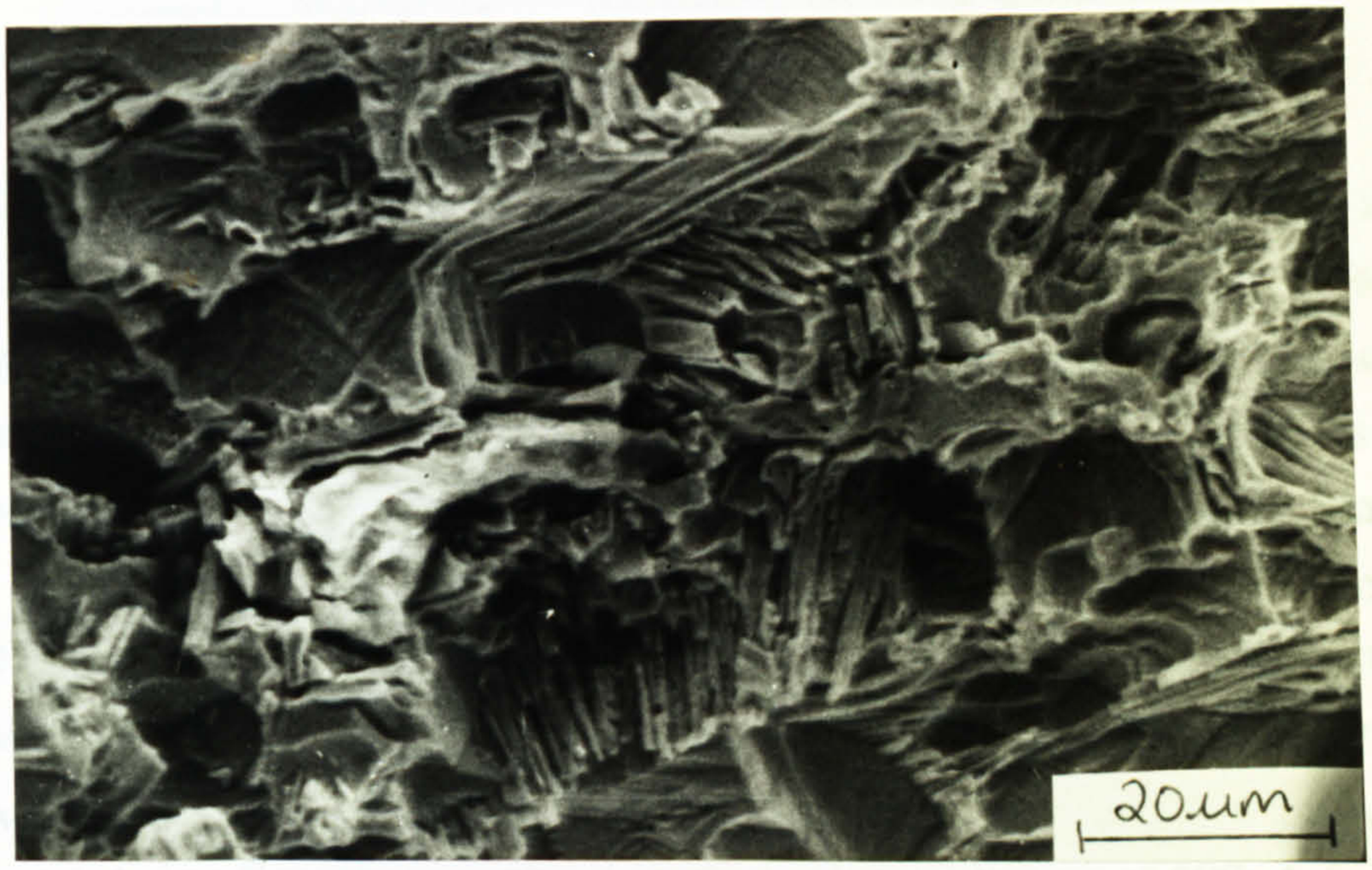


Fig. 3.19. Dendritic structure and preferential removal of the matrix on the specimen of Stellite 6, after anodic polarisation in seawater at 90°C, analogous to the attack found on the pitted wear ring.

Increased Seawater Concentration

The effect of the increased seawater concentration alone was investigated at each temperature and it was found that there was no conclusive evidence to suggest an increased corrosivity of the electrolyte from either the electrochemical monitoring or from the post-test examination as may have been expected due to the considerably higher $Cl^-$ ion concentration and the associated anticipated loss of passive film integrity. Figure 3.20 shows the virtually identical values of the polarisation parameter, $E_b$ in normal and concentrated seawater for the three materials.

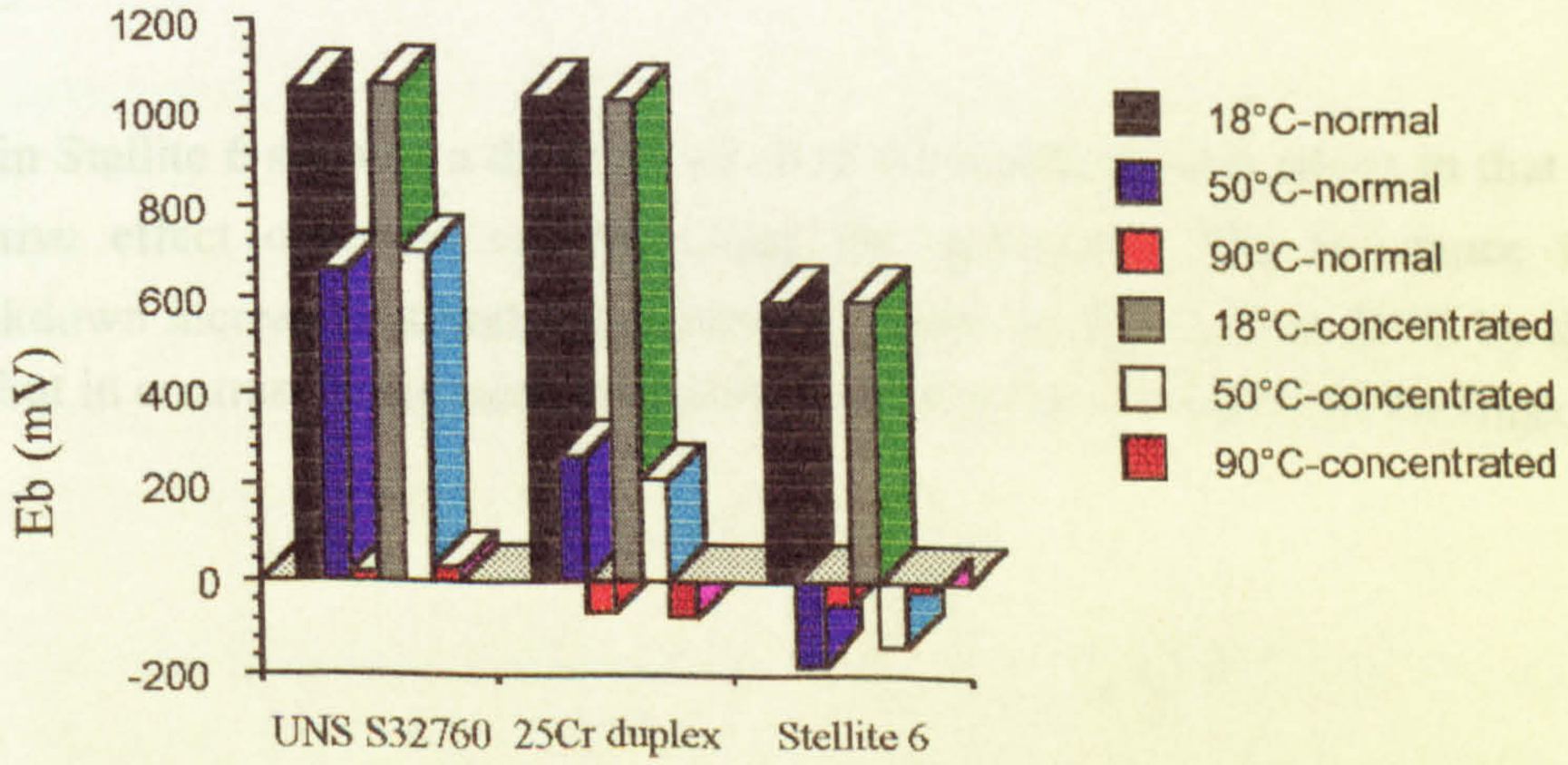


Fig. 3.20. $E_b$ parameter for the three materials to compare the efficiency of the concentrated seawater in facilitating passivity breakdown.

Effect of Deaeration

The effect of deaeration was investigated only in the case of seawater at four times normal concentration and hence relevant to the application to which the tests are aimed. Although deaeration will have implications for the progression of the cathodic reaction, only the anodic reaction has been investigated here and at all temperatures it was found that there was no effect on the passivity breakdown potential for the stainless steels in aerated and deaerated seawater. Where there was a significant difference was in the value of $I_{max}$ (assumed to be indicative of propagation rates and therefore of the material's ability to repassivate). In deaerated conditions, consistently lower $I_{max}$ values were recorded on the two materials 50°C (Fig. 3.21). At 18°C on both materials, $I_{max}$ was not significantly removed from the reversal current of 500μA for both aerated and dearated seawater.

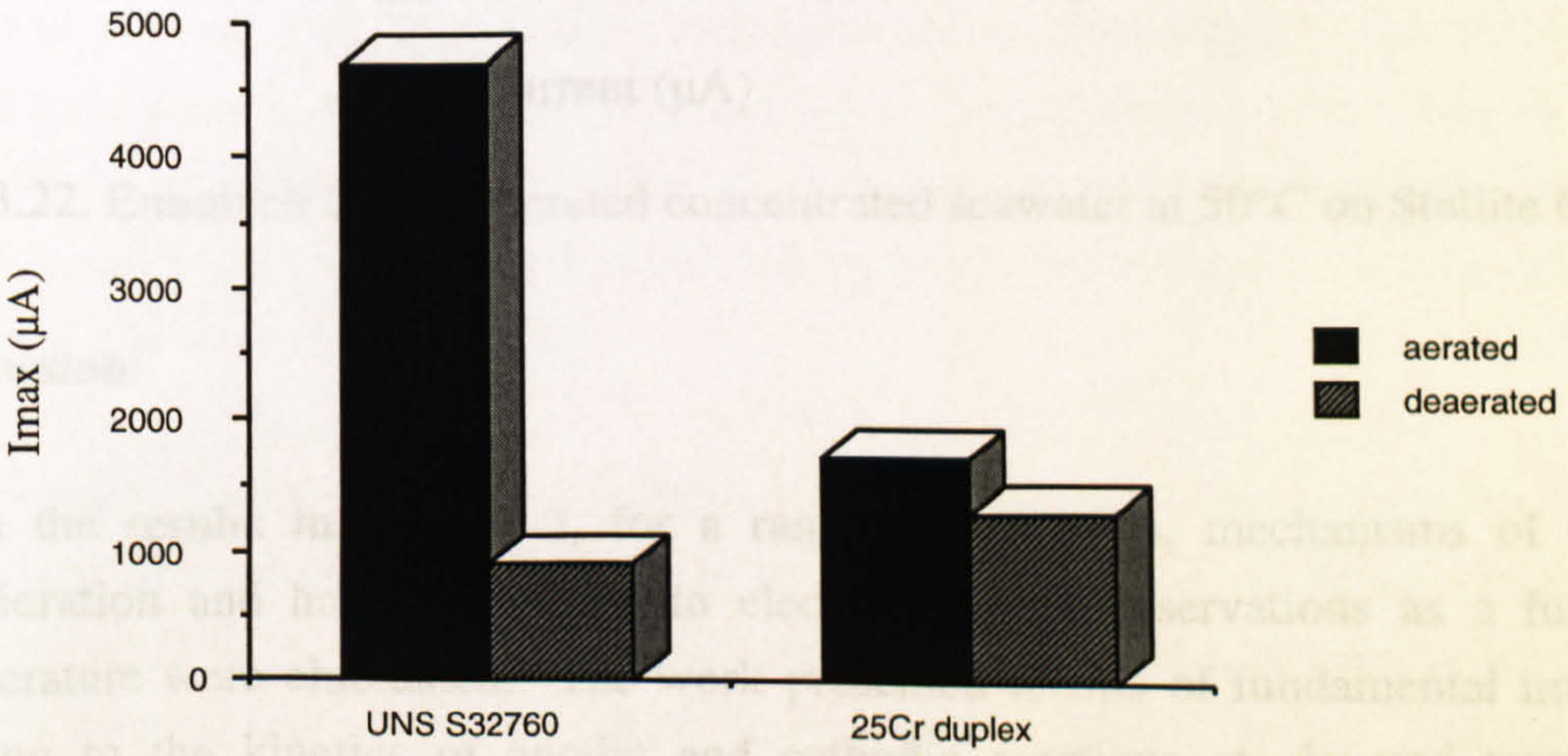


Fig. 3.21. Lower $I_{max}$ recorded in deaerated conditions than in aerated conditions at 50°C

Again Stellite 6 showed a different trend to the stainless steel alloys in that there was a positive effect observed on deaerating the seawater. The resistance to passivity breakdown increased at both temperatures, shown in Fig. 3.22 at 50°C by the ennobled $E_b$, but in contrast to the stainless steels, there was no difference in the $I_{max}$ value.

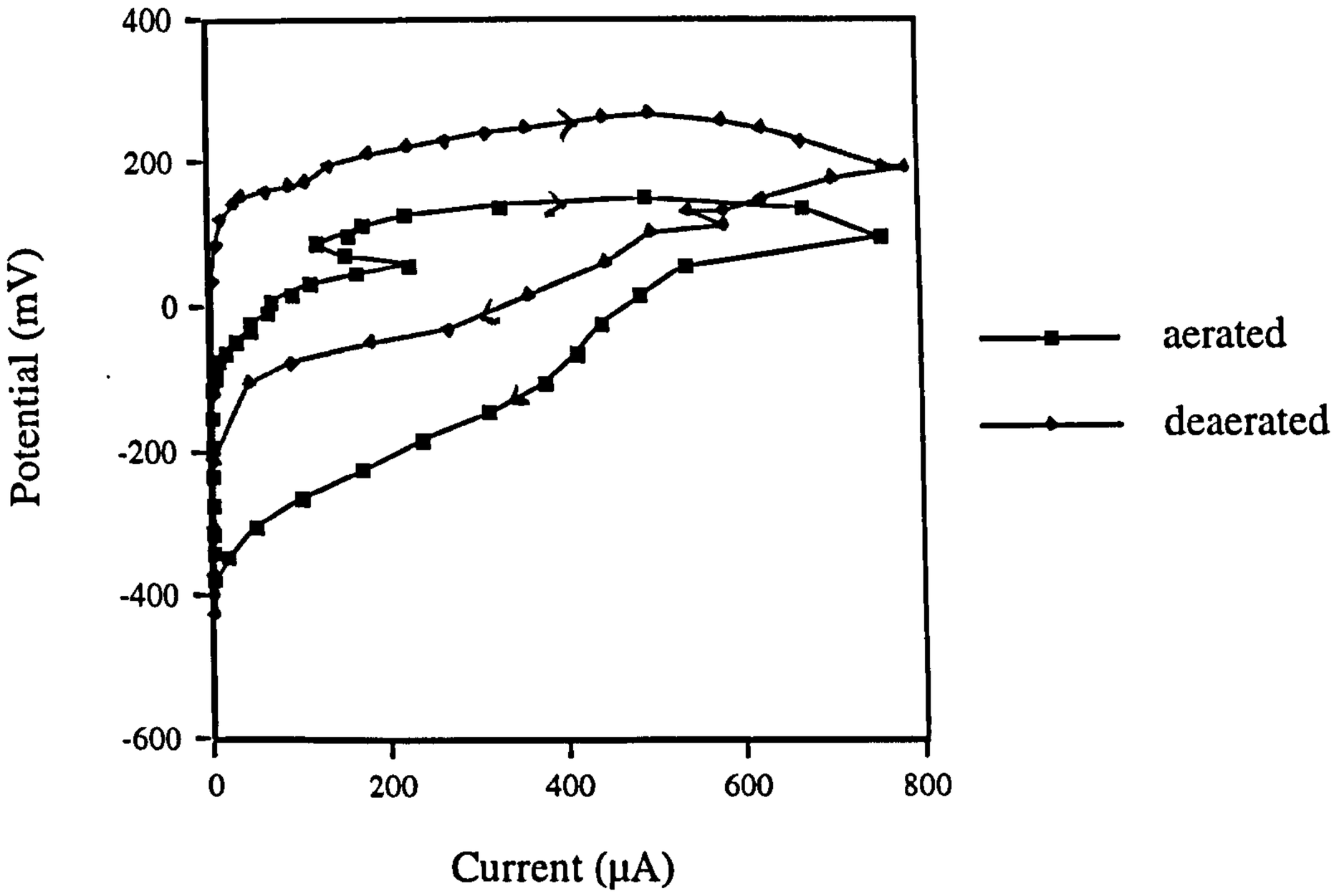


Fig. 3.22. Ennobled $E_b$ in deaerated concentrated seawater at 50°C on Stellite 6

## Discussion

From the results in chapter 2, for a range of materials, mechanisms of corrosion deterioration and how they relate to electrochemical observations as a function of temperature were elucidated. The work presented results of fundamental importance, relating to the kinetics of anodic and cathodic reactions at elevated temperatures. Practical implications emerged from these as it was demonstrated that the relative performance of alloys is heavily dependent on the seawater temperature.

The experimental programme in chapter 2 was developed primarily as a fundamental study. In contrast, the work reported in this chapter was borne from a specific engineering application and a series of tests were performed and the results analysed with this in mind. However, the study has outlined some important aspects of accelerated electrochemical tests with regard to their usefulness in accurately modelling material performance in a real application.

It had already been established in chapter 2 that the effect of increased temperature from 50°C to 90°C was to extensively enhance the extent of localised corrosion. It was therefore not surprising to observe a further decrease in the stainless steels' resistance to passivity breakdown as the temperature increased to 90°C. Of practical importance at

the high temperature is the very much reduced passive potential range on even the superduplex stainless steel. At 90°C, it can be envisaged that a temperature is being approached at which the materials, especially 25Cr duplex, will exhibit active behaviour, almost immediately the potential is increased from $E_{corr}$.

This study has shown that, on the stainless steels and Stellite 6, the resistance to passivity breakdown is dictated primarily by the temperature and in the temperature range 18°C-90°C, deaeration and increased seawater concentration are of only secondary importance in affecting the material behaviour. For each temperature, initially no differences in anodic polarisation characteristics were detected in concentrated seawater which is perhaps unexpected since the detrimental effect of $Cl^-$ on passive film stability has often been postulated [1,2]. It was observed that deaeration could enhance the $E_b$ on Stellite 6, and reduce the $I_{max}$ on stainless steel which is again unexpected since it is often assumed that the role of oxygen is to stabilise the passive film and provide protection against breakdown and assist repair. The mechanism by which the lack of oxygen can assist repassivation during anodic polarisation is not clear. On a freely corroding sample the lack of oxygen could reduce the cathodic reaction and hence retard corrosion propagation but during anodic polarisation, the cathodic reaction will not have a controlling effect.

Accelerated electrochemical test techniques, as a tool for monitoring corrosion behaviour of passive materials have been used in numerous applications and under a range of conditions. In several studies electrochemical tests are used in isolation as a tool for ranking and predicting corrosion behaviour. Hoever, in this, and indeed in all other chapters, it is emphasised that interpretation of electrochemical data can be misleading, if not supported by appropriate post-test examination. This point is strengthened in his chapter where, as exhibited on Stellite 6 at 90°C, the parameter $E_b$ would suggest that an increase in temperature from 50°C to 90°C facilitates an slightly enhanced resistance to the onset of corrosion. However, examination of the material disclosed that there was much more extensive attack at 90°C due to the fact that in the 'stable' current region from $E_{corr}$ to $E_b$, the material was not passive.

In addition, with regard to the use of accelerated test methods (i.e. DC-polarisation tests), this work has provided evidence that in modelling the conditions within which a material will operate in an engineering application, the techniques can accurately simulate the type and extent of the attack which will predominate. On Stellite 6 at 90°C, the accelerated tests were shown to produce selective attack of the matrix of the material leaving a dendritic structure, such as was observed on the Stellite 6 wear ring. The tests at the lower temperature did not cause this type of attack, consistent with the

behaviour of the component in the field. Hence the use of tests succeeded in accurately representing the changes in mechanisms of attack as the temperature increased above a certain value, which from a material selection viewpoint is important. Although on the superduplex, the tests did not show selective dissolution of the ferrite, there were three modes of attack which occurred in service which were accurately represented in accelerated tests : namely severe crevice attack, pitting attack and the occurrence of a coloured film at the attack site. This attack could be compared with the test results in chapter 2. It is therefore suggested that a possible reason for the attack not having been reproduced in the laboratory could be that the component material (25Cr/5Mo superduplex) was in some way not manufactured to specification. However, what the service failure does show is that high Cr and Mo levels do not invariably confer enhanced corrosion resistance.

Material selection for this particular application could therefore have been initially tested using the afore-mentioned techniques which could provide information on the susceptible components of any one material and perhaps design considerations could account for these. From the results in this study, it is clear that in 90°C seawater, Stellite 6 exhibits high currents immediately on commencing the anodic polarisation, indicative of the extent of corrosion occurring on the surface. Therefore, it is evident that for this application, the dissolution rates at local sites are high and can cause severe selective deterioration. In the search for alternative materials, it is recognised that the most important property of the wear ring is it s resistance to attack by mechanical wear. Hence the selection can not be made from purely corrosion resistance. However, in this application, it was the corrosion resistance which was not sufficient for the application. Not withstanding this, the current study and the work in chapter 2 has shown that, even for pure corrosion resistance, the limitations of especially 25Cr duplex and also the superduplex UNS S32760 with regard to crevice and pitting corrosion would render these materials of little use for application in these severe conditions. This has been substantiated in the field by the reported failure of a similar 25Cr/5Mo superduplex stainless steel in the tight crevice between the auxiliary sleeving and the wear ring.

Hence for effective resistance to corrosion , it may be appropriate to take a different approach to material selection and look beyond the metallic alloys. Possible alternatives would be to use ceramic components which would have the required mechanical properties and in preliminary tests have been shown to have good corrosion resistance [3]. However, it must be emphasised that preliminary testing in the severe conditions would be required before an effective material could be defined and selection could not be made relying on test data collected at ambient temperature.

## Conclusions

This study has successfully shown that, as a method of determining the extent and the mechanisms of attack in an engineering application, accelerated test techniques supported by comprehensive examination can provide an effective tool for material selection.

The determining factor in the application under study has been identified as the temperature but some unexpected results were obtained relating to the role of oxygen in corrosion, as determined during anodic polarisation tests. In the short term tests the aggressive nature of the $Cl^-$ ion was not accentuated in a concentrated seawater environment on any of the materials.

In so far as identifying an alternative material for the application, the current study went so far as illustrating that the three materials in the study would be inappropriate due to limitations in crevice corrosion and preferential corrosion of one phase of the Stellite 6 structure.

**References**

1. K. E. Heusler, L. Fischer, Kinetics of pit initiation at passive iron,*Werkstoffe und Korrosion,* Vol. 27, 1976, p551

2. H. P. Leckie, H. H. Uhlig, Environmental factors affecting the critical potential for pitting in 188 stainless steel, *J. Electrochem. Soc.*, Vol. 113, 1966, p1262

3. S. G. Cook, J. A. Little, J. E. King, Corrosion of silicon carbide ceramics using conventional and electrochemical methods, *Brit. Corr. J.*, Vol. 29, No. 3, 1994, p183

# Chapter 4

# High Velocity Impingement of a Liquid Flow - the Effect on the Corrosion Characteristics of High-Grade Alloys

## Introduction

The previous chapters focused on the corrosion characteristics of high-grade alloys and the austenitic stainless steel, UNS S31603, in static seawater and how the mechanisms change on increasing seawater temperature and salinities. Materials for seawater handling systems are required to withstand a wide range of flow velocities in pipes, valves and pumps in addition to the static conditions during for example, shutdown periods. Often high velocities are encountered in rotating components of turbomachinery and in piping when pipe diameter has been reduced to save weight and material costs. Poor system design can lead to aggressive impinging flows at areas where the flow system is not streamlined.

This chapter describes the results of a series of electrochemical tests, supported by microscopical and microanalytical techniques, conducted under the influence of a high velocity single phase seawater jet. The flow velocity of 100m/s was directed normally onto the specimen and electrochemical monitoring was conducted in-situ. Important findings regarding the modes and propagation rates of corrosion attack under the influence of a high velocity flow are discussed. Continual reference to the electrochemical behaviour and microscopical examination of the materials in static seawater is made in order to ascertain what effects the impinging flow induces in fundamental terms.

**Literature Review**

The need to minimise costs in handling fluids demands higher flow rates with the inherent risk of flow-dependent corrosion of engineering equipment [1]. Impingement attack occurs on pumps [2] as impeller speeds are increased, on pipes where high intensity turbulence exists in unstreamlined geometry changes or where the flow direction is suddenly changed and on valve seats where high velocities are induced during throttling [3]. The impingement on the pipe bend shown in Fig. 4.1 was severe enough to cause perforation over a period of twelve years.

Fig. 4.1. Perforation of a pipe bend due to liquid impingement

The pipe handled condensate from a heat exchanger system at a pressure of 275kPa and temperature of approximately 80°C. The loss of thickness on the outer material at the pipe bend can be clearly seen in Fig. 4.2.

Fig. 4.2. Loss of thickness at outer pipe curvature

Within the last 25 years, studies of the chemo-mechanical effects during flow induced corrosion have increased the knowledge of the basic processes, parameters and mechanisms. The phenomenon of flow induced corrosion must be approached from consideration of fluid mechanics in conjunction with the science of electrochemistry, material degradation, transport processes and inorganic chemistry. Levich in 1962 [4] published a comprehensive book on the subject of physicochemical hydrodynamics and this signalled an important advance in the understanding of flow processes with relation to electrochemical behaviour.

Direct impingement of a single phase flow on a surface involves complex interactions of mechanical, chemical and electrochemical effects. Although there are a number of active mechanisms during the conjoint action of single phase flow and corrosion, it is

generally accepted that mass transfer plays a crucial effect in controlling the extent of material deterioration due to corrosion [5-8]. Acceleration of mass transfer of a reactant to the surface or removal of a corrosion product from the surface can induce accentuation of corrosion [9]. Weber in his review paper in 1992 [10] summarised the effects of flow velocity on mass transfer. At low velocities near to zero, natural thermal convection is responsible for mass transfer. At moderate flow velocities, mass transfer increases due to induced convection but mechanical effects are absent. Enhanced mass transfer can be detrimental whereby damage rates are enhanced when electrochemical anodic or cathodic reactions are stimulated. However, in contrast, increased mass transfer can enhance passivation [1]by increased transport of the passivating species or in the use of inhibitors, increase the supply of inhibiting agent and thus be beneficial in retarding corrosion propagation.

Work published in the 1950's and 1960's tended to assume that for all materials, the effect of flow velocity on damage rates was the same. At low velocity, the damage rate was low and once a threshold velocity was achieved, the damage rate increased significantly. However, it has since been recognised that erosion-corrosion [11] is controlled by a number of basic mechanico-chemical processes the most important being mass transfer, momentum transfer and the generation of shear stresses. Hence the situation is much more complex and it can be very difficult to predict the influence of flow velocity. The following dimensionless expression was developed to define the interrelation between the processes,

$$\mathbf{Sh = a\,Sc^{b}\,Re^{c}}$$

where **Sh** (the Sherwood Number) describes mass transfer, **Sc** ( the Schmidt Number) describes momentum and mass transfer, the Reynolds Number, **Re**, accounts for inertial and frictional forces and a, b and c are constants This relationship is often simplified to

$$\mathbf{w = const.u^{x}}$$

where **u** is the velocity and **w** is the corrosion rate. The parameter **x** is dependent on flow parameters, the material and the fluid density. The exponential relationship is only valid for situations where mass transfer is the rate-determining step and since most practical corrosion systems exhibit mixed control, is of only theoretical importance [1]. Material loss in practical situations often occurs under conditions of disturbed flow at geometrical irregularities and, as such, knowledge of the local flow structure and related turbulence intensity is required to model such erosion-corrosion [12].

The 1960's saw a widespread increase in research activity into the effects of flow parameters on corrosion. Prior to that time Laque in 1950 [13] published data on the behaviour of Cu-Ni alloys in seawater based on data from one flow geometry which could not readily be transferred to other geometries. Laboratory evaluation of the effects of fluid velocity must involve an experimental set up which clearly defines the hydrodynamic parameters. Studies on flow-induced corrosion over the years have employed a wide range of experimental techniques.

There are two approaches from which the effects of liquid flow on corrosion can be studied namely 'rotating' techniques or techniques which involve simulating the actual flow configuration. For laboratory testing, researchers are increasingly utilising compact rotating disc electrode apparatus which was developed in the late 1950's. The rotating disc electrode operates under clearly defined hydrodynamic parameters and can be used for fundamental studies of mass transfer characteristics and the kinetics of anodic and cathodic processes. Variants on the rotating disc electrode have emerged such as the rotating cylinder electrode [9], coaxial cylinders and enclosed rotating discs opposite fixed walls [14]. The question as to whether the rotating disc velocity can be equated to an equivalent pipe flow velocity in corrosion terms was addressed in [5] where a mathematical correlation was developed. However it was heavily criticised since it used laminar flow in the rotating disc electrode to model turbulent flow (i.e. in pipes). Corrosion processes are affected by more parameters than just the mass transfer rate and as such an equivalent pipe velocity from a corrosion viewpoint can not be readily assumed [9]. Rotating cylinder electrodes have overcome the issue of laminar and turbulent flow [9] and are used to relate the annular velocities to equivalent wall jet and pipe flow velocities.

An alternative approach where modelling involved equating the wall shear stresses and turbulence in two different geometries was suggested by Silverman [9]. The corrosion mechanism is then assumed to be the same although it is recognised that rates will be different [7].

Flow loops designed to study pipe flow or to create an impinging liquid jet have been commonly used in recent years. The cost of this approach is normally much increased compared to the employment of rotating disc techniques. In addition, similarity between model and real application must be maintained. G. A. Schmitt et al. [15] investigated the validity of results obtained in flow loops experiments and those obtained in rotating probe situations and compared each to the actual component service behaviour in relation to inhibitor requirements for oilfield wells. They concluded that the flow loop seemed to better simulate the flow regime but is expensive and time

consuming. The 'rotating cage' in which the test coupons rotate in contrast was relatively inexpensive and the temperature and pressure could be more easily varied. However, analysis of the damage induced during the rotating cage components and the flow loop resulted in the authors concluding that the rotating cage exaggerated the flow conditions and that the flow loop results gave a more realistic qualification of the field application.

Turbulent impinging jets of fluid are encountered in marine environments in pipe channels, at geometric irregularities etc. and have been simulated in the study of wear on concrete [16] using full scale modelling. Although the apparatus is cumbersome, it enables the researcher to model the full scale velocities and pressure gradients associated with liquid impact. Liquid erosion is important in two respects : the occurrence of impingement in engineering systems in situations as mentioned above and also in the event of cavitation. Bubble collapse in a cavitating system results in pressure transients at a surface and also micro-jets of liquid which impinge at velocities between 100m/s-500m/s [17,19]. Investigations by C. M. Preece [18] and other workers have shown that although data for liquid erosion and cavitation tests can not readily be interchanged quantitatively, in some instances, the processes involved in deterioration are similar and the relative resistances to both types of damage is the same [19]. Using the test apparatus described by Preece, where a rotating component enabled a sample to be subjected to a defined number of liquid impacts per second, it was shown that liquid erosion tends to produce more damage per impact suggesting that in cavitation, only a small proportion of bubbles collapse to produce damage.

Liquid erosion under an impinging turbulent jet involves the progressive removal of material by repeated impulse loading at microscopically small areas. Fluid dynamics is of major importance as is also the corrosivity of the fluid in many fluid-material combinations. Mechanical effects of a high velocity impinging flow are twofold. The jet generates a high pressure region at the point of impact and in addition, shearing effects are encountered due to the lateral flow radially outwards from the point of impact [18,19]. The radially flowing re-entrant jets [18] collide with the surface along which it travels and Hammitt [20] suggested that waves of jets due to Helmholtz instabilities between the jet and substrate account for much of the damage in liquid erosion. Impact pressures approximated by early workers [21,22] to be

$$P_o = \rho_1 c_1 v \left( \frac{\rho_2 c_2}{\rho_1 c_1 + \rho_2 c_2} \right)$$

for a liquid drop impacting on a stationary elastic surface, where ρ and **c** are the density and sound wave velocity, **v** is the impact velocity and subscripts **1** and **2** pertain to the jet and the solid target respectively. It has been established that the peak pressure does not occur at the point of impact but instead in an annular region outward from it [23,24]. Estimations of the value of the peak pressure have been made [25] as $3P_0$ but experimentally determined values of $1.8\text{-}2P_0$ have been recorded [19,26].

The impinging jet flow geometry has been reviewed by D.C Silverman [9]. In cases where the corrosion is mass transfer limited, it has been proposed that the corrosion rate is a function of the wall shear stress. Giralt and Trass [27,28] suggested a formulation to work out the shear stress in the wall jet region away from the stagnation point. Figure 4.3 is a schematic representation of the impingement region

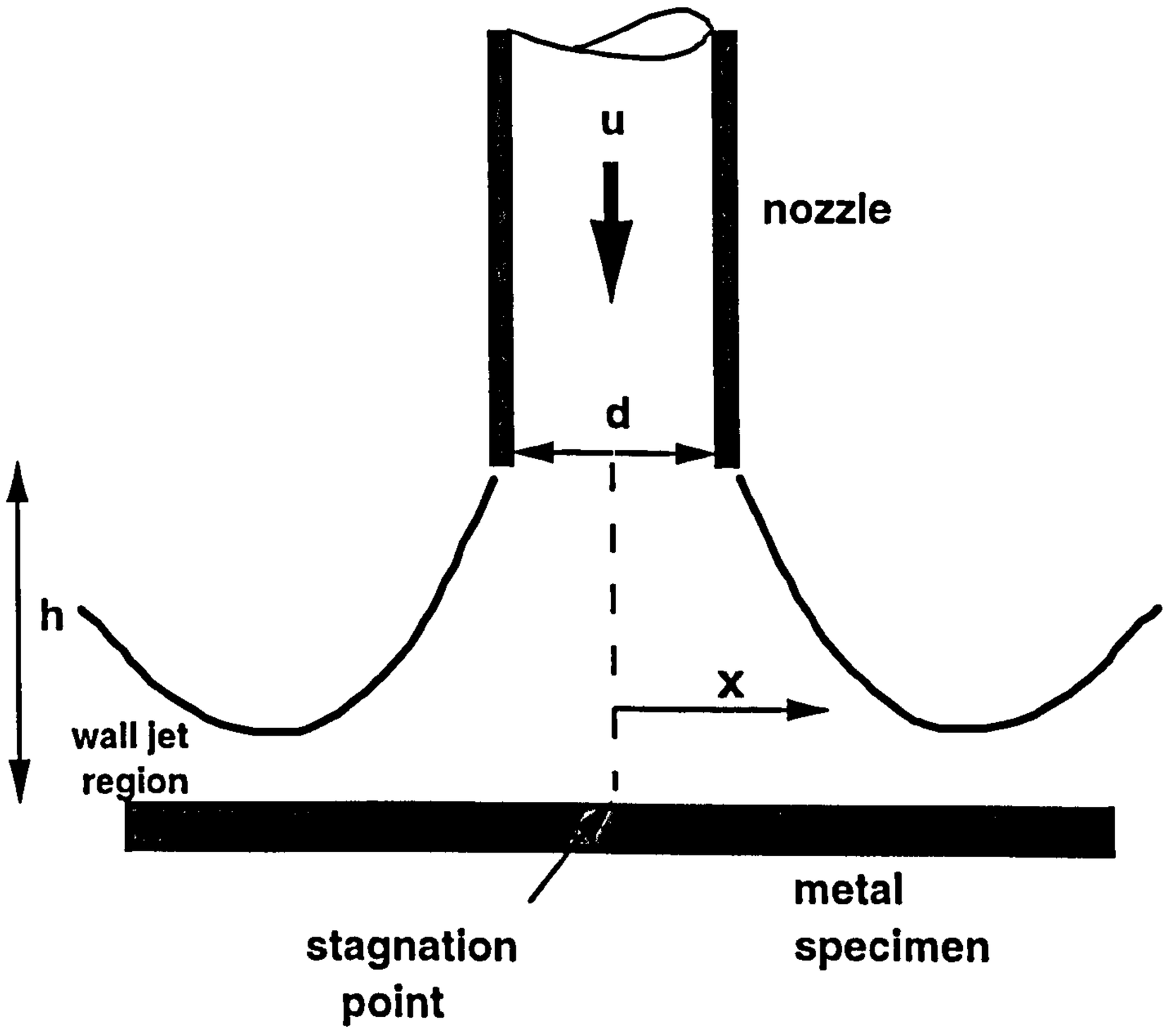


Fig. 4.3. Schematic representation of the impingement region where the liquid jet impacts the solid substrate

and the shear stress, $\tau_w$, follows the equation for ratios of x/d>2-3,

$$\tau_w = 0.0447\,\rho u^2\,Re^{-0.182}\left(\frac{x}{d}\right)^{-2}$$

It has been established [29] that the maximum shear stress occurs at a ratio x/h of approximately 0.14. In terms of the friction factor, f,

$$\frac{f}{2} = 0.0447\ Re^{-0.182}\left(\frac{x}{d}\right)^{-2}$$

In an extension to this [9], the mass transfer coefficient was calculated as a function of the shear stress in the form,

$$k = 3.78\left(\frac{\tau_w}{\rho u}\right)Sc^{-0.667}\left(\frac{r}{d}\right)^{0.8}$$

For several geometries, the mass transfer coefficient is determined by the shear stress at the wall and therefore mass transport dependent corrosion processes are influenced by shear stress. Again it must be stated that under mixed control, the correlation only forms one factor to be considered and the corrosion rate will be, in addition to shear stresses, a function of the surface and of the electrochemical parameters (i.e. the electrode potential). Previous work [7,27,28,30,31] has shown the correlation between shear stress and the extent of mechanical erosion and under conditions where the shear stress exceeds a critical value, the mechanical effects are significant. Under a high speed impinging jet there are interacting electrochemical effects and mechanical effects, some mass transfer controlled and others controlled by the environment and material characteristics.

It has been established that impact pressures can result in plastic deformation of metallic targets, evident through slip and mechanical twinning [19]. However the effect of the lateral flow which has been shown to generate large pressures, has received less attention. The joint effects of the initial impact pressures and the subsequent lateral flow are summarised in [19]. Liquid impact produces a region where circumferential cracks can occur depending on the material properties and the impact velocity. After impact, the flow movés radially and once it collides with a surface asperity, the force of impact can create a crack perpendicular to the surface. Subsequent impacts on existing cracks pits or depressions can produce accelerated damage with large pieces of surface detached.

Although liquid impingement damage can occur readily in the absence of corrosion, corrosion can readily affect the extent of damage. Mechanical damage mechanisms have been widely studied yet there is a dearth of information on the mechanisms by which high velocity impingement affects the corrosion rate and morphology.

## Experimental Methods

### Electrochemical Monitoring

Electrochemical monitoring in this section of the project was conducted while an impinging jet of seawater was being directed normally to the working electrode surface (i.e. the metal under investigation). The jet erosion rig (Fig. 4.4) comprised of a high pressure pump directing a jet of seawater at a velocity of 100m/s. The temperature of the impinging jet was thermostatically controlled at the reservoir. For tests at ambient temperature, a cooling coil of stainless steel was utilised to counteract the heat generated by the high pressure pump. Anodic and cathodic polarisation test were conducted after 4 hours impingement unless otherwise stated.

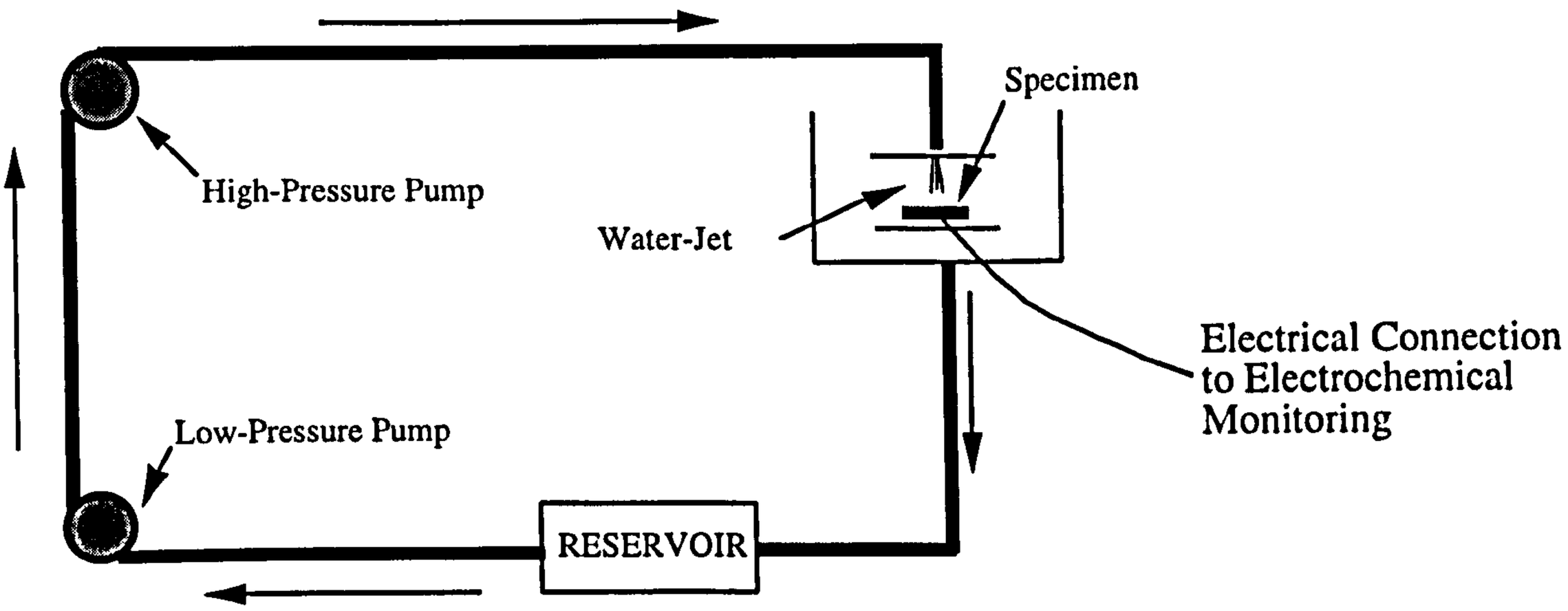


Fig. 4.4. Liquid erosion rig

Potentiostatic tests were performed under liquid erosion conditions for two purposes. The initial aim was to investigate potentials, determined by potentiodynamic means on the stainless steels and related alloys, which showed interesting features, by applying a constant potential and monitoring the current with respect to time. Another type of potentiostatic test involved the application of cathodic protection (CP) . The electrode potential of the specimen was maintained at a negative potential of -0.8V in order to reduce the rate of anodic reaction on the surface enough to render the deterioration due to electrochemical charge transfer negligible. The CP currents on different materials were then recorded as a function of time and from this, information on the cathodic reaction rate and also the relative susceptibility to corrosion could be attained.

Tests on cast iron and carbon steel were performed in liquid erosion and these materials exhibit active corrosion behaviour. In these tests the material weight loss was measured

using a balance, accurate to 0.0001g, and these results were correlated to the electrochemical test results. The results of these tests will be reported and discussed in chapter 5.

Calibration of Impinging Jet Velocity

In this study, a submerged jet was utilised, impinging on a surface at 90°. The size of the jet increases steadily as it travels away from the nozzle. Up to a certain distance from the nozzle exit there is a core of flow with undiminished velocity equal to the exit velocity. This region of flow is known to exist as a cone and is described as the potential cone. The region from the nozzle exit to the end of the cone is called the flow development region and at distances greater than the end of the cone it is fully established flow. In this work only the region of fully developed flow is considered.

Flow Calculations

Measured volume flow rate = 190ml/s

Diameter of nozzle = 1.5mm

From continuity, velocity at nozzle exit = 107.5m/s

Velocity profile from the nozzle exit follows the relationship

$$\frac{U_m}{U_o} = \frac{6.3}{x/d}$$

where $\mathbf{U_m}$ is the velocity at section **m**, $\mathbf{U_0}$ is the exit velocity, **d** is the nozzle diameter and **x** is the perpendicular distance from the nozzle exit to section **m** [29]. The required velocity for the tests was established at 100m/s and therefore the distance from the nozzle exit of the specimen was kept constant at 10mm.

**Results - Anodic Potentiodynamic Tests**

The higher-alloyed duplex stainless steels and superaustenitic stainless steel suffered little detrimental effect due to the impinging sea water jet at ambient temperature (18°C) over the relatively short test period. However, the severity of the jet directed normal to the specimen surface is illustrated by the "active" behaviour of a Cu-Ni alloy

alloys at velocities in excess of a few metres per second [32,33]. Figure 4.5 confirms the known superiority of high-grade stainless steels under high velocity flows.[2].

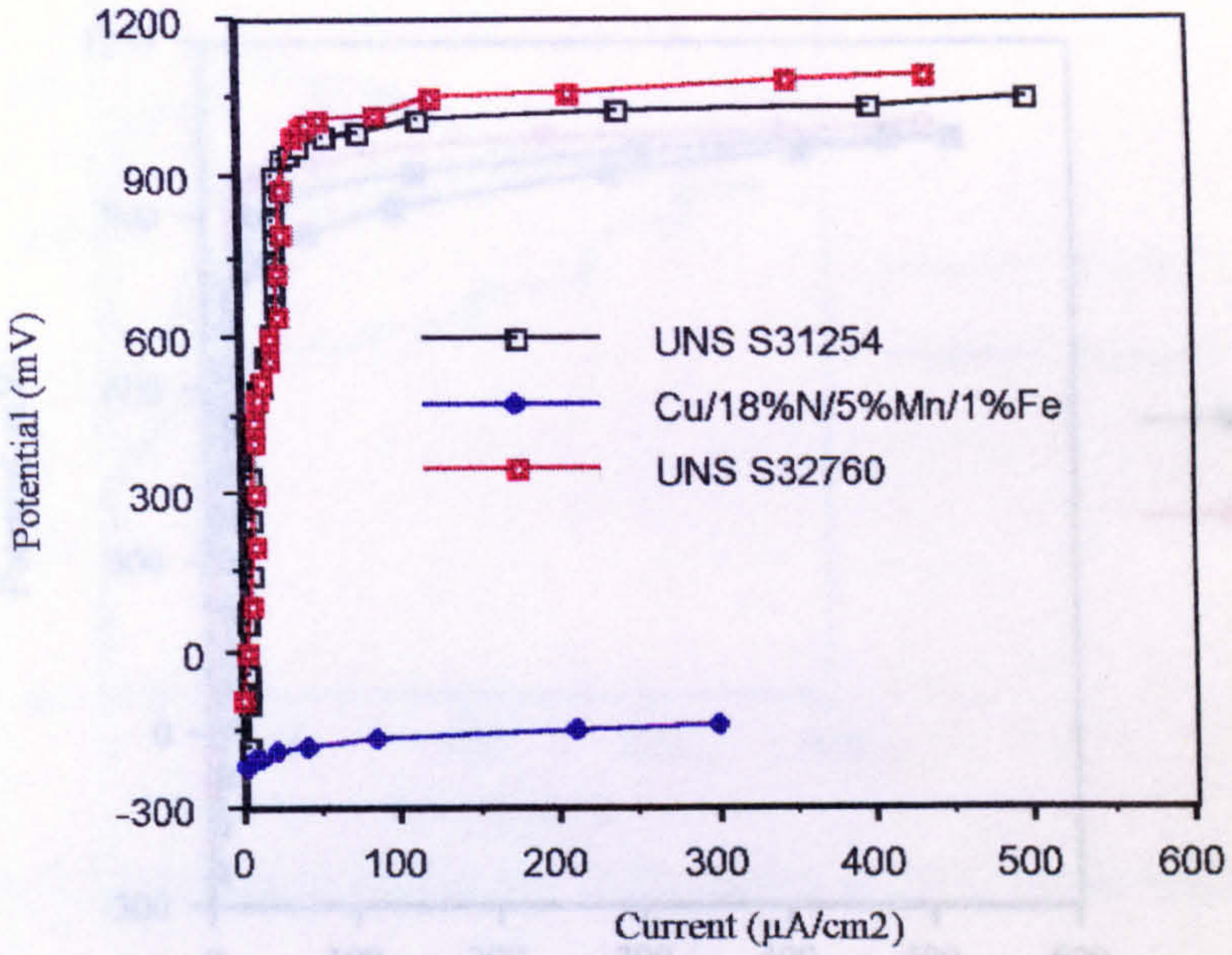


Fig. 4.5. 'Active' corrosion behaviour of a Cu/Ni alloy under the severe impinging seawater jet at 100m/s compared to the 'passive' stainless steels

At 18°C, and more so, as the temperature was increased to 30°C and subsequently 50°C, the anodic polarisation curve on the duplex stainless steels, Inconel 625 and the superaustenitic alloy displayed characteristics distinct from those under static conditions. The most apparent change was the presence of an initial significant rise in current at a potential termed $E_p$ (primary breakdown potential). This feature is evident on UNS S32760 and UNS S31254 in Fig. 4.5 at about +400mV but was more pronounced at higher temperatures (shown later). As shown in Fig. 4.5, this rise in current was followed by a relative stabilisation of the current (to a value $I_p$) and the scan proceeded (at a higher "stable" current) until final breakdown at a more noble potential.

The electrochemical data and observed types of attack after anodic polarisation are presented in Tables 4.1-4.3. Compared to the behaviour under static conditions, the anodic polarisation curves were significantly more complex, as previously mentioned, by the presence of a double breakdown potential. The result was that under the high velocity at 18°C and 30°C, the eventual breakdown potential $E_b$ was not significantly lowered for the duplex stainless steels and UNS S31254 (Fig. 4.6a) but $E_p$ was lower than $E_b$ in static conditions, shown in Fig. 4.6b for the superaustenitic stainless steel, UNS S31254 at 18°C. At 50°C, the impinging jet imposed a significant detrimental

effect on the integrity of 25Cr duplex as shown in Fig. 4.7. and $E_b$ was lowered by an appreciable amount (no $E_p$ was recorded here).

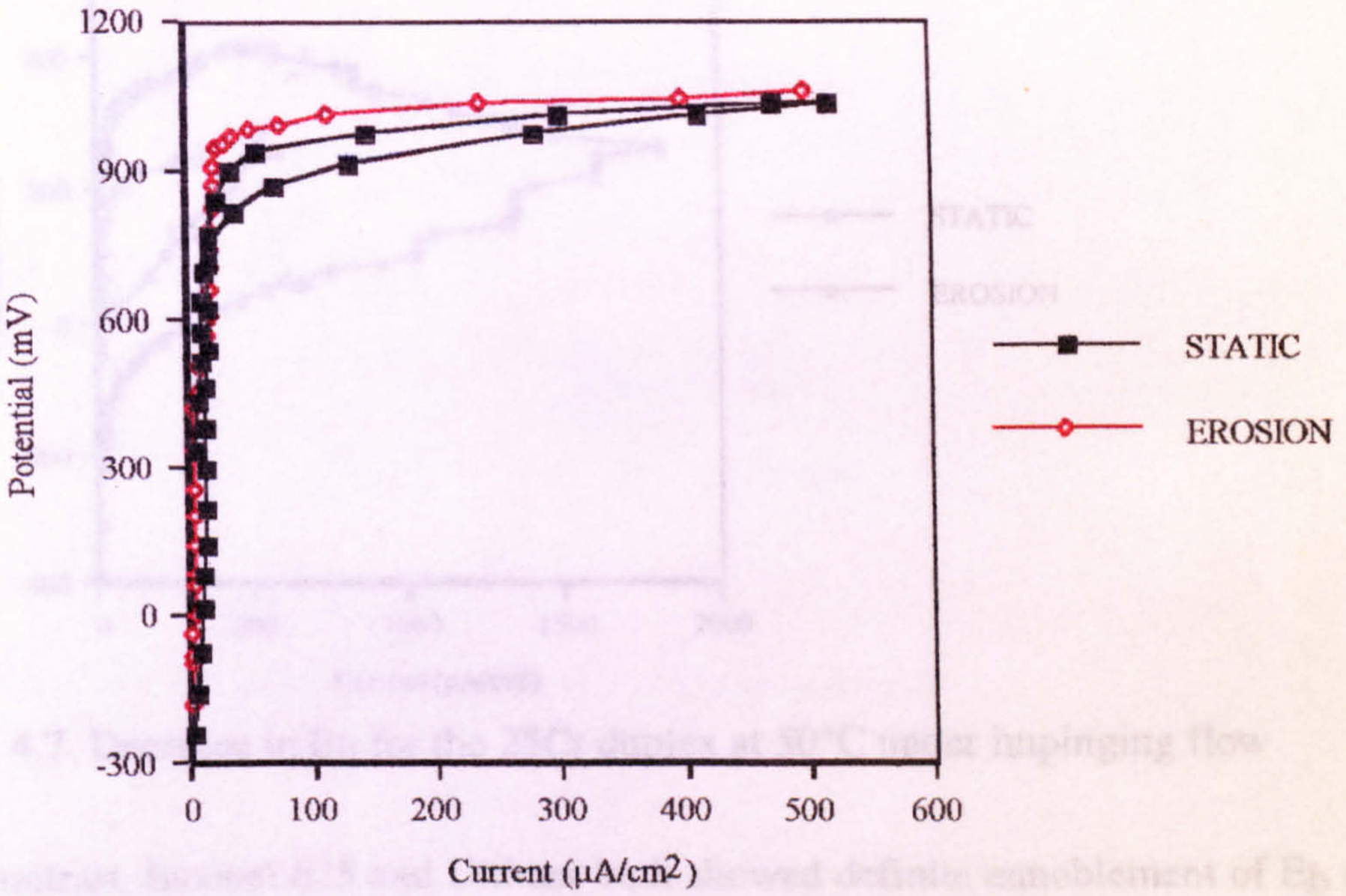


(a)

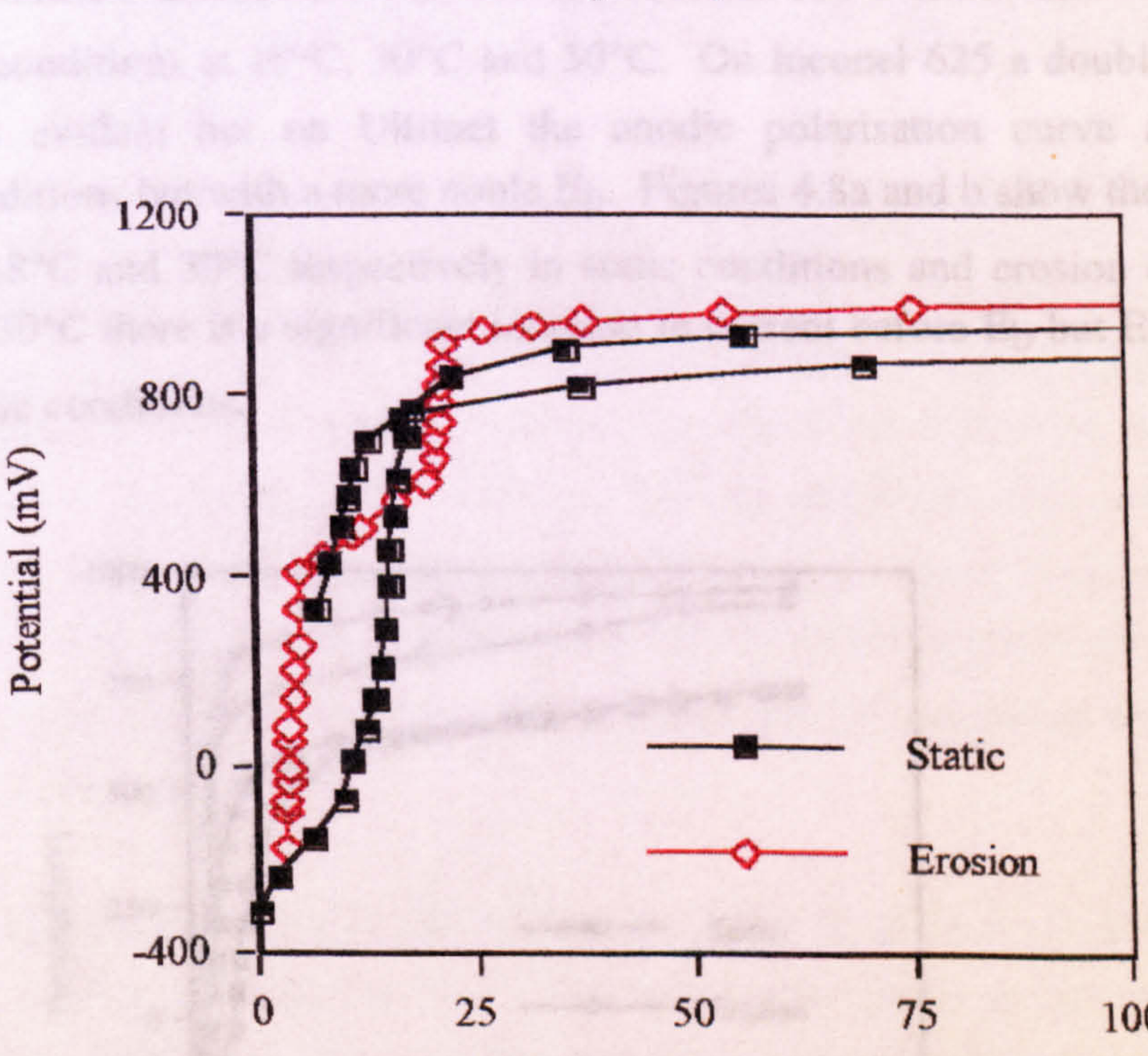


(b)

Fig. 4.6(a). $E_b$ under static conditions comparable with $E_b$ under liquid impingement at 18°C on UNS S31254 (b) rise in current associated with $E_p$

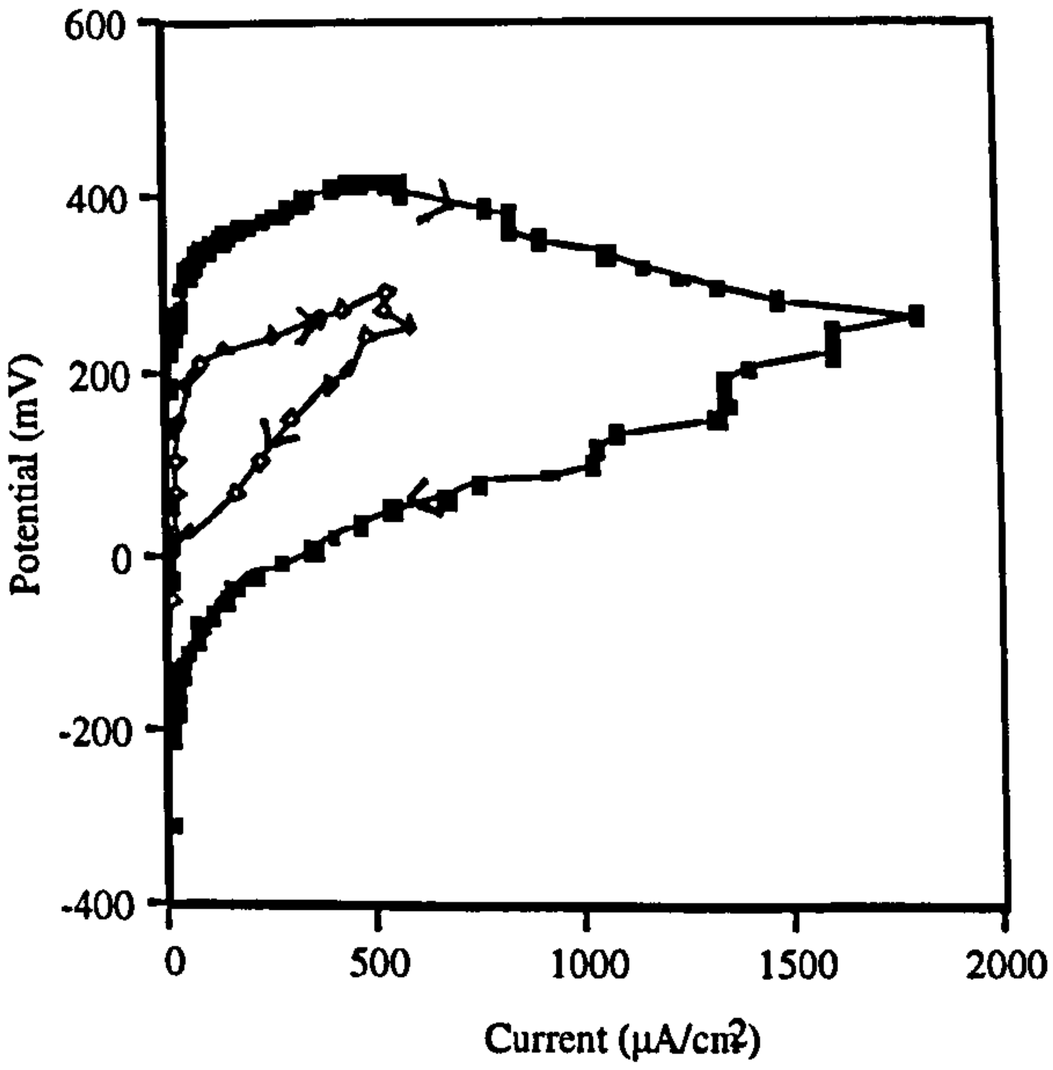


Fig. 4.7. Decrease in $E_b$ for the 25Cr duplex at 50°C under impinging flow

In contrast, Inconel 625 and Ultimet both showed definite ennoblement of $E_b$ under the jet conditions at 18°C, 30°C and 50°C. On Inconel 625 a double breakdown potential was evident but on Ultimet the anodic polarisation curve appeared as in static conditions but with a more noble $E_b$. Figures 4.8a and b show the corresponding curves at 18°C and 30°C respectively in static conditions and erosion conditions on Ultimet. At 30°C there is a significant increase in current before $E_b$ but $E_b$ is still higher than in static conditions.

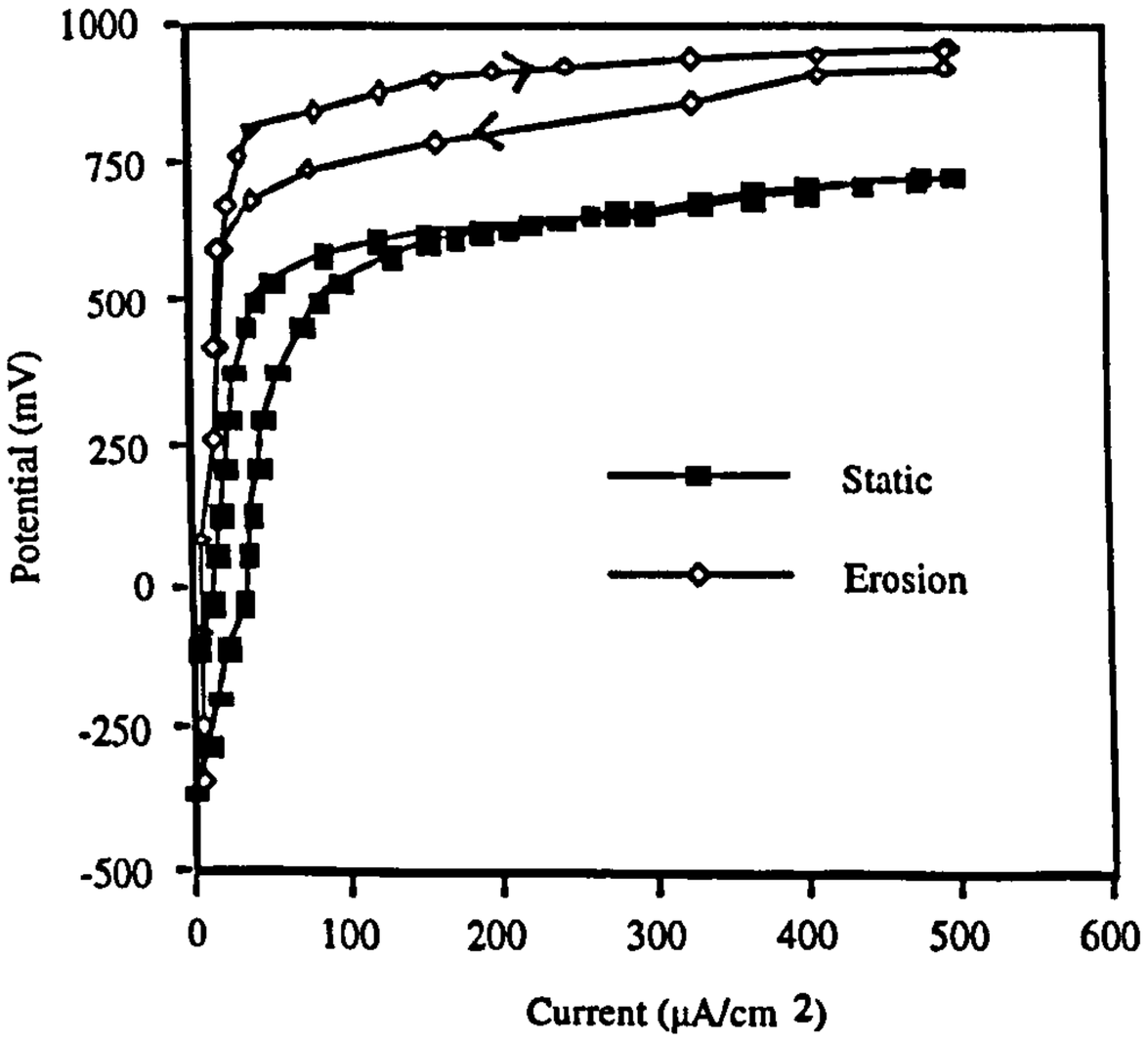


(a)

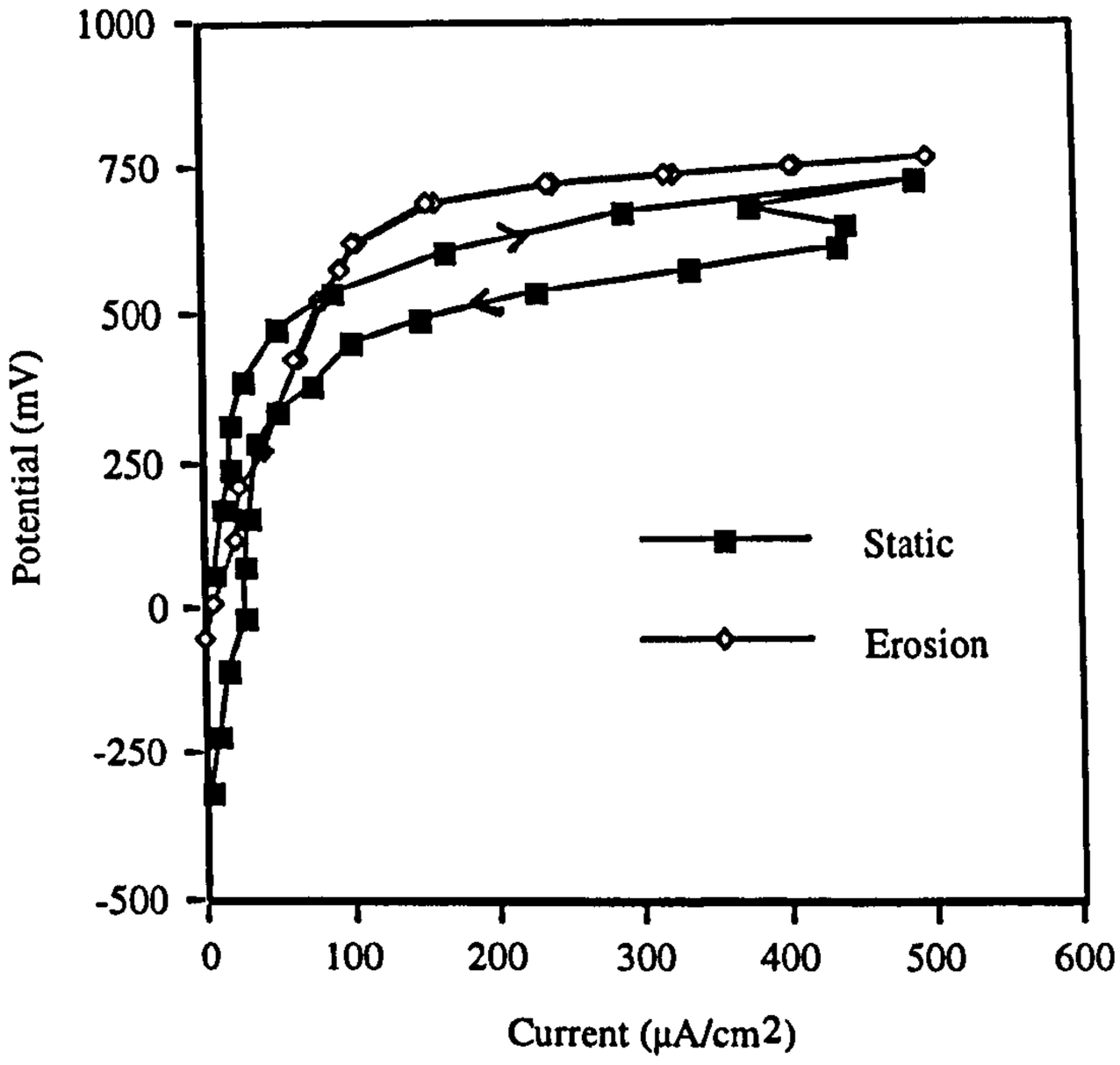


(b)

Fig. 4.8 Anodic polarisation on Ultimet in static and liquid erosion conditions (a) at 18°C and (b) at 30°C.

On the lower-chromium UNS S31603 and the cobalt-base Stellite 6, however, the direct effect of the jet at ambient temperature was to lower the breakdown potential by a significant amount (Fig 4.9a). For UNS S31603, increased temperature to 50°C, under jet conditions, subsequently reduced $E_b$ further but it must be noted that the difference between $E_b$ under static conditions and jet conditions was not enhanced (Fig 4.9b). Furthermore, although the anodic polarisation curve resembled that under static conditions, $I_{max}$ was significantly lowered and the repassivation potential $E_r$ occurred at a more positive potential (implying that the jet conditions were more favourable for repassivation).

Severe deterioration of the passive potential range was observed on Stellite 6 as the temperature increased to 30°C. The material showed passivity for only a shift of 120mV in the anodic direction at which point the current increased very rapidly and extensive pitting attack occurred over the entire surface. On further increasing the temperature to 50°C, immediate active behaviour was accompanied by severe pitting attack concentrated at the grain boundary regions. Figure 4.10a shows the evolution of the anodic polarisation scan as the temperature increased and 4.10b shows light

micrographs of the attack at the grain boundary regions at 50°C, in contrast to the minor pitting associated with anodic polarisation at 18°C.

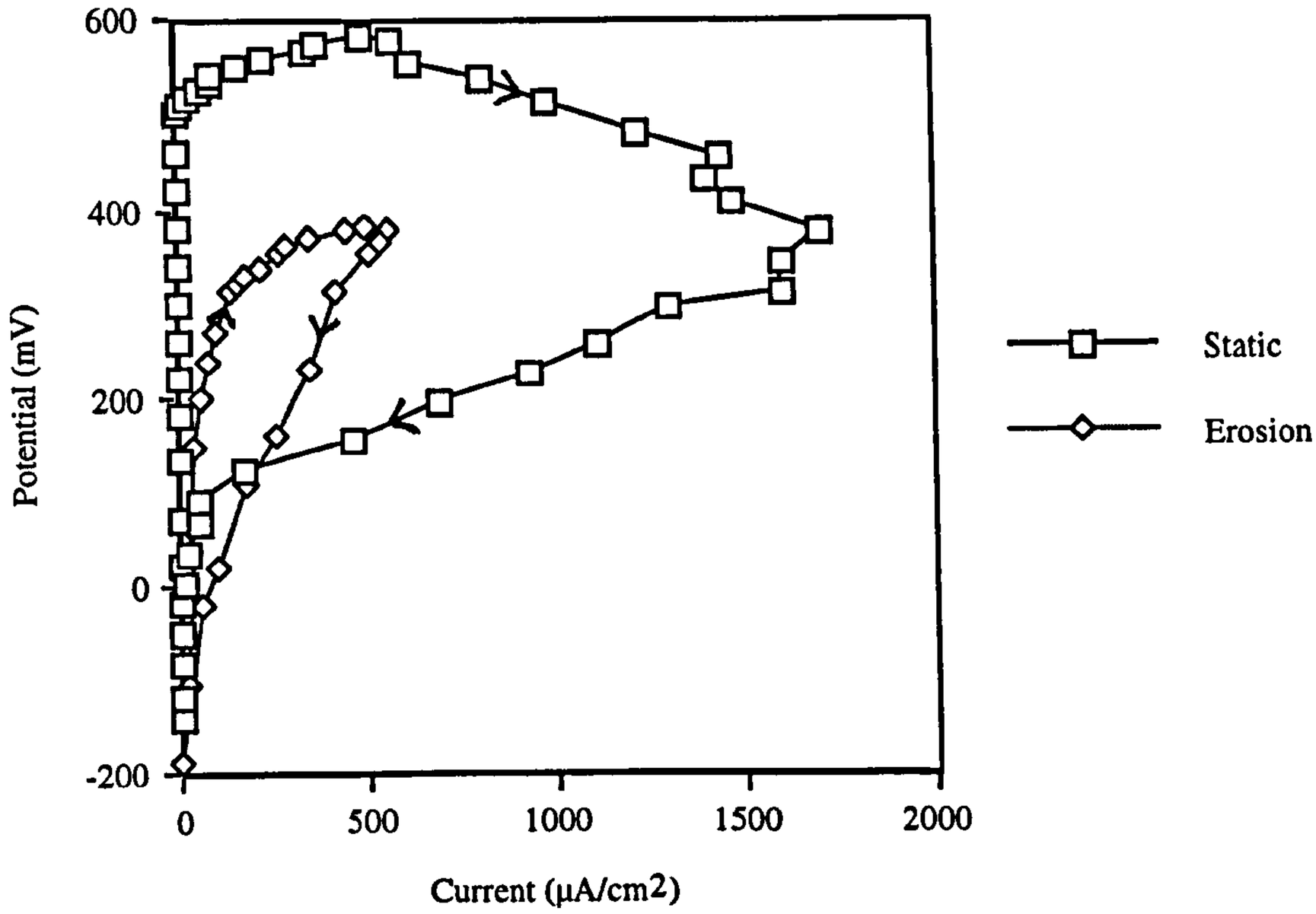


(a)

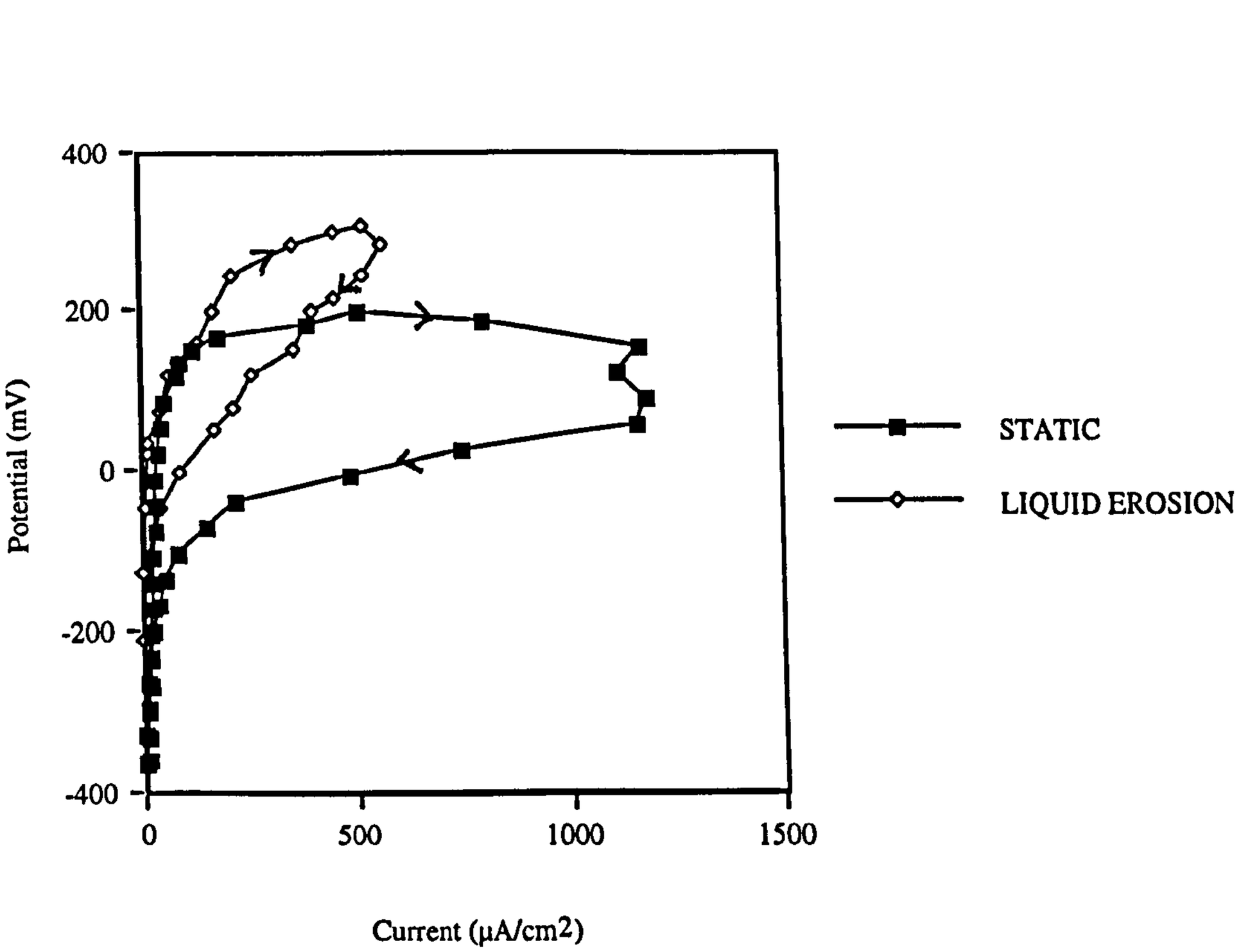


(b)

Fig 4.9. Anodic polarisation under liquid erosion compared to static conditions on UNS S31603 at (a) 18°C and (b) 30°C

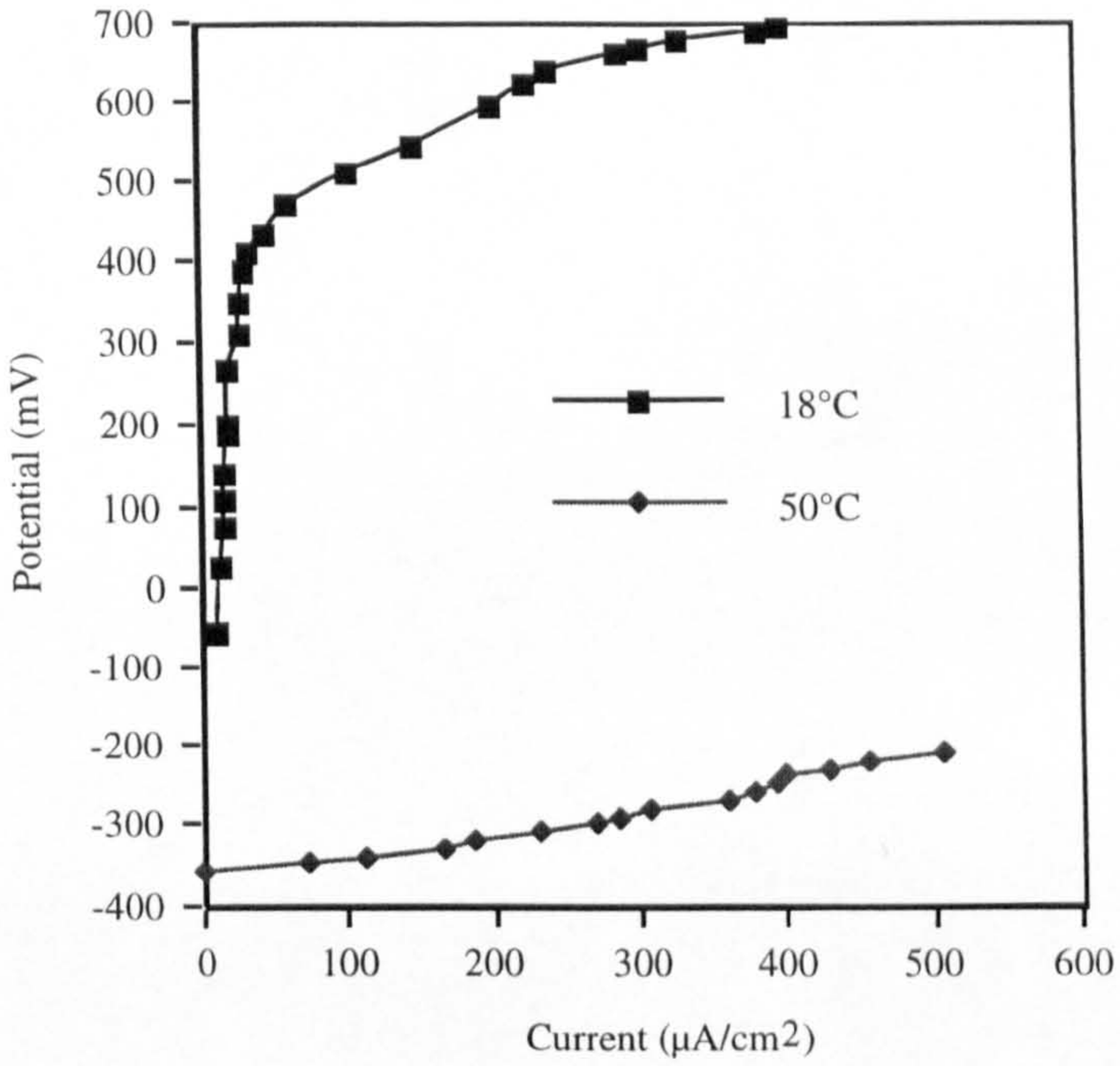
700
600
500
400
300
200
100
0
-100
-200
-300
-400
Potential (mV)
0
100
200
300
400
500
600
Current (μA/cm2)
18°C
50°C

(a)


50μm

(b)

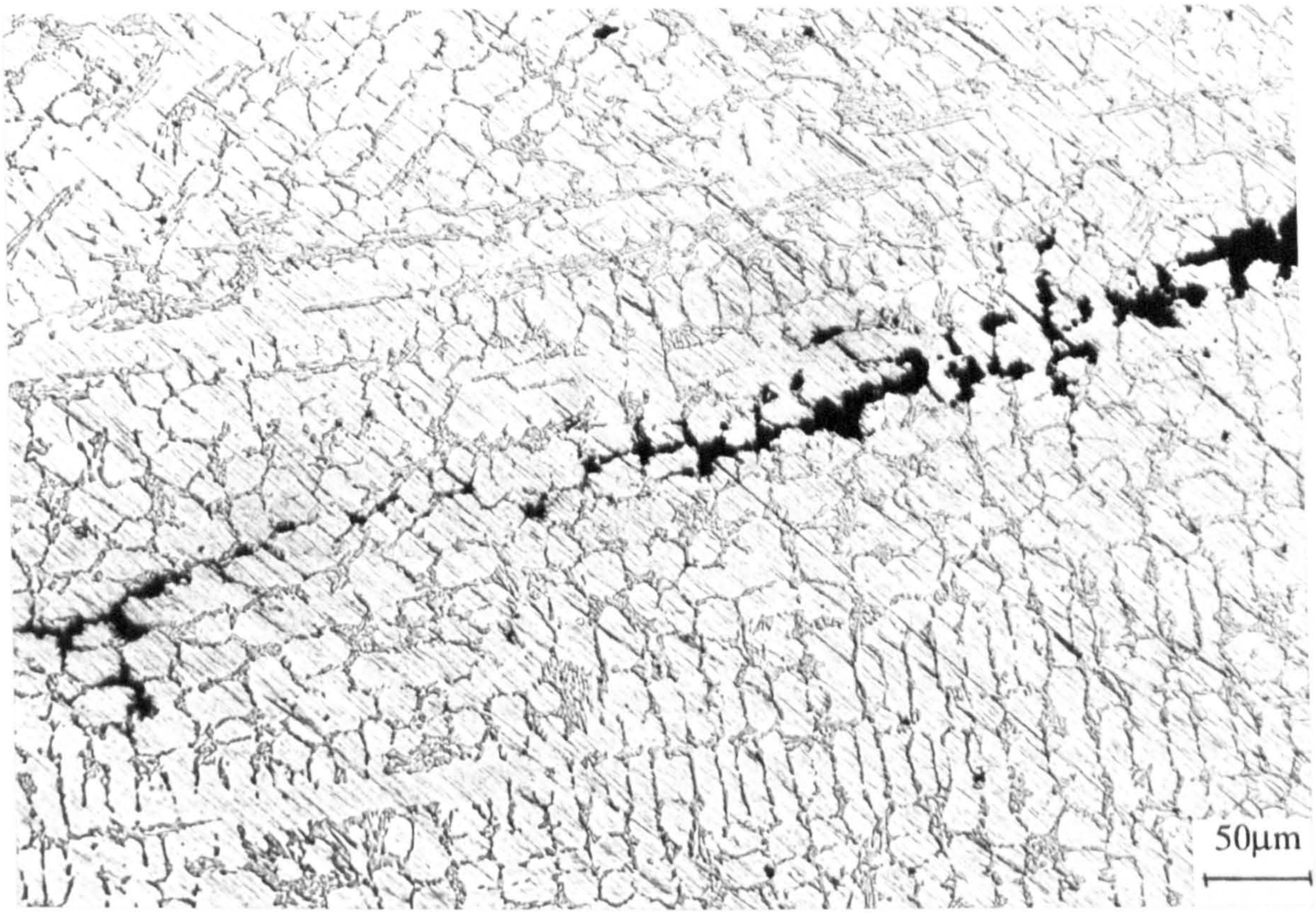


(c)

Fig. 4.10(a) Anodic polarisation on Stellite 6 under liquid erosion conditions and attack associated with (b) 18°C (c) 50°C

EPMA was conducted at the affected areas and several analyses were performed at grain boundary regions (attacked and unattacked) and remote from the grain boundaries in an attempt to ascertain what compositional differences (if any) could provide an explanation for such severe preferential attack. Figure 4.11a and b shows SEM micrographs of the attacked grain boundary regions. A large enrichment of Cr was found at the grain boundaries. Table 4.4 gives the composition, determined by energy dispersive EPMA, of the regions marked 1, 2 and 3 in Fig 4.11b.

The numerical values of the parameters $E_b$, $E_p$, $I_p$ etc., mentioned above, for each test at 18°C, 30°C and 50°C are presented in Tables 4.1-4.3. It became clear that the extent of the initial $E_p$ (quantified by $I_p$) was material dependent as well as dependent on the severity of the conditions (in this case the temperature). Figure 4.12 shows the larger $I_p$ on SAF 2205 than on the superduplex stainless steel, at 30°C and the enhancement of $I_p$ on the superduplex as the temperature increased from 18 to 30°C and 50°C. Also, as mentioned previously, at 50°C, neither the 25Cr duplex or SAF 2205 showed this primary breakdown feature but instead the normal breakdown behaviour occurred at relatively active potentials (see Fig 4.7.).

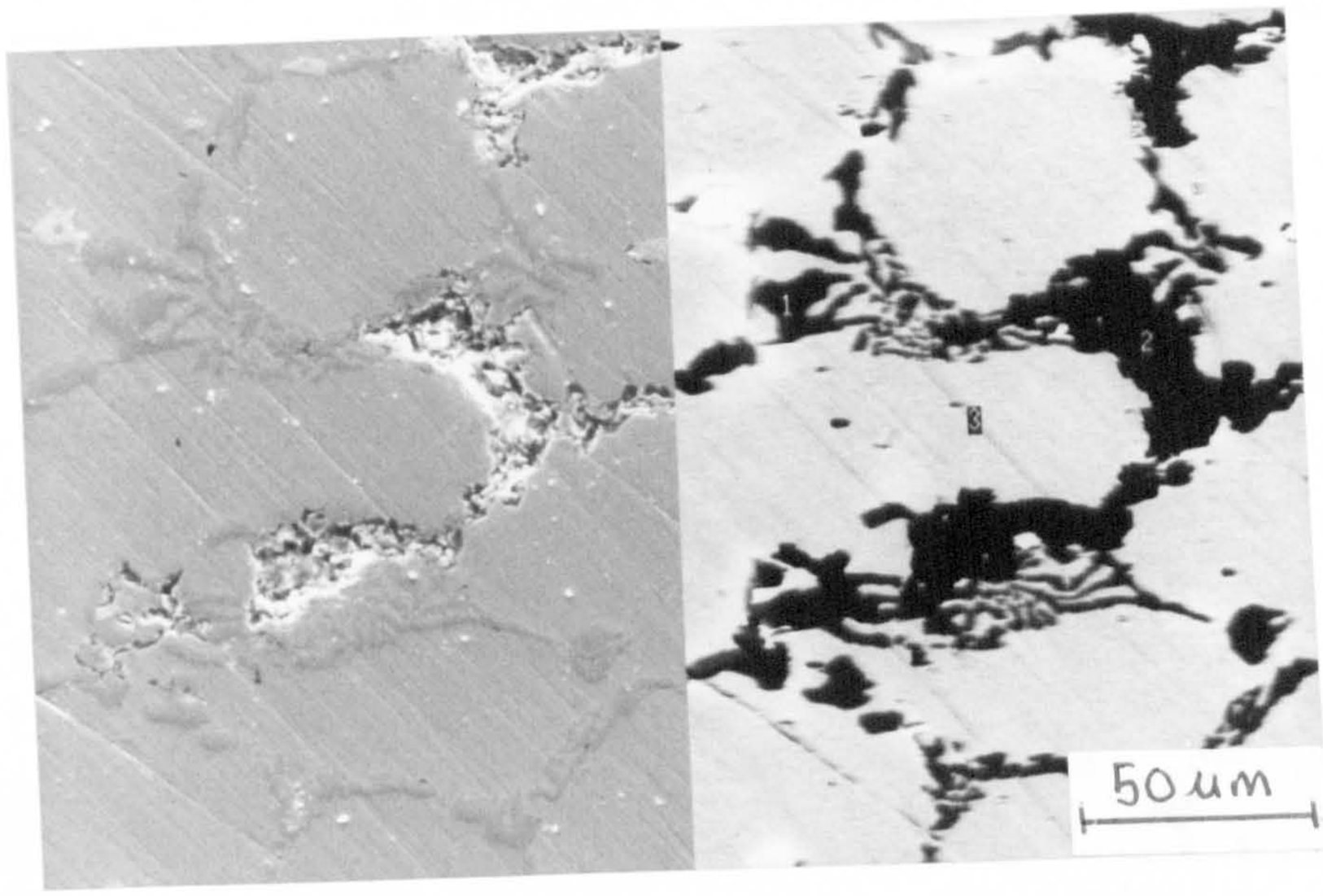


(a)

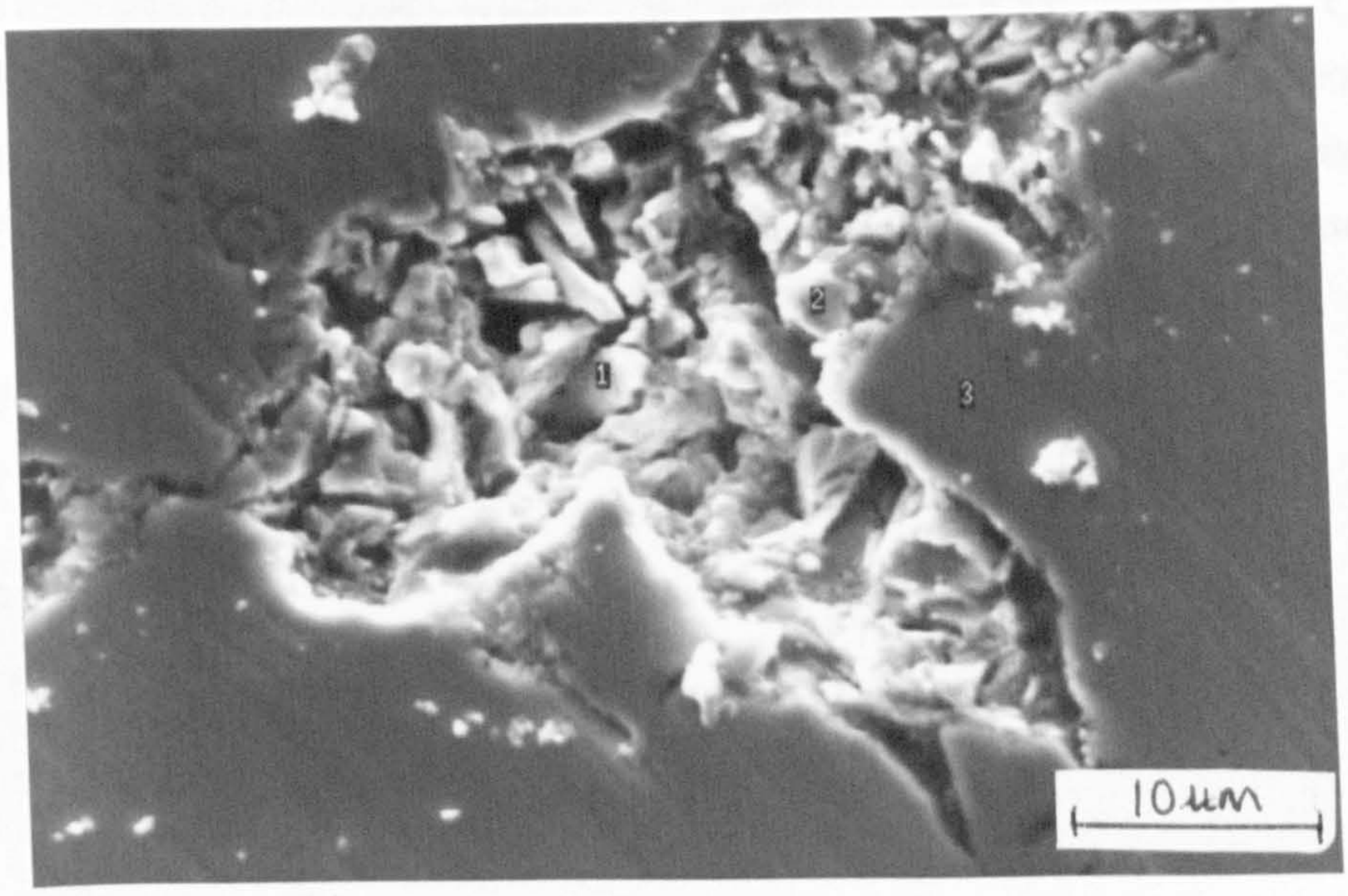


(b)

Fig. 4.11(a). Lower magnification SEM micrograph of grain boundary area on Stellite 6 after anodic polarisation at 50°C in liquid erosion and (b) SEM micrograph and chemical analysis area.

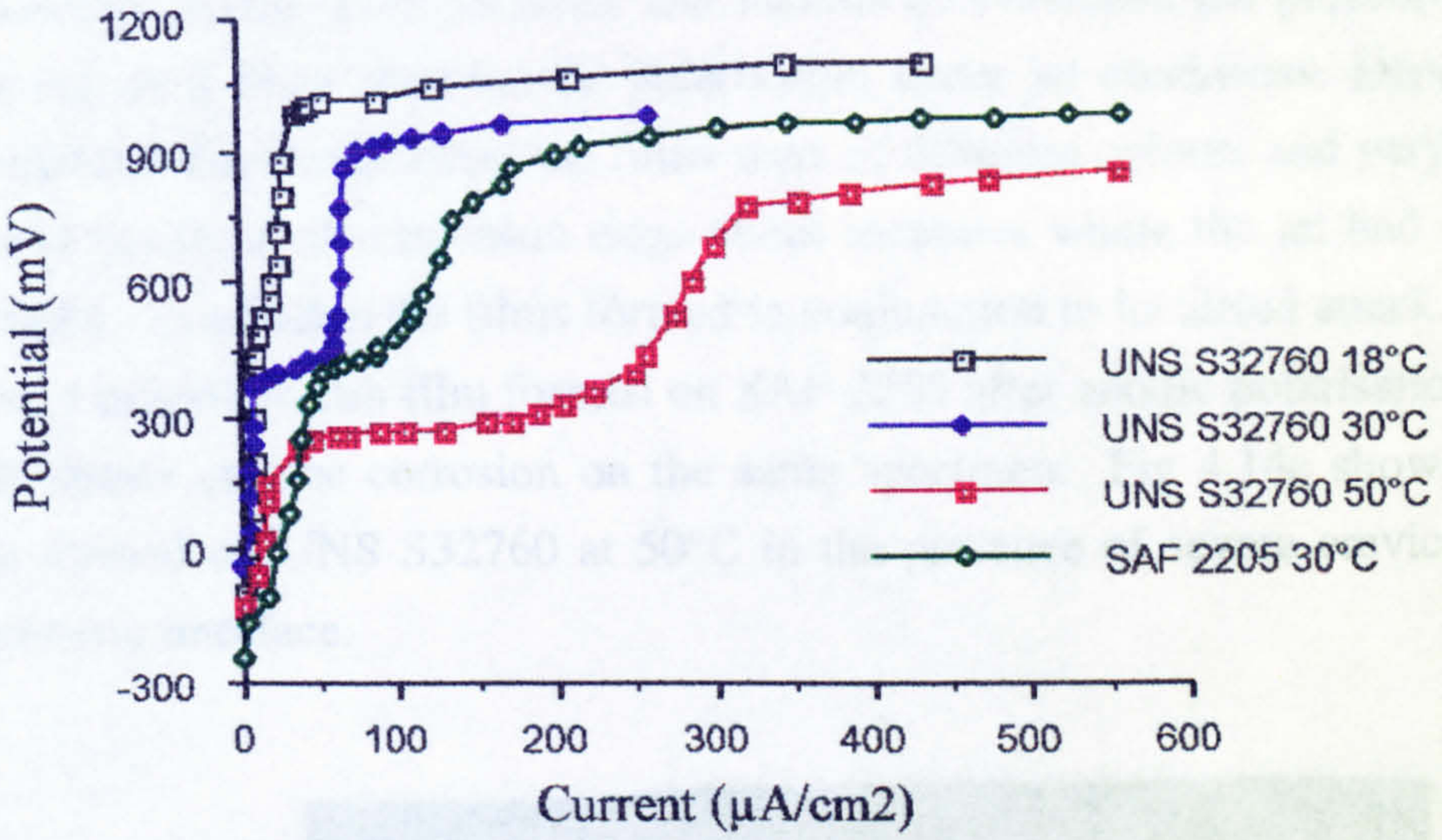


Fig. 4.12. Enhancement of $I_p$ on UNS S32760 as temperature increases and comparison with $I_p$ on SAF 2205 at 30°C

Also in common with behaviour of some alloys at elevated temperatures under static conditions, initial attempts to repassivate (upon potential scan reversal) were subsequently followed by an active region. This is shown for SAF 2205 at 30°C in Fig. 4.13. Such behaviour was also exhibited by UNS S31603 and Ultimet. In contrast, for the duplex stainless steels, superaustenitic alloy and Inconel 625, complete repassivation was achieved immediately upon scan reversal under ambient temperature, jet conditions.

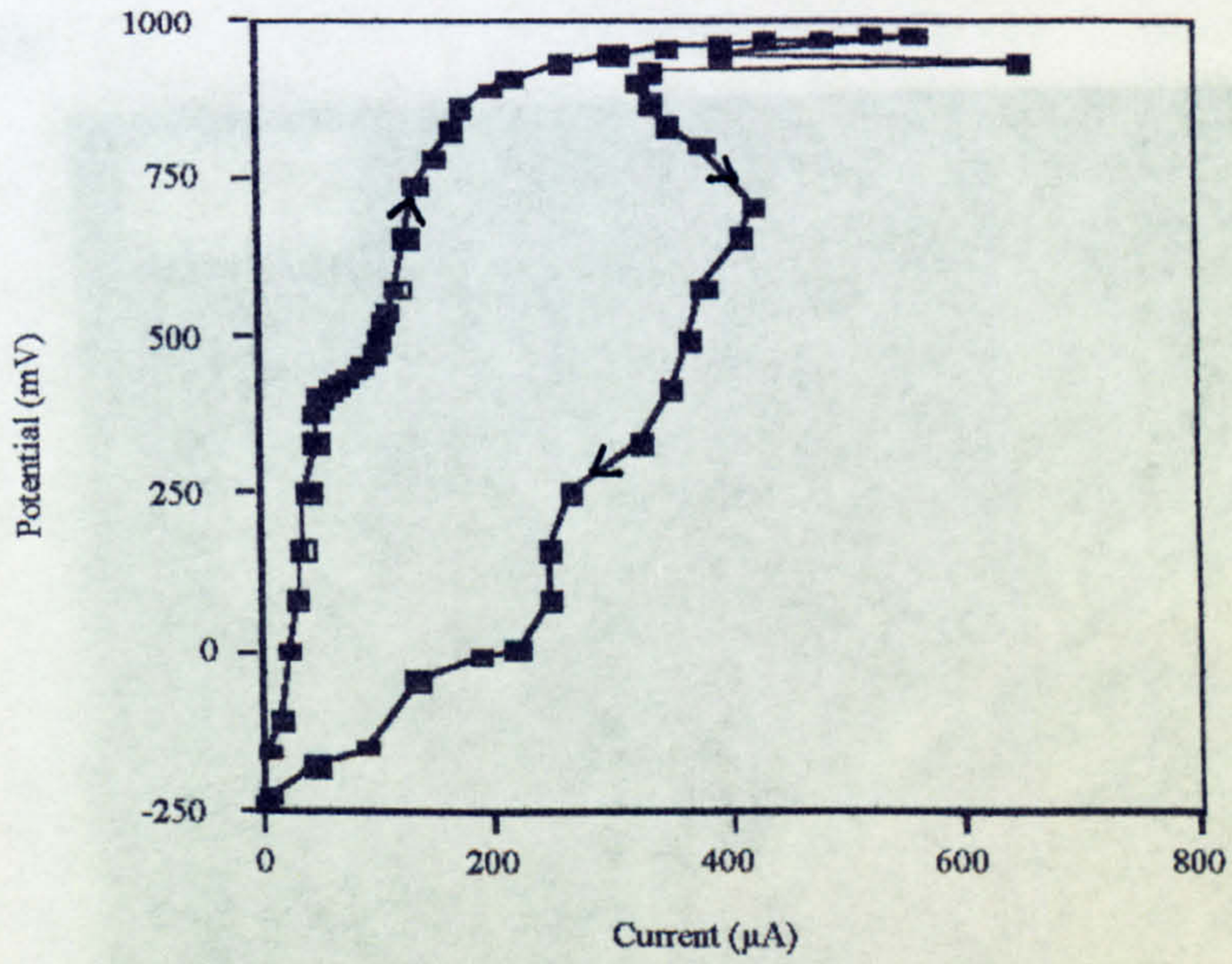


Fig. 4.13. Active loop on reverse scan analogous to behaviour in static conditions on SAF 2205 at 30°C

Microscopy on the stainless steels and Inconel 625 revealed the presence of relatively thick coloured films after anodic polarisation under jet conditions. Depending on the material and the temperature, the films were of different colours and varying thickness, often in the form of concentric rings about locations where the jet had clearly hit the specimen. In addition the films formed in conjunction to localised attack. Figure 4.14a shows a relatively thin film formed on SAF 2205 after anodic polarisation at 30°C and 4.14b shows crevice corrosion on the same specimen. Fig 4.14c shows the coloured rings formed on UNS S32760 at 50°C in the presence of severe crevice attack at the metal/resin interface.

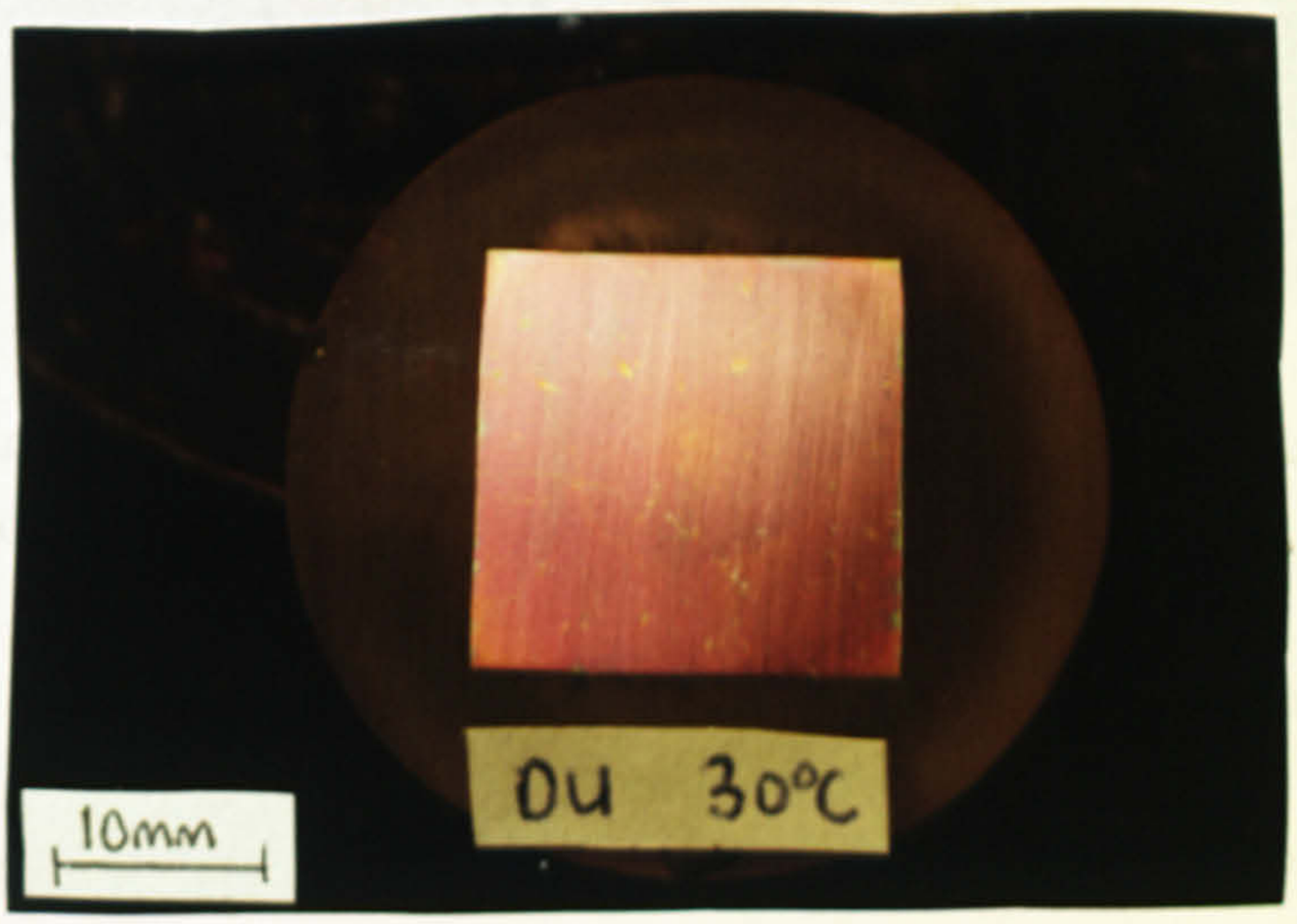


(a)

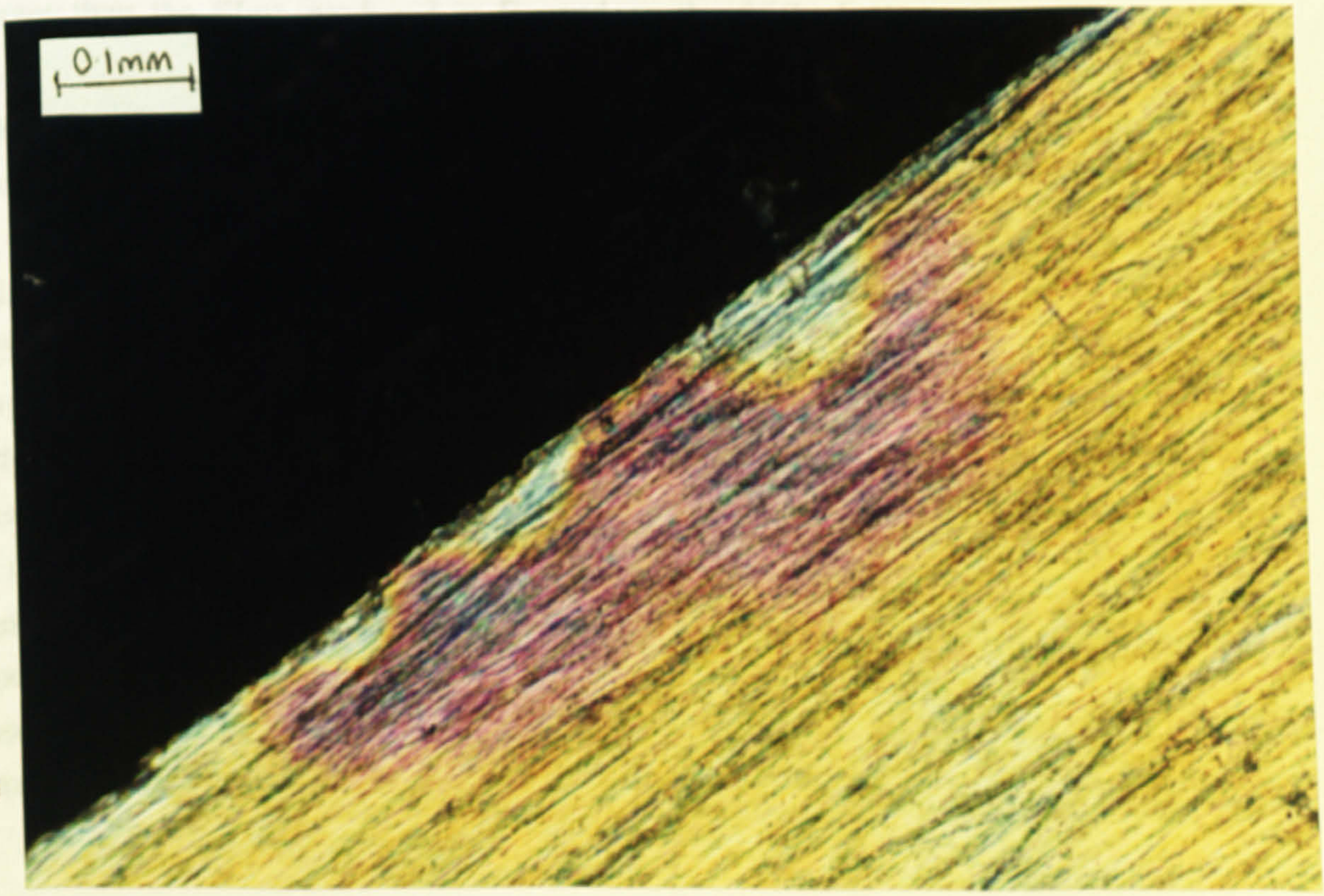


(b)

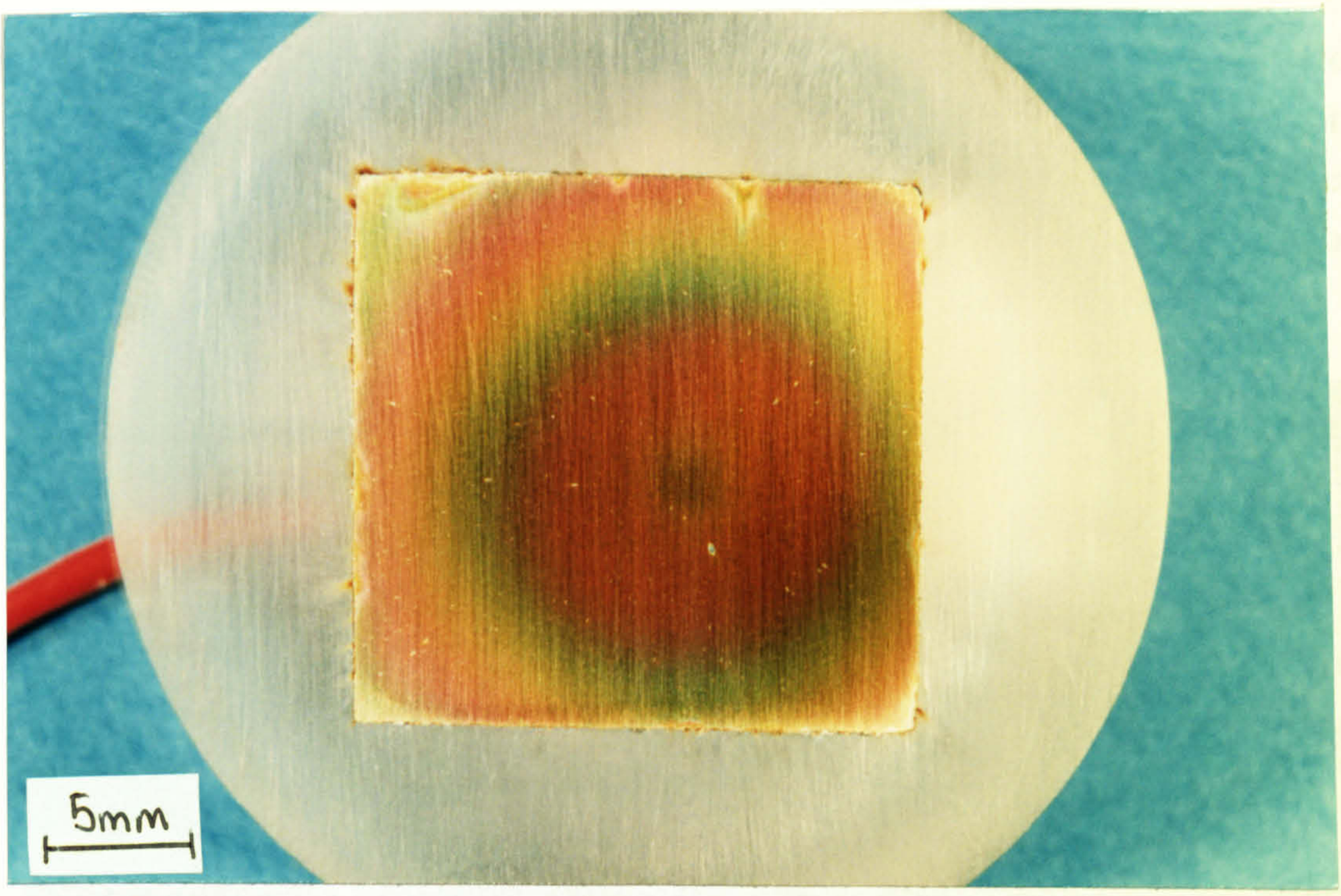


(c)

Fig. 4.14a. Coloured film formed on SAF 2205 at 30°C and (b) crevice corrosion and (c) coloured film on UNS S32760 at 50°C

It was observed consistently that where the double breakdown was present, the formation of the coloured film occurred concurrently with the rise in current at $E_p$. Where the only breakdown of passivity achieved the reversal current of 500μA (i.e. on the lower-alloyed duplex stainless steel at 50°C and UNS S31603) the film again apparently formed in conjunction with the rise in current but was evidently much thinner than the films produced at $E_p$ and on the 25Cr duplex appeared as a faint coloured etching of the surface within which pitting and crevice corrosion attack was contained (Fig 4.15). Where pitting attack was observed, the pit was clearly visible in a 'comet-like' configuration with a multi-coloured trail behind.

Using EPMA, the coloured film on the stainless steels was identified as an oxide, the EPMA probe detecting in excess of 25% oxygen at random points on its surface. Surprisingly, an enrichment of Cu and Mn was detected (with up to 9% Mn and 5% Cu) and a depletion of Cr, Fe and Ni. Also identified as an oxide, the film on Inconel 625 was found to be enriched in Mo and Fe compared to the standard analysis (Table 4.5) on unpolarised Inconel 625 with concentrations of 16%Mo and 15%Fe detected. The average composition from several analyses on the film on Inconel 625 and the superduplex, and superaustenitic stainless steels is shown in Table 4.5. On these three materials, film thicknesses of approximately 1μm were recorded but the thickness of the films on UNS S31603 and SAF 2205 was less. Without anodic polarisation, erosion

tests run for up to six days in 50°C sea water failed to produce any sign of coloured films on the surface of the superduplex alloy and SAF 2205. It is appreciated that on a film of approximately 1μm thickness, that EPMA will not produce highly accurate results due to the interference of the substrate and, as such, the enrichments recorded, compared to the alloy composition, are probably underestimates.

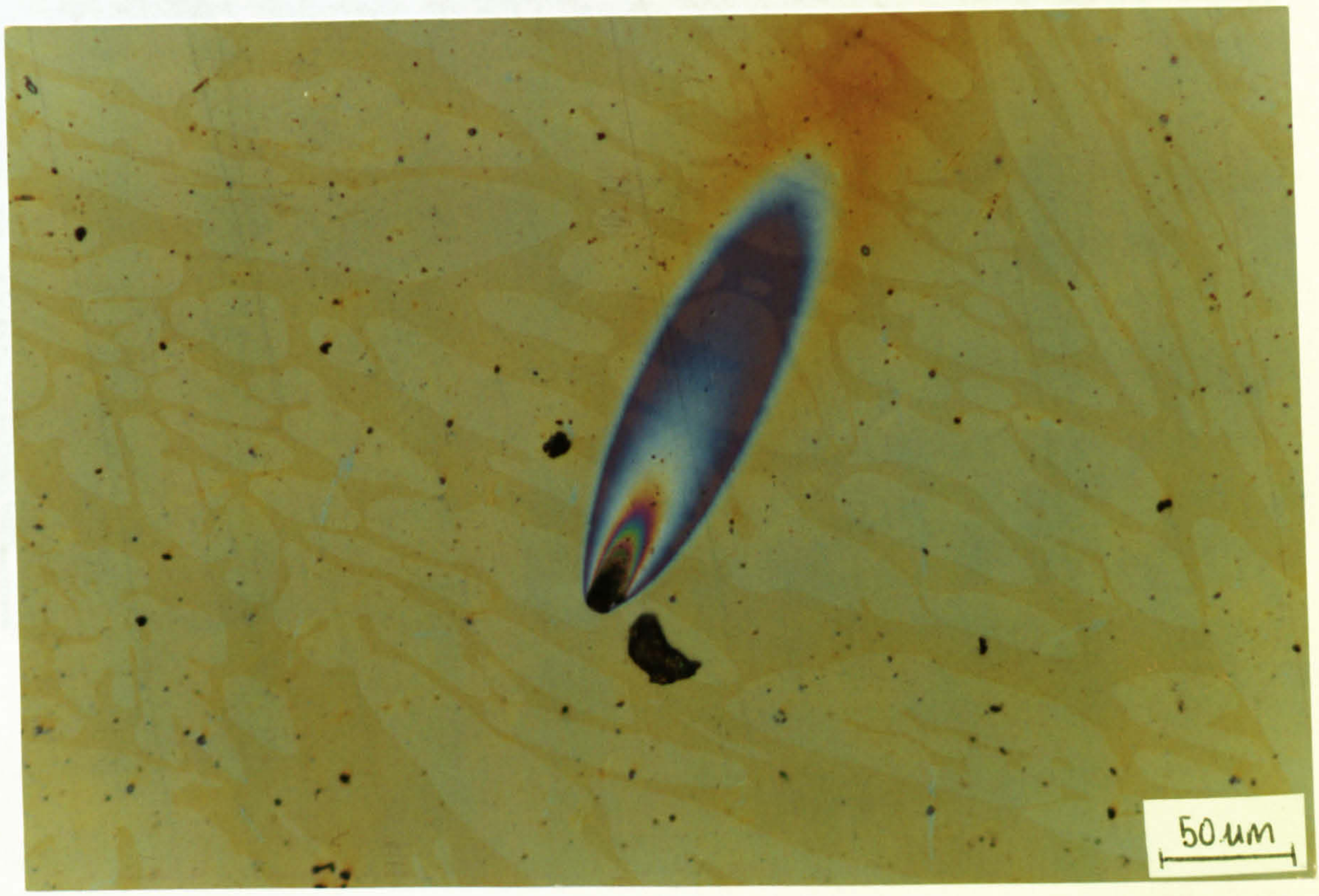


Fig. 4.15. Faint coloured etching of the surface of 25Cr duplex after anodic polarisation at 50°C and 'comet' pitting on the free surface

The double breakdown potentials were not evident on the anodic polarisation curve of the cobalt-base alloy Ultimet and only a very faint surface film was observed, not comparable with the thicker films previously mentioned and microanalysis yielded a chemical composition typical of the standard Ultimet composition.

At ambient temperature under liquid erosion, Inconel 625, the superaustenitic, the superduplex, and Ultimet all resisted any significant localised attack but on increasing the temperature to 50°C, localised corrosion was detected on all specimens with the exception of Ultimet. Pitting attack predominated, with the pits clearly visible at the head of a "comet" configuration and a multi-coloured trail behind, as described previously. The directionality of the pits (Fig. 4.16) implied that the morphology was a result of the flow parallel to the specimen out from the stagnation point, indicated by the arrow in Fig 4.16.

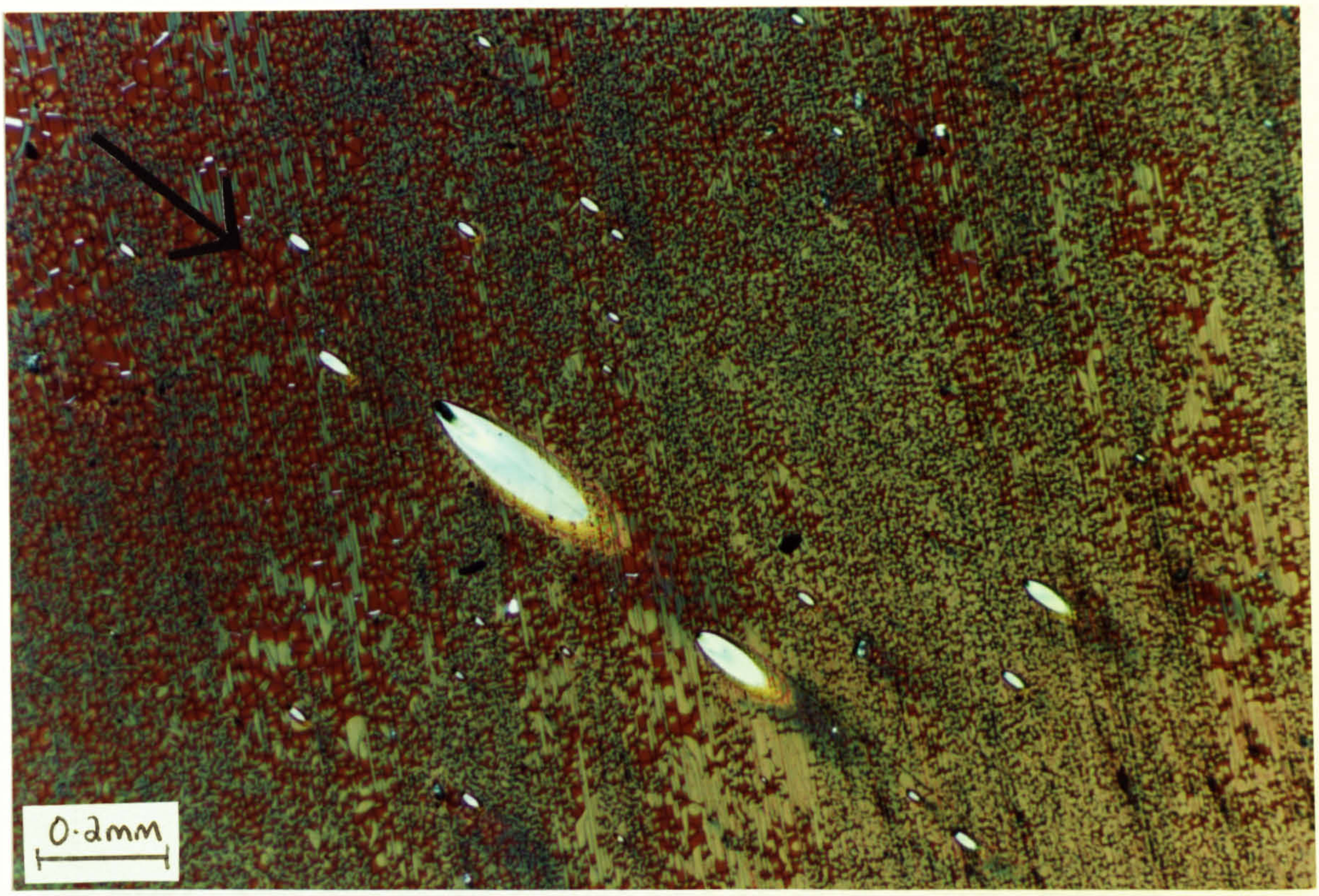


Fig 4.16. Directionality of pits formed in 'comet' arrangement on UNS S32760 at 50°C after anodic polarisation

The effect of the parallel flow seemed to be to progressively remove the corrosion products formed at the pit head causing abrasion and subsequent thinning of the film 'behind' the comet. The micrograph in Fig. 4.17 shows the film about a pitted site on the superduplex alloy where on areas 2 and 3 there is no film present.

Erosion tests conducted on commercially pure titanium also revealed formation of a coloured film after anodic polarisation to a current of 3000μA; here also with small traces of Cu and Mn detected (0.5%Cu and 2.9% Mn respectively). No increase in current corresponding to $E_p$ was achieved until a potential of +1.2V (SCE) was attained and no $E_b$ occurred up to a potential of +2.1V and termination of the experiment.

The distinctive features in the electrochemical anodic polarisation curve (i.e. the formation of double breakdown potentials, $E_p$ and $E_b$) were investigated further using potentiostatic methods followed by detailed microscopy, to determine whether one mode of attack predominated at any particular stage in the polarisation.

Initial potentiostatic tests on the 25Cr duplex and SAF 2205 alloys involved scanning the potential to +100mV(SCE) (which is below $E_b$ in static conditions for the 25Cr

duplex but above for SAF 2205) at 50°C and holding it constant. The jet was started once +100mV was reached and the resulting current was recorded with time. Figure 4.18 illustrates the current progression once the jet was started.

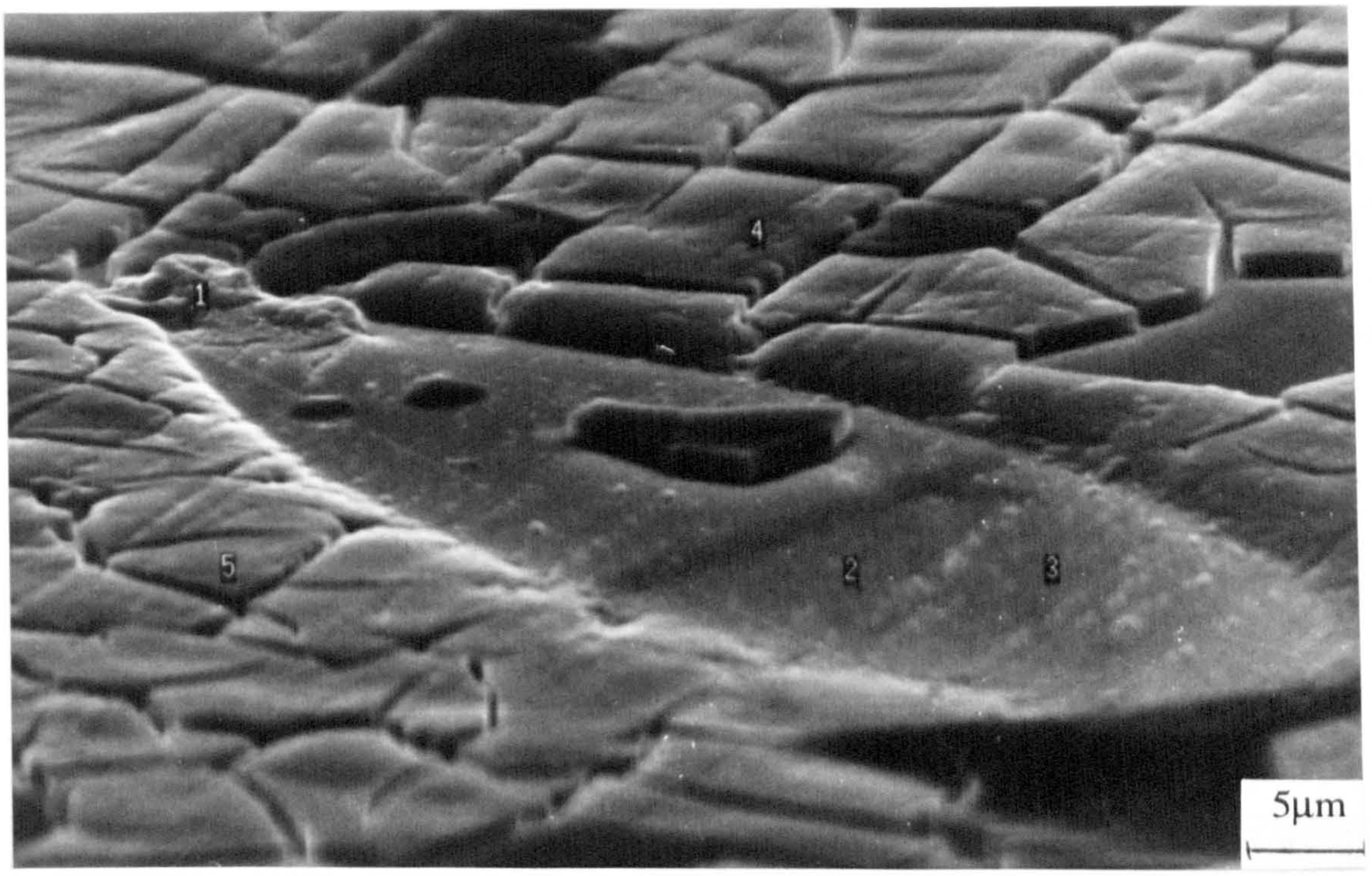


Fig. 4.17. SEM micrograph of a 'comet' pit site and the film arrangement in the vicinity of the pit head

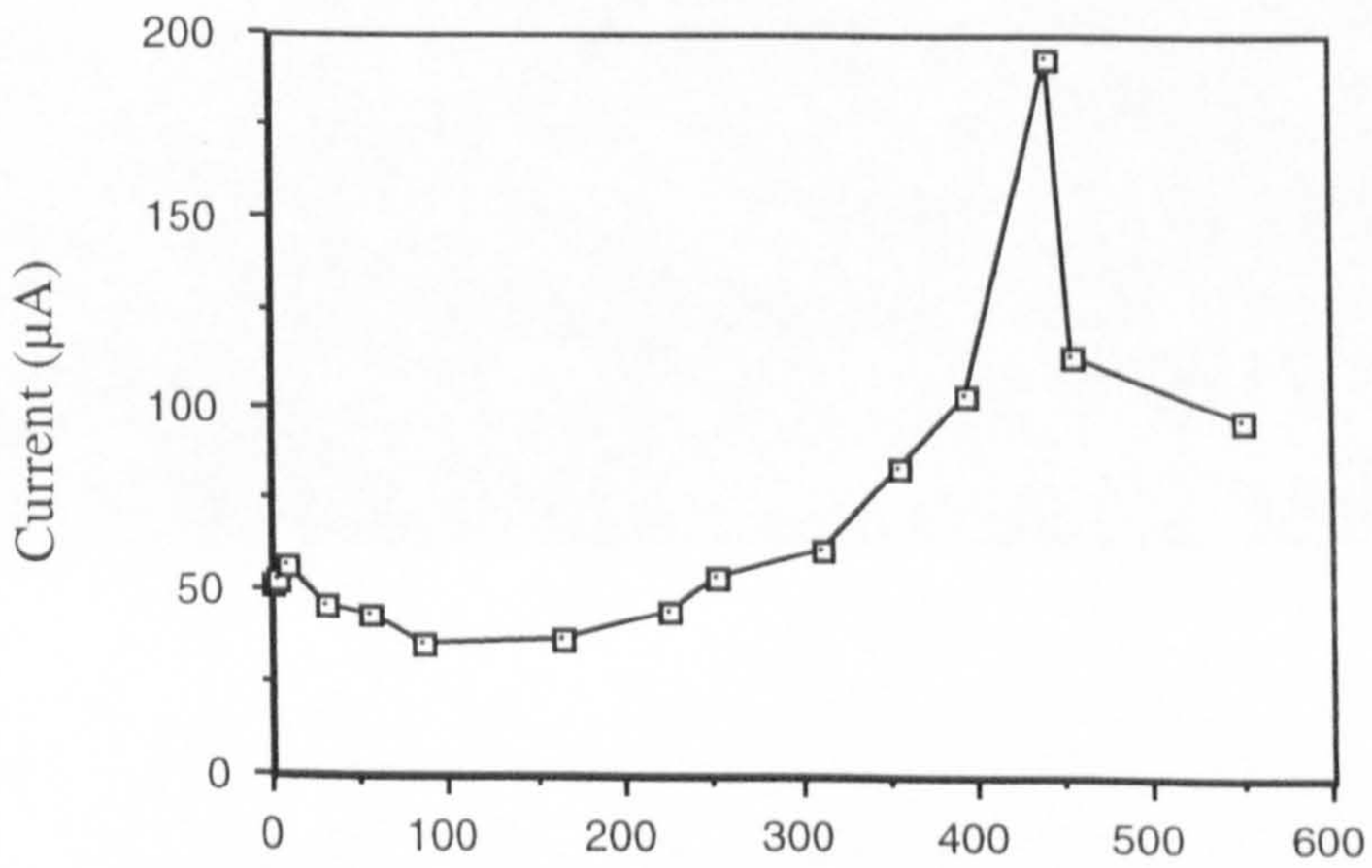


Fig. 4.18. Potentiostatic test on 25 Cr duplex at a potential of +100mV (SCE). Current progression versus time.

In a control experiment where the potential of the 25Cr duplex alloy was held constant in *static* sea water at 50°C, no increase in current was observed. High currents were recorded before the jet was started on SAF 2205 as it had already reached it's breakdown potential and so the effect of the jet was to further increase the current. On the 25Cr duplex material however, under jet conditions, the current maintained a steady value of 50-60μA for a period of 6 hours followed by a small rise to 110μA but this rise was not continued. Only a very faint surface film was present on the 25Cr duplex specimen after jet impingement and no localised effects were observed whereas a thicker film was present on SAF 2205 and pitting attack had occurred in the form of the now familiar "comet" arrangement. Fully developed pits on SAF 2205 were revealed beneath the corrosion products at the head of the comet once the surface film and corrosion products had been removed intentionally after the test (Fig. 4.19)

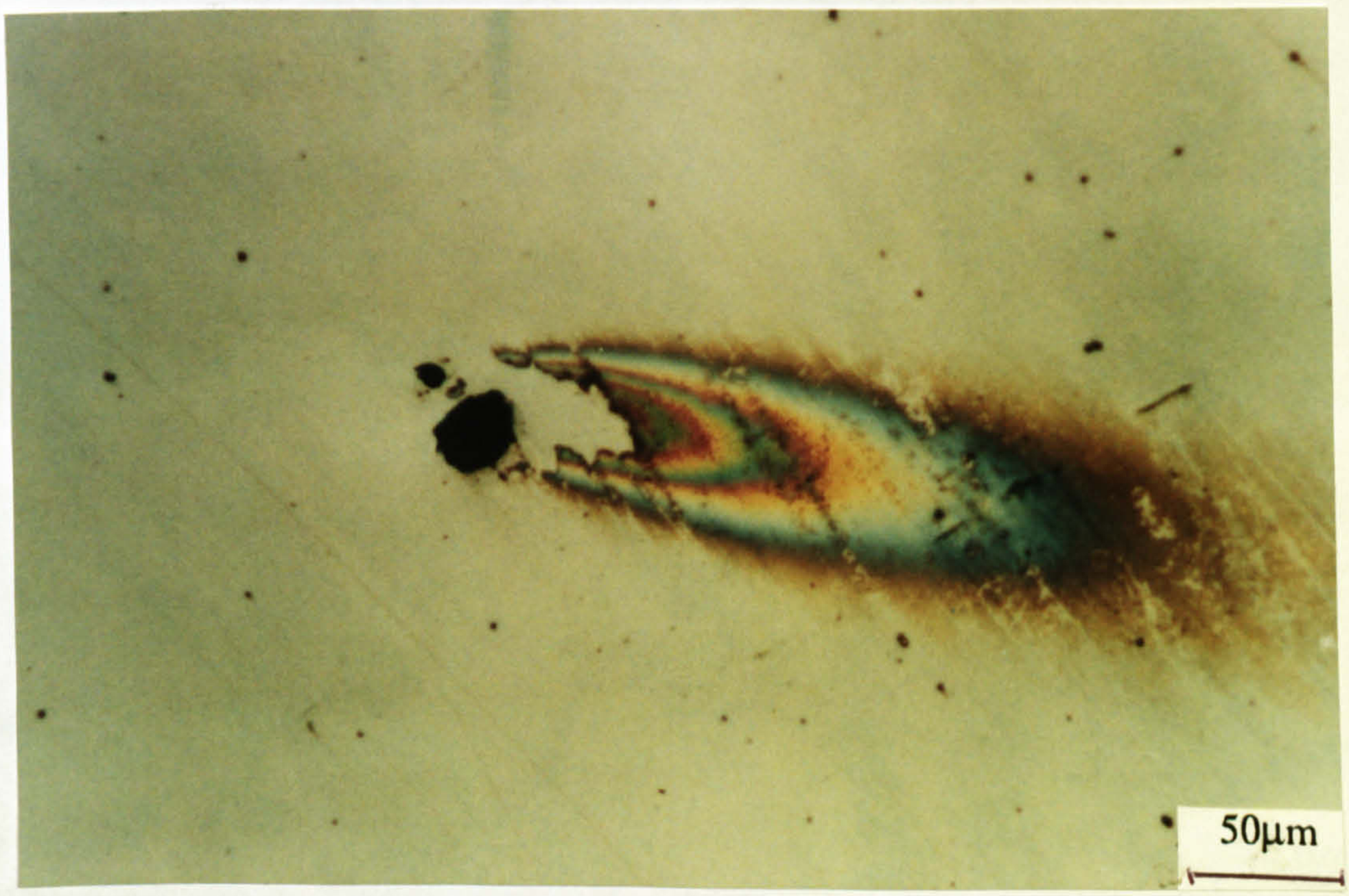


Fig 4.19. Pitting at the head of a 'comet' after corrosion products are removed on SAF 2205 after potentiostatic test at 100mV (SCE)

.

Further potentiostatic tests involved carrying out a standard anodic polarisation scan on the superduplex, and the superaustenitic alloys, under jet conditions at 50°C, until $E_p$ was reached. The potential was then held constant and again the current recorded with time. Figure 4.20 illustrates that, at constant potential $E_p$, the current initially dropped but in both cases was followed by a sharp rise and then a further decrease. During this rise a coloured film was seen to develop on the surface which proceeded to change colour as the current increased. In the subsequent region where the current dropped significantly, no changes were observed. After these potentiostatic tests, numerous pits were observed on the superduplex sample, and fewer on the superaustenitic specimen. In contrast to the pitting appearance after a complete anodic polarisation, here no comets existed, simply a small pit centred within a discontinuity in the film. This implied that only a small amount of corrosion products was formed at the pit mouth and their removal did not cause sufficient erosion of the preformed film.

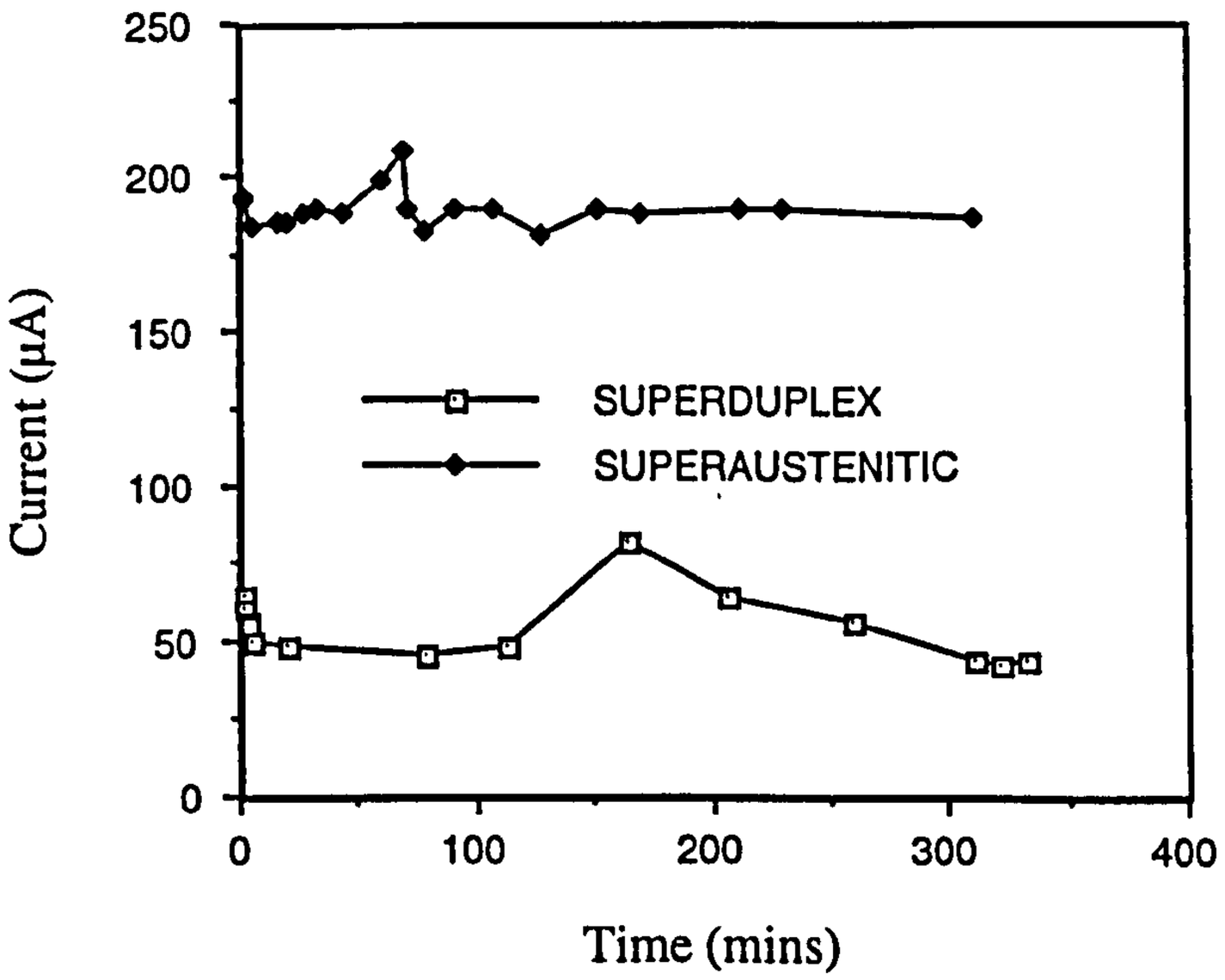


Fig. 4.20. Potentiostatic test, current versus time, for UNS S31254 and UNS S32760 at Ep

Several tests under erosion conditions were performed where the anodic scan was stopped at certain points and the specimen examined. Points of interest included the $E_p$ potential where the current had achieved its maximum, the $E_b$ potential and the reversal current of 500μA. From these tests, the association of electrochemical features with corrosion attack could be identified. The attack mechanisms associated with $E_p$ were identified as pit initiation (but not propagation) in conjunction with the formation of the coloured films. Thus the pits formed at $E_p$ were shallow and did not appear within the "comet" configuration. Further propagation of pitting attack was not observed until $E_b$ was attained and the current had increased significantly. An anodic polarisation on

UNS S31603 was carried out up to potential $E_b$, at which point the potential was allowed to continue to increase until an anodic current of 10mA was attained and the specimen was examined afterwards. It was concluded that the region at potentials more positive than $E_b$ is associated with pit propagation as illustrated by the severe comet pitting on the specimen (Fig. 4.21).

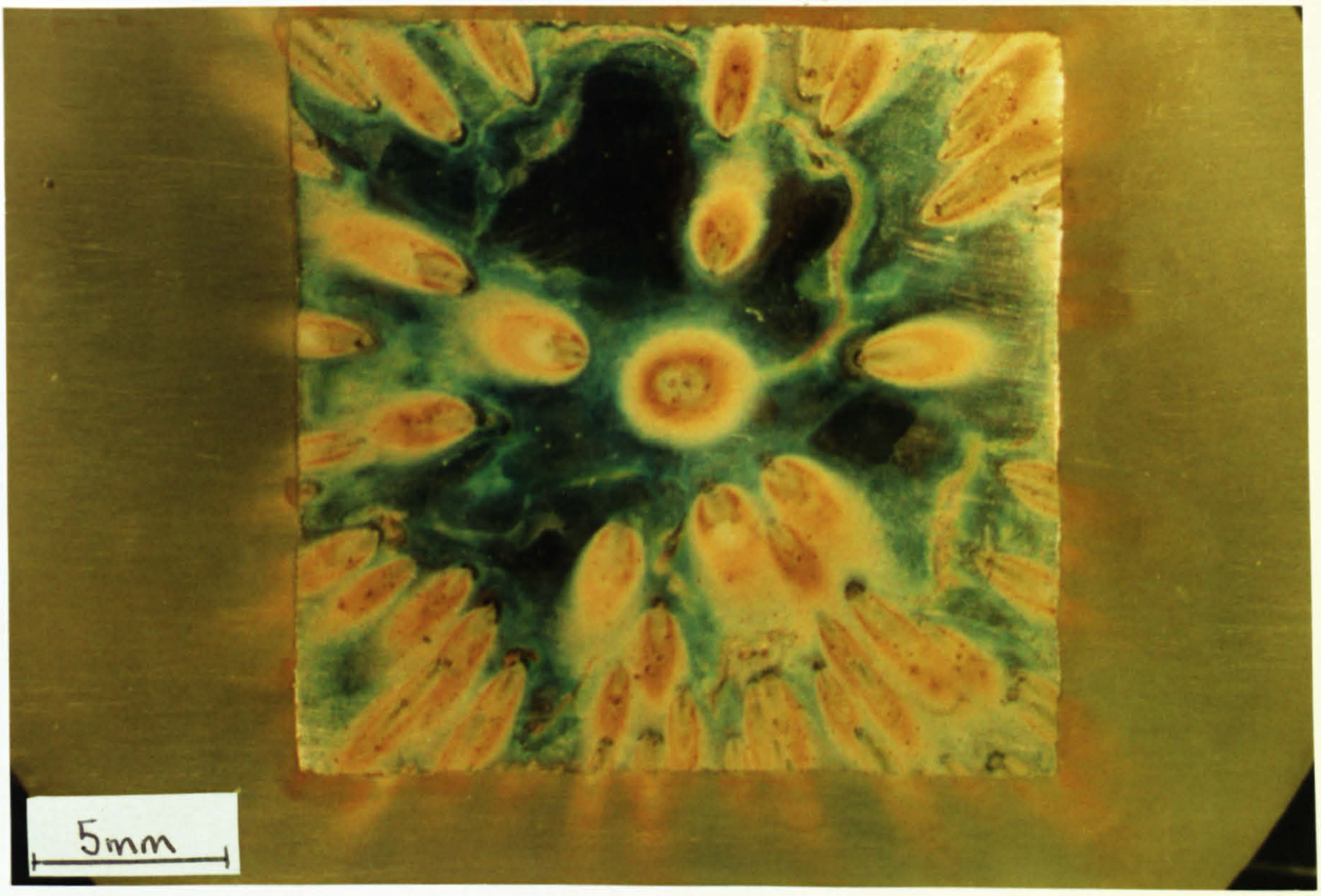


Fig 4.21. Severe pitting on UNS S31603 after high anodic currents under liquid erosion

At this point (above the potential $E_b$), crevice attack on those materials affected was also shown to be present. Where pits did not develop into "comets", the mode of attack was shown to be primarily crevice attack once $E_b$ had been attained.

**Cathodic Polarisation**

Cathodic polarisation experiments conducted under the hydrodynamic conditions imposed by the impinging jet at 100m/s, at temperatures in the range of 18°C and 50°C showed significant differences compared to static conditions. There was no initial potential range where low currents were recorded but instead the currents increased at a significant rate on shifting the potential from $E_{corr}$. The second Tafel region, shown in Fig. 4.22 by a disinct change in slope at a potential of approximately -600mV, proceeded until currents of 1500$\mu A/cm^2$ were recorded, signifying the end of the test. The Tafel slope was not comparable with the Tafel slope recorded for hydrogen evolution in chapter 2 as shown in Table 4.6.

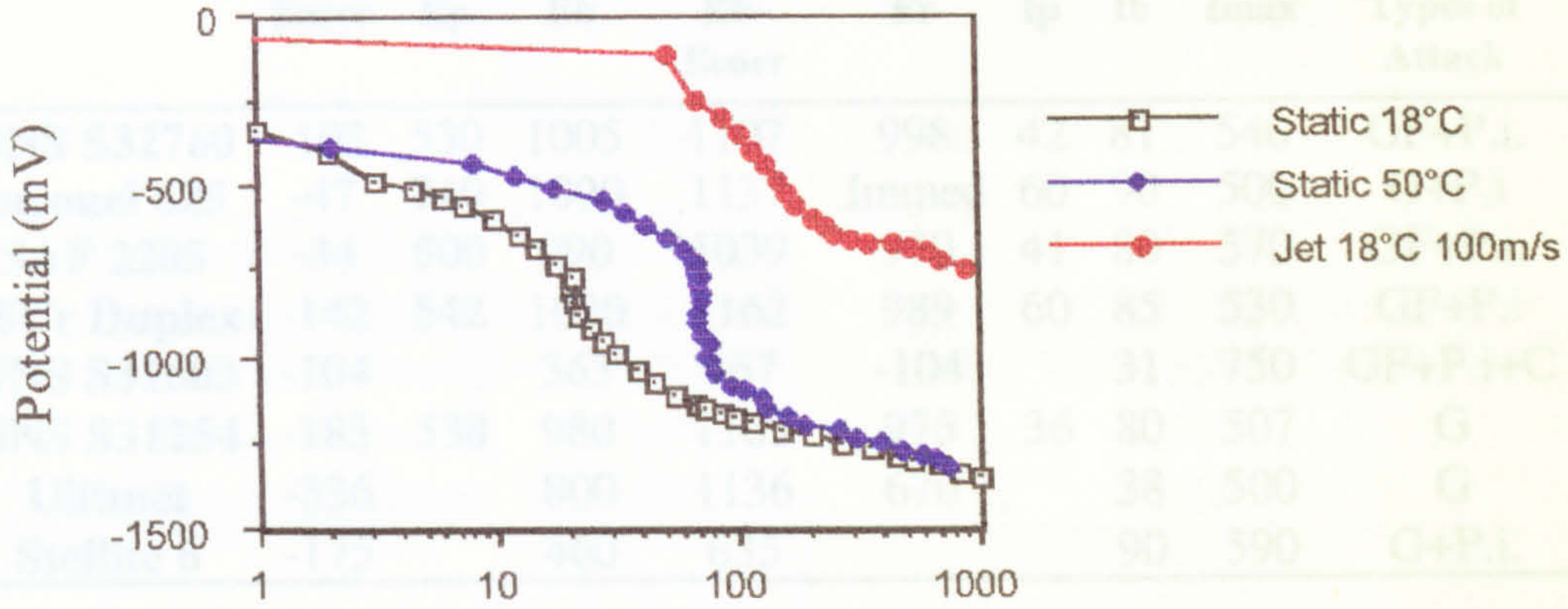


Fig. 4.22. Cathodic polarisation on UNS S32760 under liquid impingement and static conditions

Thus, in contrast to the quiescent sea water, concentration polarisation effects were not observed at current levels of between 5 and 30μA as observed in static sea water for the stainless steels but instead the reaction followed a linear E-log i relation. Depolarisation of the cathodic reaction as the temperature increased still occurred for all materials but the effect was less pronounced than in static conditions, shown in Fig. 4.23 for UNS S31603 stainless steel at 18°C and 50°C. However, consideration must be given to the fact that under jet conditions the cathodic current was substantially larger than in static conditions and so the scope for depolarisation due to temperature effects was less.

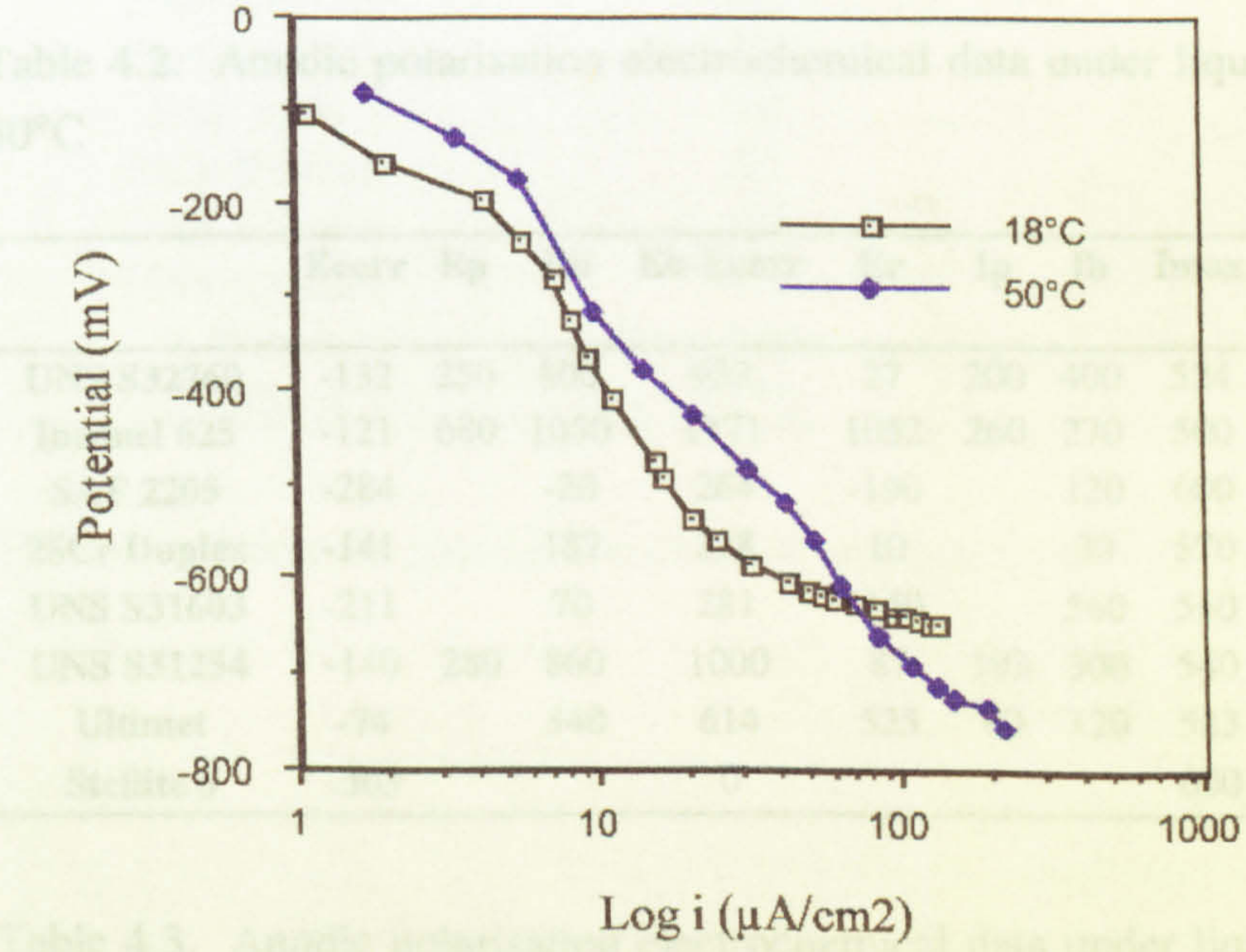


Fig. 4.23. Cathodic polarisation under impingement conditions on UNS S31603

| | Ecorr | Ep | Eb | Eb-Ecorr | Er | Ip | Ib | Imax | Types of Attack | Crevice |
|---|---|---|---|---|---|---|---|---|---|---|
| **UNS S32760** | -102 | 530 | 1005 | 1107 | 998 | 42 | 81 | 540 | GF+P.i. | |
| **Inconel 625** | -47 | 740 | 1090 | 1137 | Immed | 60 | 90 | 500 | G+P.i | |
| **SAF 2205** | -34 | 500 | 990 | 1039 | 970 | 41 | 80 | 570 | GF+P.i. | |
| **25Cr Duplex** | -142 | 542 | 1020 | 1162 | 989 | 60 | 85 | 530 | GF+P.i | |
| **UNS S31603** | -104 | | 363 | 467 | -104 | | 31 | 750 | GF+P.i+C | 4mm |
| **UNS S31254** | -183 | 538 | 980 | 1163 | 975 | 36 | 80 | 507 | G | |
| **Ultimet** | -336 | | 800 | 1136 | 670 | | 38 | 500 | G | |
| **Stellite 6** | -175 | | 460 | 635 | | | 90 | 590 | G+P.i. | |

Table 4.1. Anodic polarisation electrochemical data under liquid erosion conditions at 18°C

**P.i.**-pit initiation **GF**-General coloured film **C**-Crevice attack **G**-General attack

**Immed.**-Immediate repassivation

| | Ecorr | Ep | Eb | Eb-Ecorr | Er | Ip | Ib | Imax | Types of Attack | Crevice | M.P.D | Ia |
|---|---|---|---|---|---|---|---|---|---|---|---|---|
| **UNS S32760** | -38 | 380 | 946 | 984 | 900 | 64 | 87 | 540 | P.i+GF | | | |
| **Inconel 625** | -67 | 710 | 1061 | 1128 | Immed. | 75 | 95 | 500 | GF+C | <1mm | | |
| **SAF 2205** | -240 | 409 | 880 | 1120 | -230 | 90 | 200 | 540 | GF+P+C | 8-10mm | 0.015mm | 410 |
| **25Cr Duplex** | -104 | 390 | 920 | 1024 | | 83 | 205 | 570 | GF+P+C | 10-11mm | 0.013mm | 260 |
| **UNS S31603** | -94 | | 120 | 214 | -94 | | 47 | 700 | GF+C | 12-14mm | | |
| **UNS S31254** | 181 | 500 | 995 | 814 | 950 | 30 | 60 | 510 | GF+P.i. | | | |
| **Ultimet** | -55 | | 660 | 715 | 650 | 75 | 113 | 515 | G | | | |
| **Stellite 6** | -152 | | -32 | 120 | | 80 | | 600 | P | | 0.011mm | |

Table 4.2. Anodic polarisation electrochemical data under liquid erosion conditions at 30°C

| | Ecorr | Ep | Eb | Eb-Ecorr | Er | Ip | Ib | Imax | Types of Attack | Crevice | M.P.D | Ia |
|---|---|---|---|---|---|---|---|---|---|---|---|---|
| **UNS S32760** | -132 | 250 | 800 | 932 | 27 | 200 | 400 | 524 | GF+C+P | 5mm | 0.006mm | 880 |
| **Inconel 625** | -121 | 680 | 1050 | 1171 | 1052 | 260 | 270 | 500 | GF+C+P.i. | <1mm | | |
| **SAF 2205** | -284 | | -20 | 264 | -190 | | 120 | 600 | GF+P+C | 12mm | 0.011mm | |
| **25Cr Duplex** | -141 | | 187 | 328 | 10 | | 30 | 570 | GF+P | | 0.013mm | |
| **UNS S31603** | -211 | | 70 | 281 | -150 | | 560 | 560 | GF+P+C | 16mm | 0.0108m | |
| **UNS S31254** | -140 | 280 | 860 | 1000 | 87 | 193 | 300 | 540 | GF+P.i | | | 500 |
| **Ultimet** | -74 | | 540 | 614 | 525 | 80 | 120 | 523 | G | | | |
| **Stellite 6** | -363 | | | 0 | | | | 600 | GB | | 0.012mm | |

Table 4.3. Anodic polarisation electrochemical data under liquid erosion conditions at 50°C

| | Cr | Co | W |
|---|---|---|---|
| Area 1-inside grain | 72% | 15% | 0.16% |
| Area 2-at edge of grain | 64% | 16% | 0.20% |
| Area 3-on bulk material | 22% | 68% | 4.30% |
| Stellite 6 bulk chemical | 28% | 66% | 4.25% |
| On untested Stellite 6 | 31% | 54% | 0.70% |

Table 4.4. Chemical analysis of regions 1, 2, and 3 on Stellite 6 in Fig. 4.11b.

| | UNS S32760 | UNS S31254 | Inconel 625 |
|---|---|---|---|
| **Cu** | 5% | 4.80% | 0.10% |
| **Mn** | 8.60% | 5.20% | 0.20% |
| **Cr** | 17% | 13.40% | 3.50% |
| **Fe** | 33% | 33% | 15% |
| **Ni** | 3.50% | 10% | 2.10% |
| **Mo** | 2.50% | 6.70% | 16% |
| **O** | 25% | 24% | 24.50% |

Table 4.5. Average film composition of coloured film produced during anodic polarisation in liquid erosion conditions

| | 2nd Tafel Slope (mV/decade) |
|---|---|
| **UNS S32760** | -65 |
| **Inconel 625** | -50 |
| **SAF 2205** | -70 |
| **25Cr Duplex** | -80 |
| **UNS S31603** | -80 |
| **UNS S31254** | -75 |
| **Ultimet** | -110 |
| **Stellite 6** | -110 |

Table 4.6. Cathodic polarisation characteristics in liquid erosion conditions at 18°C

**Discussion - Anodic Polarisation**

In hydrodynamic systems, materials are often subjected to high velocity flow in pipes, valves and pumps as examples and the effect of liquid impingement on the electrochemical corrosion behaviour and on the mechanical material degradation processes is important. This study has focused on an impinging flow at an extremely high velocity (100m/s) which is above typical fluid velocities in most engineering systems but is representative of upper velocities encountered in geometric irregularities where impingement may occur. Also it is of the same order of magnitude as the estimated micro-jet impinging velocities which exist during cavitation bubble implosion.

Under erosion conditions, electrochemical ranking (based on $E_b$ and $E_b$-$E_{corr}$) produced the ordering as in Fig. 4.24 where it can be seen that as under static conditions, at ambient temperature, very little difference could be detected between the duplex and superaustenitic stainless steels. An important observation is the increased susceptibility of UNS S31603 to passivity breakdown, even at 18°C, compared to static conditions and this shows that there is a threshhold velocity, above which the material performance is detrimentally affected. Work by Todd [34] has shown that at 40m/s, the resistance of UNS S31603 to corrosion is good. In this study, the behaviour of Inconel 625 using the electrochemical parameter, $E_b$, as the assessing factor was comparable with the four superior materials.

At 50°C however, using the same criteria, the material ranking was rearranged and clear distinctions in electrochemical behaviour between each material were apparent. At higher temperatures, the erosion-corrosion resistance of all the materials was lower than at 18°C with the vulnerability of the lower-alloyed stainless steels and Stellite 6 being especially increased and the Ni-base alloy, superaustenitics and superduplexes affected to a lesser extent.

The attack on Stellite 6 was concentrated at the grain boundary regions in the form of pitting attack which proceeded to dislodge the material in the grain boundary region. Microanalysis showed enrichment of Cr at the grain boundaries in the as-received state which was enhanced after a period under liquid impingement conditions and anodic polarisation. Within the attacked grain boundaries, no significant variations in chemical composition were recorded but it is accepted that the rough surface on which the EPMA was carried out is not entirely suitable for identifying small variations in composition. It is suggested that, typical of intergranular corrosion of stainless steels, regions

depleted in Cr accompany the detected areas enriched in Cr and the lower Cr regions are more susceptible to attack by corrosion. Moreover the brittle areas enriched in Cr are affected by the high velocity flow and this leads to attack at the grain boundaries being a combined result of mechanical effects and corrosion effects.

**MATERIAL RANKING UNDER EROSION CONDITIONS**

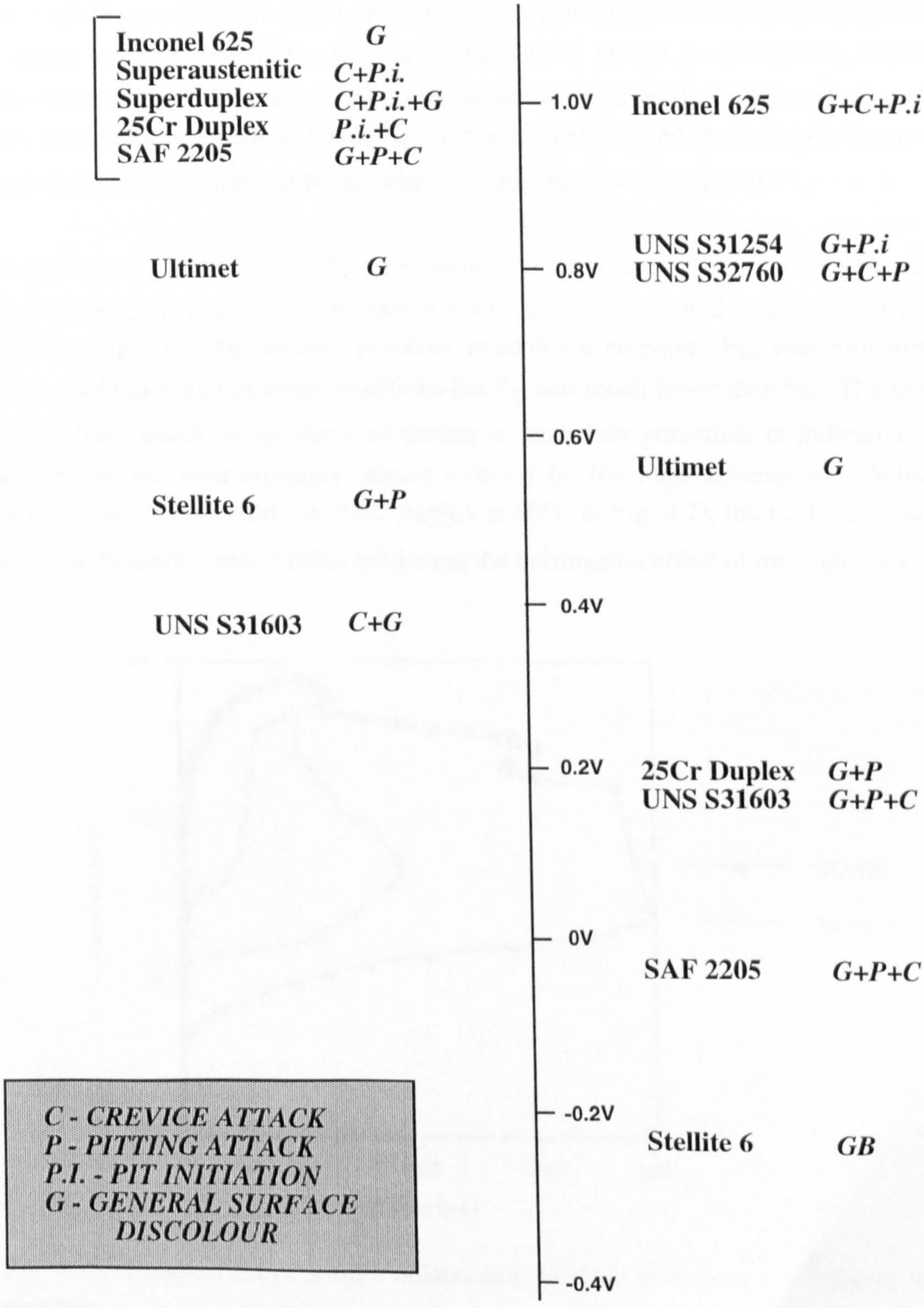


Fig. 4.24. Material ranking in liquid erosion conditions

Comparison of the behaviour of the materials under static and erosion conditions at elevated temperatures suggests that pit initiation occurred at a more active potential under the severe impingement conditions. However, it was apparent that pit propagation during the transient anodic polarisation scan was retarded since under erosion conditions the MPD for a particular material (measured using light-microscopy techniques) at a certain temperature was invariably smaller than in static conditions, although there were evidently more pitted sites. It is suggested that pit propagation was retarded by the removal of corrosion products from the pit mouth thereby eliminating the sheltered conditions which would facilitate the creation of a cell for pit propagation. The correlation between MPD and $I_{max}$ was further verified by the lower $I_{max}$ values recorded under erosion conditions where pitting attack was observed.

Comparison of complete anodic polarisation curves under static and erosion conditions showed that, where a primary breakdown was observed (i.e. on the superduplex alloy, at 50°C in Fig 4.25, the eventual passivity breakdown potential, $E_b$, was comparable or more noble than that in static conditions but $E_p$ was much lower than $E_b$. The initiation of localised attack in the form of pitting at such low potentials is indicative of the severity of the hydrodynamic impact induced by the high velocity jet. Where the feature was not observed (i.e. 25Cr duplex at 50°C in Fig. 4.7), the $E_b$ in jet conditions was significantly lower, further indicating the detrimental effect of the high velocity jet.

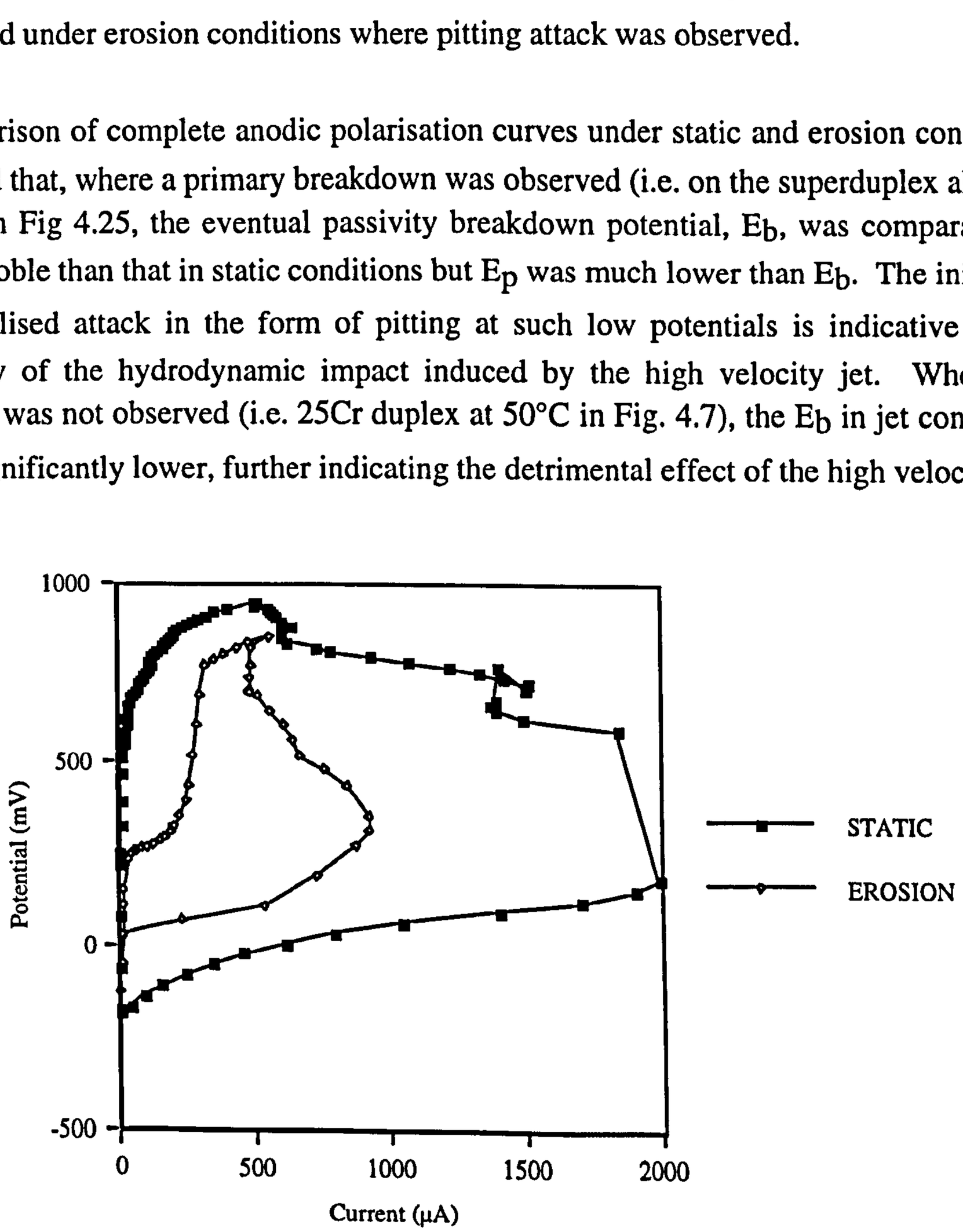


Fig. 4.25. Comparison of anodic polarisation in static and erosion conditions on UNS S32760

Two possible alternatives were suggested to explain the formation of relatively thick coloured oxide films at $E_p$ or $E_b$. Either the $Cr_2O_3$-rich thin passive layer could, under the severe high-velocity flow and applied potential, break down to form a different, much thicker corrosion product or alternatively the conditions enabled the formation of a deposit, via electrodeposition, onto the substrate from metal ions in the sea water.

Since analyses, initially on the stainless steels, showed concentrations of Cu and Mn not typical of the material composition, it was considered possible that metal ion contamination of the sea water (possibly from a corroding phosphor-bronze impeller in the low-pressure pump) was the cause of deposition onto the specimen. Replacement of the low-pressure pump by one containing all stainless steel internal components ensured that in no part of the flow system did the water come into contact with components that were likely to cause contamination. Anodic polarisation scans carried out (and taken to high currents) in the completely stainless steel rig in distilled water still produced the surface films and water analysis on distilled water samples taken before and after circulation in the erosion rig using atomic absorption spectroscopy to determine Cu and Mn content both showed very small levels (0.04mg/l and <0.2mg/l respectively). Later, detection of high Mo levels on Inconel 625 using EPMA further confirmed that the formation of the film was not due to contamination in the liquid flow.

The chemical thermodynamics of the proposed film formation was considered and calculations of the equilibrium electrode potential ($E_o$) for the $Cu^{2+}/Cu$ and $Mn^{2+}/Mn$ half reactions were made for the experimental conditions. It was shown that the potentials at which the films typically form ($E_p$ or $E_b$) are significantly more positive than $E_o$ for both reactions thus suggesting that cathodic deposition under these specific conditions is not thermodynamically favourable (see Fig. 4.26).

Consideration was then given to the work of Vetter [35] relating to the formation and reduction of oxide layers in an attempt to correlate the increases in current to the formation of oxygen via an anodic reaction. Anodic oxygen formation takes place on metals which are covered by a very thin layer of oxide in the presence of small anodic currents. His work distinguished between anodic oxygen formation which occurs at low anodic currents, the product of which forms a chemisorbed layer on the surface and oxygen evolution in which appreciable currents are recorded and which requires a large overvoltage (typically 0.4V). Equilibrium electrode potentials for the *formation* of oxygen, calculated for the conditions in this work, closely correspond to those at which $E_p$ occurred in the temperature range 18°C and 30°C. At 50°C however, current

increase was recorded at less positive potentials than $E_o$ for oxygen production. Hence at 50°C the formation of oxygen could not explain the emergence of the anodic current increase, implying that also at the lower temperatures this does not play a part.

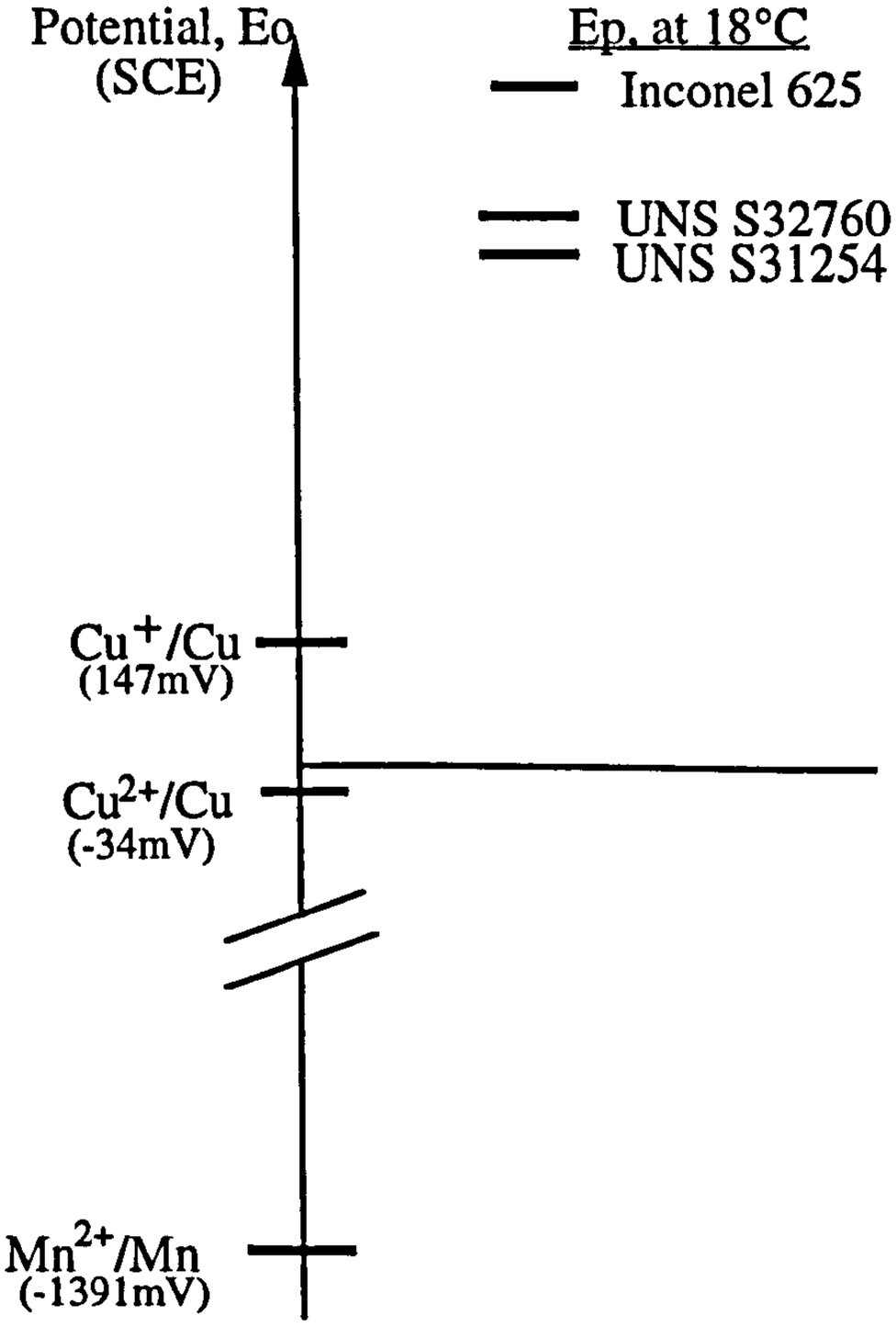


Fig. 4.26. Equilibrium potentials for Cu and Mn cathodic deposition half reactions and $E_p$ values obtained at 18°C under liquid impingement conditions

Microscopical examination of specimens after polarisation to $E_p$, and above $E_p$, confirmed that the processes of pit initiation and formation of the coloured oxide film could not be isolated from each other. This implies that the electrochemical feature $E_p$ represents a composite, interactive effect of pit initiation and coloured film formation.

The anodic increase in current was then thought to consist of two components. The first and the most important from a practical viewpoint is the initiation of pitting and the resulting dissolution of metal at such sites, releasing metal ions into the solution. The second is then representative of the component responsible for the formation of the oxide film which is thought to be via a reaction of the type:

$$MnO_2(s) + 4H^+ + 2e \rightarrow Mn^{2+} + 2H_2O$$

which, in the conditions of our experiments, has $E_o$ values which drive the reaction in the anodic direction. The mechanism by which the film is ultimately enriched in some elements of the metal composition may be explained from the knowledge that pitting susceptibility increases at non-metallic (e.g. Mn-rich) inclusions and discontinuities in the passive film but this could also involve selective dissolution of alloying elements such as Mn, Cu or Mo at the depassivated sites where pitting initiates and could represent the selective dissolution as reported by Postlethwaite [36] for Mo in chloride containing media. The observed stabilisation of the current may represent a steady state condition where the sites of pit initiation are continually being created but the formation of the oxide film to repassivate the active areas occurs simultaneously.

A feature of the above mechanism is that it is in accordance with the observed occurrence of the coloured film under impingement conditions only since (in contrast to static conditions) corrosion products at the initiated site cannot be retained in-situ and an occluded site does not become established. Thus the corrosion products are available to precipitate an oxide outwith the pit and severe pit propagation does not occur (again in accordance with the observation under impingement conditions); indeed repassivation is favoured because the local chemistry within the pit does not become more aggressive. Further evidence to support the linkage of the pit initiation process to the formation of the coloured film comes from observations that, where no pitting was observed on Inconel 625 at 18°C under erosion conditions, no coloured film was observed. Also at 50°C, the only material not showing susceptibility to pitting attack was Ultimet which also failed to produce a current peak at $E_p$ and a coloured film.

Although significant from an electrochemical viewpoint the production of the coloured oxide film at and above the potential $E_p$ is of very limited practical importance. The production of the film has been shown to be limited to a thickness of less than 1μm. Of greater potential importance, evidence of pit initiation at potentials much lower than the breakdown potential recorded in static sea water illustrates how effective the impingement is in initiating localised attack but propagation seems to be retarded. Hence conflicting actions appear to complicate the rate and mechanisms of attack under the high velocity flow.

**Cathodic Polarisation**

Under the severe hydrodynamic conditions of liquid impingement, concentration polarisation effects were no longer a factor controlling the progression of oxygen reduction. The superduplex alloy cathodic polarisation curve (Fig. 4.23) was severely

depolarised and the oxygen-reduction reaction proceeded to attain currents of $1500\mu A/cm^2$ and no concentration polarisation effects were observed. The increased turbulence at the electrode surface induced mixing of the concentration boundary layer which exists in static conditions ensuring that oxygen was constantly supplied. On removing the jet during cathodic polarisation (at point **A** on Fig. 4.27), the cathodic current immediately dropped off to quickly reach values comparable to $i_L$ in static conditions. Thus the two Tafel regions are assumed to be representative of the oxygen reduction process, by a two step process as was postulated in chapter 2.

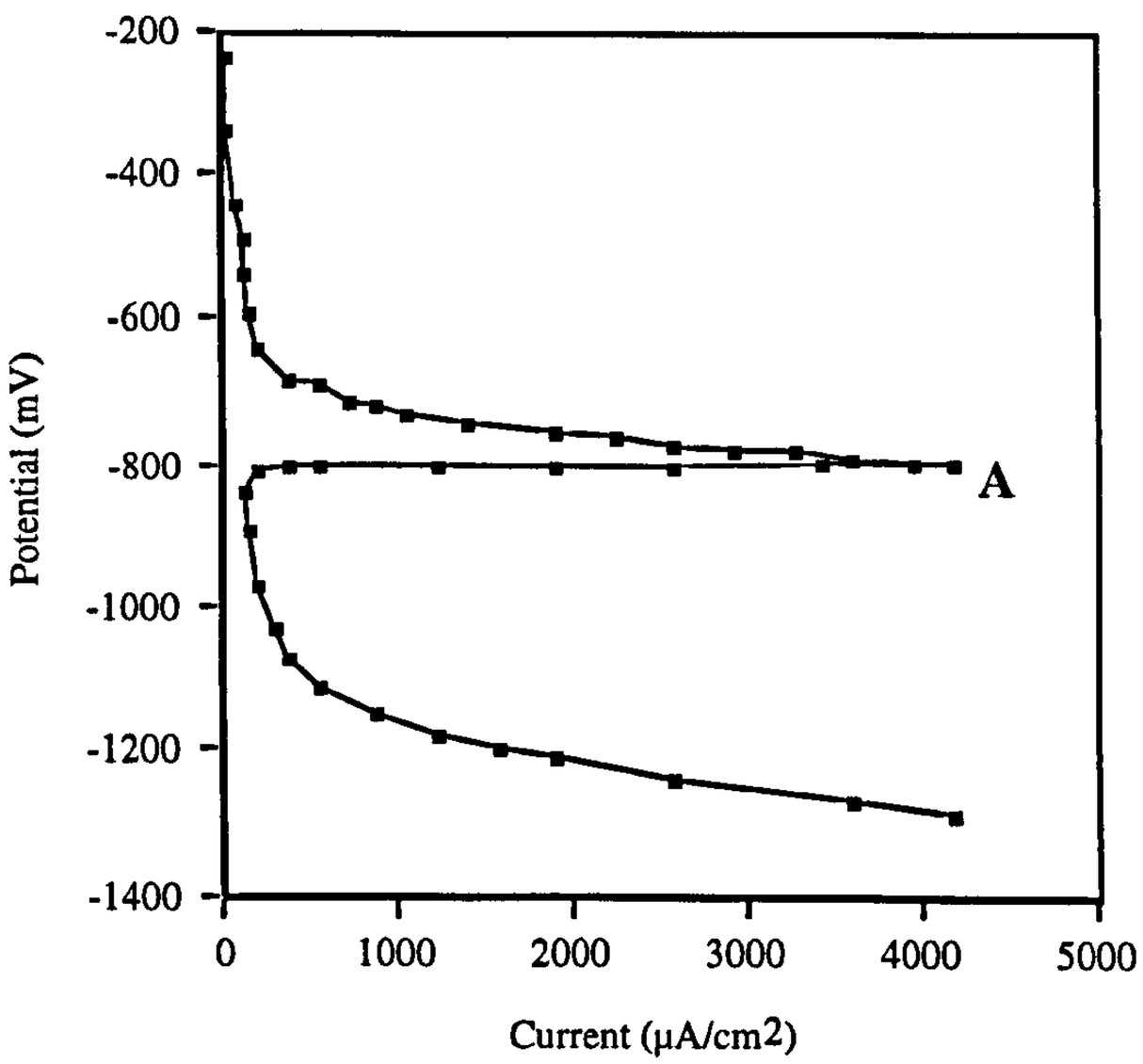


Fig 4.27. Cathodic polarisation under liquid impingement at 100m/s until point **A** where impingement is stopped

Lowering of the velocity of the jet to 25m/s proved that there is a threshold velocity required to overcome the concentration polarisation effects since at this velocity on SAF 2205 duplex at 18°C a limiting current of $150\mu A/cm^2$ was attained. The cathodic oxygen-reduction reaction is therefore influenced by the supply of reactants to the surface due to the turbulence and also the rate of consumption at the surface, determined by the reaction kinetics.

Although the cathodic reaction rate is a factor determining the rate of corrosion propagation, in the conditions of the high velocity impingement, the situation is further complicated since it is necessary to consider the conflicting effect of increased

turbulence in removing the occluded conditions which in static conditions facilitate the propagation of localised attack.

## General Hydrodynamic Discussion

The joint effects of liquid erosion and aqueous corrosion in this study has yielded information to suggest that corrosion is more readily initiated under an impinging jet, yet the jet facilitates reduced propagation rates. These observations point to the fact that in such a system, there are numerous hydrodynamic and electrochemical factors to dictate the type and rate of reaction.

Electrochemically, the anodic reaction (metal dissolution) in the passive region has been shown to increase (with evolution of $E_b$) and similarly the cathodic reaction is depolarised. Hence a major effect of the jet is to stimulate the electrochemical processes. Another possible interaction of the jet is the mechanical damage it can impose by the pressure at the point of impact and the shear stresses in the wall jet region. In this system, the pressure has been estimated as 150MPa at the point of impact and the maximum shear stress as 0.104MPa at a distance, x, of 1.05mm (Fig 4.3). According to microscopical examination, no detrimental effect on the surface of the materials was observed after periods of up to 8 days impingement. Only once corrosion had been induced via electrochemical techniques was the effect of the jet apparent (by removing corrosion products from pits etc.). It is therefore postulated that although the mechanical effects were not apparent in the short term, once corrosion in a real engineering system initiates, the mechanical effects become very important. The case in this study where the mechanical effects, in the short term were of insufficient magnitude to rupture the passive film on the stainless steels and related alloys a 18°C and 30°C, the situation is one of mass transfer affected corrosion in which the turbulence of the jet plays an important role. However, at 50°C the initial active behaviour of Stellite 6 suggests that its passive film integrity is reduced at such a high temperature and in this case, there are combined mechanical erosion and corrosion effects.

## Conclusions

The effect of the high velocity impingement on the corrosion resistance of the materials at ambient temperature was illustrated by:-

- lower $E_b$ on all except Inconel 625 and Ultimet

- evidence of double breakdown on some materials during anodic scans with the first breakdown, $E_{p.}$, occurring in conjunction with the initiation of pits and formation of a coloured oxide film but not leading to severe metal loss

- more pits (in the form of "comets") evident than in static conditions

On increasing the temperature under impingement conditions, the detrimental effects were illustrated by:-

- pitting attack initiated at the relatively negative potential, $E_p$

However, for impingement conditions in comparison to static sea water:-

- pit depths were lower at the same temperature signifying retarded localised corrosion propagation

- repassivation occurred at a more positive potential than in static conditions after reversal of the anodic scan

With respect to materials comparison, this study has illustrated that under the combined effect of high temperature and a high velocity flow, the materials which resist significant attack on a localised level are the nickel-based Inconel 625, the cobalt-based Ultimet and the superaustenitic alloy. Indeed Inconel 625 has displayed excellent resistance to localised corrosion over the entire temperature range 18-60°C and a superior resistance to loss of passivity in impingement than in static conditions. As a group, the duplex stainless steels significantly lose resistance to passivity breakdown as the temperature exceeds 40°C, more so than the superaustenitic alloy. Drastic reductions in the corrosion resistance of Stellite 6 have been observed with even modest temperature increases above ambient. Moreover this material becomes particularly susceptible to attack at 30°C and 50°C under jet conditions - this is relevant considering that Stellite 6 is chosen for wear resistance.

**References**

1 E. Heitz. Chemo-mechanical effects of flow on corrosion, *Corrosion*, Vol. 47, No. 2. 1991

2. T. J. Glover, Recent developments in corrosion-resistant materials for construction of seawater pumps, *Mat. Perf.*, July 1988

3. B. Todd, Corrosion and materials selection in seawater systems, *I. Mech. E Publications*, 1979

4. V. G. Levich, *Physicochemical Hydrodynamics*, Prentice-Hall, Englewood Cliffs, NJ, 1962

5. B. T. Ellison, W. R. Schmeal, Corrosion of steel in concentrated sulphuric acid, *J. Electrochem. Soc.*, Vol. 125, p524, 1978

6. B. K. Mahato, C. Y. Cha, L. W. Shemilt, Unsteady state mass transfer coefficient controlling steel pipe corrosion under isothermal flow conditions, *Corros. Sci.*, Vol. 20, p421,1980

7. D. C. Silverman, Rotating cylinder electrode for velocity sensitivity testing, *Corrosion*, Vol. 40, No. 5, p220, 1984

8. T. K. Ross, G. C. Wood, I. Mahmud, The anodic behaviour of iron-carbon alloys in moving acid media, *J. Electrochem. Soc.*, Vol. 113, p334, 1966

9. D. C. Silverman, Rotatng cylinder electrode - geometry relationships for prediction of velocity sensitive corrosion, *Corrosion*, Vol. 44, No. 1, p43, 1987

10. J. Weber, Flow induced corrosion : 25 years of industrial research, *Brit. Corros. J.*, Vol. 27, No. 3, 1992

11. J. O'M, Bockris, *Comprehensive treatise of electrochemistry,* Vol. 6 :1983, New York, Plenum Press

12. B. C. Syrett, S. S. Wing, Effect of flow on corrosion of copper-nickel alloys in aerated seawater and in sulphide polluted seawater, *Corrosion*, Vol. 36, 1980, p73

13. F. L. Laque, J. F. Mason, *Proc. Am. Petroleum Inst.*, Div. Refining, 1950, 30M, 103

14. E. Heitz, G. Kreysa, C. Loss, *J. Appl. Electrochem.*, Vol. 9, 1979 p243-253

15. G. A. Schmitt, W. Bruckhoff, K. Faessler, G. Blummel, Flow loop versus rotating probes - experimental results and service applications, *Mater. Perf.*, February 1988

16. A. Momber, R. Kovacevic, Fundamental investigations on concrete wear by high velocity water flow, *Wear,* 177 (1994) 55-62

17. H. Rieger, in A. A. Fyall (ed.), *Proc. 2nd Int. Conf. on Rain Erosion and Allied Phenomena*, Royal Aircraft Establishment, Farnborough, 1970, p907

18. C. M. Preece, J. H. Brunton, A comparison of liquid impact erosion and cavitation erosion, *Wear*, 60 (1980), 269-284

19. F.G. Hammitt, F. J. Heymann, Liquid-erosion failures, *ASM Metals Handbook,* Vol. 10, 8th Ed. pg160-167

20. F. G. Hammitt, J. B. Huang, T. M. Mitchell, D. O. Rogers, E. E. Timm, in A. A. Fyall and R. B. King (eds), *Proc. 3rd Int. Conf on Rain Erosion and Allied Phenomena*, Royal Aircraft Establishment, Farnborough, 1970, p907

21. F. W. Gardner, *Engineer*, 153 (1932) 146, 202

22. P. de Haller, La corrosion par cavitation et par choc de gouttes liquides, *Schweitz. Arch.*, 6 (1933) 61

23. W. F. Adler, Particulate damage predictions, *Presented at the 8th In. Conf. on Erosion by Liquid-Solid Impact*, Cambridge, Sept. 1994

24. C. S. J. Pickles, C. R. Seward, J. E. Field, Important considerations in the simulation of high velocity rain erosion, *Presented at the 8th In. Conf. on Erosion by Liquid-Solid Impact*, Cambridge, Sept. 1994

25. F. J. Heymann, *J. Appl. Phys.*, 40 (1969) 5113

26. M. C. Rochester, J. H. Brunton, in A. A. Fyall and R. B. King (eds), *Proc. 3rd Int. Conf on Rain Erosion and Allied Phenomena*, Royal Aircraft Establishment, Farnborough, 1974, p371

27. F. Giralt, D. Trass, *Can. J. Chem. Eng.*, Vol 53, p505, 1975

28. F. Giralt, D. Trass, *Can. J. Chem. Eng.*, Vol 54, p148, 1976

29. N. Rajaratnum, *Turbulent Jets - Developments in water science*, Elsevier, 1976

30. K. D. Efrid, *Corrosion*, Vol. 33, No. 1, p3, 1977

31. P. A. Lush. S. P. Hutton, J. C. Rowlands, B. Angell, *Proc. 6th European Congress on Metallic Corrosion*, London, p137, 1977

32. Illustrated Case Histories of Marine Corrosion., *European Federation of Corrosion Publications No. 5*, 1990, p111. Institute of Metals, London.

33. F. P. Ijsseling, General guidelines for corrosion testing of materials for marine applications. Literature review on seawater as test environment., *Brit. Corros. J.*, 13, 1 (1989)

34. B. Todd, Material choice and design of pumps and valves for seawater handling systems, *INCO Europe Ltd*, 1986

34. K. J. Vetter, *Electrochemical Kinetics*, Academic Press, London 1967

35. J. Postlethwaite, R. J. Scoular, M. H. Dobbin, Localised corrosion of molybdenum-bearing Ni alloys in chloride solutions, *Corrosion,* Vol. 44, No. 4 (1988)

# Chapter 5

# An Investigation of Corrosion and Wear in Liquid-Solid Particle Erosion

## Introduction

This chapter extends the study of erosion-corrosion to investigate the effect of a two-phase liquid-solid flow impinging on a metal substrate. In contrast to the work reported in the previous chapter, mechanical removal of material by impinging solid particles plays a significant role in material deterioration.

The materials used in the study include a C-Mn steel, cast iron, duplex and austenitic stainless steels and the hard, Stellite 6 and Inconel 625. Electrochemical monitoring in conjunction with weight loss measurements enabled the components of material degradation attributed to mechanical and electrochemical processes to be isolated. Microscopical examination yielded information on the modes of attack predominant at and around the impingement area and the interactive effects between mechanical erosion and corrosion processes.

The effect of fluid corrosivity on the corrosion and wear behaviour was examined by varying the temperature and salinity of the carrier fluid. The latter part of this work, as will be described later, formed an investigation into the wear of materials for a river water application containing a high concentration of suspended solids.

## Literature Review

The term corrosive wear can be used to describe deterioration by the joint action of electrochemical corrosion and mechanical wear. In the chapter 4, the mechanical and mass transfer effects of an impinging single phase liquid jet were considered. The effect of suspended solids in the impinging stream is considered in this chapter.

Wear-corrosion can encompass a range of mechanical processes such as abrasion, adhesion, sliding wear and erosion or can be a combination of several processes when debris from one wear process acts as the eroding particles for another wear process. G. Silva studied the interactive and additive effects on wear of more than one process acting simultaneously within a hydraulic pump [1]. The findings, which suggest that when more than one mechanical wear process acts, the resultant damage is greater than the sum of the damage from the independent processes, were substantiated by the study of Madadnia and Owen [2]. They concluded that, on valves subject to both cavitation and erosion, the wear rate was significantly enhanced compared to the sum of the individual processes.

Erosive wear is the phenomenon under study in this section of research and occurs when solid particles, entrained in the carrier fluid impact the wetted surfaces causing material removal. Much work has been reported on the erosion of materials in a gaseous carrier fluid [3,4], termed 'dry erosion' and represents an advance in the early findings of the work of Finnie [5]. The book by Hutchings [6] gives a comprehensive guide to erosion and other wear mechanisms, concentrating on dry conditions The contrasting behaviour of ductile and brittle materials under dry erosion is described with respect to impact angle. The relationship shown in Fig. 5.1 has become widely recognised as a guide for the prediction of the behaviour of materials when the angle of impingement is defined. This relation has been shown by Hutchings and Burnstein [7] to be different in conditions of liquid-solid erosion, in that the erosion rate remains at a maximum for impact angles in excess of 40°.

Solid particle impingement erosion testing has been carried out by several research groups, concentrating on the response of metallic materials and coatings to repeated impact in a two-phase, gas-solid system. The research has emerged from an inherent requirement of the aerospace industry to develop materials resistant to wear, for gas turbine and compressor components and for applications within the chemical process industry where flame-sprayed coatings are often used on structural steel to protect against wear and corrosion [8]. Thus experimental studies have been carried out in high temperature, high-pressure systems. The degradation processes during solid

particle erosion in high temperature oxidation environment involve simultaneous scale growth and removal due to impacting particles. Much research has focused on defining 'regimes' in which the oxidation is dominant or where the erosion is dominant [3,4]. Stack et al. [9] developed erosion-corrosion maps to describe the different dominant regimes.

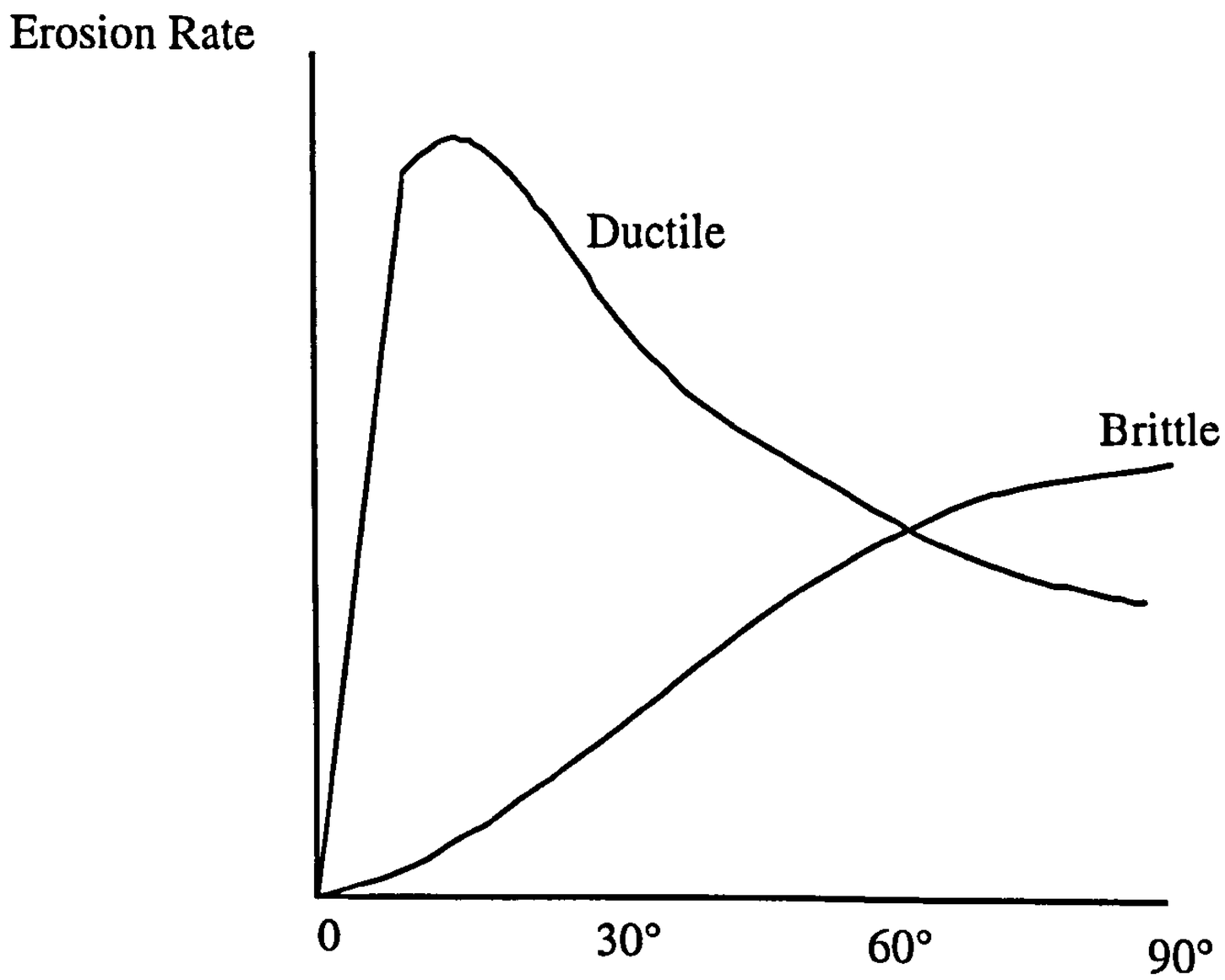


Fig 5.1. Solid particle impingement relationship with impact angle for ductile and brittle materials

Erosion-corrosion in an aqueous stream involves interactive mechanical effects of particle impact in conjunction with electrochemical corrosion and although it is an independent phenomenon, analogies have been drawn to airborne or gaseous solid particle erosion. Ductile/brittle relations have been demonstrated for aqueous systems and particle impacts have been shown to produce damage in the form of surface ripples and fatigue striations as in high temperature systems [10].

Background and Practical Relevance

Much of recent work in the field of erosion-corrosion has focused on the assessment of newly developed alloys and surface engineering techniques to combat premature failures due to wear. The need for materials to withstand increasingly severe downhole conditions in the oil and gas industry has assumed great importance to operators, over the past two decades, reflecting the increased activity in that industry in which some of the most severe and costly failures have been encountered. Nevertheless, problems due

to the combined effect of erosion and corrosion are by no means exclusive to the offshore sector. Recent studies have highlighted the extent of erosion-corrosion problems in, for example, the pulp and paper industry, chemical and mineral processing industries [11,12] and in mining applications [13]. Susceptible components range from pumps [14] (wear rings, impellers, casings, seals), shell and tube heat exchangers [15], valves [16] and mechanical seals [17]. As an example of the immense costs incurred by failure due to wear and corrosion, one major offshore operator recently estimated the annual cost for replacement of valve internals at in excess of £8m.

An especially appropriate illustrative example of an engineering system in which mixed erosive wear mechanisms are encountered in an aqueous stream, is the centrifugal pump. Feicht in 1976 [18] showed that 70% of pump failures could be attributed to the effects of fluid movement and contamination with solid particles thus illustrating the endemic nature of wear-corrosion problems. Handling a slurry flow, as is often the case in the pulp and paper industry and in oilfield applications, three modes of erosive wear can be identified [19]. At the leading edge of the impeller, and in the back shroud the predominant erosive wear mechanism is direct impingement where particles in the flow repeatedly impact at a common angle. Random impingement signifies a complex array of impact angles and is prevalent between the impeller shrouds and the trailing edge of the pumping vane. The third mechanism, sliding bed wear, represents a mechanism by which particles are dragged in contact with the surface 'en masse' all with a common velocity. The volute casing periphery is particularly susceptible.

Material degradation in a centrifugal pump can appear as surface ripples which are governed by the flow pattern and the resultant angle of impingement of the particles. At the inlet to the impeller, directional impingement can result in the level of deformation shown at the vane inlets in Fig. 5.2a. The pump was in service in the test rig used for the erosion-corrosion programme. Precise details on the service conditions are not available but it is estimated between 240-300 hours of intermittent service. Figure 5.2b. shows clearly the severe erosion on the back shroud of the impeller. At the impeller outer periphery, some of the flow is deflected as leakage flow to the lower pressure region at the rear and as it flows parallel to the impeller surface, causes erosion. The perpendicular impingement, as shown in the schematic Fig 5.3a, produces a symmetrical groove on the rear of the impeller which represents a significant loss of material. The actual damage can be seen in Fig. 5.3b.

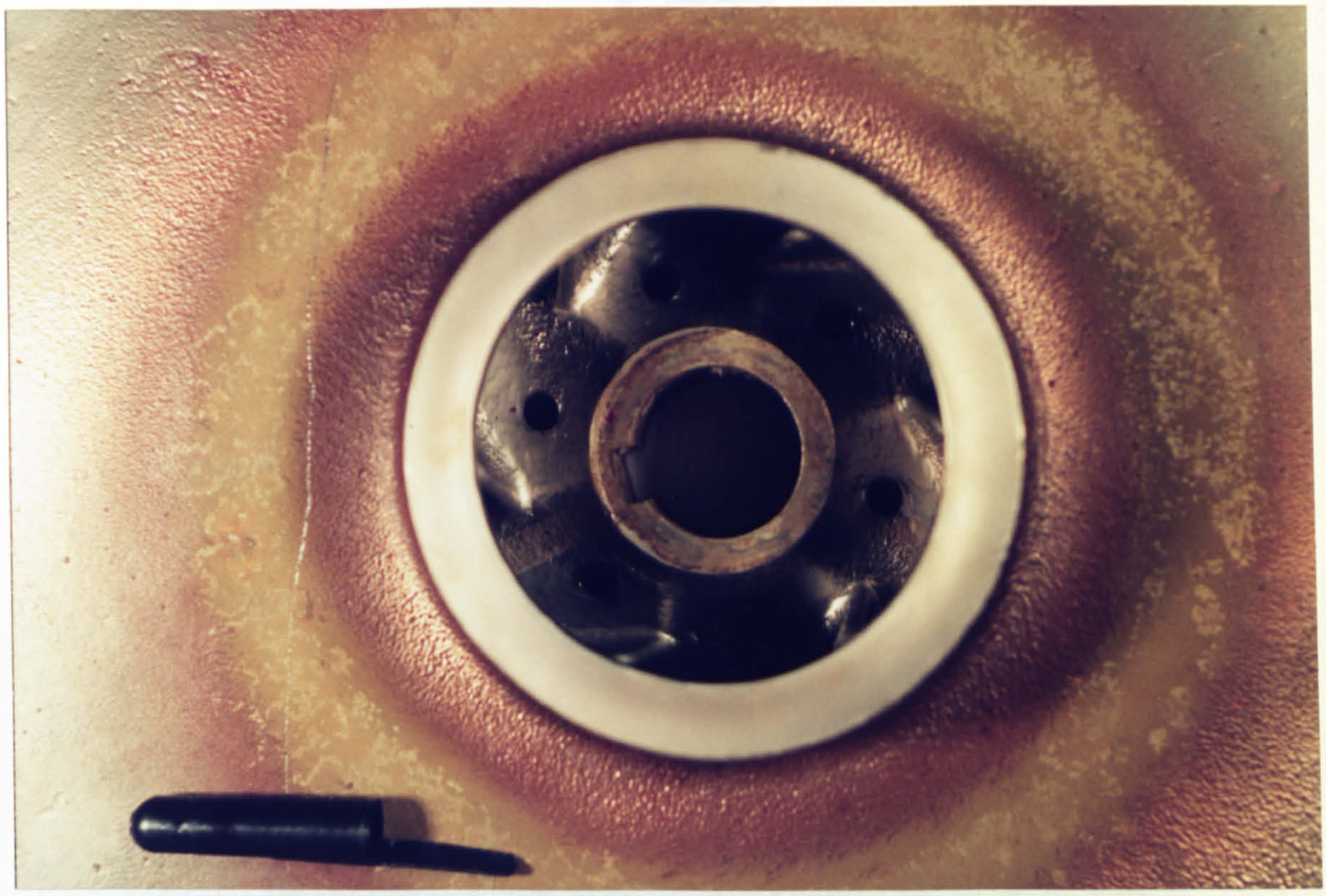

(a)

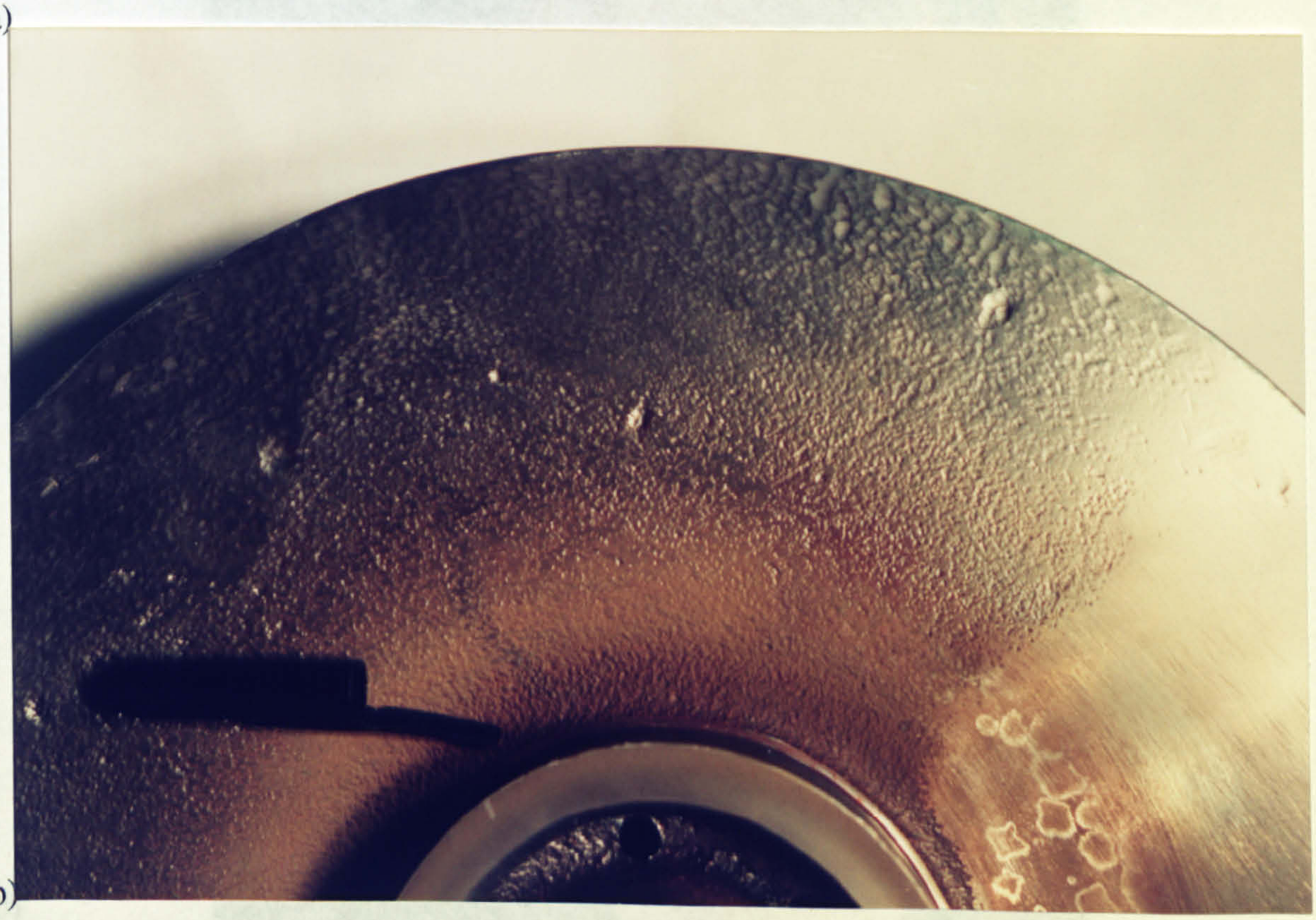

(b)

Fig. 5.2. Deformation on a UNS S31603 centrifugal pump impeller at (a) the inlet and (b) the back shroud

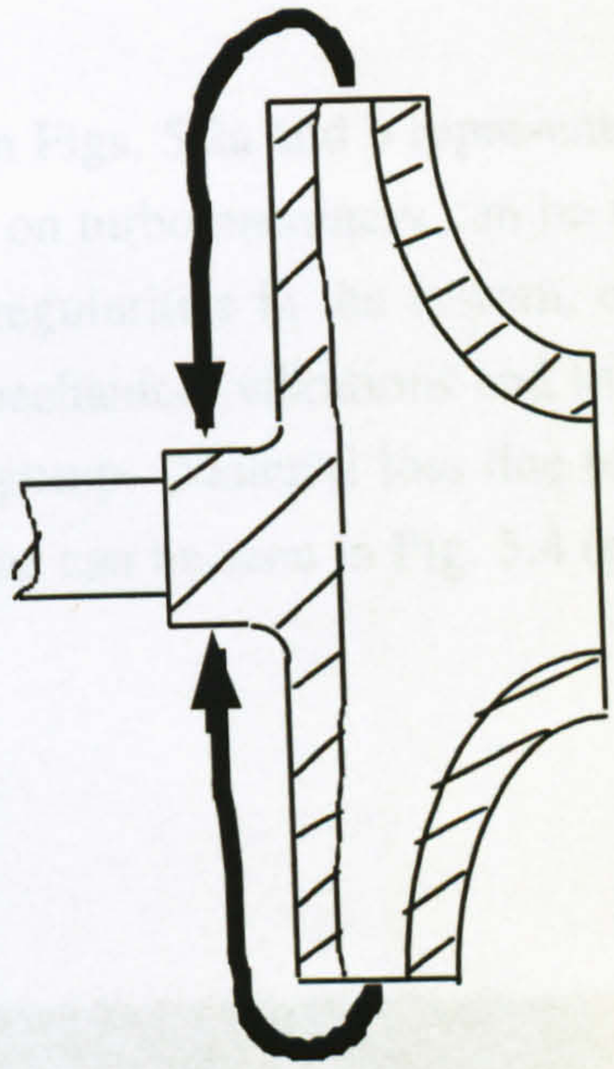


(a)

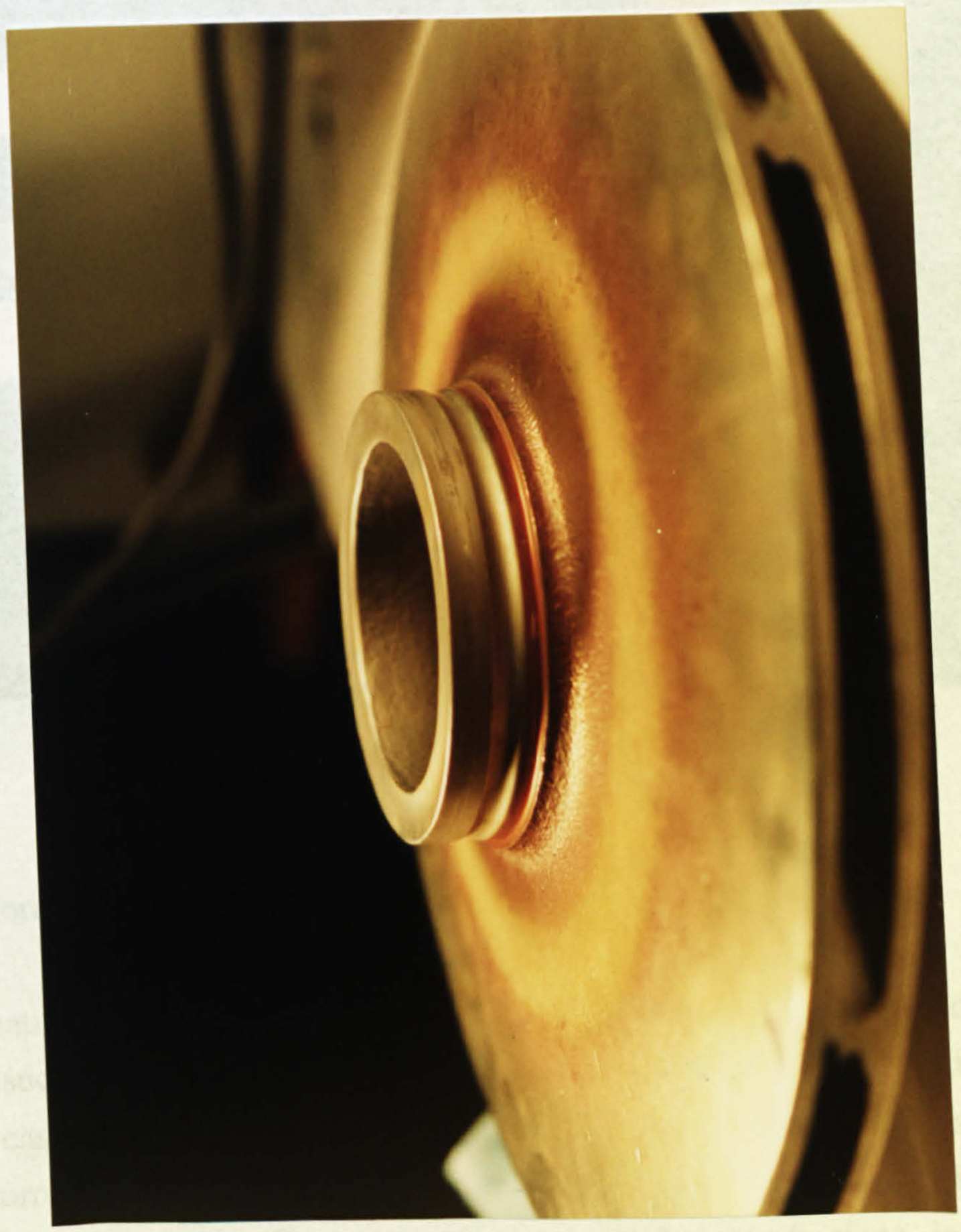

(b)

Fig. 5.3. (a) Schematic representation of leakage flow impingement and (b) actual damage

Damage to the extent shown in Figs. 5.2a and b represents a minimal thickness loss of material yet the consequences on turbomachinery can be significant. The gouging due to erosion can induce flow irregularities in the system, especially within the impeller vanes resulting in increased mechanical vibrations and loss of efficiency manifested in loss of delivered head of the pump. Material loss due to erosion-corrosion leading to perforation of the impeller vane can be seen in Fig. 5.4 (photo looking radially into the impeller).

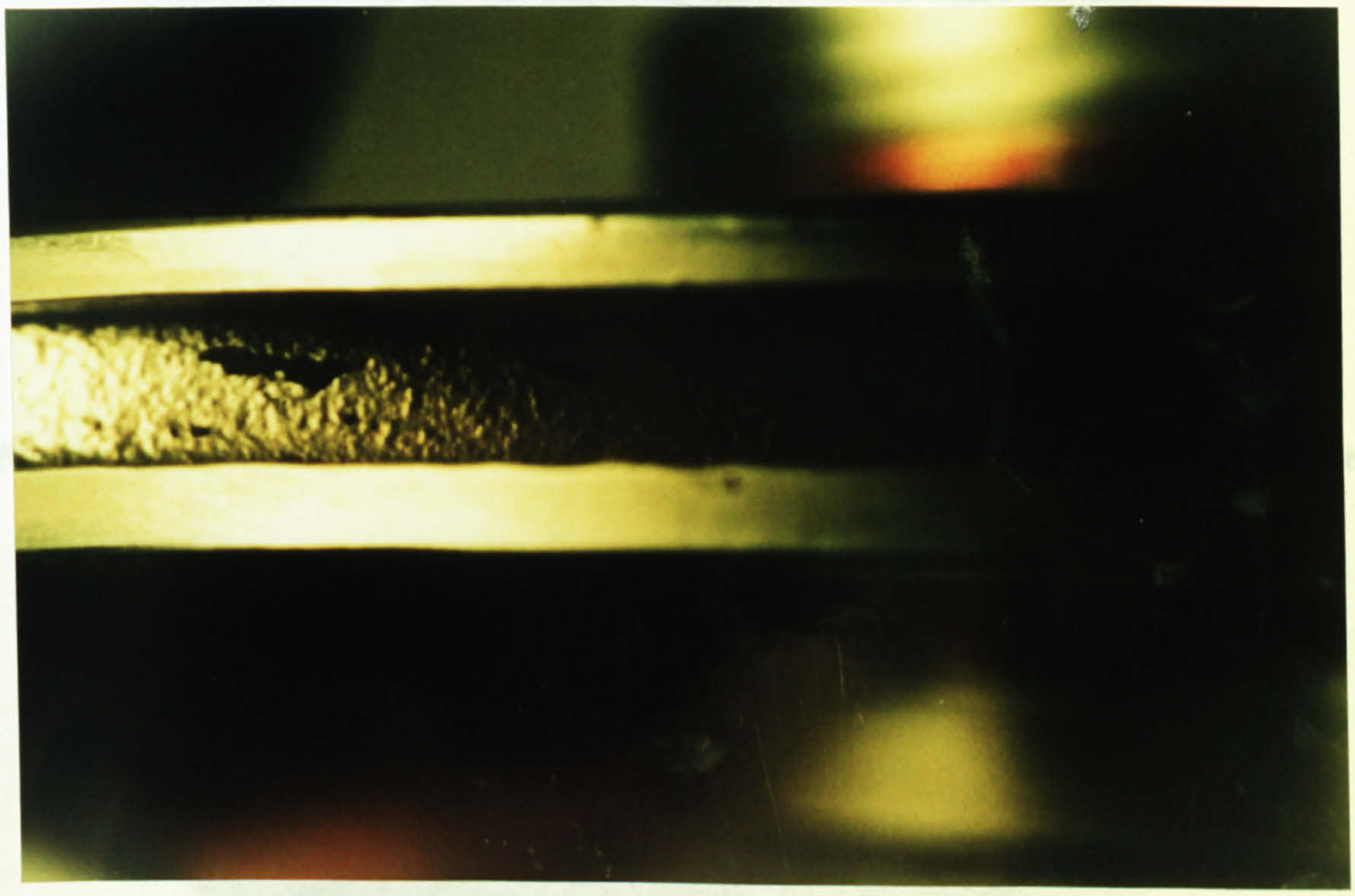

Fig. 5.4. Perforation of the impeller vane due to erosion-corrosion

Although rotating plant is particularly vulnerable to erosion-corrosion, hydrodynamic components such as valves and piping systems often suffer severe degradation. Figure 5.5 shows a cast iron valve subjected to liquid slurry flow in the erosion test rig where the severe corrosive attack can be seen. In erosion conditions in a liquid containing solids, corrosion damage is often not evident on stainless steels since, in contrast to materials such as cast iron, adherent corrosion products can not be seen. This is shown

on the pump casing in Fig. 5.6. However, it will be demonstrated later that corrosion does indeed play a significant role.

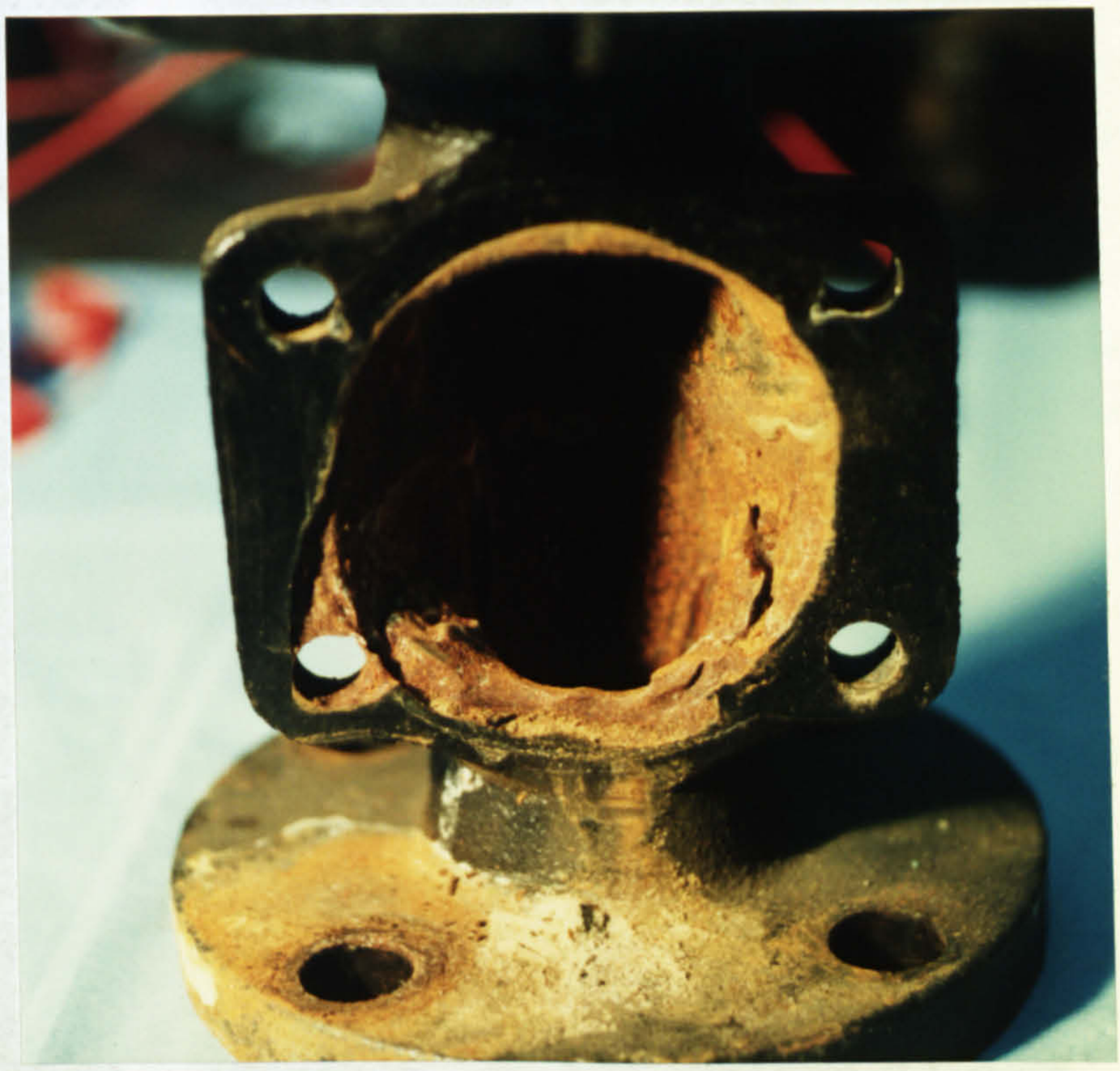

Fig. 5.5. Deterioration of a cast iron valve from the test rig after 240-300 hours service

(a)

(b)

Fig. 5.6a and b. Erosion on the UNS S31603 pump casing after 240-300 hours in periodic service

Aqueous Erosion-Corrosion

The erosion-corrosion rate in a slurry flow is recognised to be dependent on numerous factors. Clark in [20] summarised the parameters which dictate the erosion rate in slurry flow in conditions but corrosion was not considered. Combining the findings of several workers [19,20], the dominating factors have been found to be mainly :

- the liquid (viscosity, density, pH, TDS, temperature)
- the target (ductility, metallographic structure, work hardening, residual stress levels)
- particles (size distribution, density, shape, hardness)

- flow-field (angle of impact, Re number, particle-particle interactions, squeeze film)

The interaction of all these factors has led to increased awareness of synergistic mechanisms. The word synergy in erosion-corrosion studies in two phase, liquid-solid flow can be used in several different contexts to mean the enhancement of erosion in the presence of corrosion, the enhancement of corrosion in erosion conditions and also the two joint effects In recent studies of the synergism between erosion and corrosion, Pitt and Chang and Spencer et al. [21-23] defined the synergistic effect of corrosion in enhancing erosion, by measuring electrochemical corrosion rates in-situ. Alternatively, Postlethwaite et al. [24,25] determined the total weight loss in aerated and deaerated slurries assuming that corrosive weight loss in deaerated slurry would be negligible. Thus caution must be taken when comparing the synergism quoted by different workers and attention must be paid to the definition of the synergistic factor.

There has been no successful conclusion to attempts to relate the resistance of a material to a single material property. Correlations of erosion-corrosion resistance to microhardness have, in some instances, produced data to suggest increasing hardness yields a more erosion resistant surface but since hardness is only representative of the deformation aspects of damage, the correlation is normally not valid where mass transfer and corrosion play a significant role [26,27].

The detrimental effects of a corrosive fluid on the erosion of a material have been suggested by several authors to be the removal of a work hardened layer by corrosion, thus decreasing it's built up erosion resistance, the increase of stress concentration sites due to pitting corrosion and the preferential attack at grain boundaries which loosens grains and induces an enhanced mass loss [28].

Finnie in 1960 [5] recognised that the erosion rate in slurry flow would be determined by the number of particles impacting a surface, the velocity and their direction. Still there is a dearth of data to accurately describe the behaviour and trajectories of solid particles in a liquid flow. J. A. Humphrey [29] reviewed the fundamental knowledge of fluid motion in erosion by liquid-solid particle impact. Importantly, he stressed that the velocity of the particles moving in a fluid towards a target is not equivalent to the free stream fluid velocity. In this work, the importance of the squeeze film between the solid particle and the surface is realised in determining the final impact velocity of the particle. The cushioning effect of the squeeze film determines whether the particle will impact the surface or indeed be diverted by the streamlines as it approaches in the free stream. The squeeze film describes the area at the target surface in which the fluid

must be exuded to enable impact by the particles. Often the pressure required to remove the fluid layer is large enough to slow the particle to a very low or negligible velocity and therefore impact is avoided. Experimental investigations by Clark and Burmeister [20,30,31] have confirmed that the velocity of the particles on impact can be as low as 10% of the free stream velocity. The importance of the kinetic energy dissipated in impact has been recognised and correlations have been made between impact crater size and the particle velocity.

Aqueous erosion-corrosion has, in the past been studied by weight or volume loss comparisons to provide a ranking of resistance to material loss through particle impact. Although this quantitative information is important from a practical viewpoint in determining the rate of material loss, it does not indicate how the individual processes of erosion and corrosion interact. Recent developments of electrochemical techniques applied to in-situ corrosion monitoring have enabled the amount of information on mechanistic interactions between modes of material loss to be elucidated [32-34]. In addition, the components of wear attributed to different modes of material loss have been investigated in deionised water in an attempt to eliminate the effects of corrosion [35]

## Experimental Methods

The experimental conditions in the liquid-solid impingement rig consisted of a slurry flow, at a velocity $25ms^{-1}$, with combined 3.5%NaCl (Fisons technical grade) and 1000ppm silica sand. The angle of impingement was 90° in all tests. Modifications to an existing liquid/solid particle impingement rig (Fig. 5.7) were made to enable in-situ electrochemical testing. The temperature of the flow was 50°C for the majority of the tests, chosen for its relevance to oil field injection situations [36] where pumping of aggressive saline streams, containing suspended solid particles, is common. Some additional tests were conducted where the salinity and the temperature of the liquid stream were varied to 30°C and 500ppm TDS respectively.

The sand particles chosen for the study contained a wide distribution of sizes ranging from 53μm to 850μm as can be seen in Fig. 5.8.

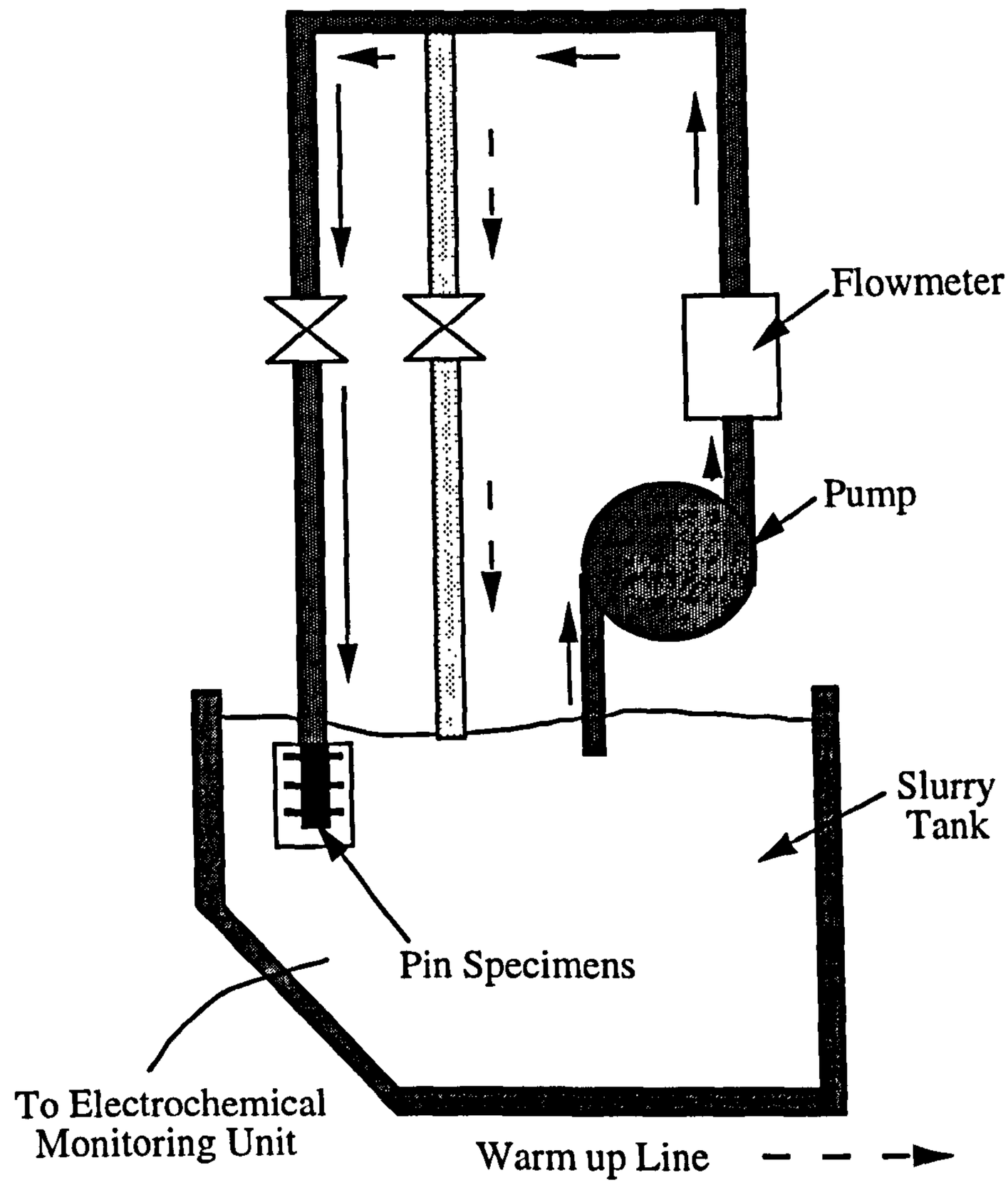


Fig 5.7. Liquid-solid impingement rig

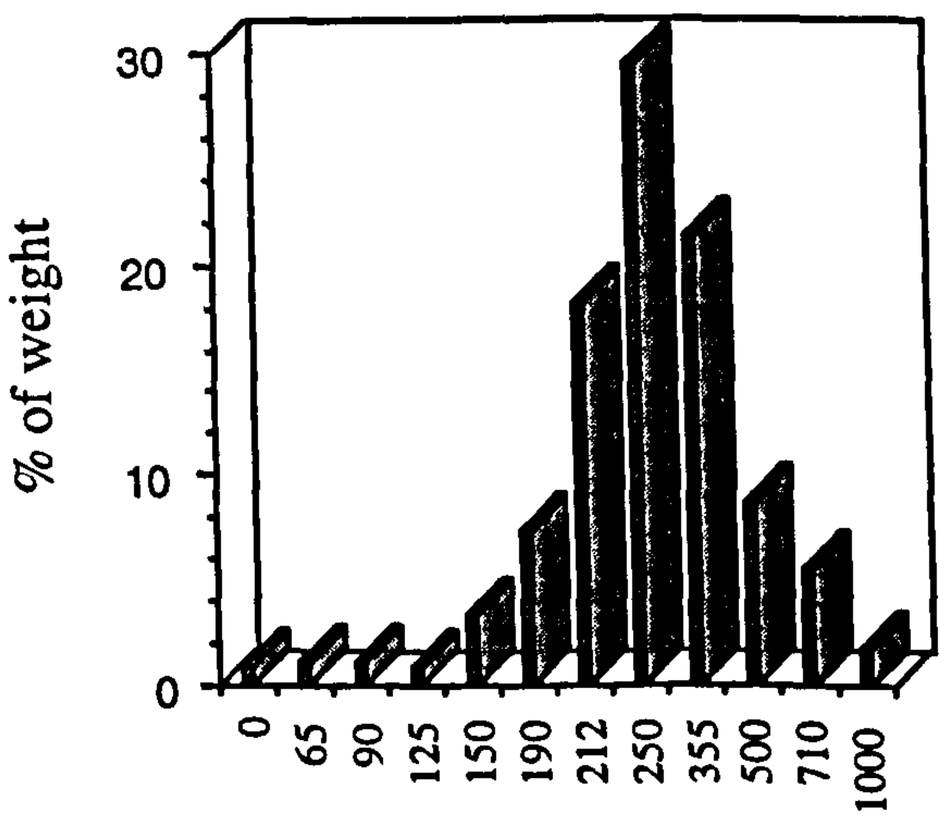


Fig. 5.8. Sand particle size for all tests in slurry flow

Potentiodynamic tests in the liquid-solid erosion conditions comprised anodic polarisation tests, the data from which was then plotted on a semi log scale (E-Log I)

and this procedure permits the evaluation of the "corrosion current, $I_{corr}$" of actively corroding materials by the well-known Tafel extrapolation technique [37]. The corrosion rates can be calculated via Faraday's Law from the $I_{corr}$ data.

The potentiostatic tests consisted of two types. The first involved shifting the potential from $E_{corr}$ by a small amount (+50mV) with no impinging flow. Once a steady current was attained the impingement by a liquid-solid stream was started and the subsequent progression of the current was recorded. This technique was used to try to assess the effect on the anodic current as the sand hits the specimen surface. The second approach involved shifting the potential from $E_{corr}$ in the negative direction to a value of -0.8V (SCE) which represents a potential usually used to cathodically protect steel from corrosion. The cathodic protection (CP) potential, when applied to the specimens under liquid/sand erosion, was first applied during the "warm-up" period when the flow bypasses the specimens but they are submerged in the 3.5%NaCl solution.

Via a system of 3 tests, all of which could be carried out in the same one-hour test period and therefore under the same conditions, unravelling of the main components contributing to wear, under liquid/solid erosion, could be achieved. These tests consisted of : -

- total weight losses (**TWL**) measured after one hour at the free-corrosion potential
- anodic polarisation and Tafel extrapolation to give the corrosion component of the total weight loss (**C**)
- weight loss with applied CP to give the pure erosion component (**E**) of the total weight loss

This enabled, via simple arithmetic, the calculation of the synergistic factor, **S**, a flow containing 1000ppm suspended solids, impinging the surface at $25ms^{-1}$.

A series of galvanic tests was performed in which specimens were coupled and the resulting current flow measured. Some tests involved one specimen under erosion and the other in the static electrolyte (sometimes specimens of the same material) while other tests involved specimens of the different materials being exposed to the same erosion-corrosion conditions.

The liquid-solid particle impingement rig accommodated pin-type specimens 6mm x 6mm x 30mm long. A stainless steel screw with a wire soldered to the end was inserted in a tapped hole on one end of the specimen. An initial series of tests was

performed in which 4 sides were exposed to the electrolyte but in all the experiments reported here, three sides and both ends were covered with a shrink fit rubber sleeving to insulate the pin from the metal holders, leaving only one face with dimensions 6mm x 22mm was exposed to the impinging flow. The surfaces of the specimens for liquid and liquid-solid impingement tests were abraded on 600-grit abrasive paper prior to testing.

Twelve specimen holders and attached nozzles were inserted into the rig at one time. The nozzles contained ceramic (Mg-stabilised Zirconia) inserts to minimise the wear and deformation of the cylindrical nozzle exit. The distance from the nozzle exit to the specimen surface was constant at 5mm. The specimen, specimen holder and nozzle arrangement are shown in (Fig. 5.9).

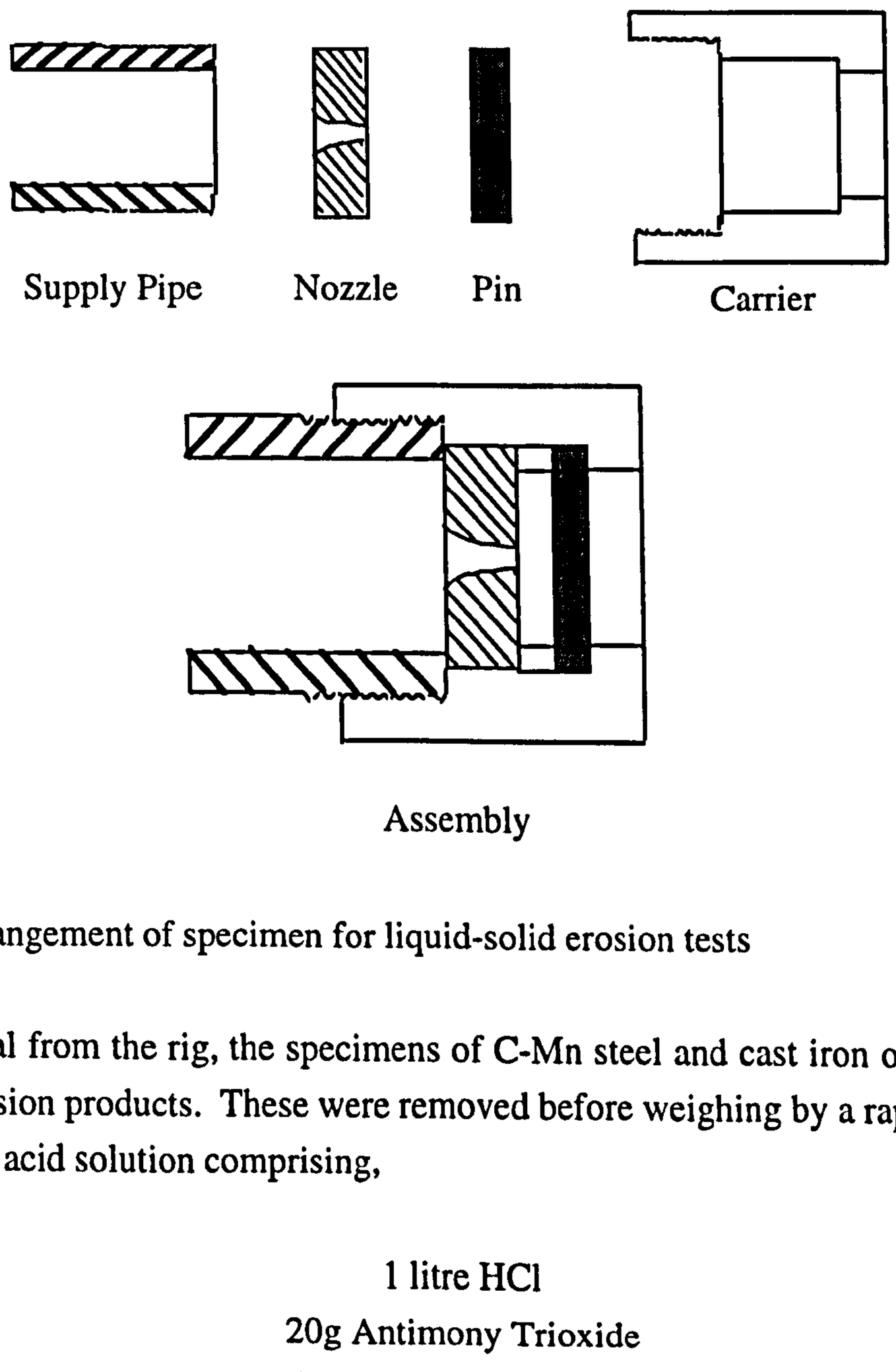


Fig. 5.9. Arrangement of specimen for liquid-solid erosion tests

After removal from the rig, the specimens of C-Mn steel and cast iron often contained visible corrosion products. These were removed before weighing by a rapid cleaning in an inhibitive acid solution comprising,

1 litre HCl
20g Antimony Trioxide
50g Stannous Chloride

followed by air drying. The stainless steels were simply immersed in tap water and air dried after completion of the test.

The erosion rig accommodated 12 pin specimens which enabled the scatter inherent in liquid-solid erosion testing to be minimised. The nozzles were numbered and a calibration test on 12 UNS S31603 pins was performed in which the scatter was found to be 4%. The nozzles were then 'paired', the highest weight loss with the lowest and so on to give a scatter range between pairs of less than 1.5%. The results presented in this chapter are therefore an average of two pairs of nozzles which further reduces the percentage scatter. In each test, two control pins of UNS S31603 pins were inserted to enable comparison of results between different test runs. The rig was flushed out before each test to remove any residual sand from previous tests but inevitably some sand will remain, hence, the weight loss measured on UNS S31603 was taken to be the standard, to measure whether the test results for a particular run are valid or not. Each test run, which would include at least two specimens but normally four specimens of each material, was carried at least three times during the project.

In this chapter the results of some comparative tests on cast iron will be reported. This involved performing an identical series of tests in liquid erosion conditions to separate the components of weight loss due to erosion, corrosion and to try to identify any interaction between the two. This was not possible on stainless steels under liquid erosion, since as seen in chapter 4, the materials were still passive under the impinging jet and, as such, the infinitely small weight loss could not be accurately determined.

## Results

### In 3.5%NaCl at 50°C

#### Free Corrosion Potential

Although from the free corrosion potential, no quantitative information can be obtained on the corrosion rate, it can be useful, in conjunction with DC-polarisation scans, to give information on how the relative rates of anodic and cathodic reactions are changing.

This work has focused on two main categories of material. The 'passive' materials (characterised by their behaviour in static seawater) include the stainless steels, the Co-base and the Ni-base alloys. Secondly, there are the materials which, in static seawater at ambient temperature, actively corrode, due to the absence of a protective film

On the stainless steels, Co-base and Ni-base alloys the free corrosion potential exhibited a shift in the active direction, immediately the sand bombardment commenced. For the period of the test, the free corrosion on all these materials drifted in the positive direction by a small amount. On stopping the impingement, the free corrosion potential continued to move in the positive direction but at an increased rate. Figure 5.10 shows the trend in potential on a stainless steel and the Ni-base alloy (UNS S31603 and Inconel 625) and also on the C-Mn steel and the cast iron. In contrast, the cast iron and the C-Mn steel displayed an initial shift in the positive direction on commencing liquid-solid impingement followed by a steady shift in the active direction (to a greater extent than the positive shift on the stainless steels, Co-base and Ni-base alloys). Once the flow was stopped, the free corrosion potential on cast iron was observed to remain at a steady value, the effect of the removed impingement not immediately apparent. A drift in the negative direction was observed immediately on C-Mn steel.

There was an obvious effect of flow velocity observed on the stainless steels, the Co-base and Ni-base alloys in that on reducing the flow velocity a shift of the free corrosion potential in the positive direction was observed. The value would then move in the active direction on increasing the velocity as illustrated in Fig. 5.11 on the SAF 2205 duplex stainless steel.

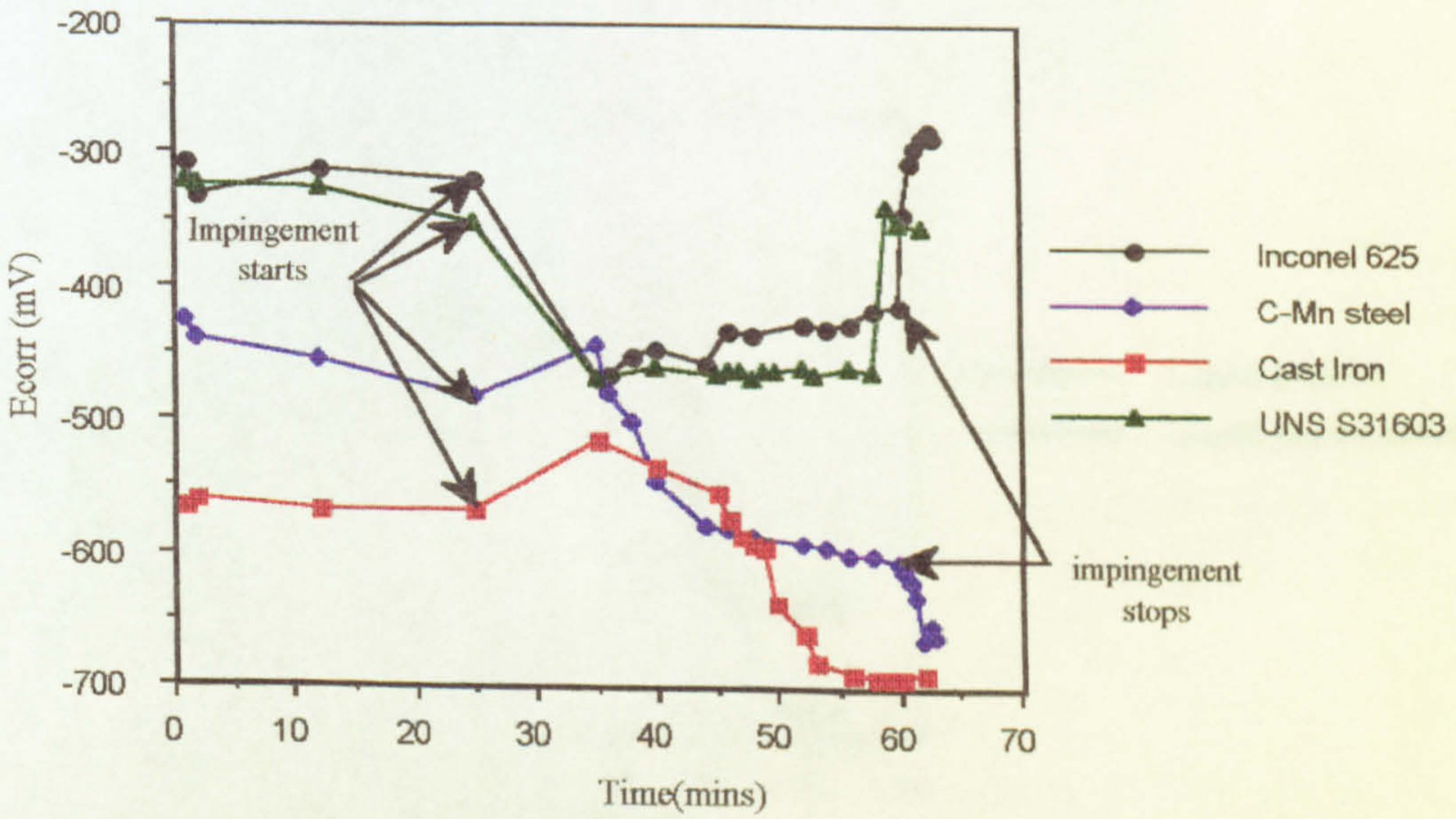


Fig. 5.10. Free corrosion potential during liquid-solid erosion on UNS S31603, Inconel 625, C-Mn steel and cast iron in 3.5%NaCl at 50°C

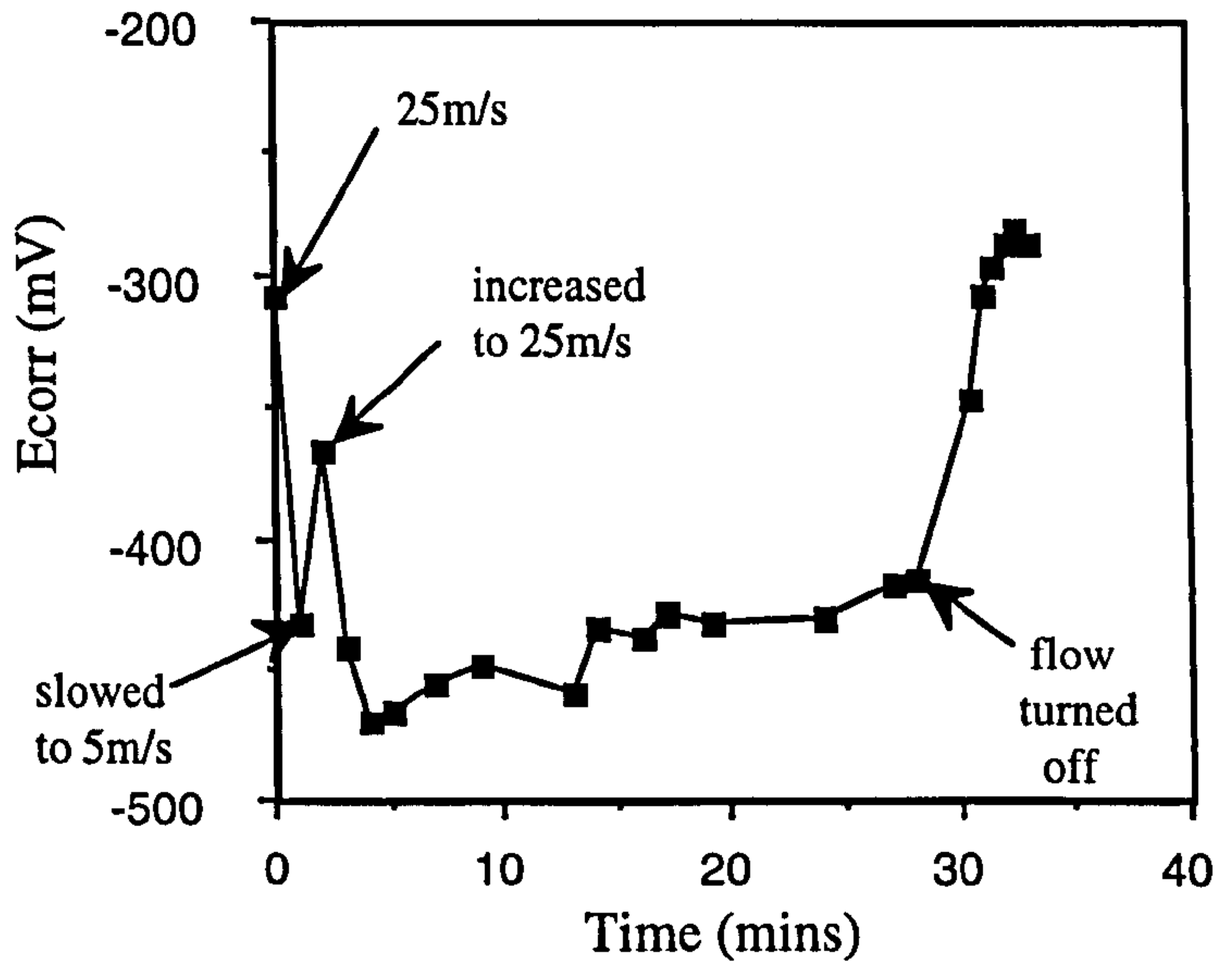


Fig. 5.11. $E_{corr}$ on the duplex stainless steel SAF 2205 as the flow velocity is altered

In liquid erosion, it was shown in chapter 4 that on the stainless steels and the other alloys studied, the normal trend was for the free corrosion potential to shift in the positive direction on commencing impingement, mainly due to the depolarisation of the cathodic reaction as oxygen supply to the surface is increased. Indeed the C-Mn followed this trend but in contrast, on the cast iron, under liquid erosion, the free corrosion potential shifted initially in the positive direction on applying the impinging jet but then by a significant amount in the active direction during the test period. Figure 5.12 shows the evolution of $E_{corr}$ with the jet being applied after 25 minutes and removed after 60 minutes.

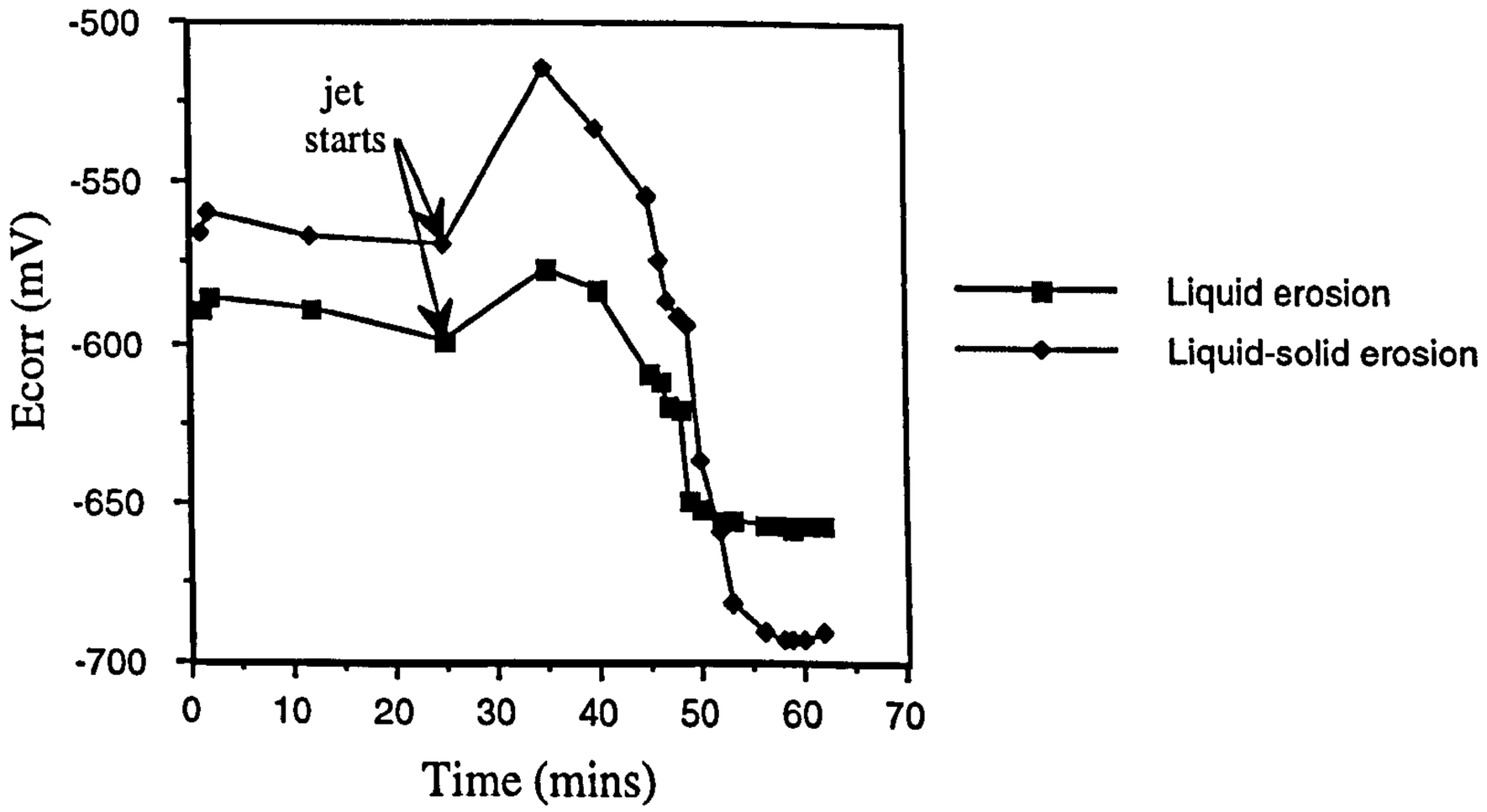


Fig. 5.12. Free corrosion potential on the cast iron during liquid and liquid-solid erosion in 3.5%NaCl at 50°C

Weight Loss Comparisons

The total material loss during a one hour test was measured, after the removal of any corrosion products and, as expected, under the severe conditions of the solid-laden impinging jet, the weight loss on cast iron and on the C-Mn steel was significantly greater than on the stainless steels, Co-base and Ni-base alloys although significant differences were also measured between these materials, as shown in Fig. 5.13. It is apparent that the behaviour of the two Co-base alloys and the Ni-base alloy is very similar. Also comparable weight losses were recorded on both the austenitic (UNS S31603) and the superaustenitic (UNS S31254) stainless steels. The superduplex stainless steel showed better resistance to material loss than the standard duplex stainless steels (SAF 2205 and 25Cr duplex), albeit inferior to the Co and Ni-base alloys.

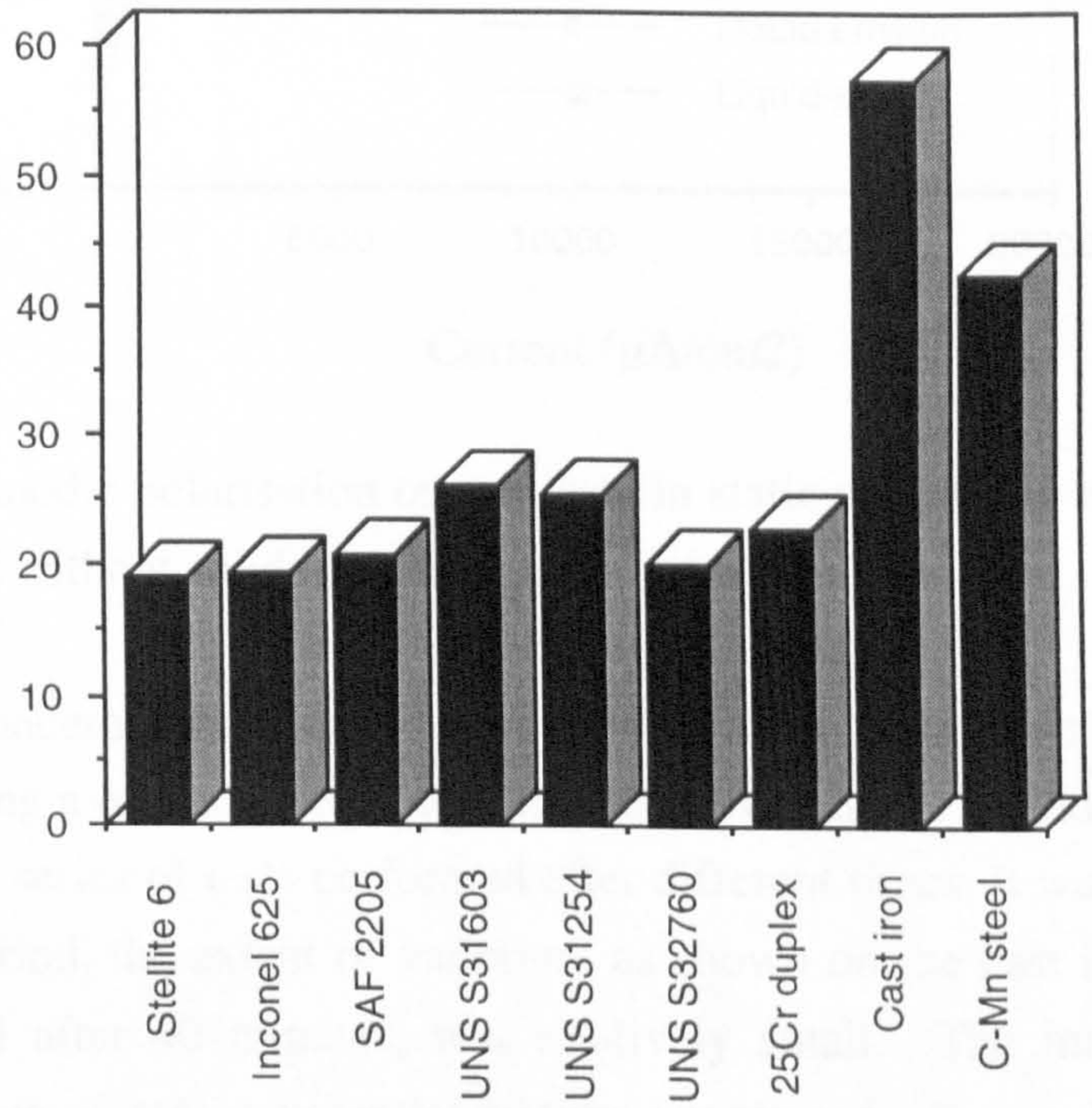


Fig. 5.13. Total weight losses during a one hour liquid-solid erosion test in 3.5%NaCl at 50°C. Each figure represents an average of twelve specimens of one material, results taken over three test runs. Typical scatter on, for example, cast iron, $\pm$0.79mg and on UNS S32760 $\pm$0.31mg

DC-Anodic Polarisation Scans

C-Mn steel and cast iron, as mentioned previously, both actively corrode in 3.5%NaCl at ambient temperature and at 50°C (the temperature relevant to this part of the study). This behaviour is manifested by a rapidly increasing current as the potential is swept in the positive direction from the starting potential ($E_{corr}$) during anodic polarisation.

Both materials continued to exhibit active corrosion behaviour under liquid impingement and with the presence of solids in the liquid flow, as expected. The widely different values of $E_{corr}$ in Fig. 5.14 on cast iron are indicative of the substantial influence of the hydrodynamic parameters on the corrosion process.

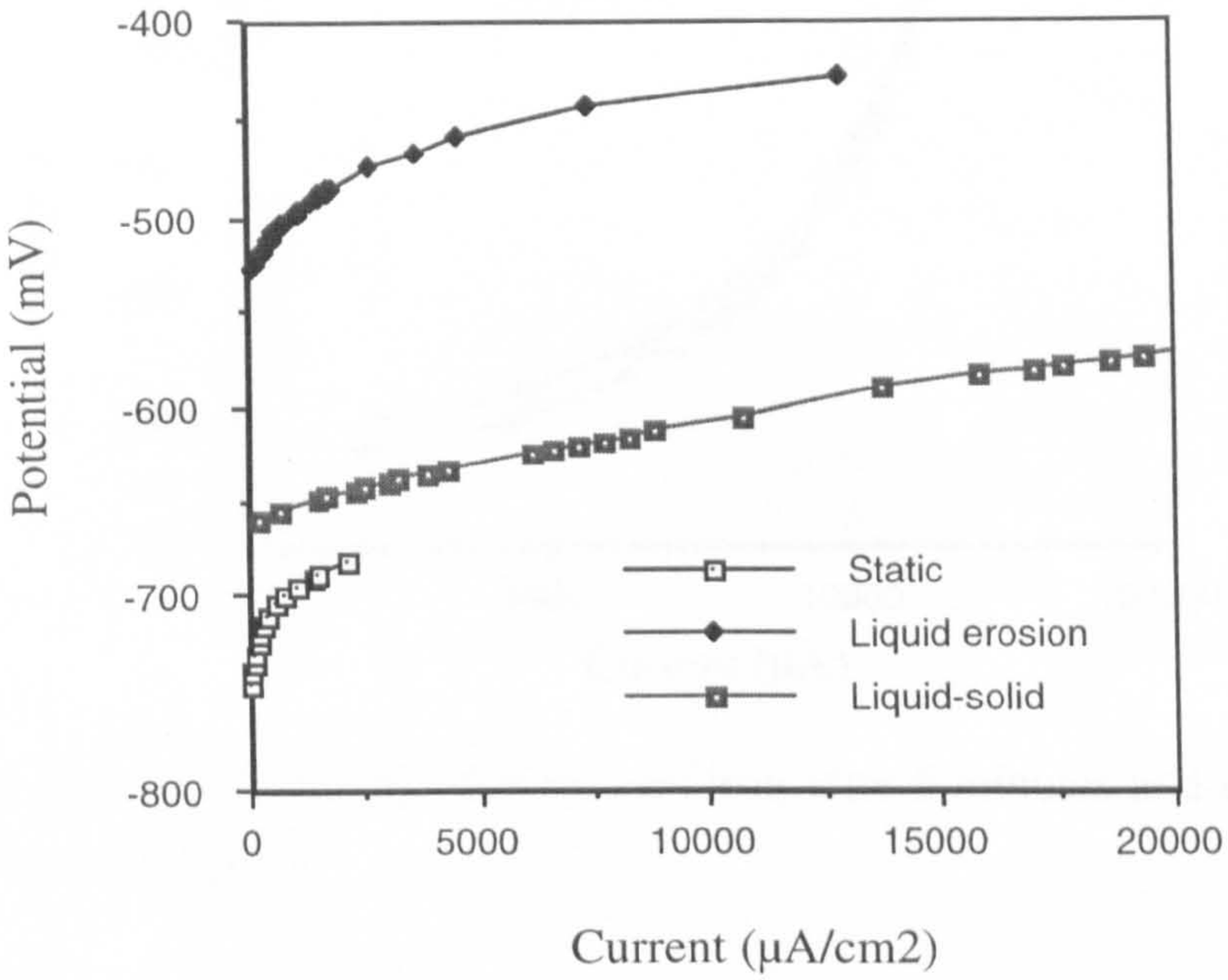


Fig. 5.14. Anodic polarisation on cast iron in static conditions and under an impinging jet (with and without solids) at 50°C

An initial concern regarding the measurement of the corrosion rate under liquid-solid erosion during a one hour test was how the corrosion rate would change during the test period. In a series of tests performed after different times, it was found that within the one hour period, the extent of variation, as shown on the cast iron in Fig 5.15 after 5 minutes and after 40 minutes, was relatively small. The main difference was the change in free corrosion potential as time progressed. It was decided for consistency that all anodic polarisation measurements would be performed after 25-35 minutes. The corrosion rate would therefore be assumed to be constant over the hour test.

Another reason for choosing the 25-35 minute interval was due to the evolution of the sand particle size as time progresses. SEM examination of new and used sand inferred that there was little change in the particle size after the initial 5-10 minutes. Figure 5.16a shows the original sand particles and they can be compared to the sand after 5 minutes (Fig. 5.16b) and after 55 minutes (Fig. 5.16c). Particle size analysis yielded a distribution at the start as was shown in Fig. 5.8. Figure 5.17 shows the distribution after 5 minutes and there is very little further change in the particle size from that initial change.

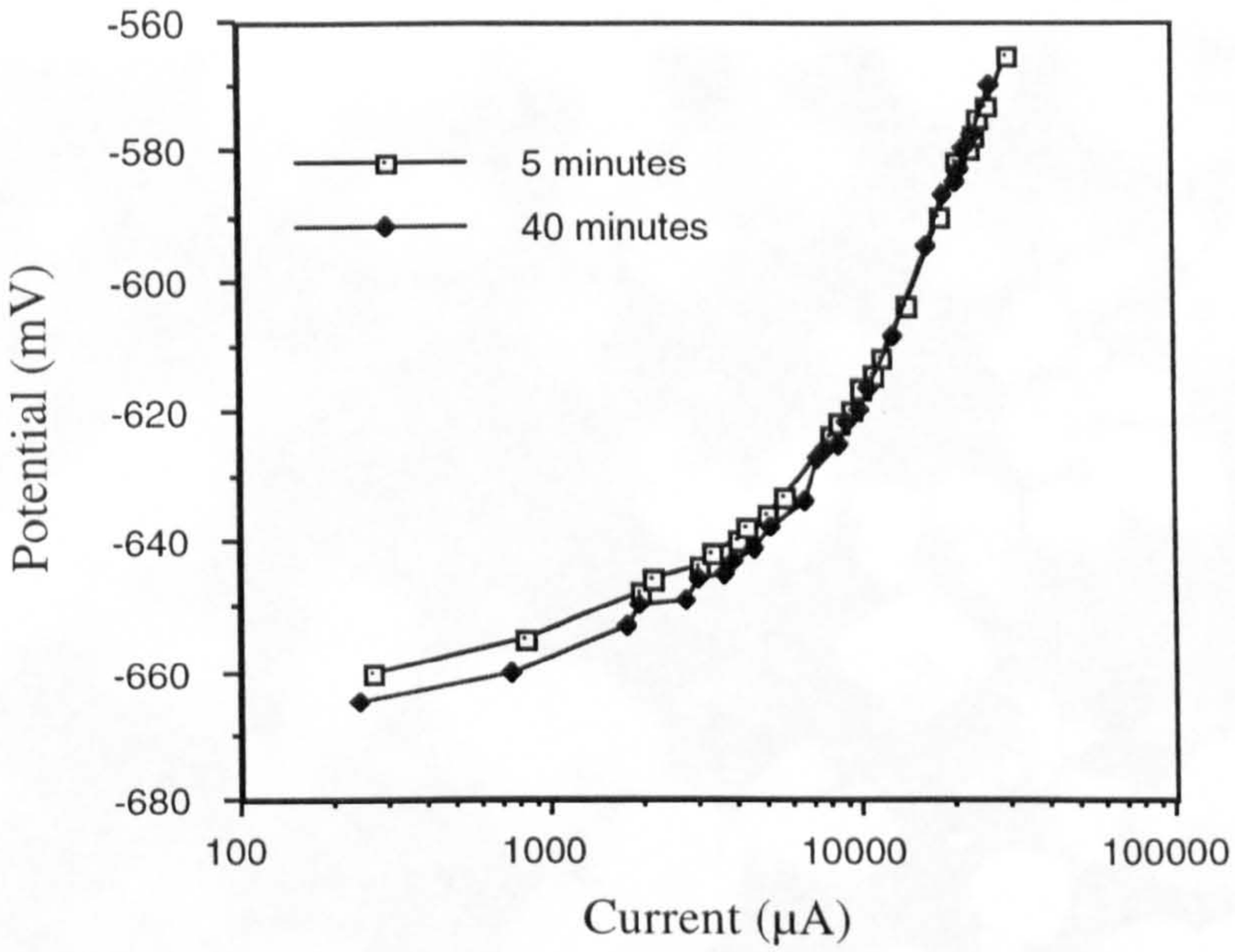


Fig. 5.15. Anodic polarisation on cast iron after 5 minutes and after 40 minutes under liquid-solid erosion

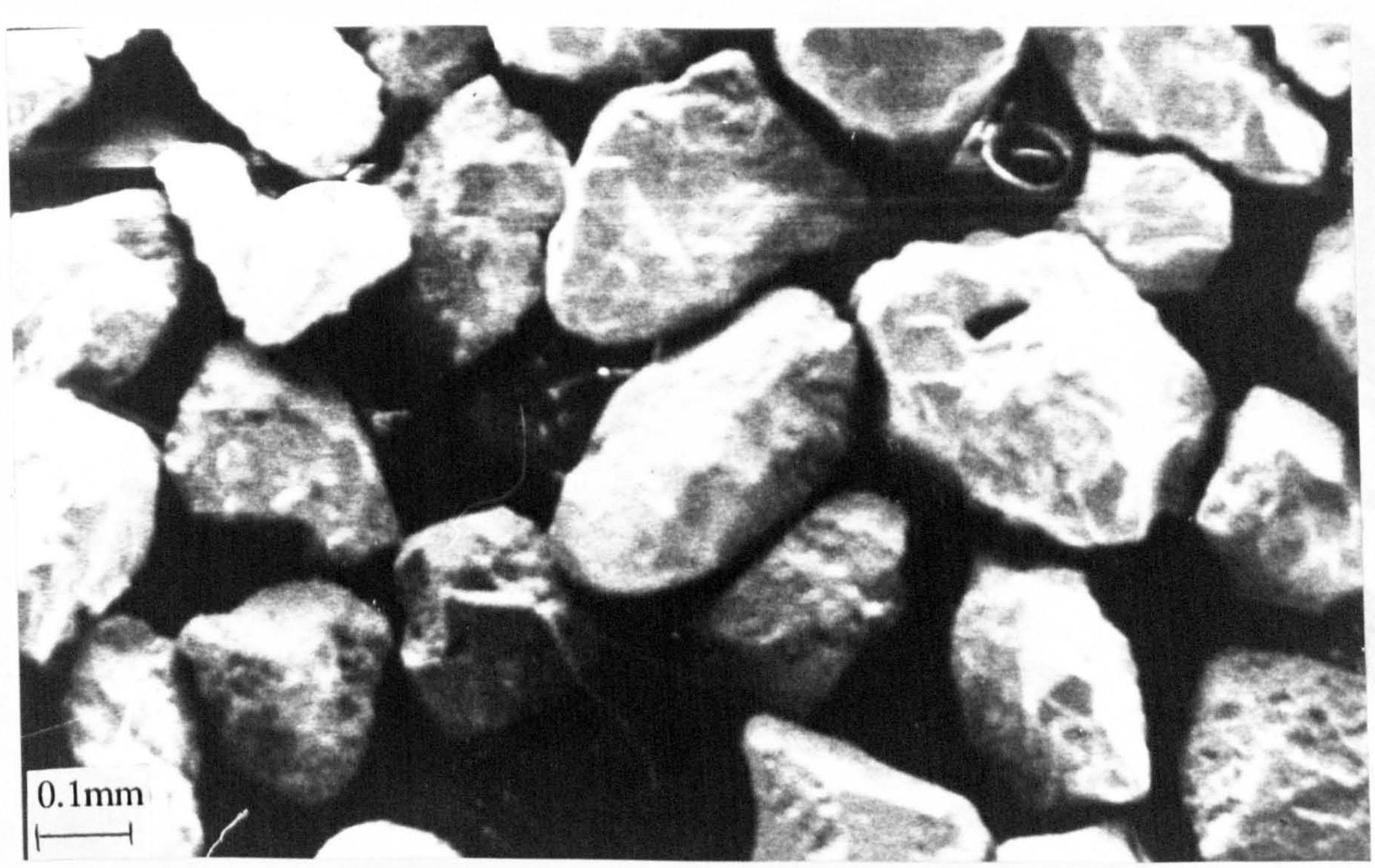


(a)

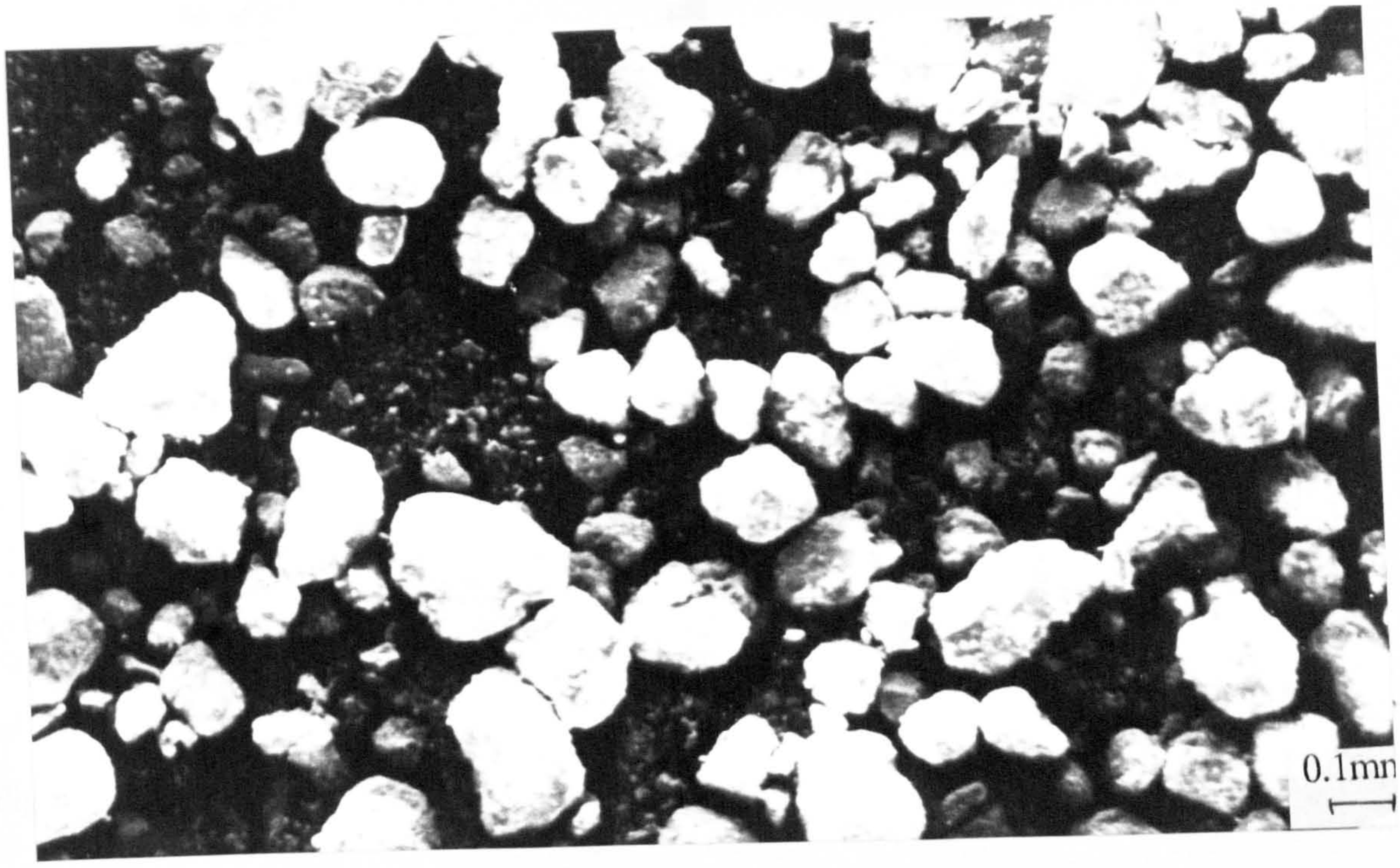


(b)


(c)

Fig. 5.16. SEM micrograph of sand (a) before test, (b) after 5 minutes in test rig and (c) after 55 minutes in test rig

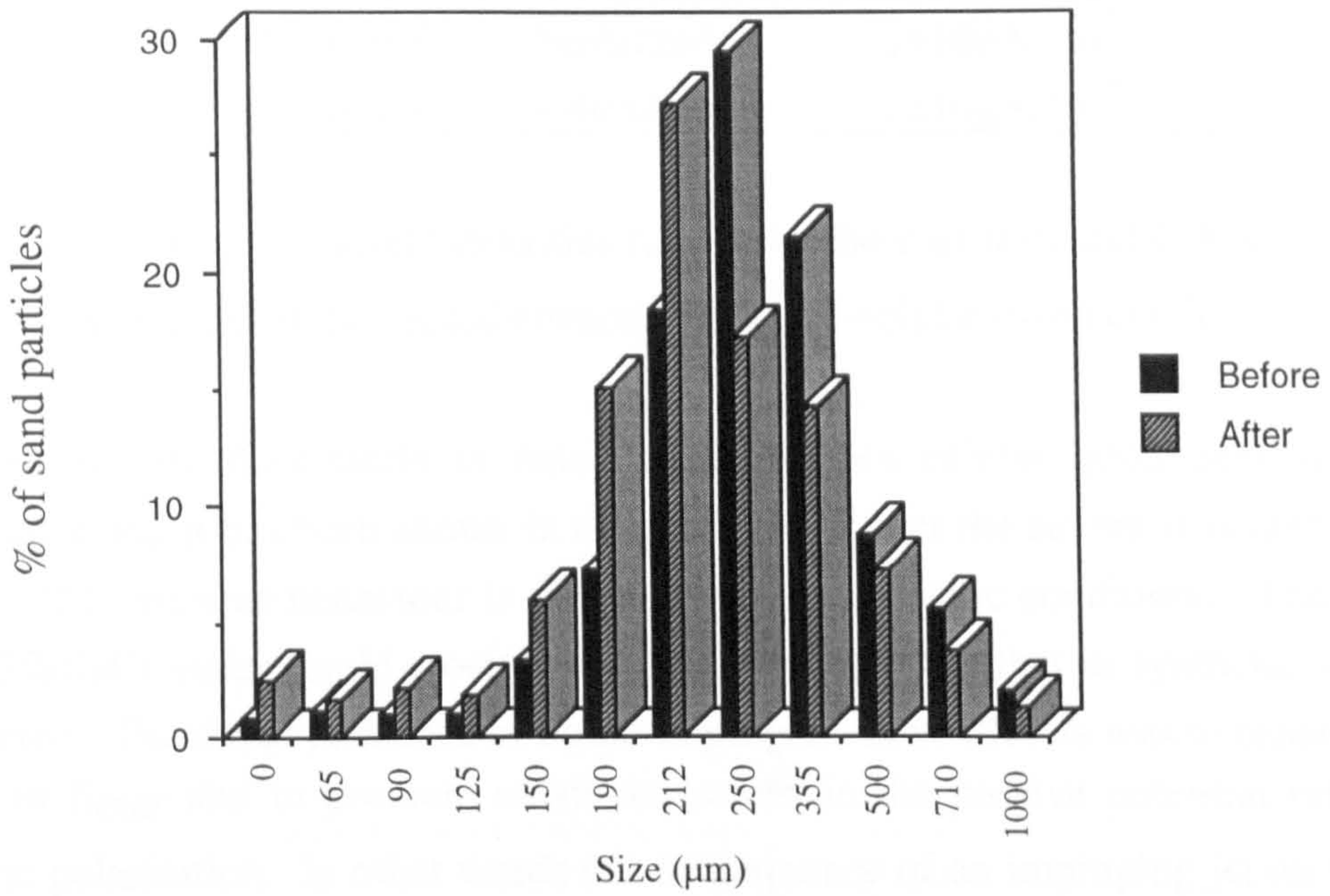


Fig. 5.17. Particle size distribution of sand before and after liquid-solid erosion testing

The behaviour of C-Mn steel was somewhat similar to cast iron, in that in both static and liquid erosion conditions, active corrosion was observed. However, differences were observed in the corrosion rates of the two materials and the corrosion current densities are given for both materials in the three conditions in Fig. 5.18. The cast iron in every condition exhibited a higher corrosion rate, the largest difference being under liquid erosion.

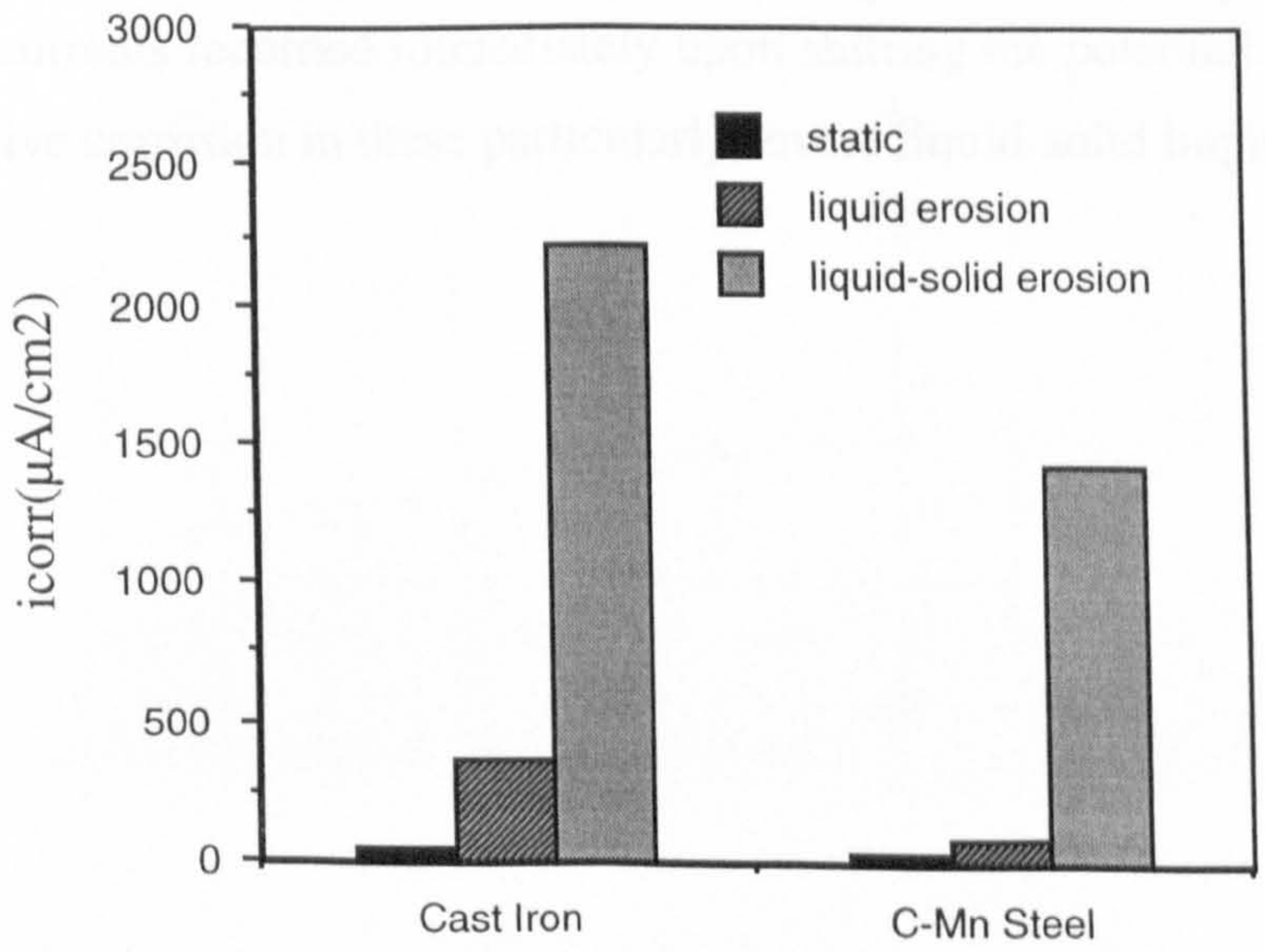

| | Static | Liquid erosion | Liquid-solid erosion |
|---|---|---|---|
| **C-Mn Steel** | 30μA/cm$^2$ | 79μA/cm$^2$ | 1410μA/cm$^2$ |
| **Cast iron** | 43μA/cm$^2$ | 364μA/cm$^2$ | 2210μA/cm$^2$ |

Fig. 5.18. Corrosion current densities ($i_{corr}$) for the cast iron and C-Mn steel at 50°C in 3.5%NaCl under static, liquid erosion and liquid-solid erosion conditions.

In contrast, stainless steels in many circumstances exhibit good general corrosion resistance and it has been shown in chapter 4 that under the severe seawater impinging jet at 50°C, passive behaviour is still observed, as in static conditions. The behaviour in 3.5%NaCl under liquid erosion is virtually identical to that in synthetic seawater as expected. The direct influence of liquid impingement at 100m/s was to cause a positive shift in $E_{corr}$ and to promote small reductions in the passive potential range during anodic polarisation. In other words the consequence of an impinging jet on the surface of the stainless steels was very modest. The Co-base alloy, Ultimet, and the Ni-base Inconel 625 displayed very similar passive characteristics to the stainless steels under liquid erosion, but tended to show an enhanced resistance to passivity breakdown compared to static conditions (see chapter 4). In contrast, drastic changes in the behaviour of these materials were brought about by the presence of sand particles in the impinging NaCl solution. These changes are clear in Figs. 5.19a, b and c which show that on the austenitic (UNS S31603), the standard 25Cr duplex and the superduplex (UNS S32760) the free corrosion potential during liquid-solid erosion was considerably more negative (active) than in static and liquid erosion (in contrast to the situation on the cast iron and the C-Mn steel).. More importantly, the figures demonstrate via the high currents recorded immediately upon shifting the potential from $E_{corr}$, a transition to active corrosion in these particularly severe liquid-solid impingement conditions.

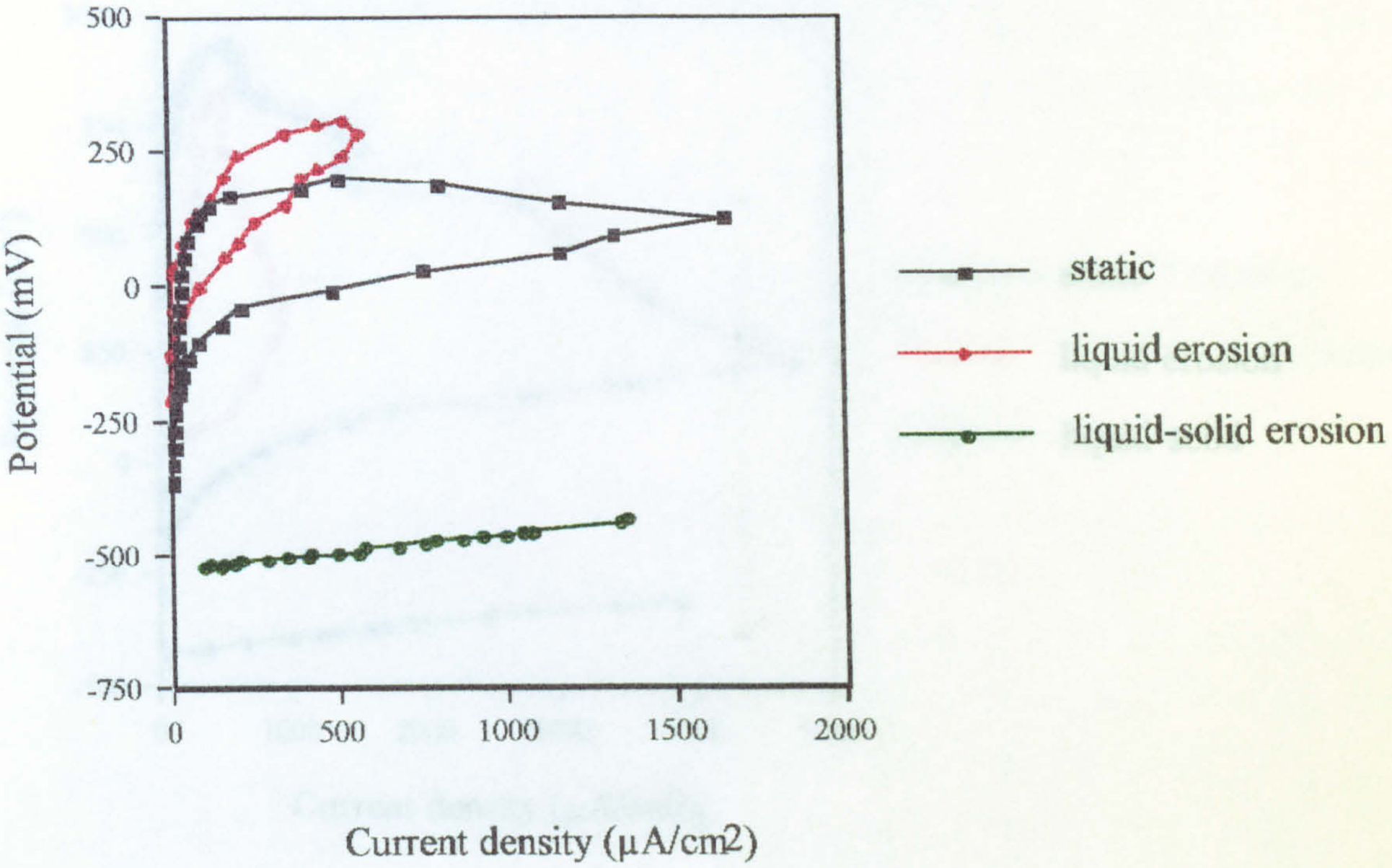
500
250
0
-250
-500
-750
Potential (mV)
0
500
1000
1500
2000
Current density (μA/cm2)
static
liquid erosion
liquid-solid erosion

(a)

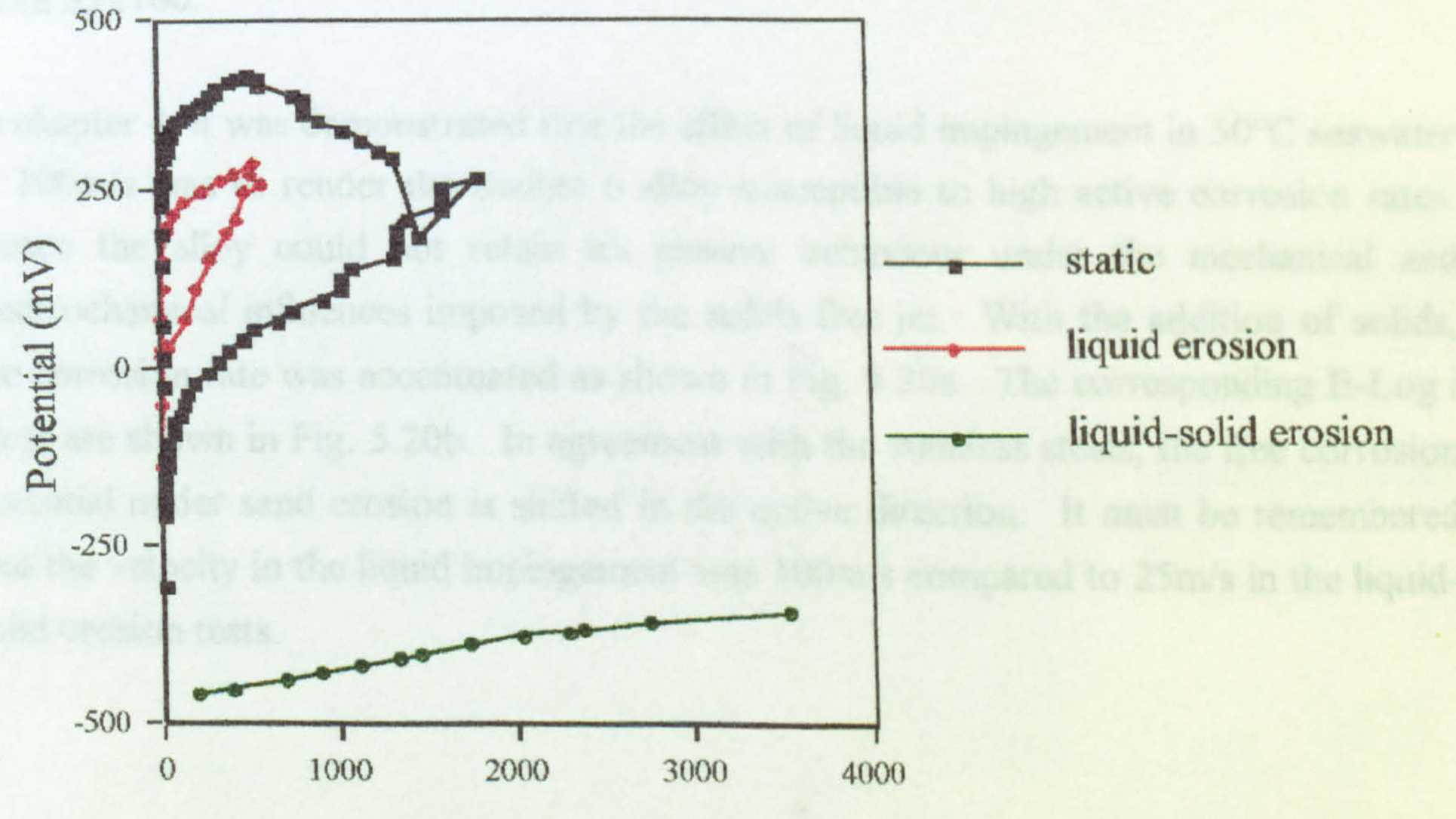
500
250
0
-250
-500
Potential (mV)
0
1000
2000
3000
4000
Current Density (μA/cm2)
static
liquid erosion
liquid-solid erosion

(b)

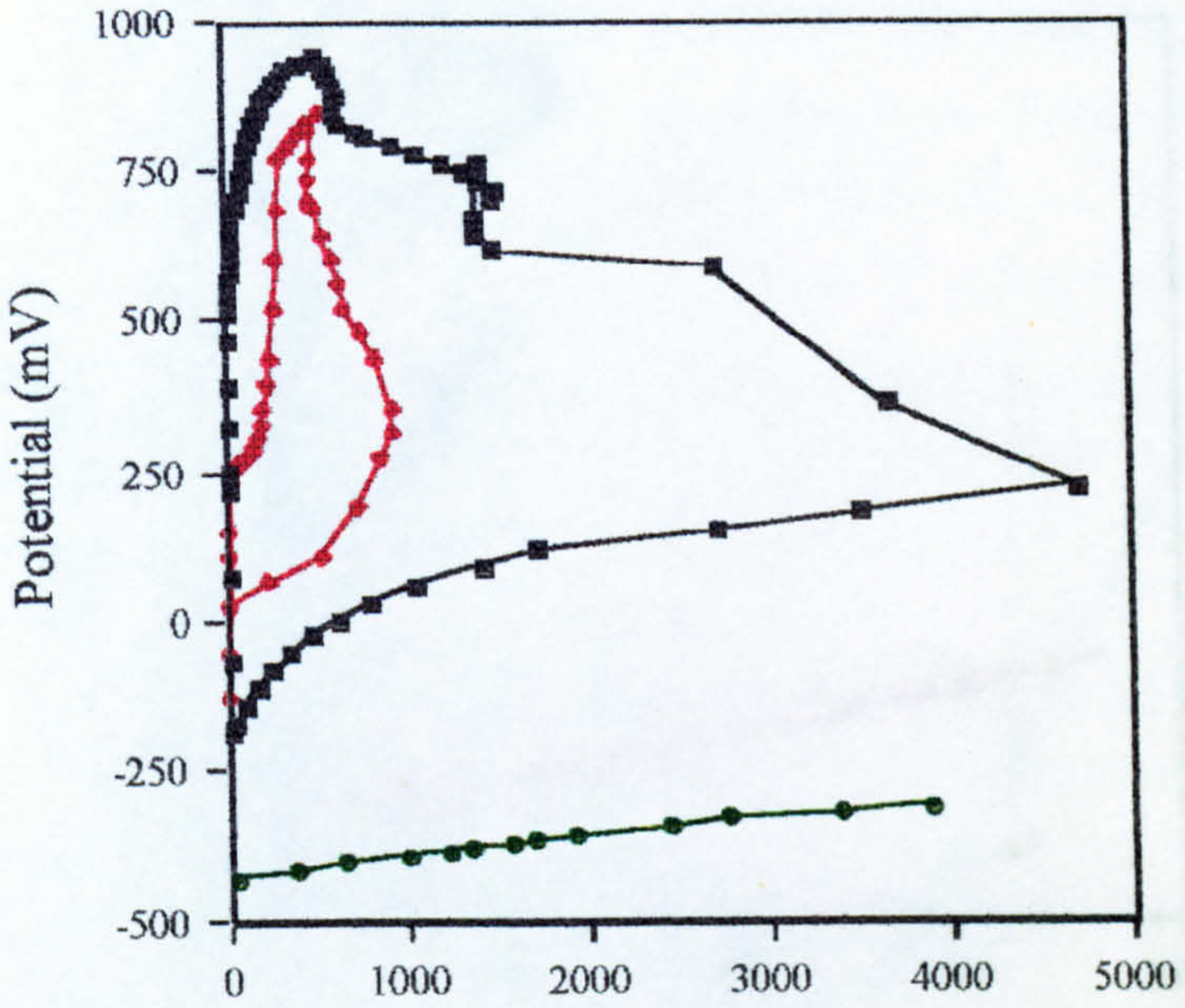


(c)

Fig. 5.19. Comparison of anodic polarisation in static, liquid erosion and liquid-solid erosion conditions at 50°C on (a) UNS S31603, (b) 25Cr duplex and (c) superduplex UNS S32760.

In chapter 4, it was demonstrated that the effect of liquid impingement in 50°C seawater at 100m/s was to render the Stellite 6 alloy susceptible to high active corrosion rates. Hence the alloy could not retain it's passive behaviour under the mechanical and electrochemical influences imposed by the solids-free jet. With the addition of solids, the corrosion rate was accentuated as shown in Fig. 5.20a. The corresponding E-Log i plots are shown in Fig. 5.20b. In agreement with the stainless steels, the free corrosion potential under sand erosion is shifted in the active direction. It must be remembered that the velocity in the liquid impingement was 100m/s compared to 25m/s in the liquid-solid erosion tests.

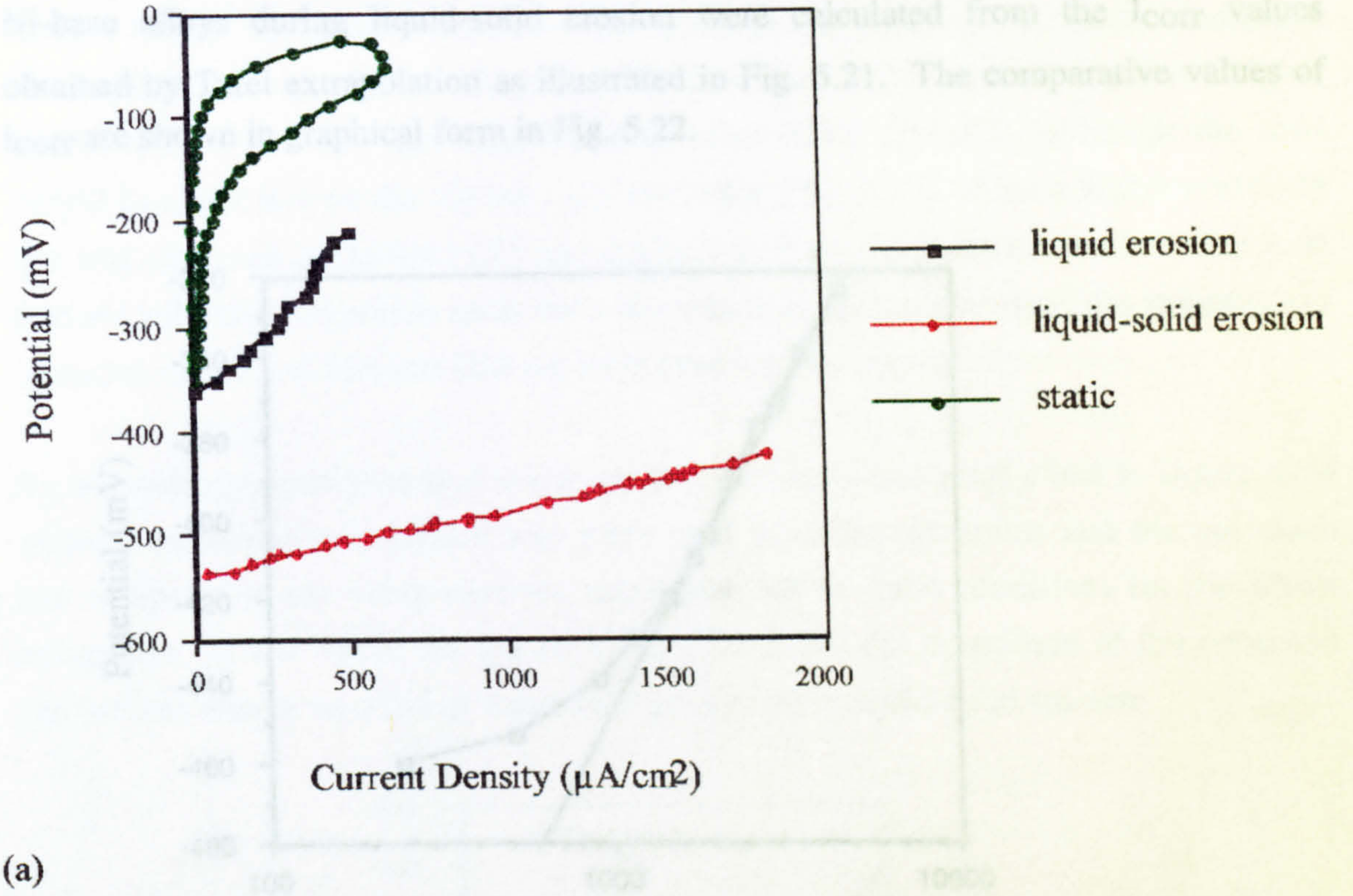


(a)

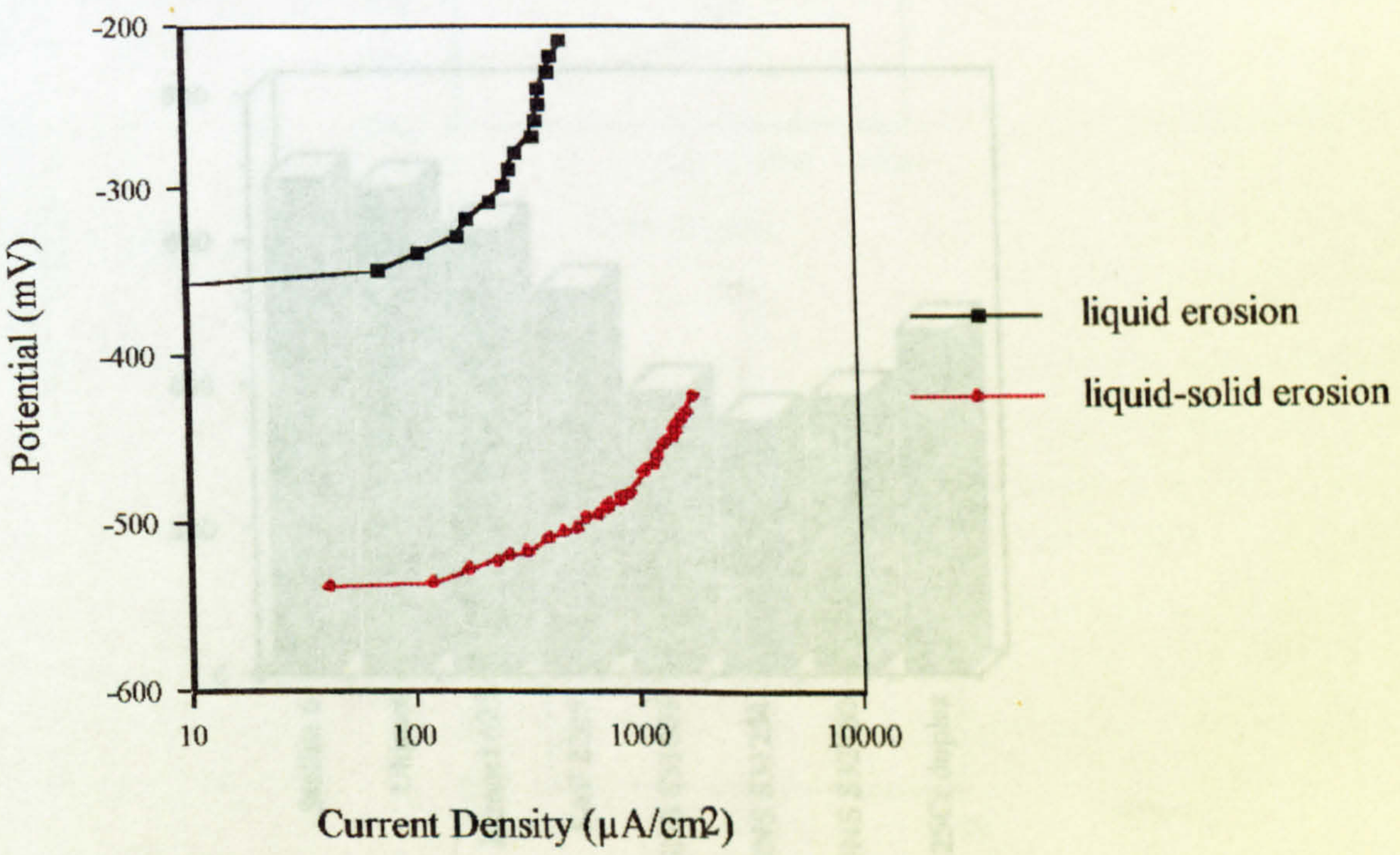


(b)

Fig. 5.20. Anodic polarisation showing increased corrosion rate in liquid-solid erosion (a) in linear form with static condition comparison and (b) in E-Log i form

As for cast iron and C-Mn steel, the rates of corrosion of stainless steels, Co-base and Ni-base alloys during liquid-solid erosion were calculated from the $I_{corr}$ values obtained by Tafel extrapolation as illustrated in Fig. 5.21. The comparative values of $i_{corr}$ are shown in graphical form in Fig. 5.22.

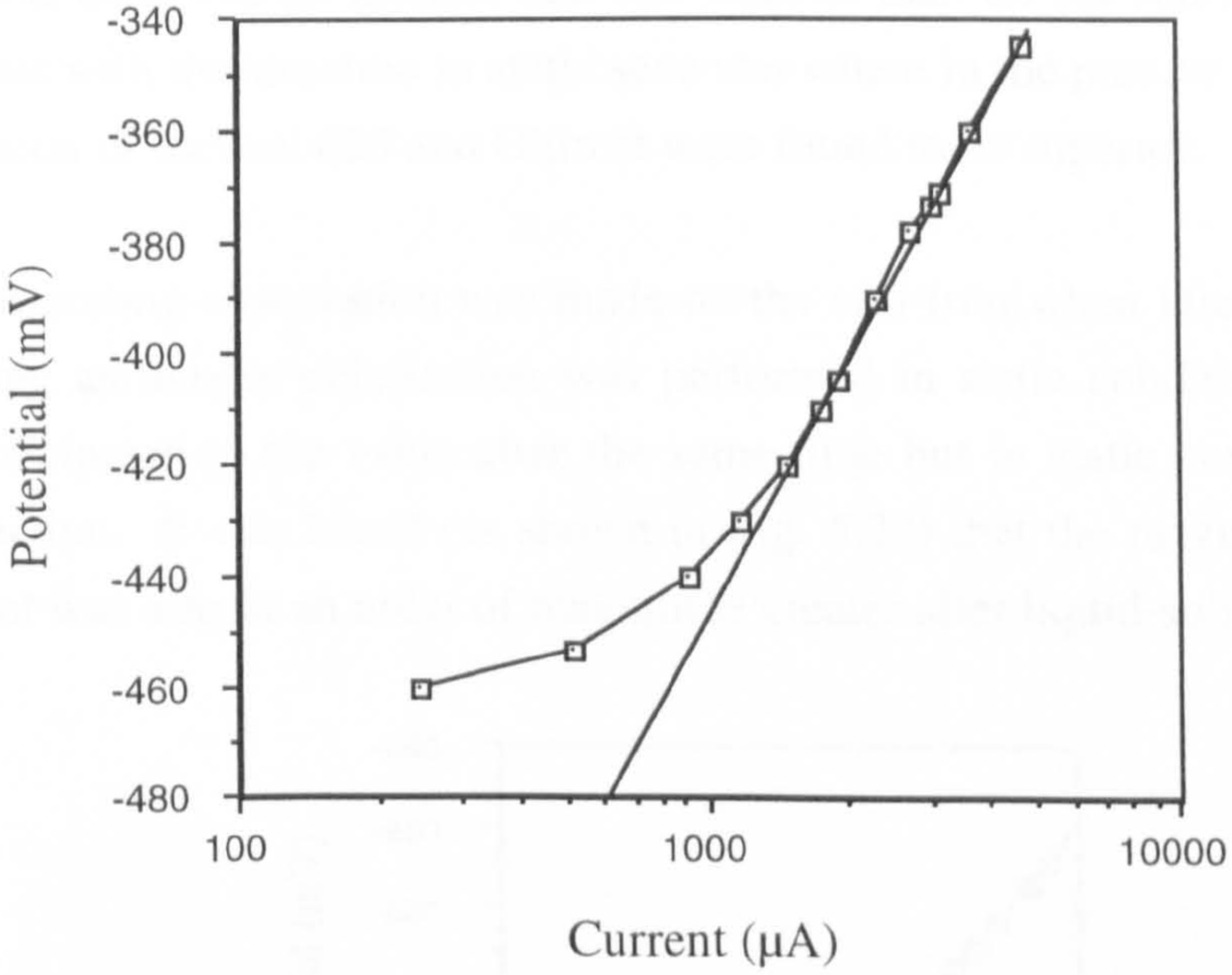


Fig. 5.21. Tafel extrapolation for the 25Cr duplex under liquid-solid erosion

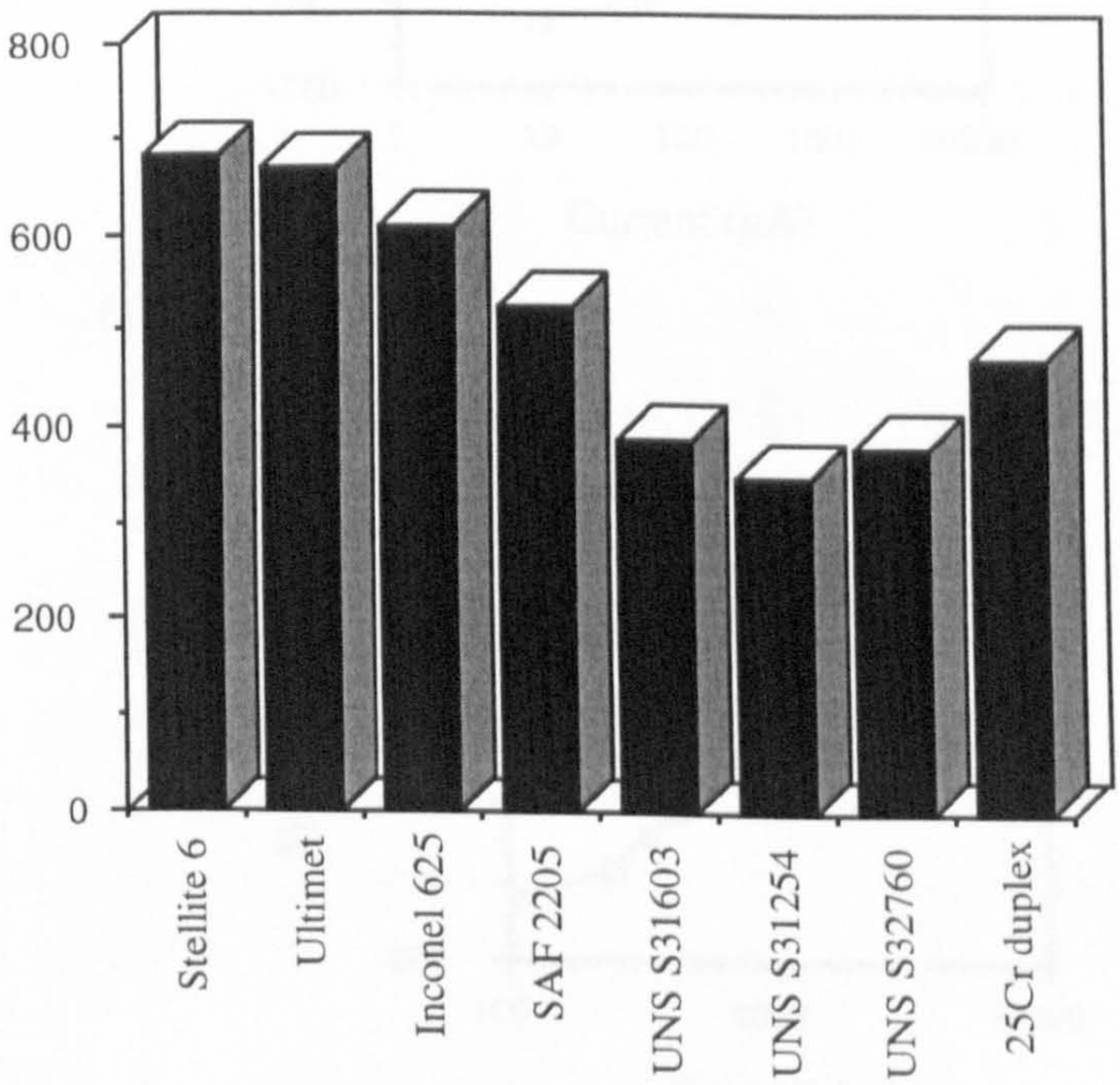


Fig. 5.22. Corrosion current densities of the 'active' stainless steels, Co-base and Ni-base alloys during liquid-solid erosion in 3.5% NaCl at 50°C. Six results taken for each material from three test runs.

From Fig. 5.22, it can be seen that the trends in corrosion rate of the materials does not directly follow the relative behaviour (as given in the rankings) in static conditions. More precisely, the duplex alloys (SAF 2205 and 25Cr duplex) exhibit a higher corrosion rate than the austenitic stainless steel (UNS S31603), although the total weight loss was less on the duplex stainless steels (Fig. 5.13). Also a higher corrosion rate was observed on Inconel 625 and Ultimet than on the stainless steels which is in contrast with the situation in static seawater where in the passive state, the resistance to corrosion of Inconel 625 and Ultimet were found to be superior.

An interesting observation was made on the cast iron when after a test in liquid solid erosion, an anodic polarisation was performed in static conditions and the corrosion rate compared to the value after the same time but in static conditions for the whole immersion. It was found (as shown in Fig. 5.23) that the magnitude of the corrosion current was almost an order of magnitude greater after liquid-solid erosion.

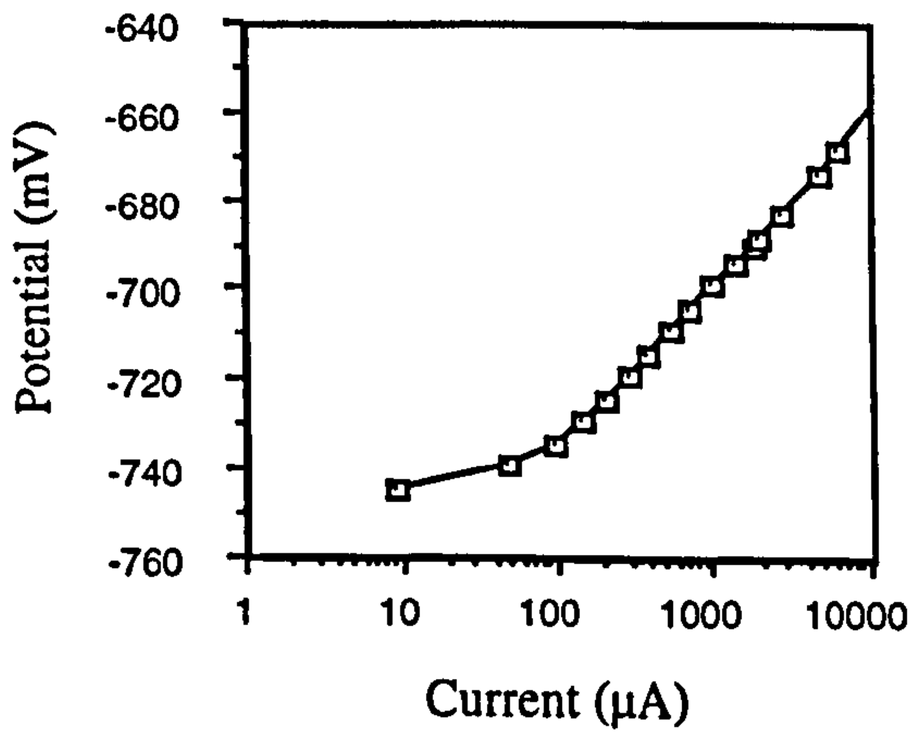


(a)

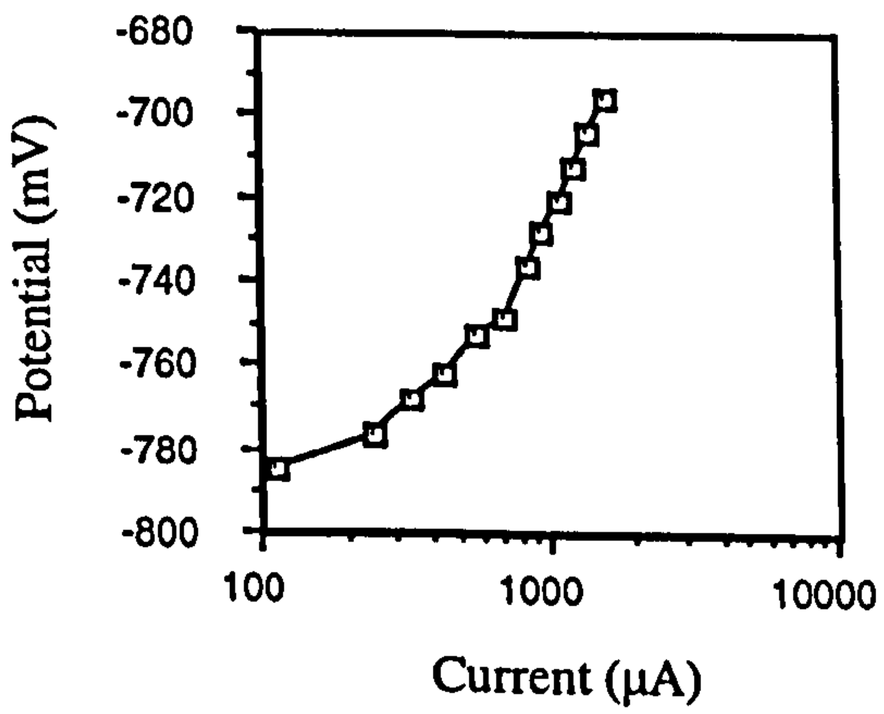


(b)

Fig. 5.23. Anodic polarisation (a) in static conditions and (b) after sand erosion on cast iron at 50°C

Cathodic Potentiodynamic Tests

Only limited cathodic polarisation tests were done in this part of the study, used mainly as a validation of the $I_{corr}$ from anodic polarisation tests. As can be seen in Fig. 5.24, there is a severe depolarisation of the cathodic reaction under liquid-solid erosion, compared with liquid erosion. If the rate of reaction was purely dictated by the rate of supply of oxygen to the surface of the electrode then it is surprising to find that the presence of solids enhances the reaction rate. Hence it is suggested that the surface state of the electrode is important and from that respect an active surface promotes a higher cathodic reaction rate. The mechanism for this is not fully understood but has perhaps relevance to the effect of the oxide film.

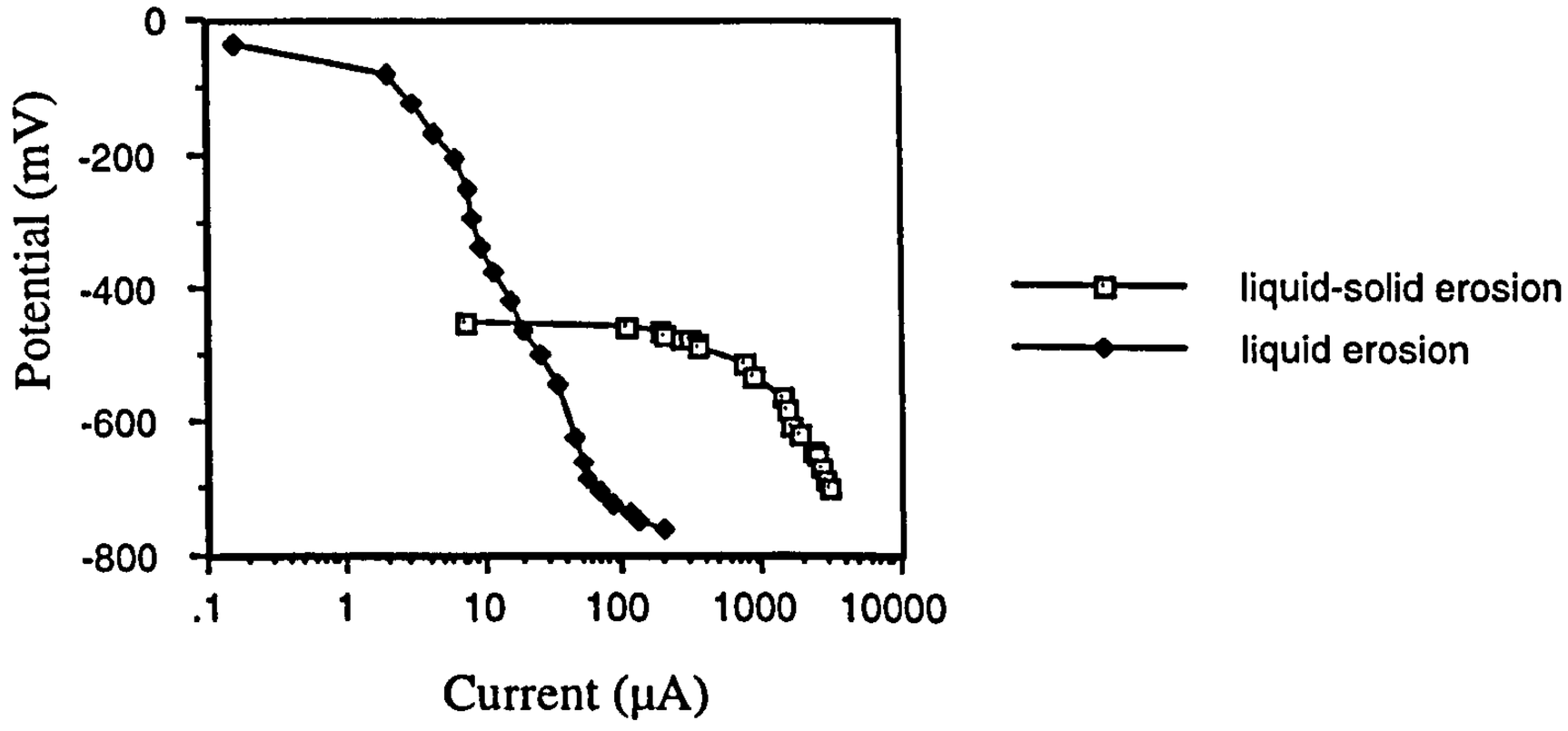


Fig. 5.24. Cathodic depolarisation with solids present in impingement on UNS S32760

Potentiostatic Tests

Potentiostatic tests were performed in this work for three main purposes. The principal intention was to apply cathodic protection to the specimens in-situ to enable the pure corrosion component of weight loss to be eliminated. Secondly a series of tests performed under potentiostatic control at a potential of 50mV more positive than $E_{corr}$ were used in order to quantify different rates of depassivation of the passive alloys due to sand impingement and also repassivation trends. Thirdly, tests were performed under anodic potentiostatic control to assess the effect of an applied anodic potential on the total weight loss.

*Cathodic Protection*

As anticipated, on application of cathodic protection during the liquid-solid erosion test, a reduction in the Total Weight Loss (TWL) was recorded for each material which, when combined with the data from the electrochemical measurements, was shown to be greater than that due to solely corrosion. A synergistic effect defined as the enhancement of the TWL due to the effect of *corrosion* on the *erosion* process was therefore identified and quantified for each material. This concept, shown to be strongly material dependent, is best illustrated in the diagrammatic form of Figs. 5.25a-j. The actual weight losses attributed to erosion, corrosion and the synergy are presented in Fig. 5.26. The data in mg is presented in Table 5.1 at the end of the 'Results' section.

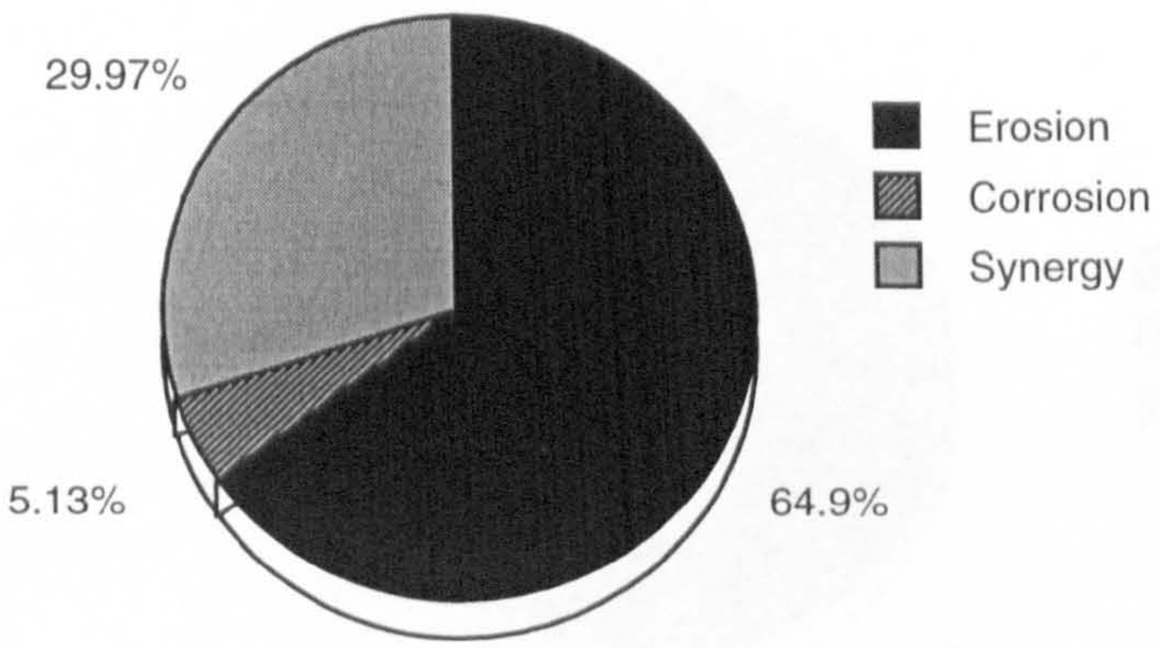


(a) C-Mn steel

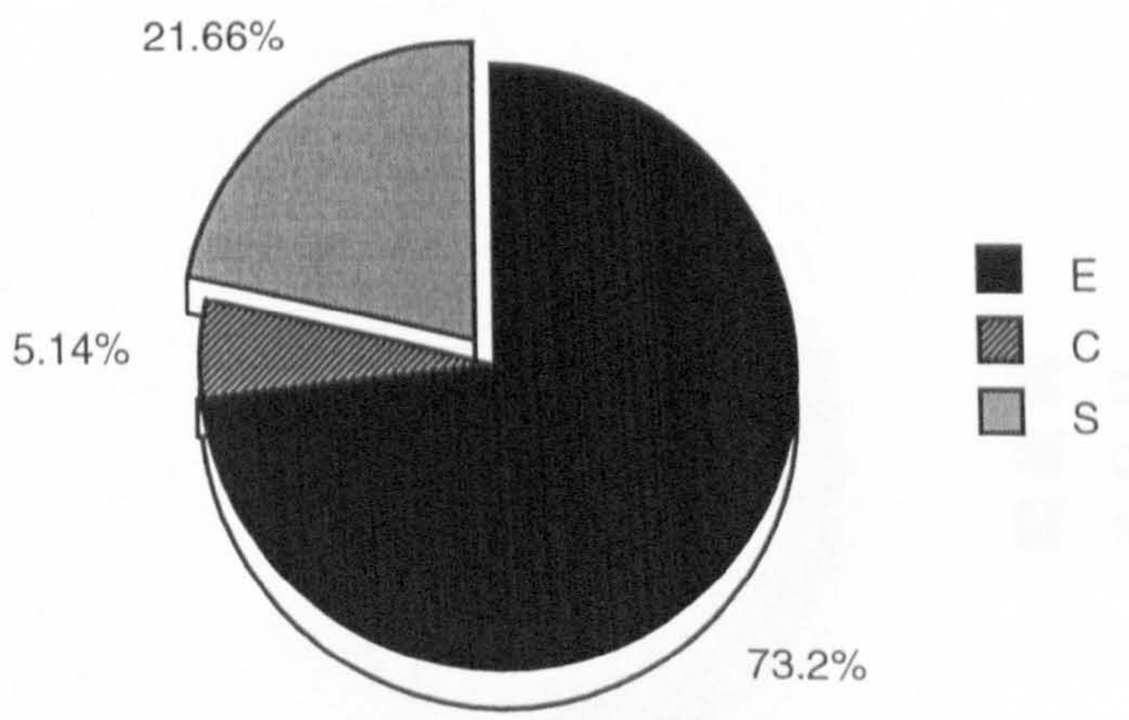


(b) Stellite 6

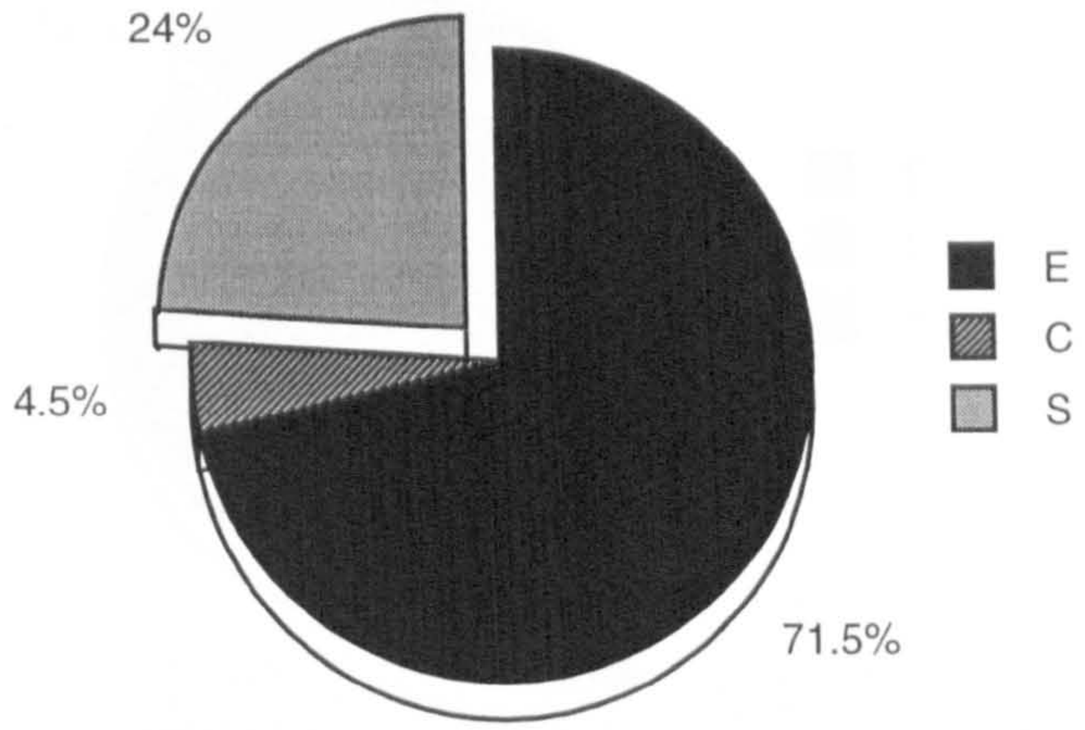


(c) Inconel 625

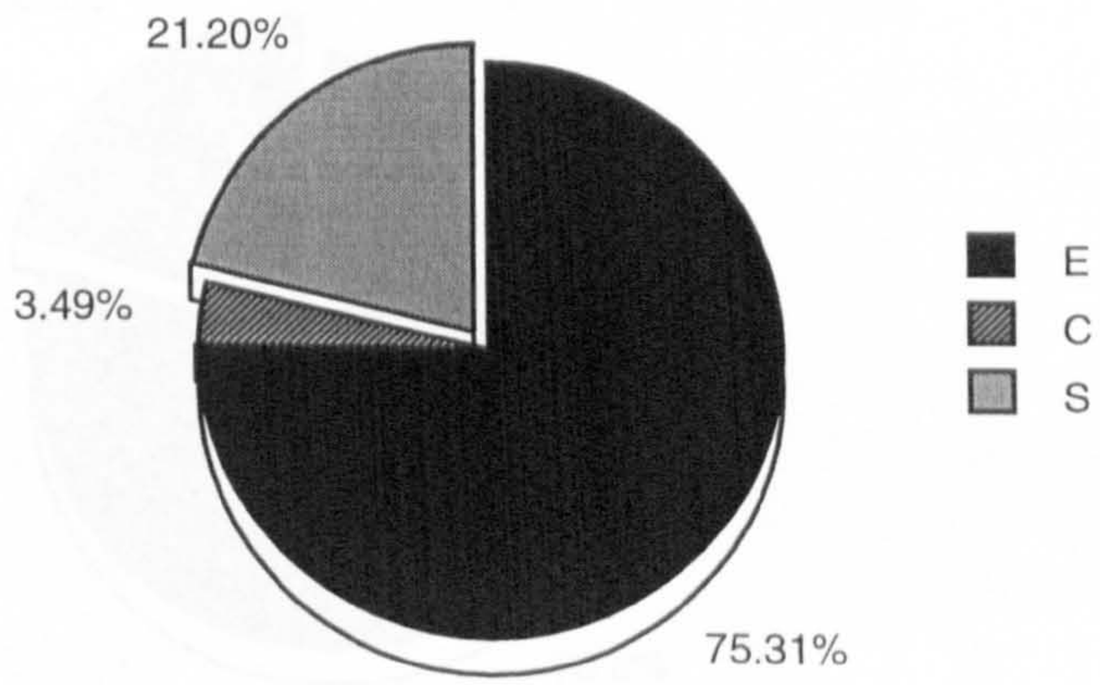


(d) SAF 2205

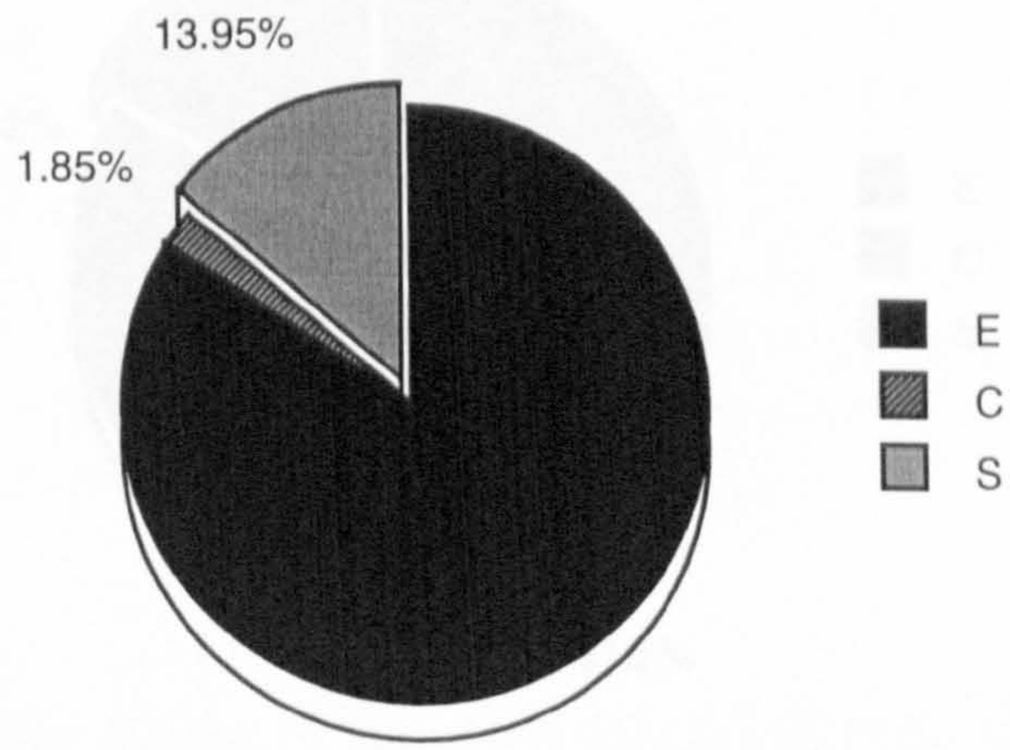


(e) UNS S31254

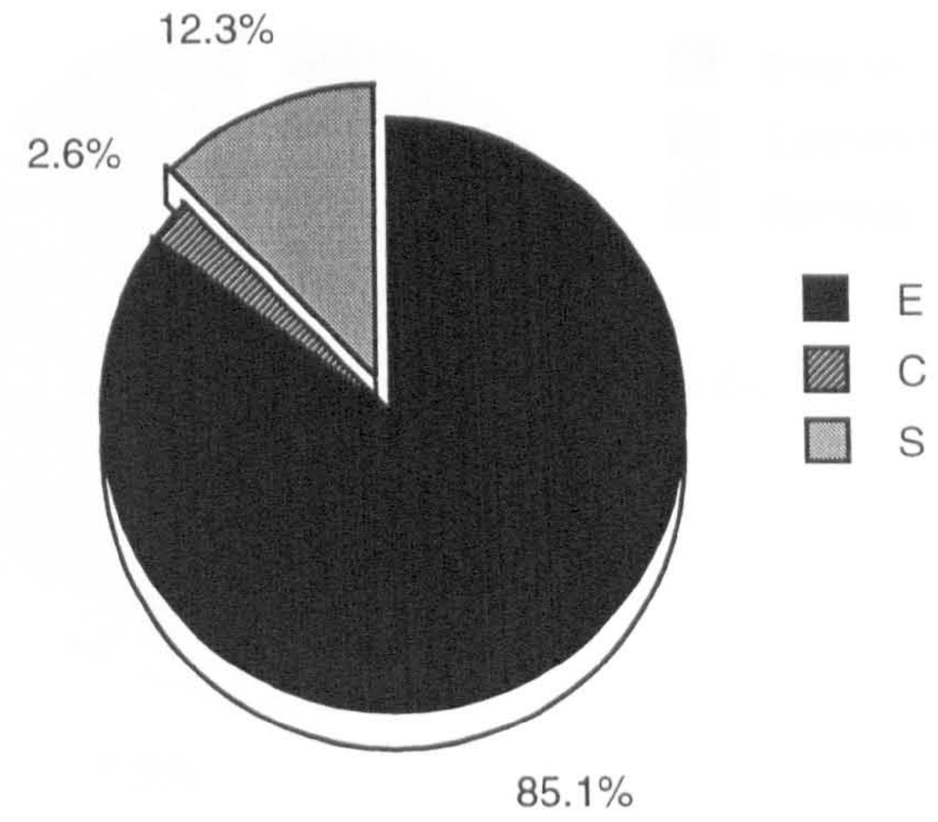


(f) UNS S32760

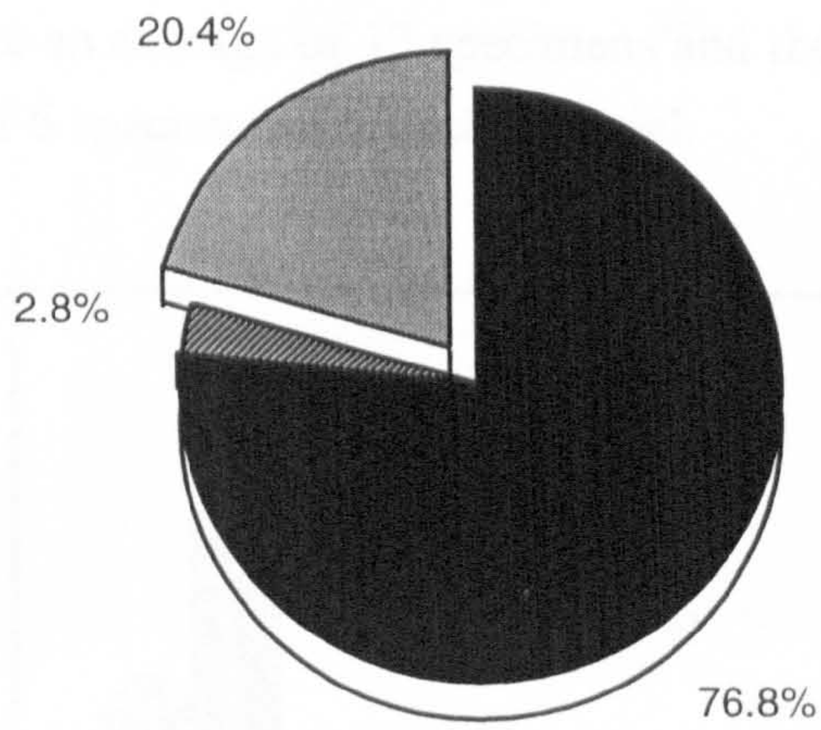


(g) 25Cr duplex

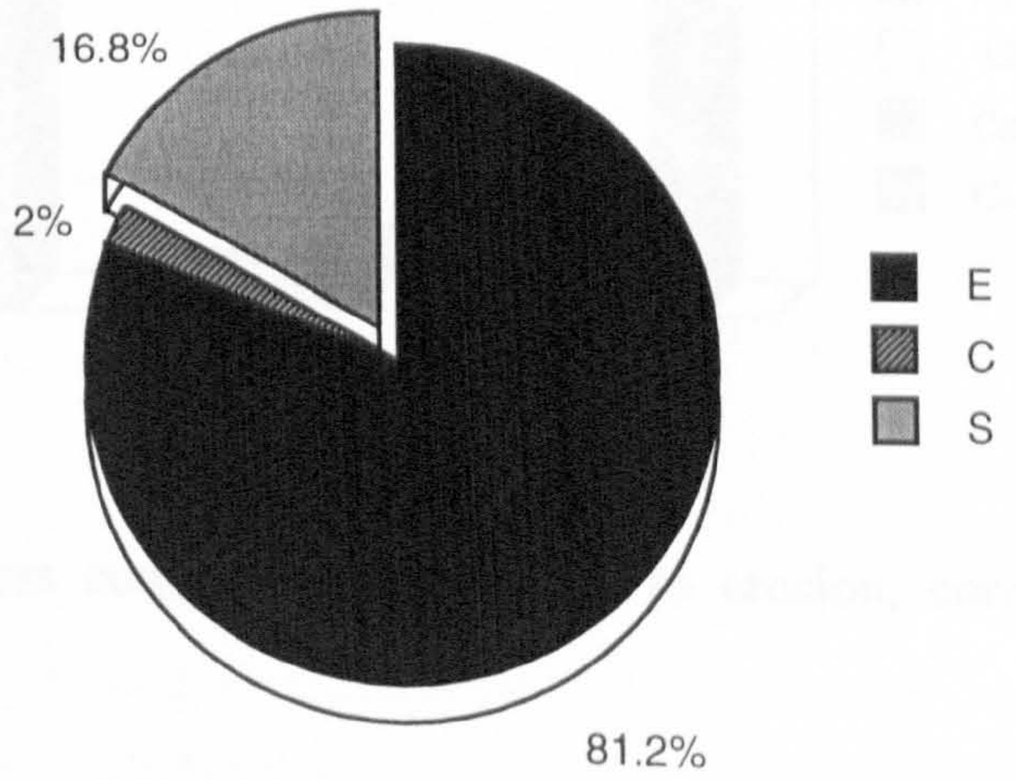


(h) UNS S31603

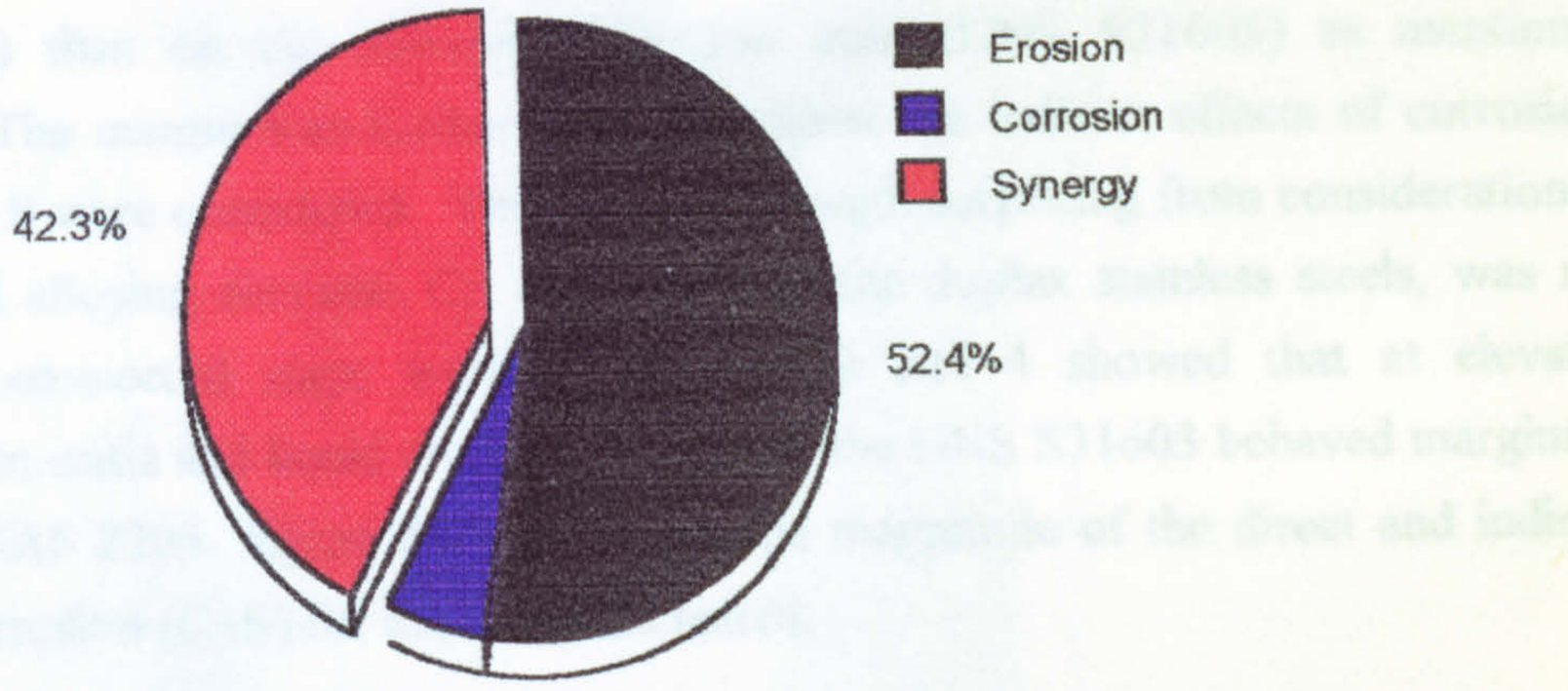


(j) Cast Iron

Fig. 5.25. Proportions of total weight loss due to erosion, corrosion and the synergistic factor in 3.5%NaCl at 50°C. Total weight losses used for calculation of the proportions of weight loss were an average of 12 specimens and the corrosion and CP weight losses were an average of 6 specimens for each material.

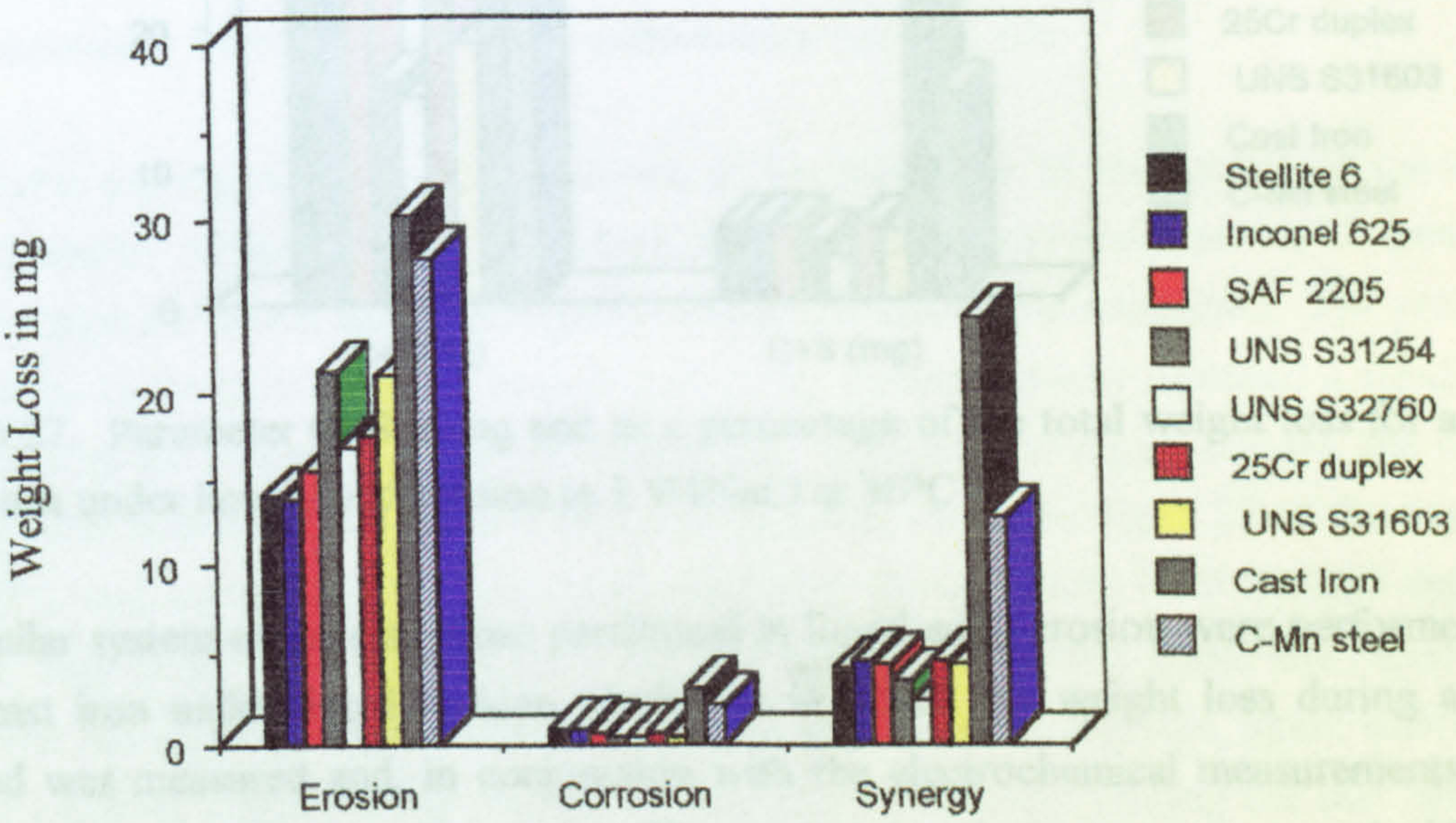


Fig. 5.26. Actual weight loss components in mg due to erosion, corrosion and the synergistic factor

As can be seen from the distribution of the total weight loss, the pure corrosion component (measured by electrochemical techniques) of weight loss is very small. However, the component, S, the synergistic component is a measure of how the corrosion affects the total weight loss by it's interaction with the mechanical erosion process. Hence assessment of the effect of corrosion must take into consideration the corrosion and the synergistic components (C+S). It can be seen that the pure corrosion component of weight loss was greater on the duplex stainless steels (SAF 2205 and

25Cr duplex) than on the austenitic stainless steel (UNS S31603) as mentioned previously. The margin was further increased when the indirect effects of corrosion, quantified by S were considered. This finding although surprising from consideration of the increased alloying elements Cr, Mo and N in the duplex stainless steels, was not completely unexpected since work in chapters 2 and 4 showed that at elevated temperature in static and liquid erosion conditions, the UNS S31603 behaved marginally better than SAF 2205. Figure 5.27 illustrates the magnitude of the direct and indirect effects of corrosion (C+S) for the materials tested.

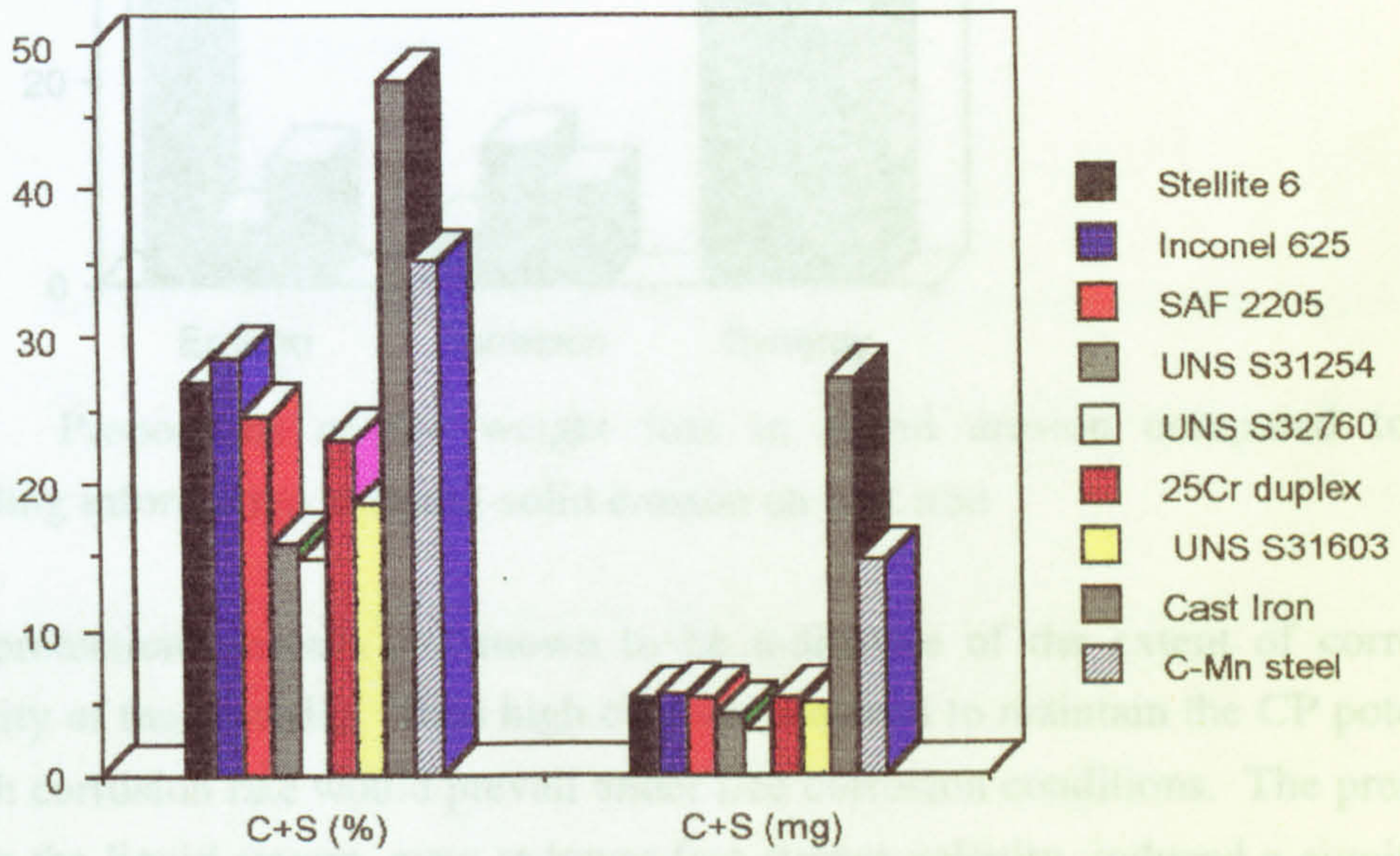


Fig. 5.27. Parameter C+S in mg and as a percentage of the total weight loss for a one hour test under liquid-solid erosion in 3.5%NaCl at 50°C

A similar system of tests to those performed in liquid-solid erosion were performed on the cast iron under liquid erosion conditions in which the weight loss during a test period was measured and, in conjunction with the electrochemical measurements, the proportions of weight loss due to the different deterioration processes were elucidated. The tests were performed at 18°C and at 50°C. After a one hour test period, the weight loss was very small and therefore could not be measured accurately. Therefore the tests were run over a 24 hour period and an average weight loss was measured for the hour period to compare with liquid-solid erosion. The specimens were in the form of pins as were used in the liquid-solid erosion tests. Figure 5.28 shows the reversal of the proportion of the weight loss due to erosion comparing liquid erosion and solid-liquid erosion on the cast iron. The weight losses in mg are presented in Table 5.2.

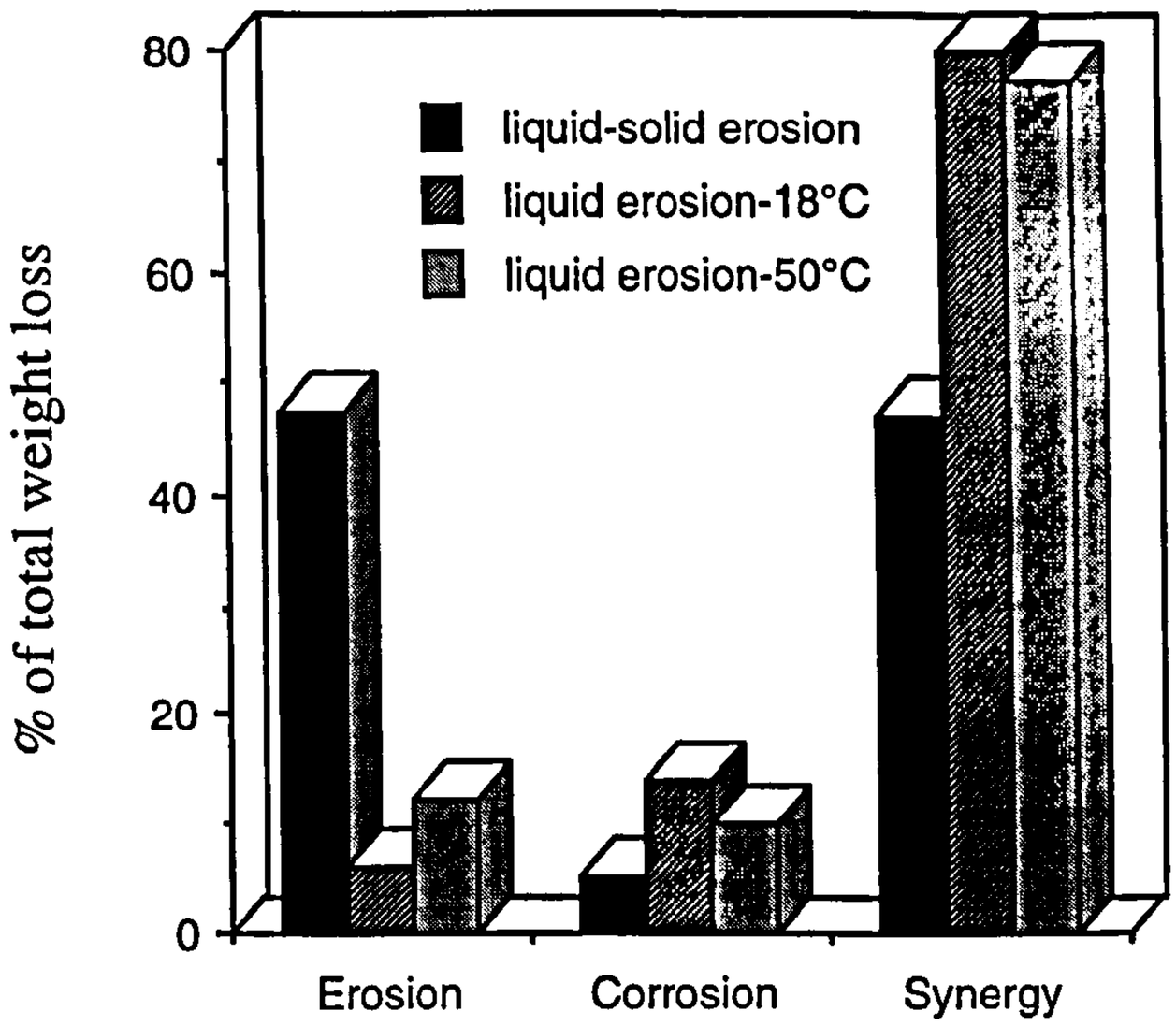


Fig. 5.28. Proportions of the weight loss in liquid erosion compared to the corresponding information in liquid-solid erosion on cast iron

Cathodic protection currents are known to be indicative of the extent of corrosion susceptibility of the material. Thus high currents required to maintain the CP potential infer a high corrosion rate would prevail under free corrosion conditions. The presence of solids in the liquid stream, even at lower free stream velocity, induced a significant increase in the current requirement during CP. Compared to liquid erosion, the liquid-solid erosion demand was almost four times greater, shown in Fig. 5.29 on the cast iron at 50°C and was more than four times greater on the austenitic UNS S31603 stainless steel, Fig. 5.30. Similarly to the corrosion currents measured under the liquid-solid erosion, the CP currents were found to be very dependent on material, again with C-Mn steel and cast iron distinctly registering higher CP currents. During the one hour test period (starting after 20 minutes warm up period), the CP currents were found to fall on all materials with the exception of cast iron and Stellite 6. The current on cast iron, as shown previously in Fig. 5.29, remained relatively constant over the test period whereas in Fig. 5.31, it can be seen that the current on Stellite 6 increased significantly. The maximum cathodic protection currents for all the materials are given in Table 5.3.

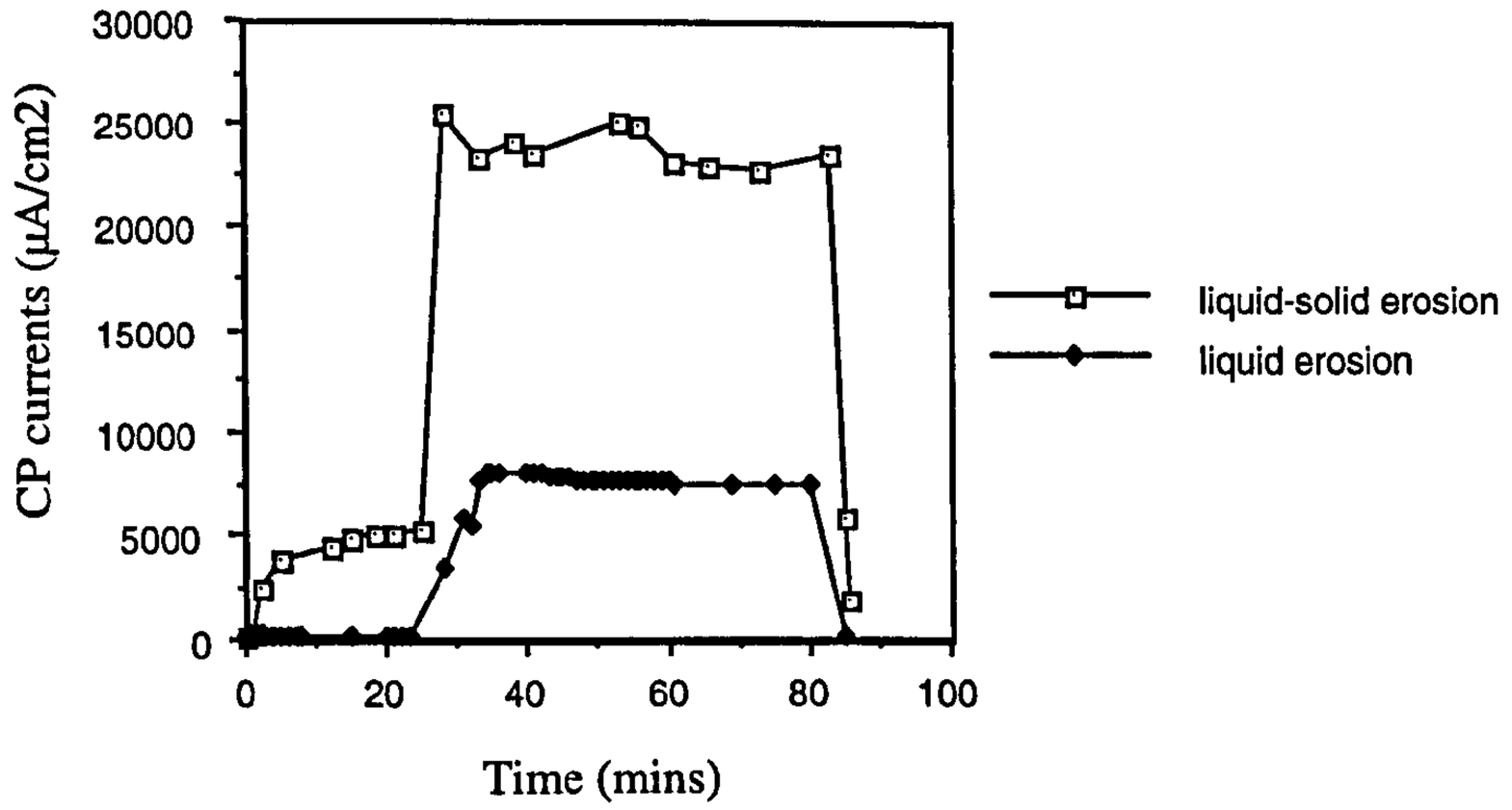


Fig. 5.29. Cathodic protection currents on cast iron under liquid and liquid-solid erosion on cast iron at 50°C

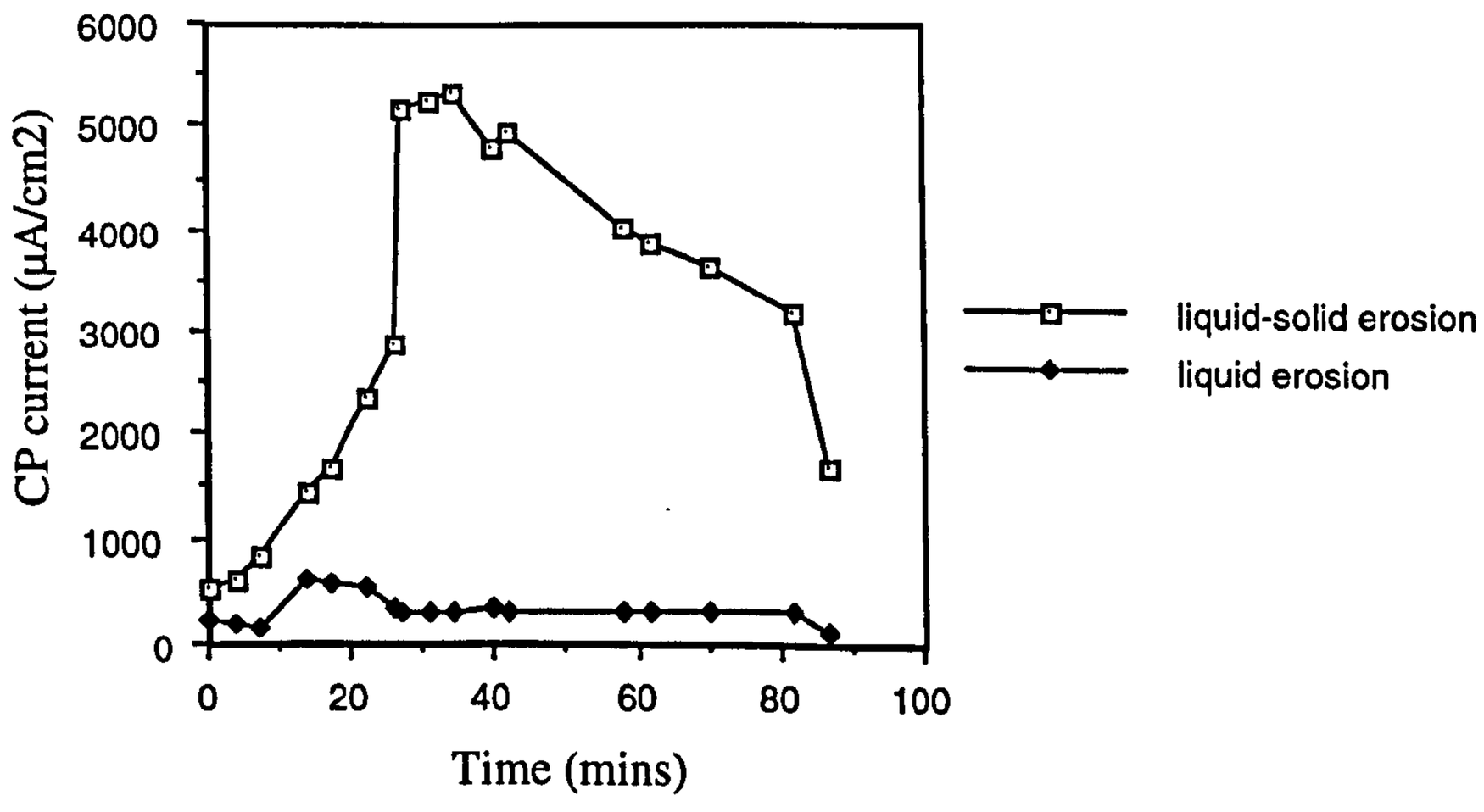


Fig. 5.30. Cathodic protection currents on UNS S31603 under liquid erosion and liquid-solid erosion at 50°C

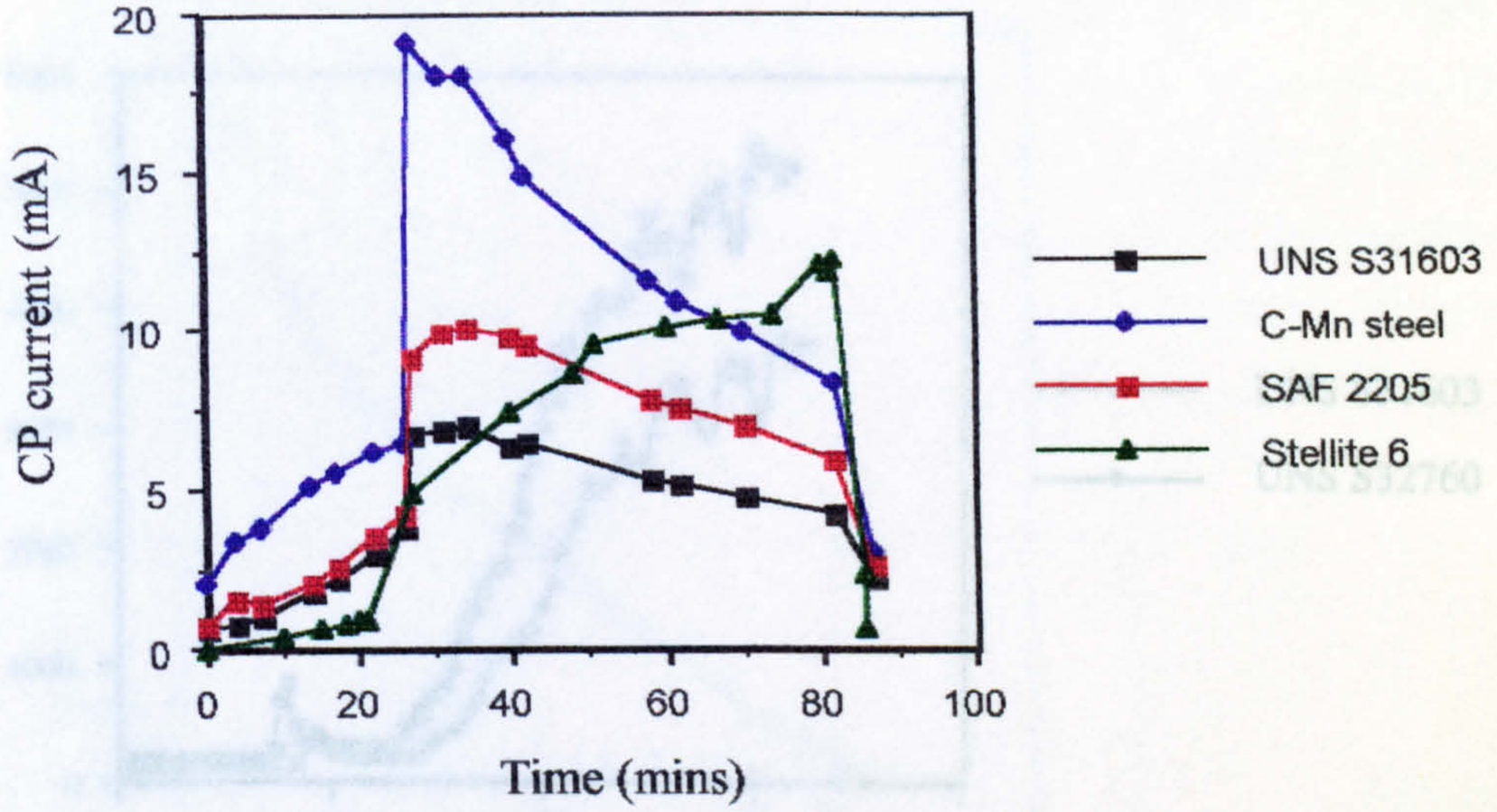


Fig. 5.31. Cathodic protection currents during liquid-solid erosion at 50°C

*Anodic Potentiostatic Tests*

In a system of potentiostatic tests, analogous to those under applied cathodic protection, the potential of specimens of selected materials was held at 50mV more positive than $E_{corr}$ and the resulting current recorded. The use of high frequency data logging enabled the progression of the current to be followed at the moment the solid particle impingement started and also once it ended. Figure 5.32 shows on the austenitic stainless steel UNS S31603 and on the superduplex stainless steel UNS S32760 the rapid increase in current due to the ability of the sand in the liquid stream to remove the passive film and render the surface active. Hence the large increase in current signifies the depassivation process and Fig. 5.32 shows the slower rate of increase of anodic current on UNS S32760 than on UNS S31603. In addition UNS S32760 attained a lower absolute current value as would be expected since, during anodic polarisation tests, UNS S32760 exhibited a lower corrosion current. The current increased on the C-Mn steel but not by as great a proportion since the initial current was larger.

On removing the liquid-solid impingement, the current fell off quickly as shown in Figure 5.33a. There was very little difference between the austenitic stainless steel and the superduplex in the rate of current decrease but the final current on UNS S31603 was larger. Figure 5.33b shows the corresponding data for C-Mn steel where it can be

seen that the absolute fall in current is larger but it decreases steadily and not as a sharp rapid decrease as on the stainless steels.

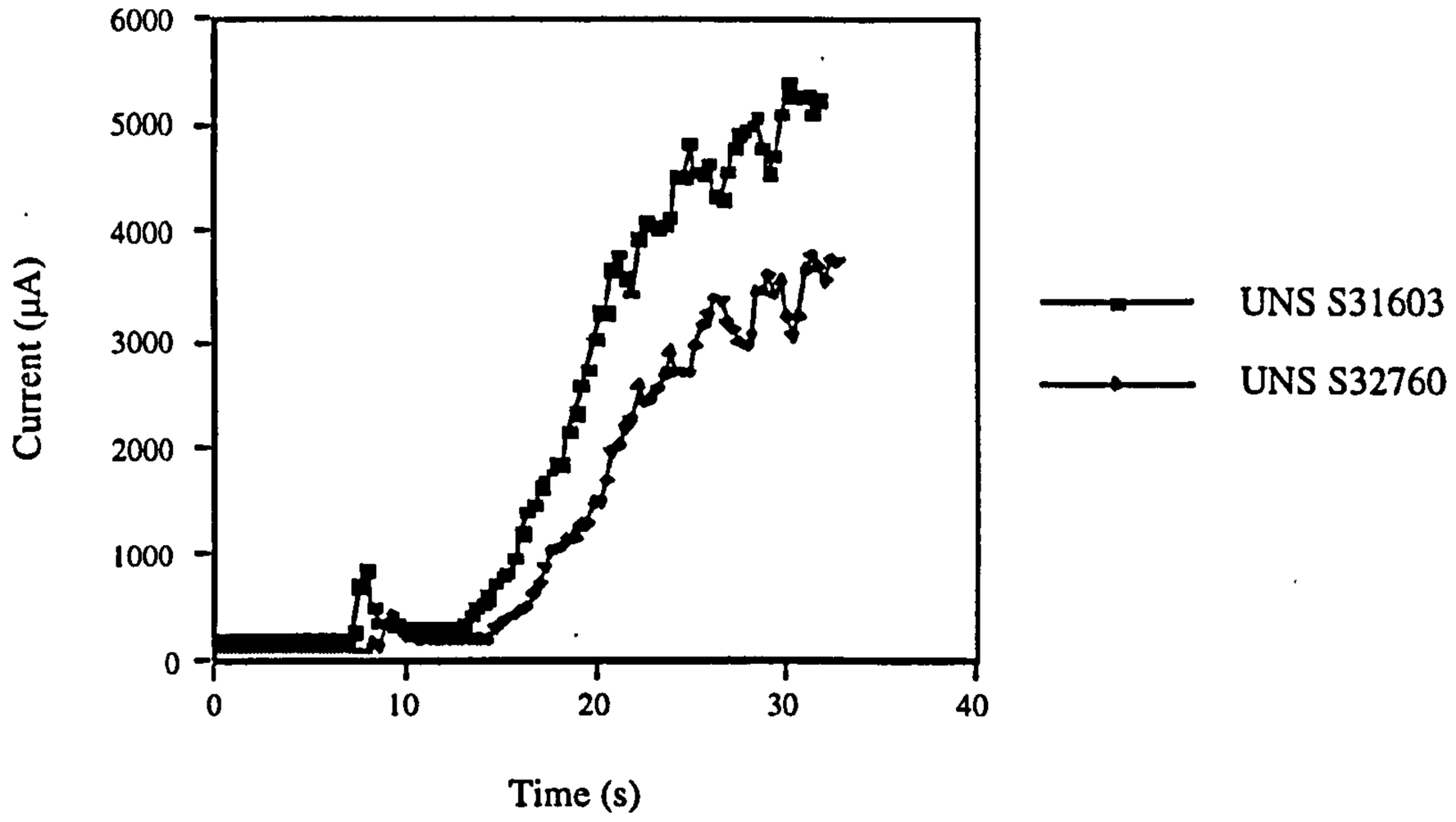


Fig. 5.32. Breakdown of the passive film by sand addition, represented in a significant increase in current. Potential held at 50mV more positive than $E_{corr}$. On UNS S31603, -430mV and on UNS S32760, -410mV. In 3.5%NaCl at 50°C.

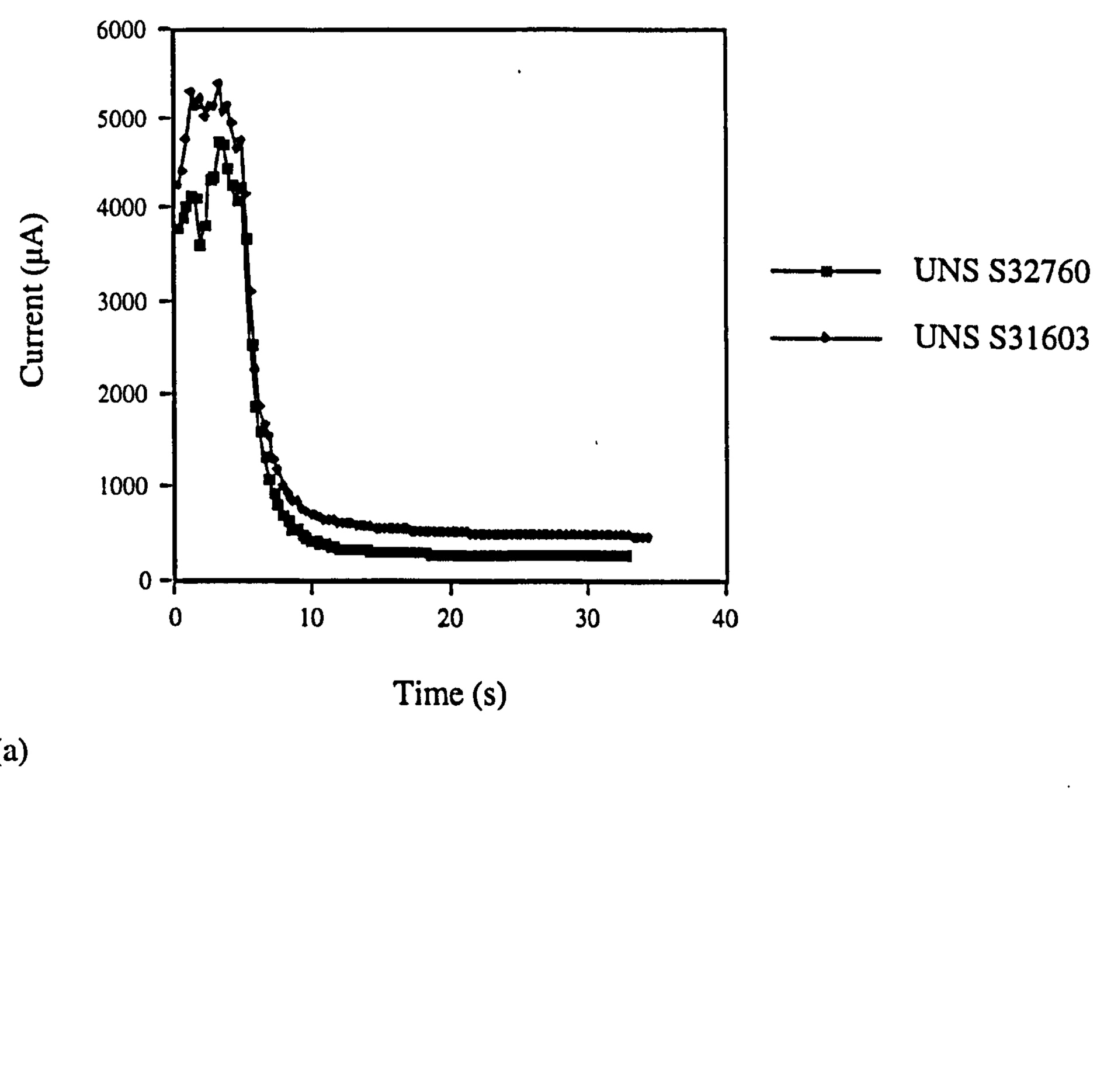


(a)

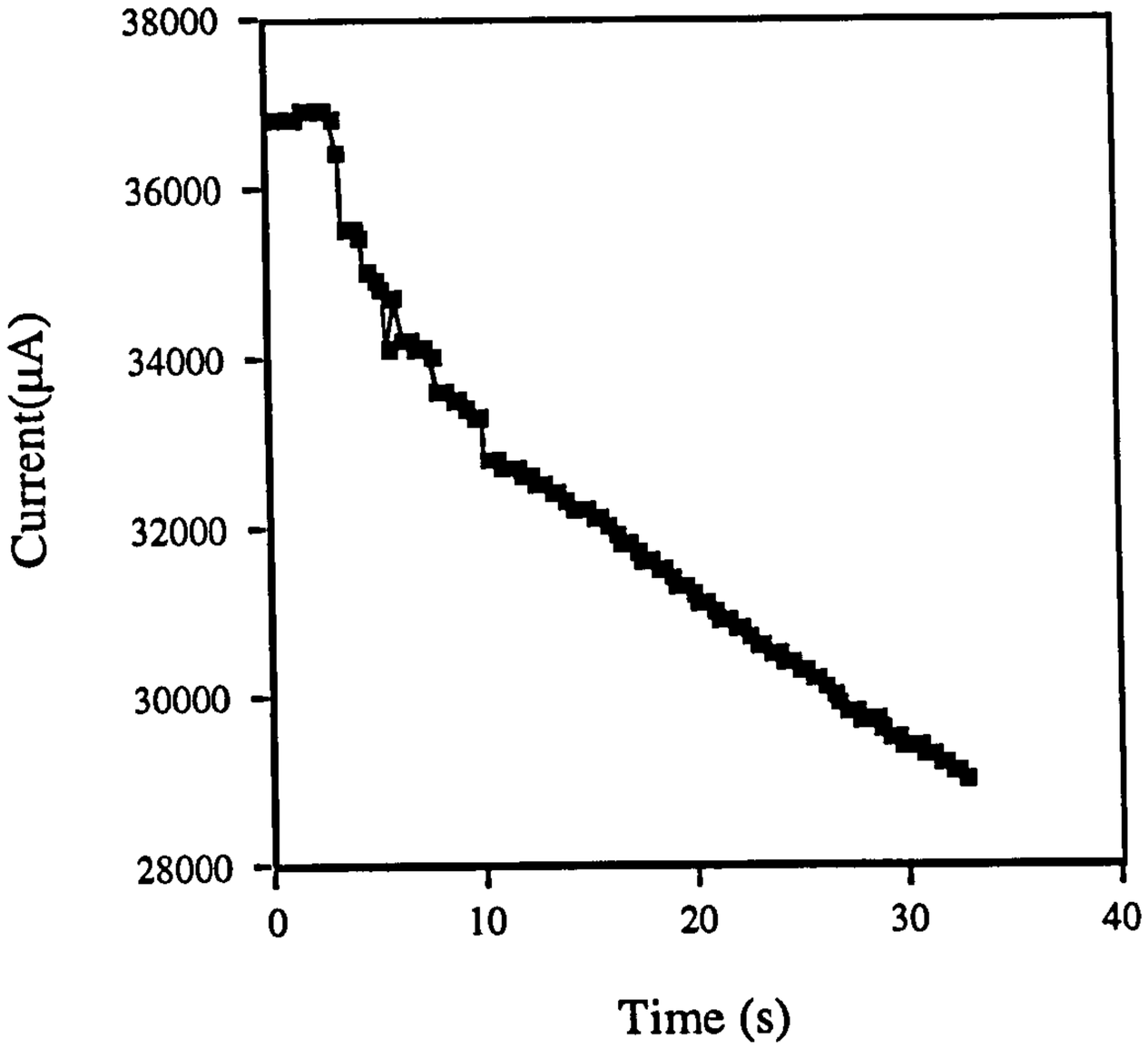


(b)

Fig. 5.33. Decrease in current on UNS S31603 after removal of eroding stream and (b) fall in current as liquid-solid impingement is stopped on C-Mn steel

A short final set of potentiostatic tests was carried out on Stellite 6 which involved a potential of +600mV (SCE) being applied to the material during the whole test. The applied potential was very much more positive than $E_{corr}$ (typically -450mV-500mV) and the intention was to induce a high anodic current and therefore a high rate of metal dissolution during the one hour test. The weight loss was then compared to the weight loss of Stellite 6 under free corrosion conditions in order to assess whether there was an analogous synergistic factor to that defied after application of cathodic protection, which accentuated the weight loss by more than the corrosion element imposed by potentiostatic control. The weight loss on three potentiostatically controlled specimens were compared to the weight loss on specimens under the free corrosion potential. It was found that there was an increase in the weight loss of 80% of the free corrosion weight loss. The weight loss under free corrosion was 19mg per hour. Under potentiostatic control, the weight loss increased to 34.2mg. The current registered in the electrochemical cell ranged from 7mA to 8.1mA which is representative of a weight loss rate of 7.7-8.9mg per hour. The results therefore suggest a very significant increase in weight loss is induced when accentuated corrosion currents are imposed. This is further evidence of a very strong influence of *corrosion* on mechanical *erosion* of materials.

Another important observation, found during anodic potentiodynamic tests and potentiostatic tests was the fluctuation of current when sand was present in the liquid stream. These fluctuations were studied by means of high frequency measurement of the current via an oscilloscope and were found to be much greater on the stainless steels than on the C-Mn steel although the magnitude of the current was greater on C-Mn steel. Figure 5.34 illustrates the greater fluctuation of current on a smaller mean value on SAF 2205 compared to the lower fluctuations on C-Mn steel.

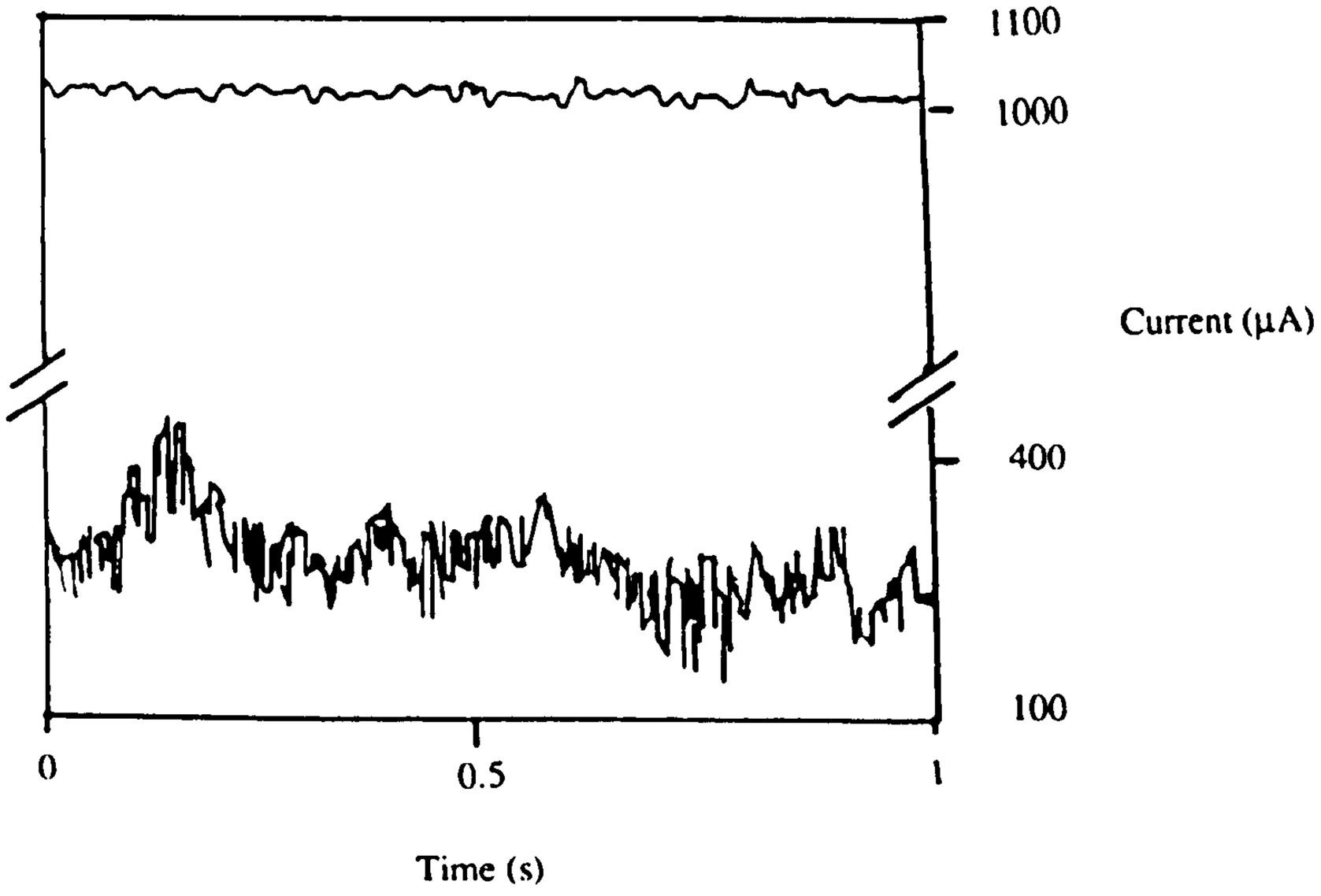


Fig. 5.34. Fluctuation of current on SAF 2205 compared to the lower fluctuations on C-Mn steel.

Galvanic Coupling

In engineering systems components are often in electrical contact and attention is paid to the obvious 'dangerous' galvanic coupling aspects of a large passive stainless steel or related alloy component to a small component of an actively corroding material. However this work has shown that in liquid-solid erosion, the so-called passive alloys exhibit a large drop in the corrosion potential to active values and associated active corrosion. It was therefore decided to investigate, for a few alloys, the galvanic interactions which exist when the materials (one or both) are exposed to severe liquid-solid impingement.

The first two alloys investigated were Stellite 6 and it's interaction with the superduplex UNS S32760 and as an initial test the galvanic currents were measured while both materials were under the severe conditions of liquid-solid impingement. As

a control, the currents under static conditions were measured. Figure 5.35 shows the resulting progression of the current with time for a one hour test. The Stellite 6 alloy was, for the entire test, the 'anode'

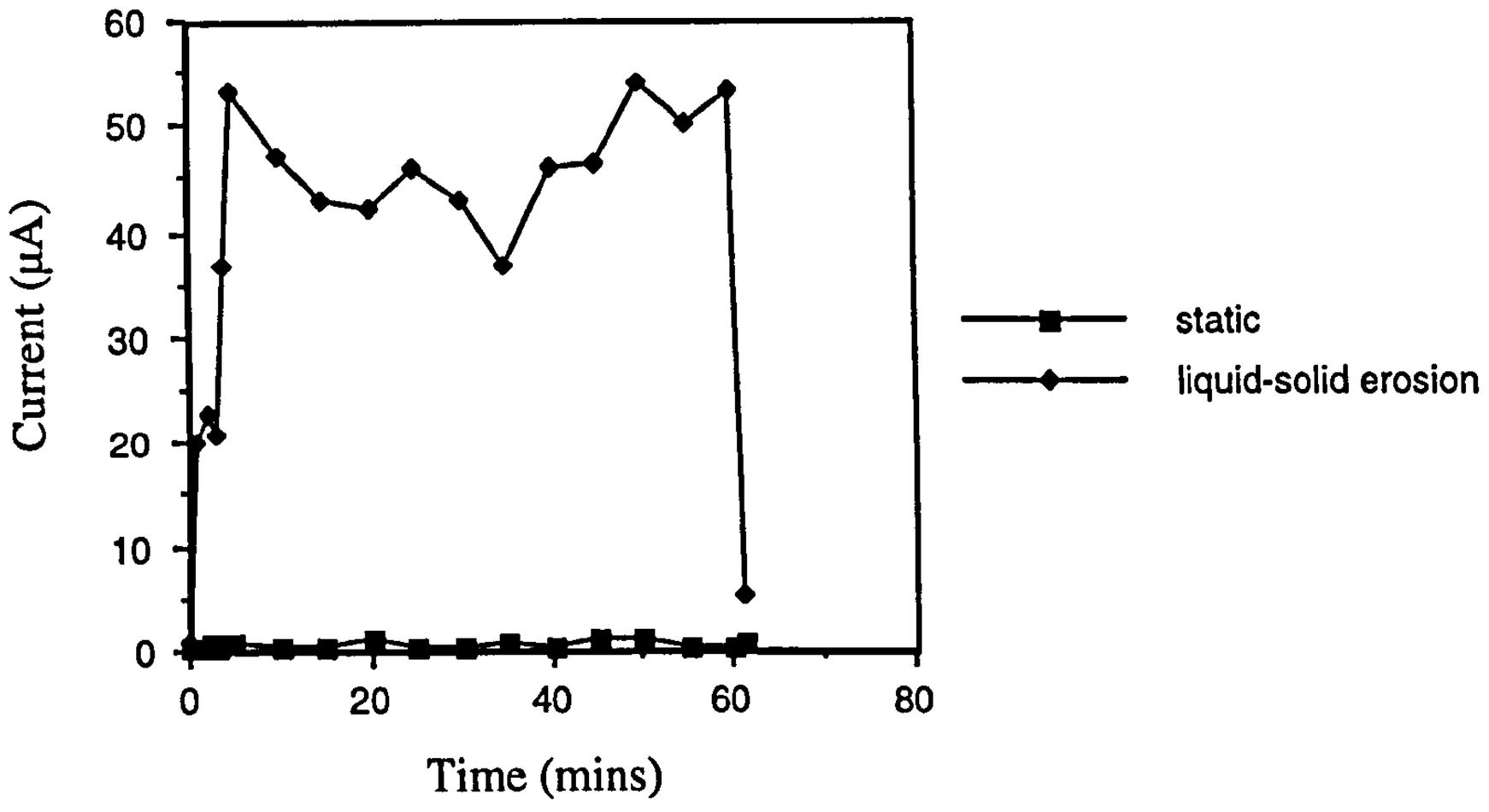


Fig. 5.35. Galvanic Current between Stellite 6 and UNS S32760 in static conditions and under liquid-solid erosion

Under the liquid-solid erosion conditions, the galvanic current increased once the jet was directed onto the specimens. This occurred even although the difference in the corrosion potentials was actually greater under static conditions. In static conditions the potential difference between Stellite 6 and UNS S32760 was approximately 170mV and under liquid-solid erosion, the difference was 45-50mV. Both the corrosion potential of the Stellite 6 and of the UNS S32760 shifted in the negative direction on exposing to liquid-solid erosion.

The condition where only the Stellite 6 is exposed to liquid-solid erosion and is coupled to the superduplex was investigated, thought to be of importance in practical applications where a component chosen for it's resistance to wear (Stellite 6) is galvanically in contact with a component chosen principally for it's corrosion resistance and strength (typically UNS S32760). One example could be a wear ring of Stellite 6 on a pump shaft of UNS S32760. As can be seen from Fig. 5.36, the galvanic current is significantly increased once the Stellite 6 is exposed to the impinging jet such that the galvanic currents correspond to a dissolution rate of the Stellite 6 of 1.42mg/hour. The potential of Stellite 6 under liquid-solid erosion is more negative than the free corrosion potential of UNS S32760 in static conditions by a margin of approximately 280mV. This represents a significant rate of metal dissolution due to corrosion, but of further importance is the fact that the actual rate of metal loss will be greater since the

galvanic current does not quantify take account of the additional metal loss on the anode [38] due to local corrosion cells associated with the cathodic reaction rate enhancement due to the presence of the impinging jet. Since cathodic data were not collected for Stellite 6, it was impossible to obtain the actual cathodic current which would exist on the coupled material at the coupled potential 110mV more positive than the uncoupled $E_{corr}$. Hence an estimation was made from extrapolation using the line between the current at -0.8V (obtained from CP experiments) and $I_{corr}$ (at $E_{corr}$). This produced a cathodic current of approximately 400-500μA which, when considered in conjunction with the galvanic current (ranging from 600-1200μA) represented a dissolution rate of 1000μA-1700μA. The test therefore shows that coupling of the specimen can greatly enhance the rate of dissolution compared to an uncoupled specimen on which the corrosion current was measured at 900μA.

The second pair of materials investigated was cast iron and the interaction with the austenitic UNS S31603. This combination, like the Stellite 6/UNS S32760 combination, has relevance in pumping situations where a cast iron pump casing is in contact with a stainless steel impeller. The galvanic currents were recorded while both specimens were under the impinging flow and when only UNS S31603 was subjected to the flow. The current flow in the galvanic cell was always such that the cast iron specimen represented the anode, even though from anodic polarisation tests it had been shown that both materials actively corrode under the severe conditions. Figure 5.37a shows the resulting currents and of importance is the point at which the jet begins to impact and at which point the galvanic current suddenly decreases. This drop in current corresponds to changes in $E_{corr}$ of uncoupled specimens of the two materials which on the cast iron tend initially to shift in the positive direction and on UNS S31603 in the negative direction. Hence at the instant the impingement begins, there is a period where the driving force for galvanic current is lowered. Figure 5.37b shows these progressive changes in $E_{corr}$ and it can be seen that as impingement continues, $E_{corr}$ of cast iron reverts back to more negative values thus retaining a larger $E_{corr}$ difference between the two materials and favouring larger galvanic currents. The $E_{corr}$ of UNS S31603, in contrast, maintains a relatively constant value over the impingement period. The $E_{corr}$ values of the uncoupled specimens (Fig. 5.37b) also accounts for the lower galvanic currents (Fig. 5.37a) between eroded UNS S31603/non-eroded cast-iron. Incidentally these galvanic currents in Fig. 5.30a represent a significant enhancement of the corrosion rate of the cast iron (Faraday's Law calculation indicating this to be between 0.1-0.2mg/hour) but this is still a very minor proportion of the extremely high wastage rates (in excess of 50mg/hour) under the severe erosion-corrosion conditions.

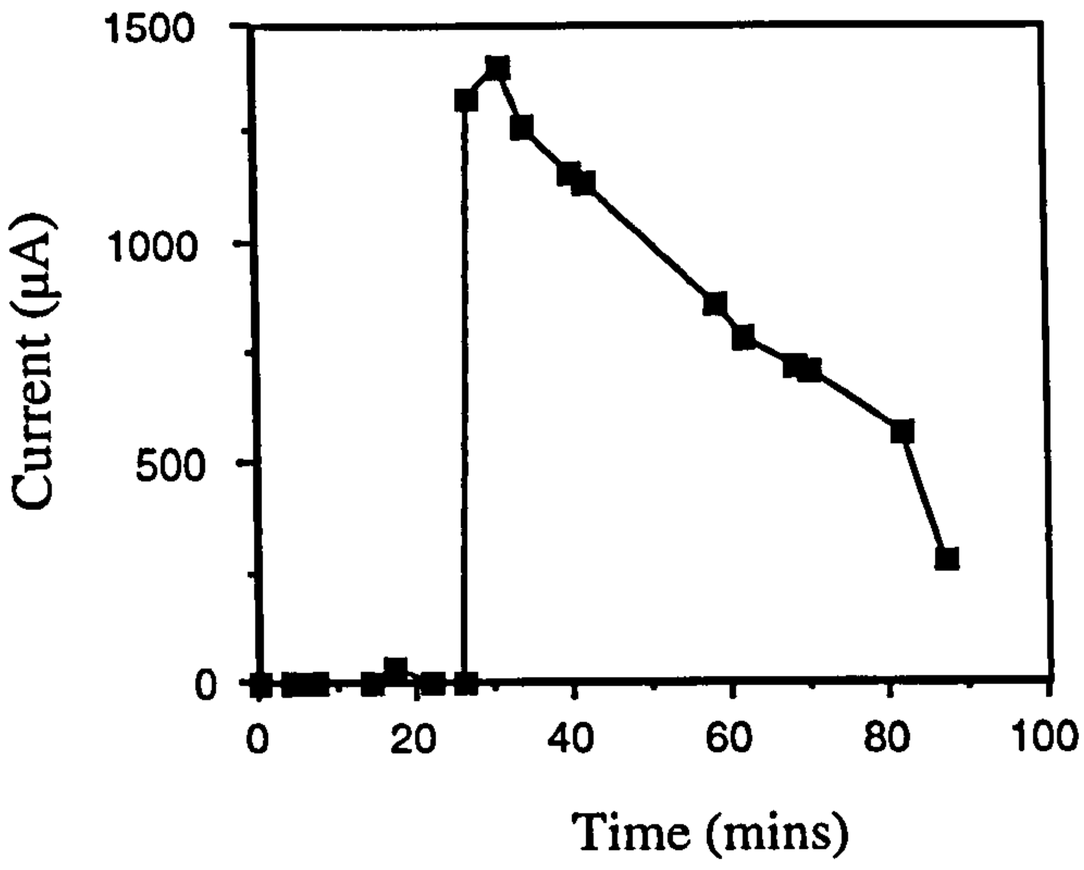


Fig. 5.36. Galvanic current when only Stellite 6 is under liquid-solid erosion

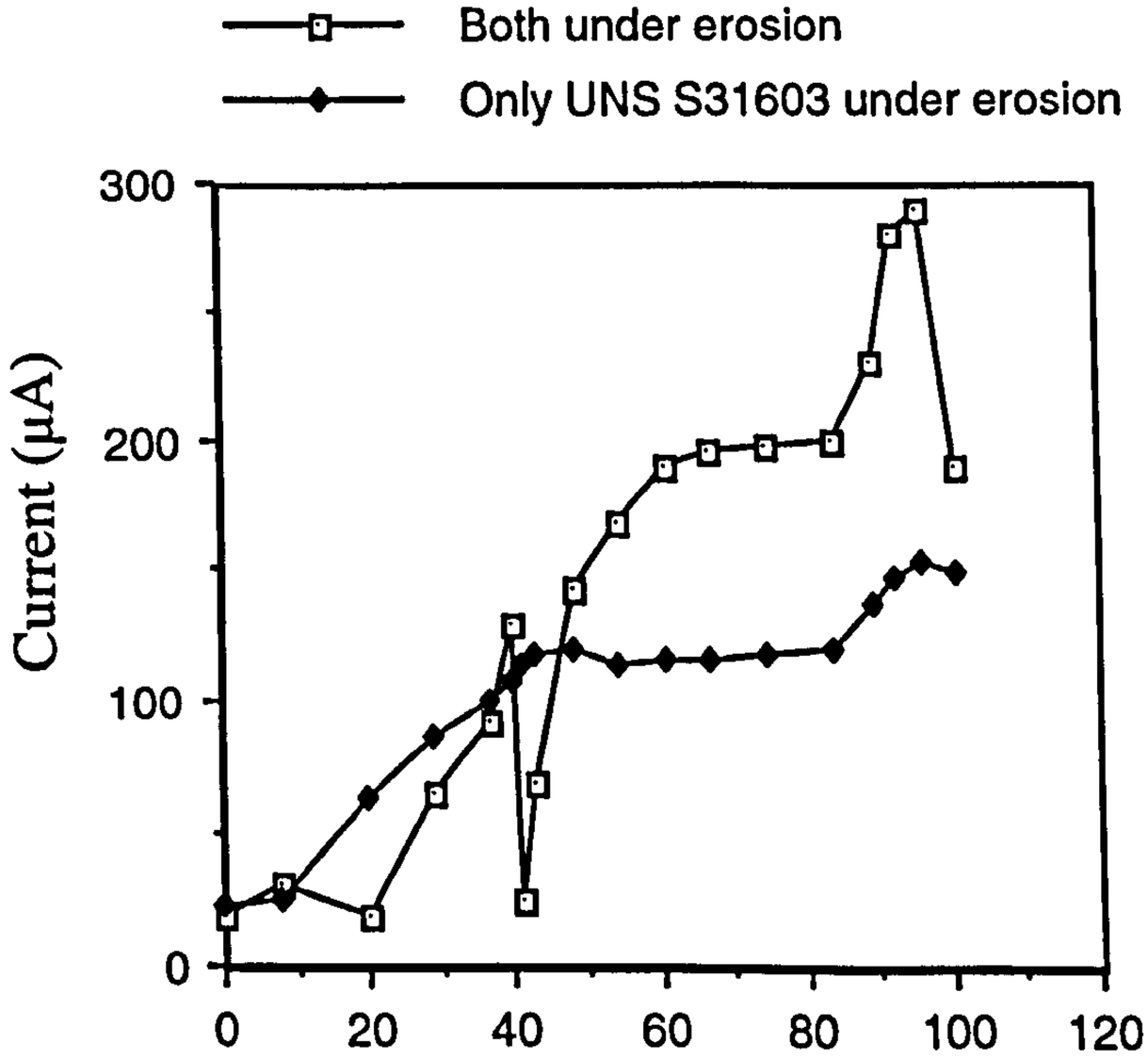


(a)

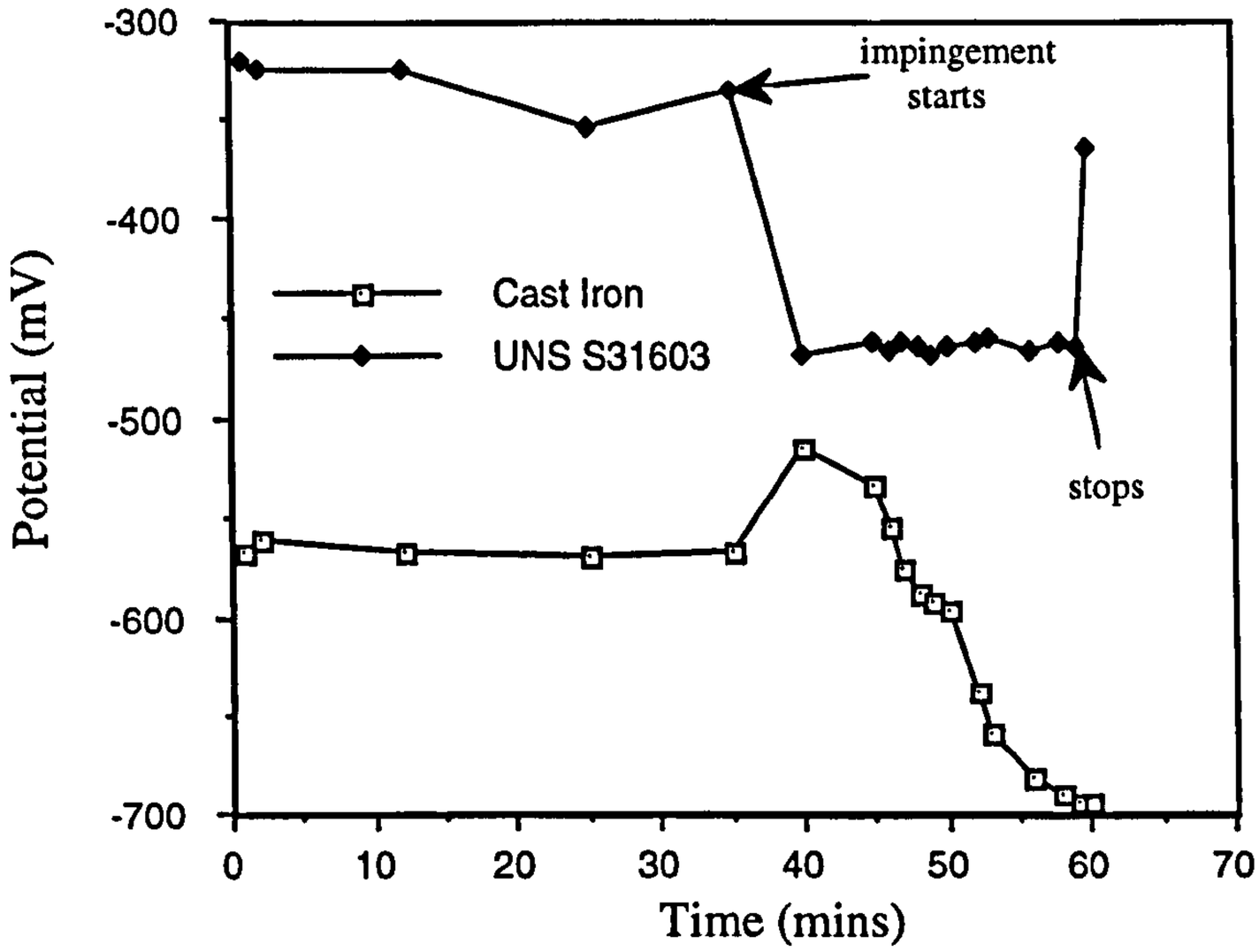


(b)

Fig. 5.37 (a) Galvanic currents between cast iron and UNS S31603 and (b) the changes in free corrosion potential under liquid-solid erosion in 3.5%NaCl at 50°C.

Specimen Examination

The visual appearance of specimens after exposure to the various environments correlated well with the findings from electrochemical monitoring mentioned previously.

After a one hour period under liquid erosion, on the C-Mn steel there was no visible sign of corrosion products. However, after 16 hours at the free corrosion potential, corrosion products were readily visible on the surface as shown in Fig. 5.38. The copious corrosion products reflected the flow pattern of the liquid across the specimen surface. The arrow indicates the region where thick corrosion products were found out from the central area (darker in the photo) which was virtually free from corrosion products.

Under liquid-solid erosion, after a one hour test, corrosion products could be clearly seen on the surface. The deterioration due to erosion and corrosion effects was in the form of a localised wear scar, the form of which, in cross section appeared as in Fig. 5.39a. The scar related to the flow pattern associated with jet impingement as represented schematically in Fig. 5.39b where the inner area of minimum loss of material thickness represents the stagnation point and the outer increased loss of

thickness corresponds to the area of higher shear stress. Application of cathodic protection significantly reduced the visible corrosion products (Fig. 5.40) on the wear scar surface which is verification of the measured weight loss results.

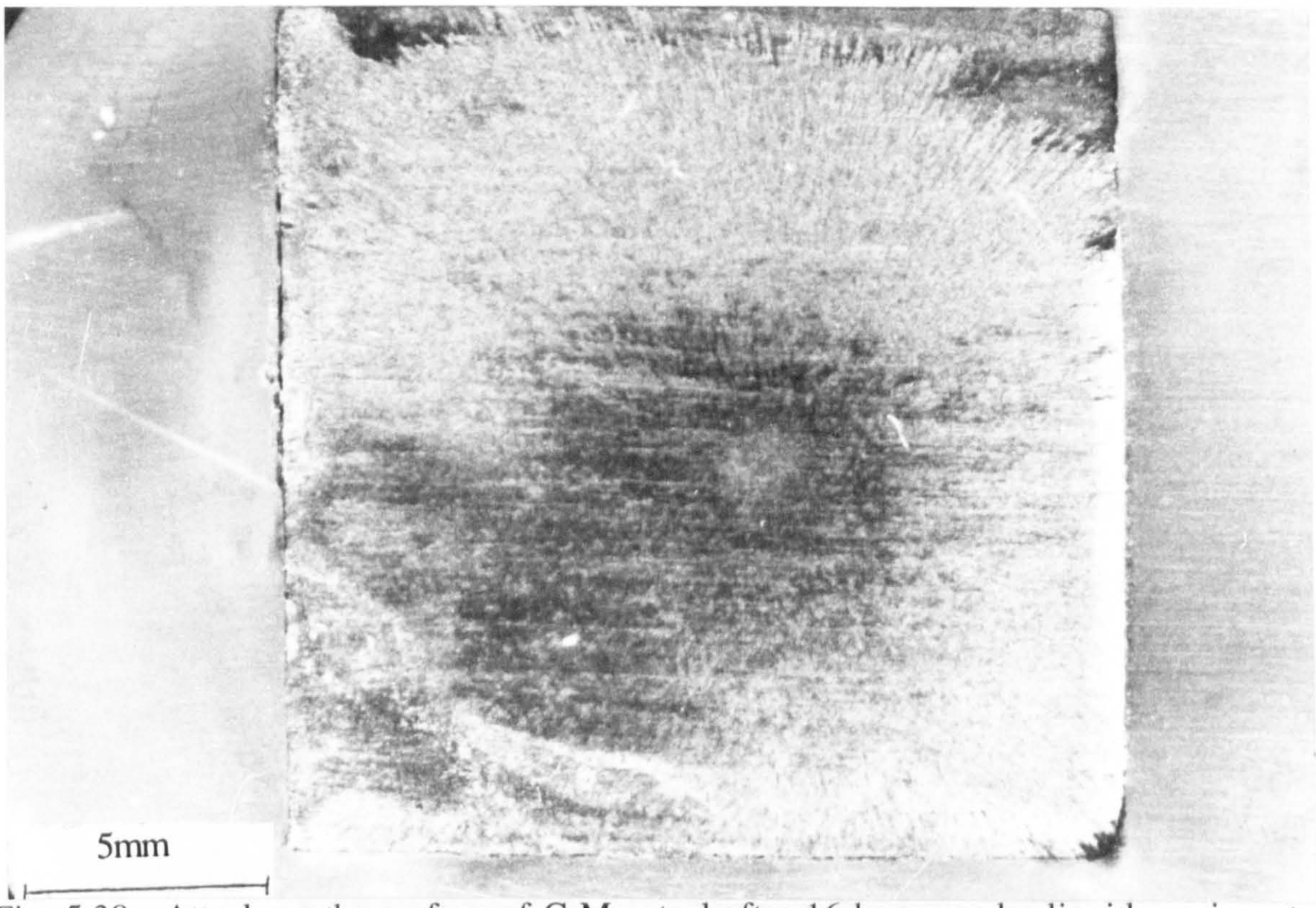


Fig. 5.38. Attack on the surface of C-Mn steel after 16 hours under liquid erosion at the free corrosion potential. 3.5%NaCl at 50°C.

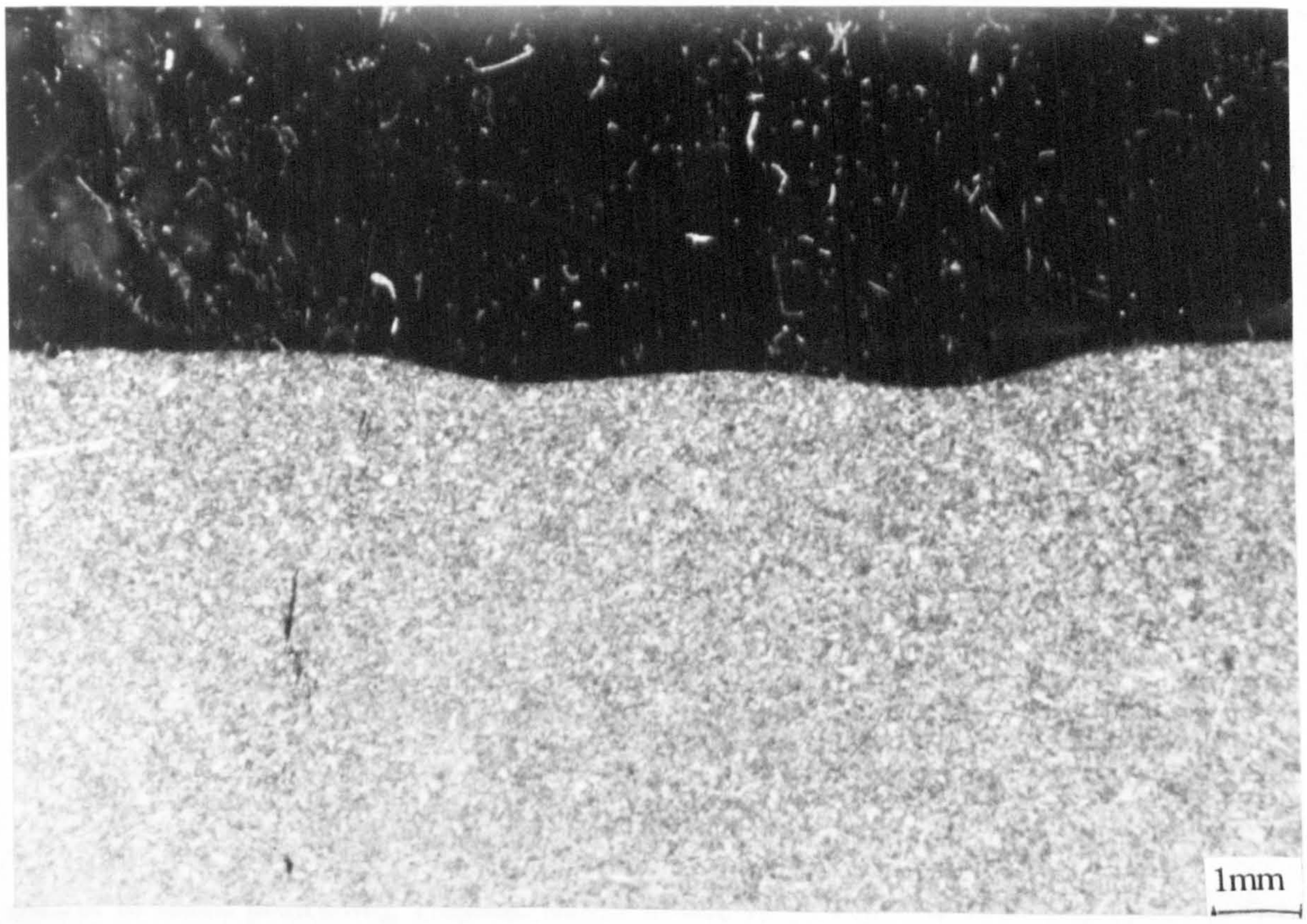


(a)

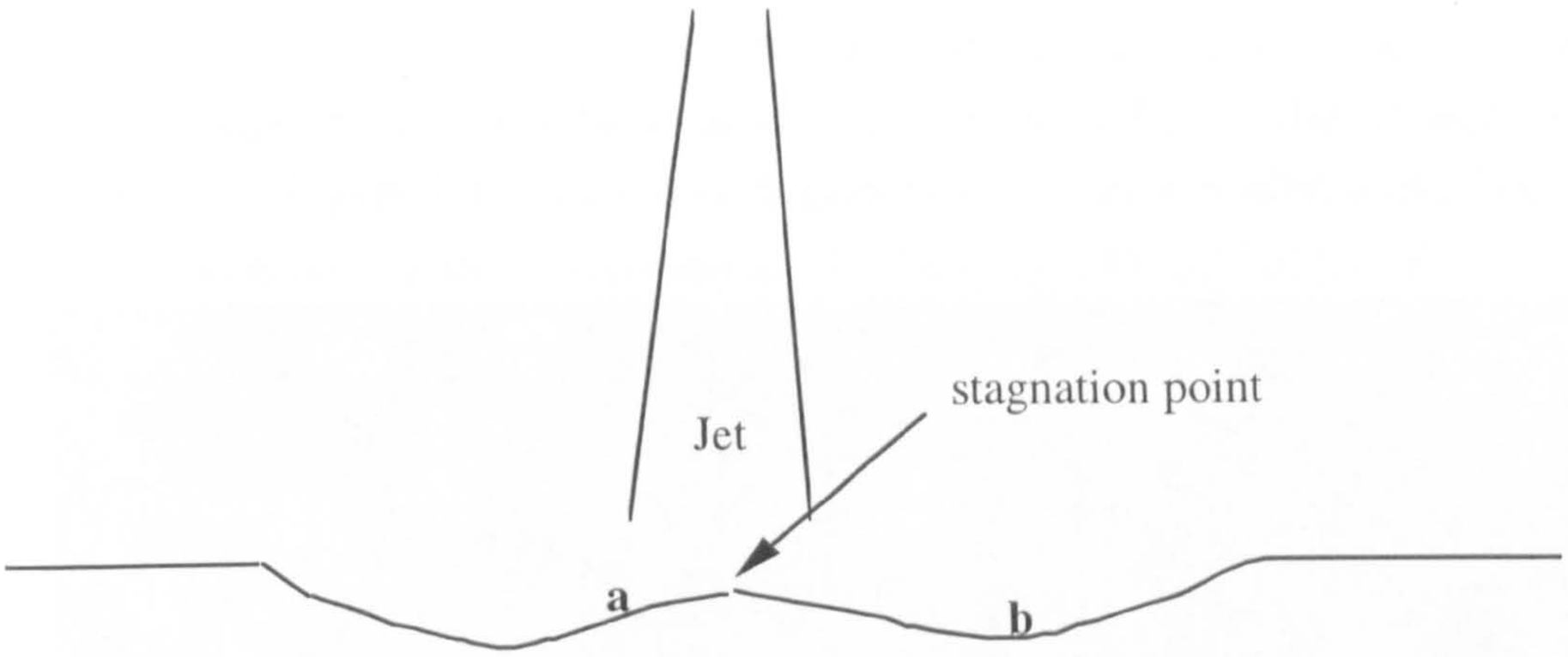


Cross section of wear scar

(b)

Fig. 5.39. Wear scar cross section (a) actual specimen of C-Mn steel after one hour in 3.5%NaCl at 50°C and (b) schematic representation

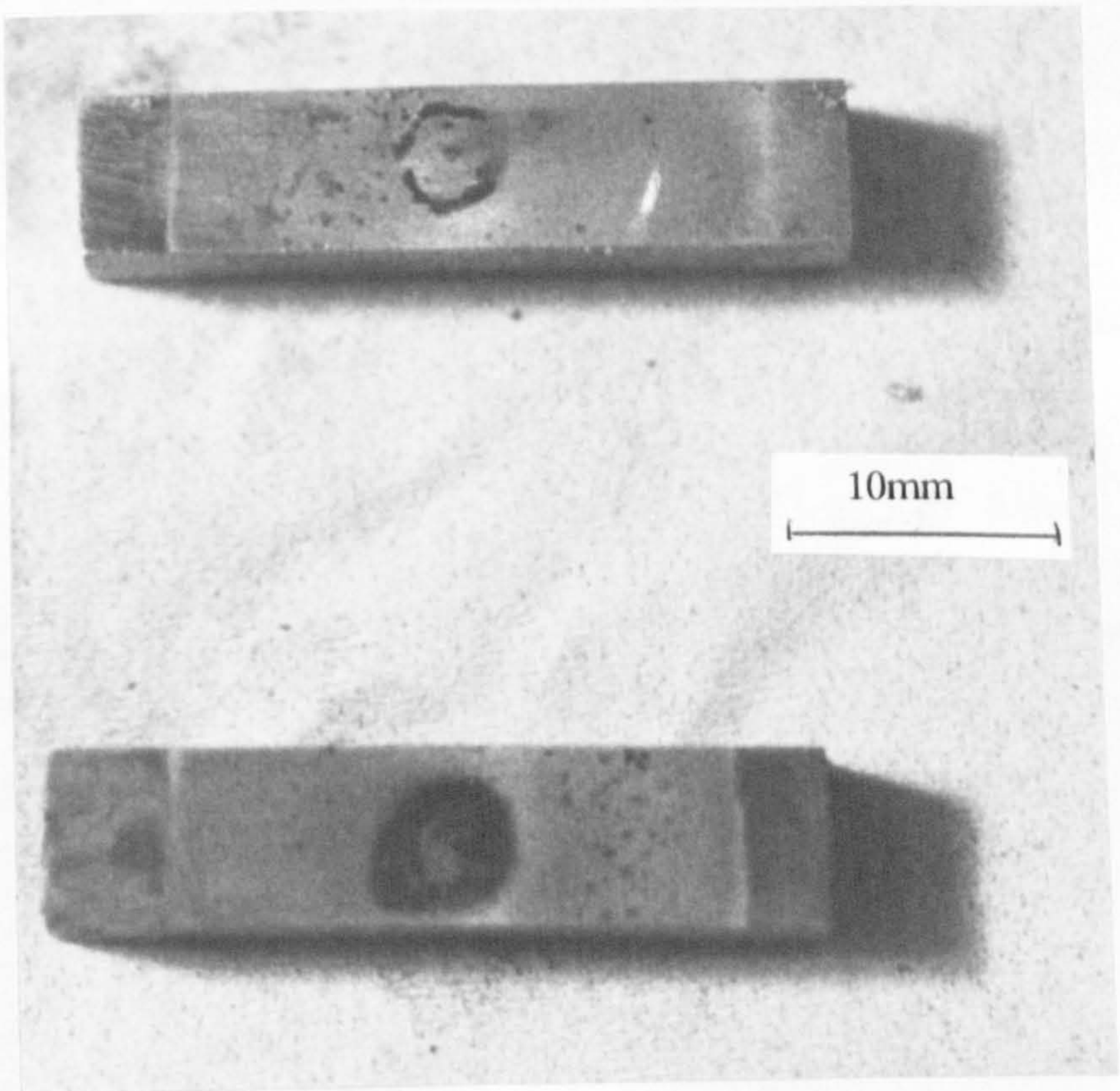


Fig. 5.40. Reduced corrosion visible on the surface of C-Mn steel after one hour with applied CP (top). Specimen without applied CP (bottom)

On cast iron, the mechanism of attack in static conditions is dissolution of the iron-rich matrix to leave protruding graphite flakes as shown in Fig. 5.41(a). The effect of an

impinging jet, solids-free and containing solids, was to change the attack mechanism such that material removal involved removal of the graphite flakes due to an opening out of the adjacent areas similar to attack reported in studies of sliding wear by other workers [39]. Figure 5.41b shows the degradation on cast iron after a one hour period under liquid erosion at the free corrosion potential and with applied CP (Fig. 5.41c).

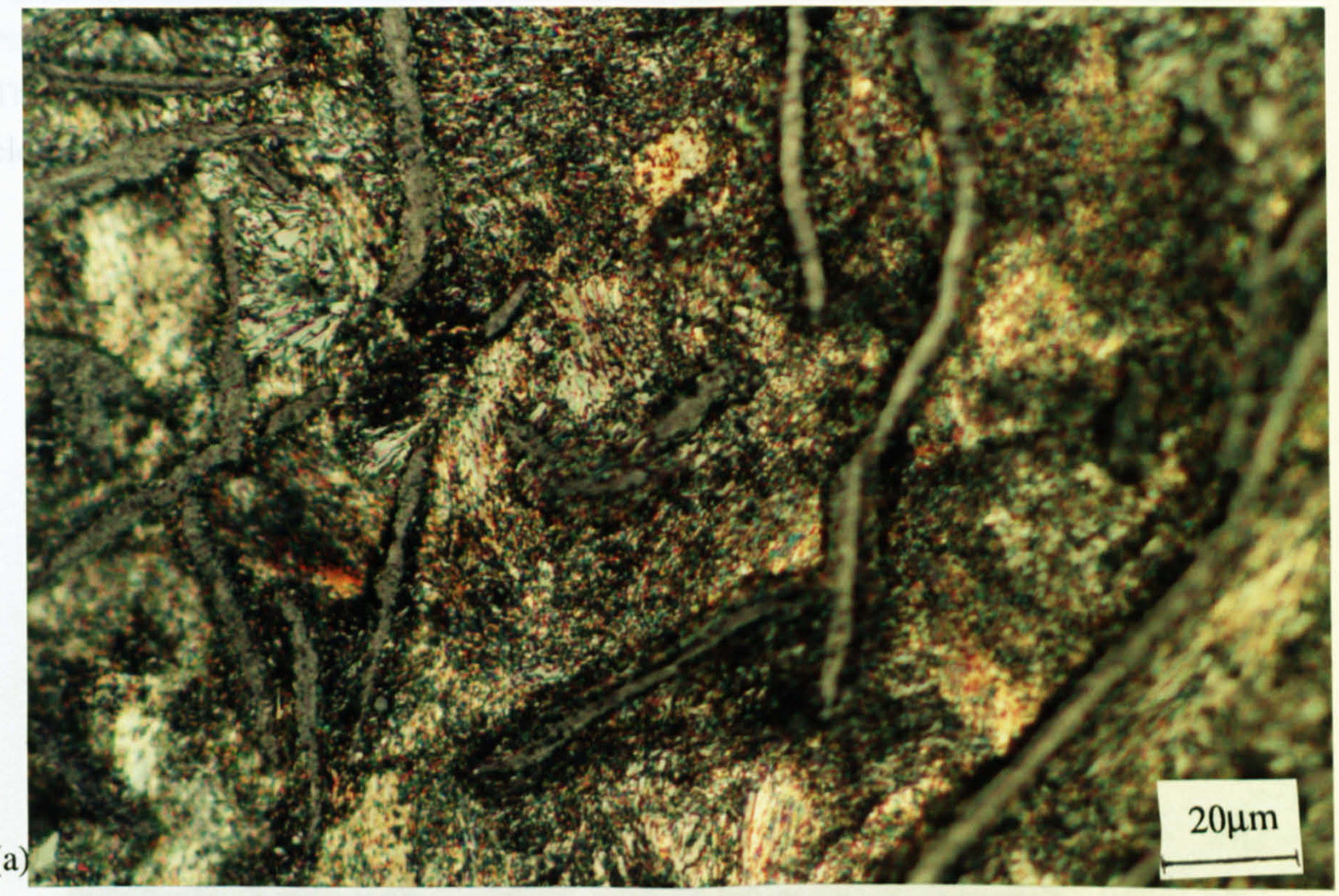


(a)


(b)

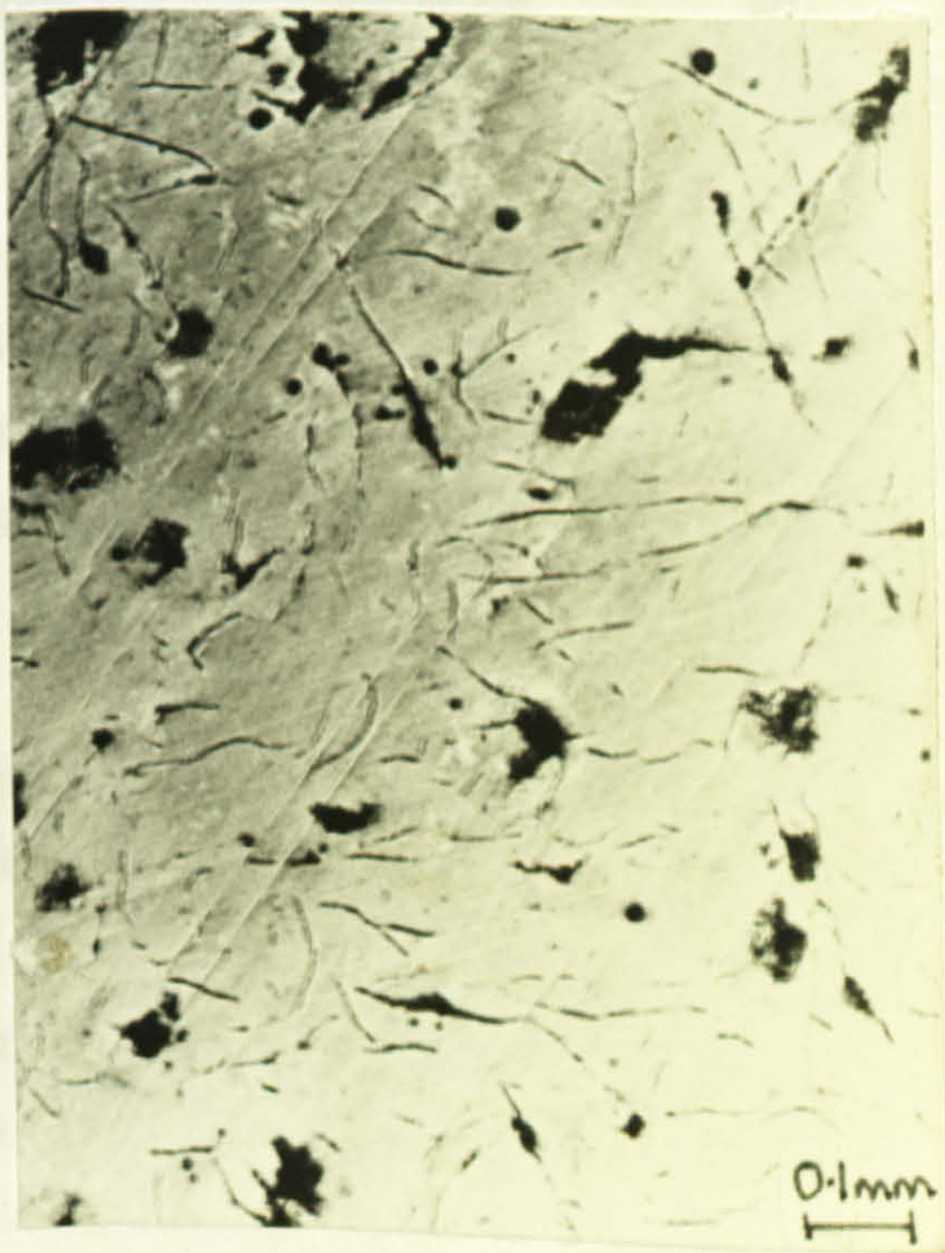


(c)

Fig. 5.41.(a)Attack on cast iron after anodic polarisation in static conditions, (b) after a one hour test under liquid erosion at the free corrosion potential and (c) with applied CP

The wear scar configuration on cast iron under liquid-solid erosion was similar to the form of that on C-Mn steel. In addition, a significant reduction in corrosion products was found on application of cathodic protection as shown in Fig. 5.42. The wear scar, when examined in plan, showed the corrosion products on the unprotected specimens but once removed the surface appeared roughened, similar to a shot-blasted surface. The directionality of the flow, outwards from the stagnation point could be seen clearly.


Fig. 5.42. Reduction in corrosion on application of cathodic protection on cast iron in liquid-solid erosion at 50°C in 3.5%NaCl. UNS S31603 stainless steel (top) after one hour test in 3.5%NaCl at the free corrosion potential, cast iron (second) with applied cathodic protection after the same test and cast iron at the free corrosion potential (lower two specimens).

The detailed dispersion of the graphite could not be seen on the cast iron specimens in plan after liquid-solid impingement in 3.5%NaCl at 50°C due to the severity of the deterioration. However when examined in cross section, revealed were areas in the wall-jet region [40] out from the stagnation point where the joint effect of erosion and corrosion seemed to result in the dislodging of material due to attack of the surrounding graphite regions. Figure 5.43a shows a region of enhanced attack at a graphite-rich region and Fig. 5.43b shows the apparent commencement of removal of a portion of material surrounded by the attacked graphite areas. On the cathodically protected specimens, examination of the wear scar cross-section showed an apparent roughening

of the surface but there were no signs that the material removal was following any metallurgical features. On the stainless steel specimens, examination of eroded specimens in cross section did not provide conclusive evidence that there were effects similar to that on cast iron, occurring at the grain boundaries. However, on one superduplex specimen (Fig. 5.43c) there is some evidence of attack down the grain boundary facilitating removal of a complete grain.

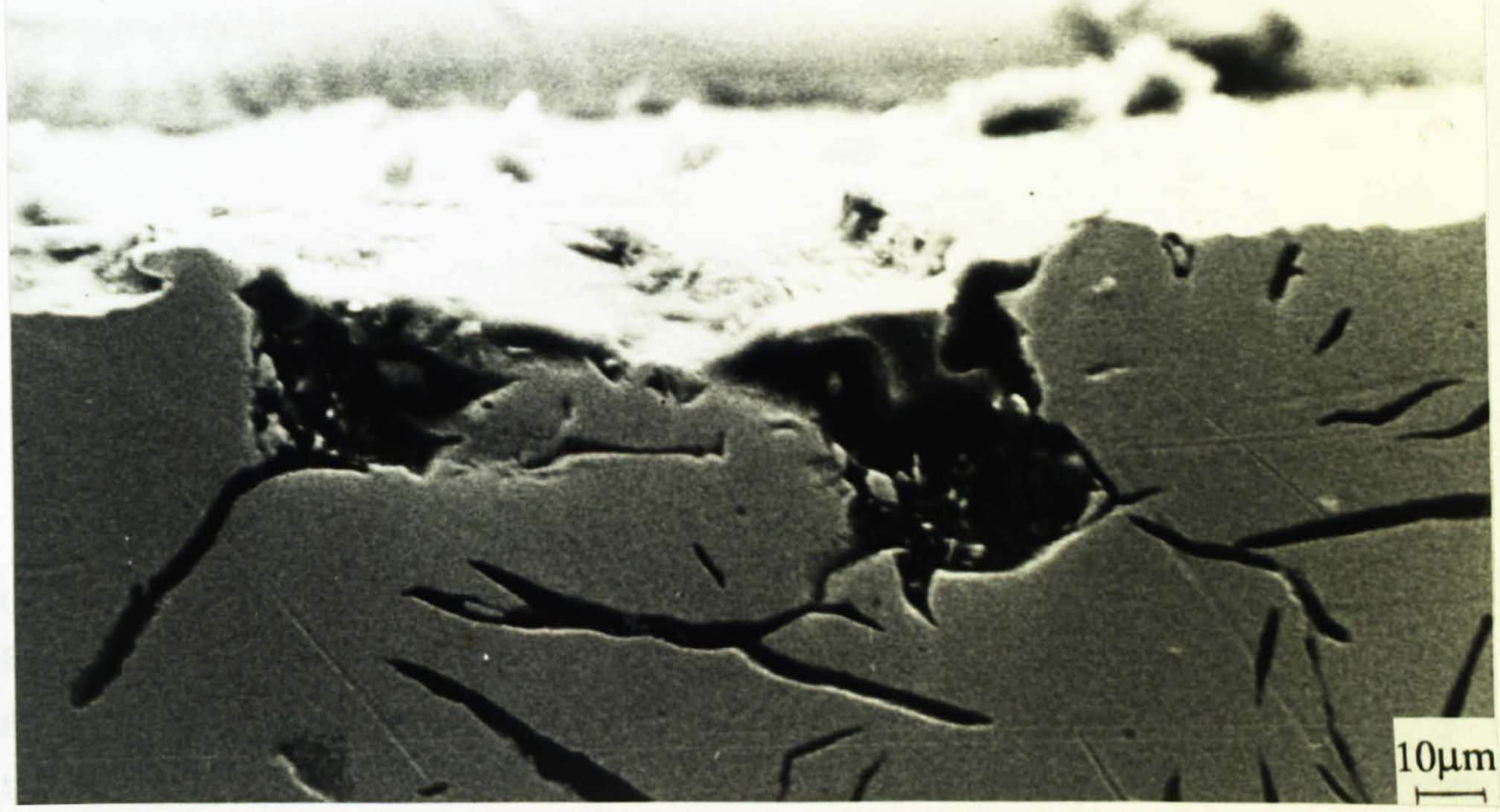


(a)

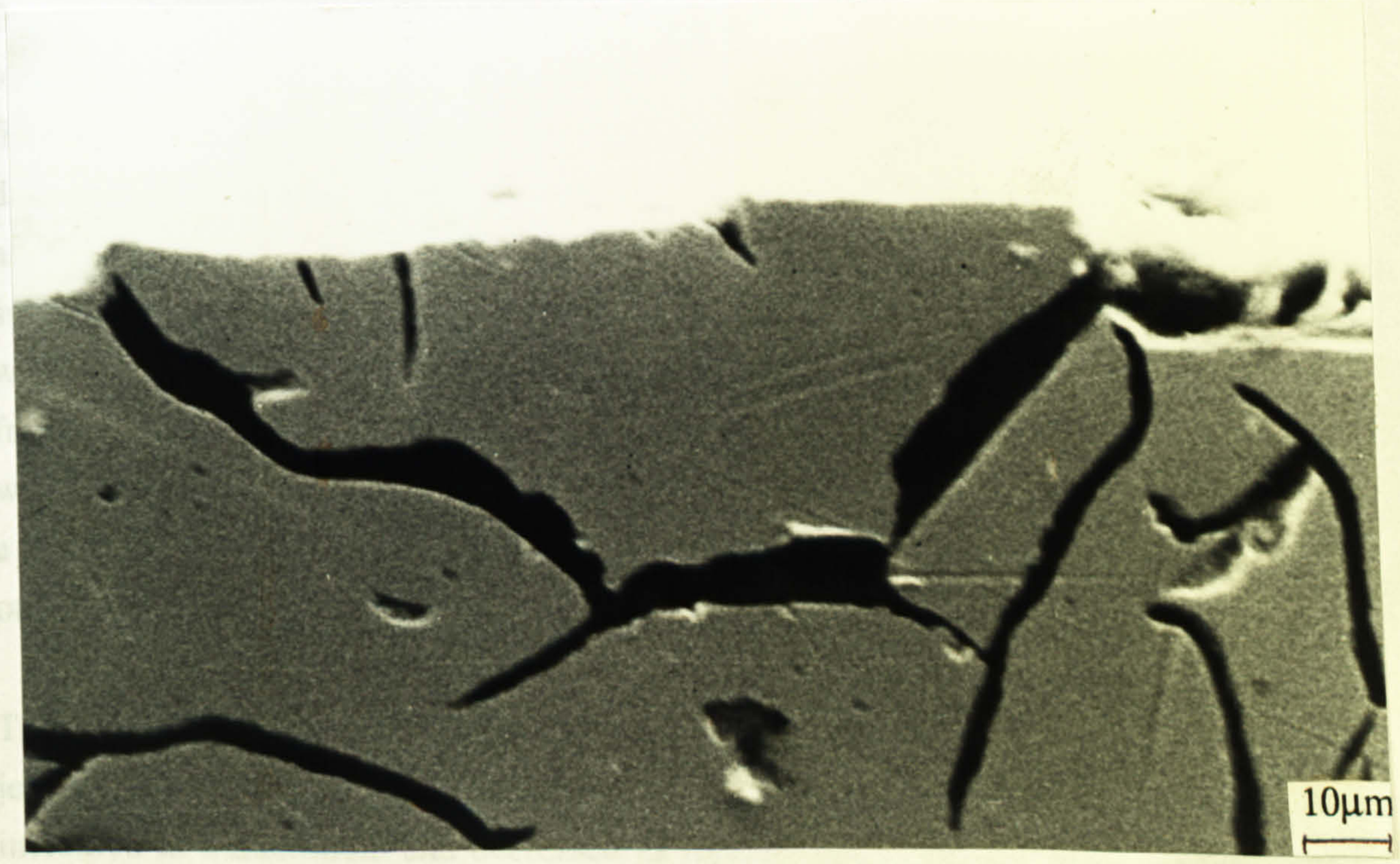


(b)

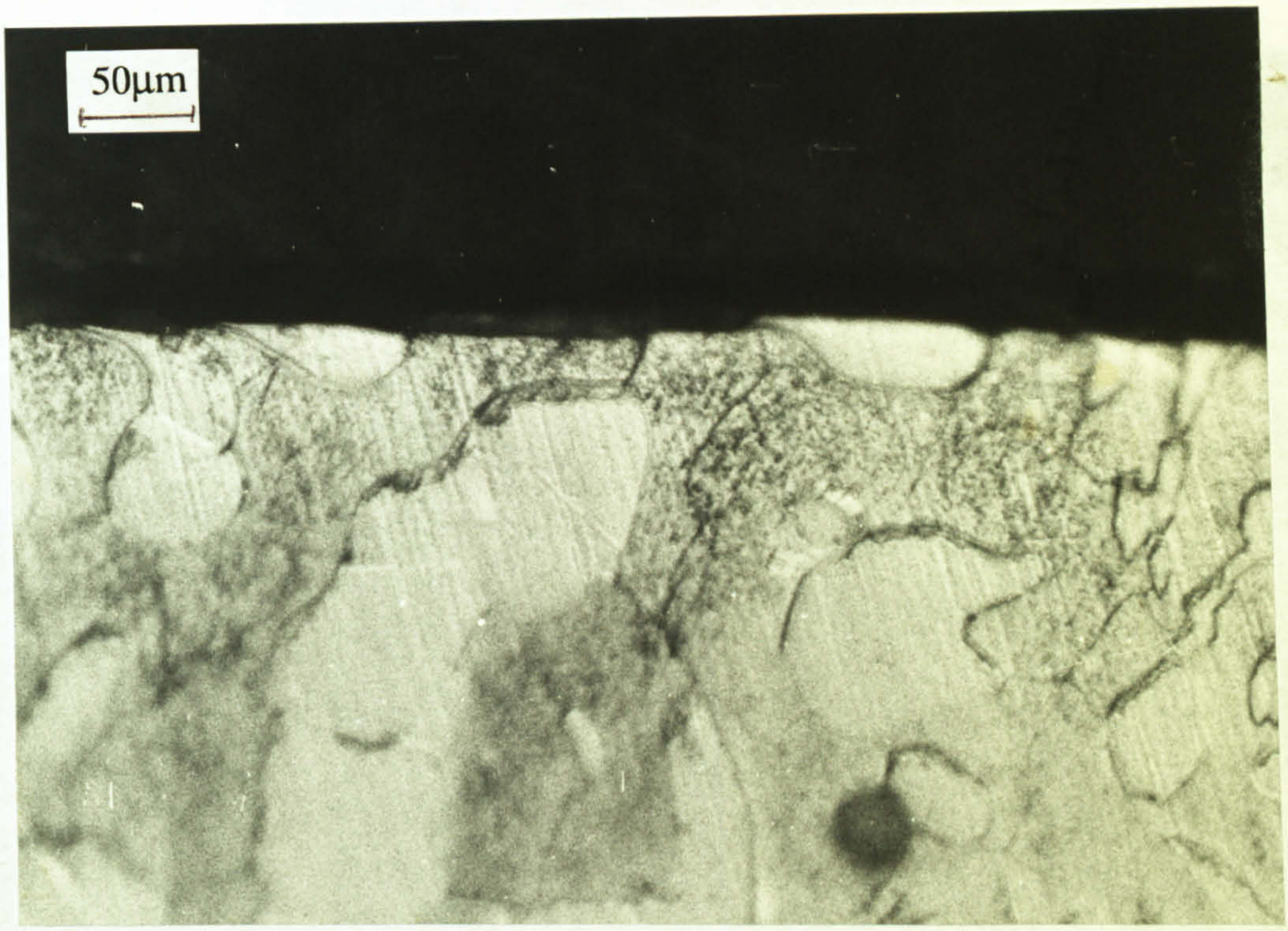


(c)

Fig. 5.43(a) Enhanced attack at a graphite area on cast iron and (b) removal of material due to attack around the graphite flakes (c) suspected attack at the superduplex grain boundaries

Exposure of stainless steels to liquid impingement at the free corrosion potential failed to produce any visible attack after a period of up to 8 days - indicating that the passive film remained intact. However, exposure to an impinging liquid, containing solids drastically changed the extent of deterioration. The good resistance to damage was lost as signalled by the weight loss and the electrochemical measurements. In plan, the surface contained a wear scar as on the cast iron and C-Mn steel but in contrast, there were no corrosion products visible except under high magnification where small fragments of loosely adherent corrosion products could be seen. Figure 5.44 shows the wear scar on SAF 2205 (top), on UNS S31603 (middle) and Inconel 625 (bottom) after a one hour test. The damage on these material closely resembling the damage on the other stainless steels and Ultimet.

The symmetrical form of the wear scar showed a central region in which the impinging jet nominally hits the surface at 90°C. Outwards from this region, the deterioration increased to a maximum and decreased as represented in the schematic in Fig. 5.39b. Measurement of the depth of penetration across the wear scar profile revealed different depth of penetration for each material but the maximum depth tended to be at the same

distance outwards from the stagnation point as shown in Fig. 5.45 on Stellite 6 and cast iron..

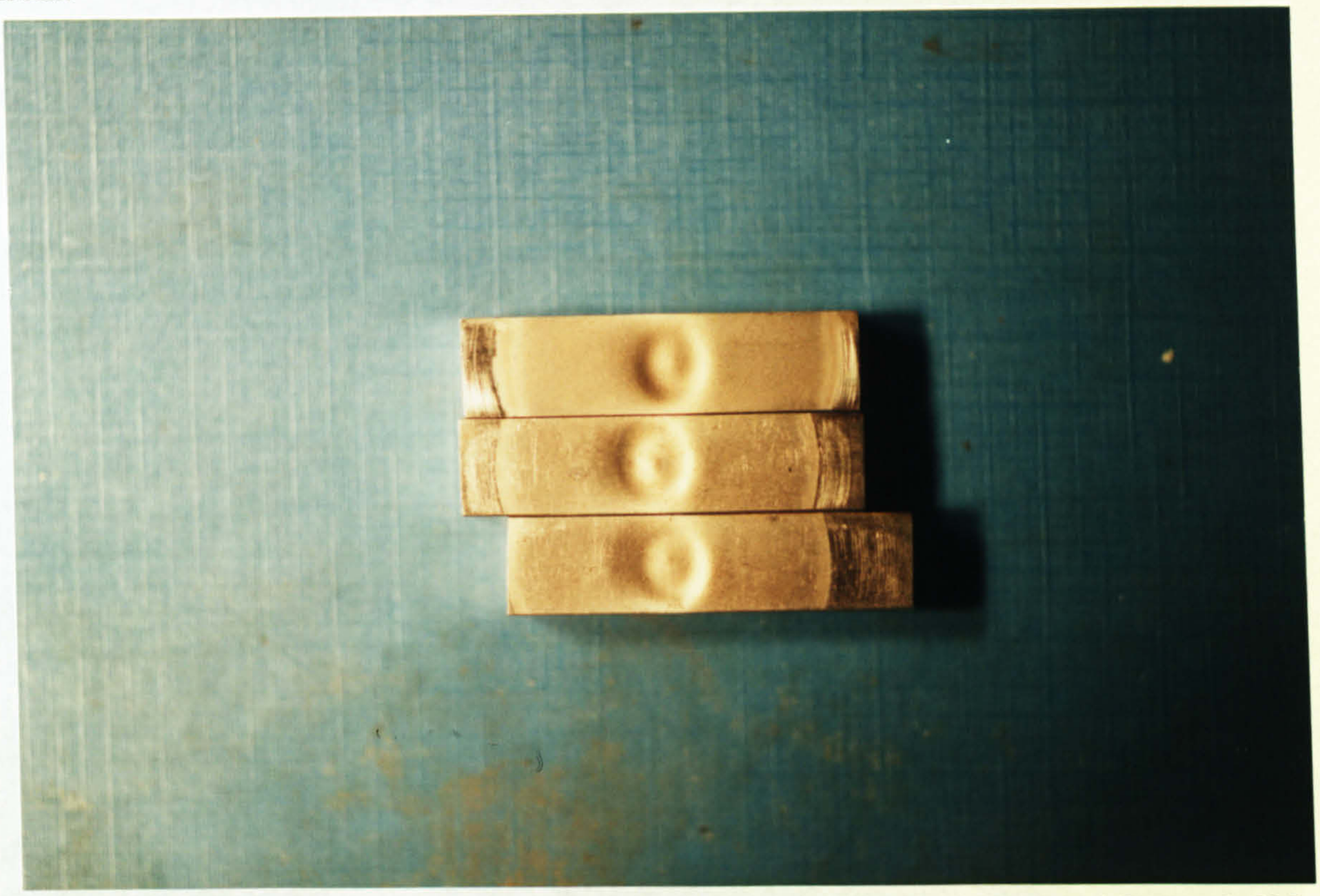

Fig. 5.44. Wear scar on SAF 2205 (top), on UNS S31603 (middle) and Inconel 625 (bottom) after a one hour test under liquid-solid erosion in 3.5%NaCl at 50°C

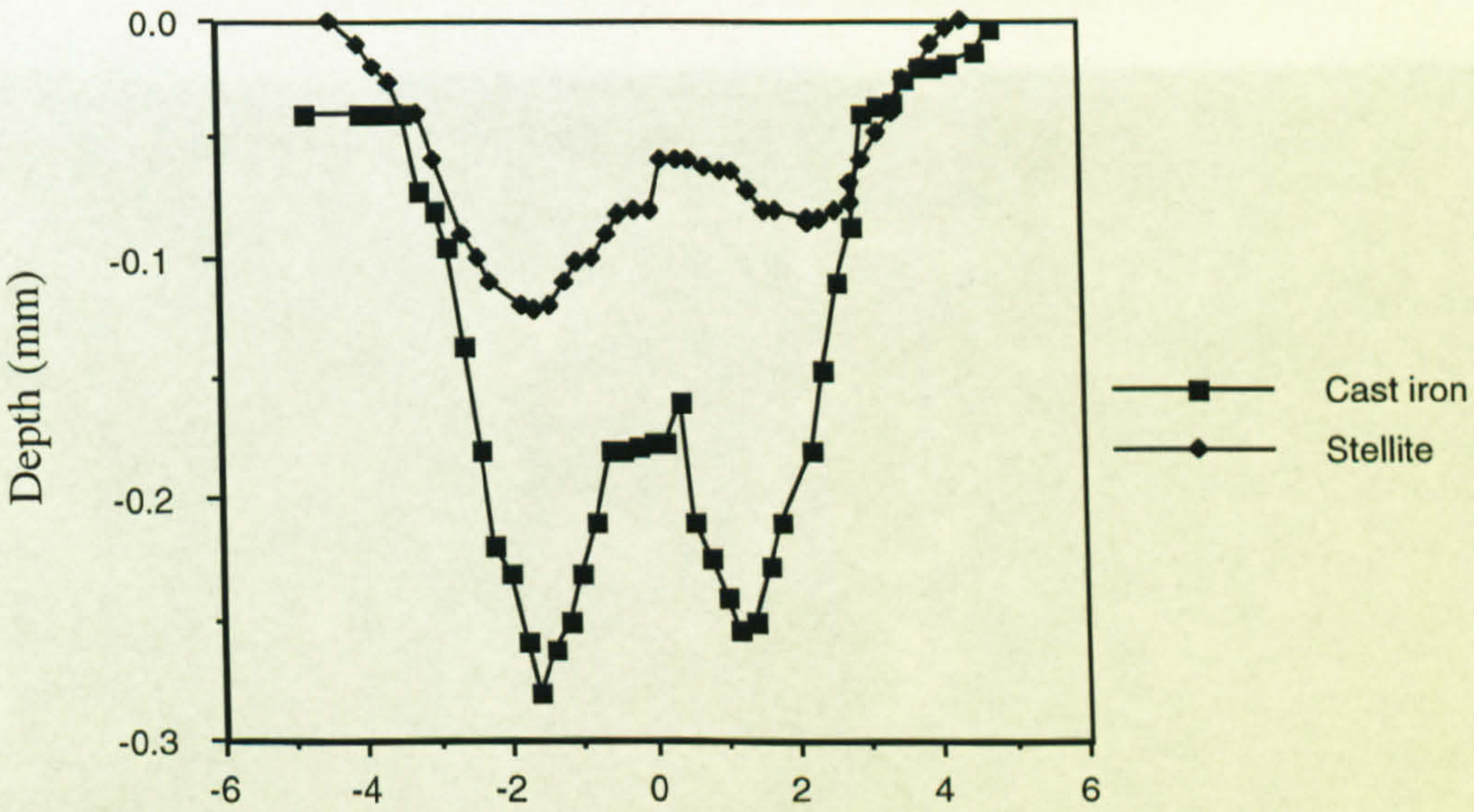


Fig. 5.45. Depth of penetration on Stellite 6 and cast iron under liquid-solid erosion

In the central region, the deterioration appeared as a series of small indentations (Fig 5.46 on UNS S31603) in contrast to the directional ploughing of the material and the

long, deep troughs formed at the outer areas where the flow would be nominally in the radial direction parallel to the surface. Figures 5.46b and c show this effect on UNS S31603 and the arrow indicates the direction of the flow. Also there is evidence of fatigue-like striations on the eroded surface (located by the arrow on the micrograph in Fig. 5.46b).

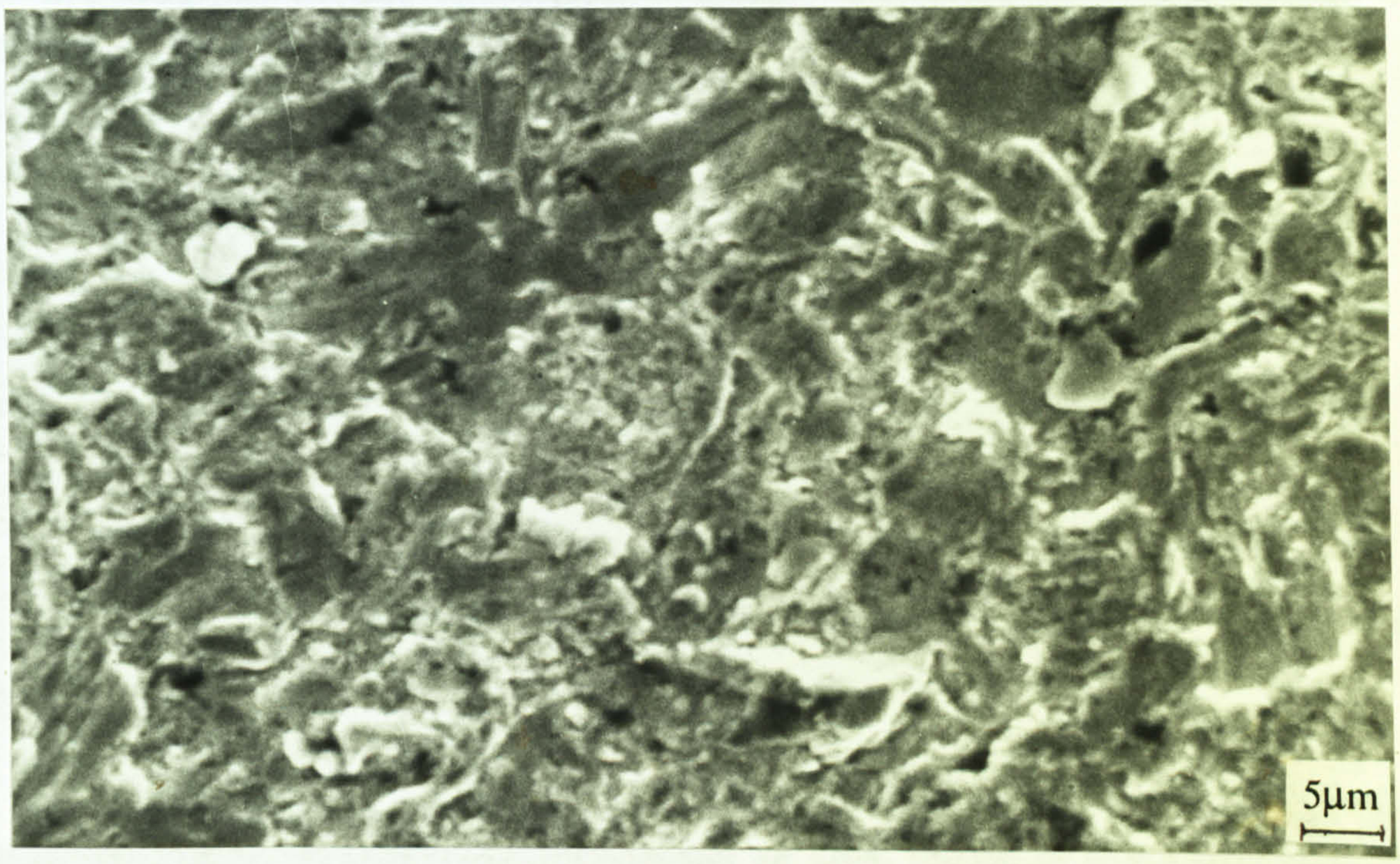


(a)

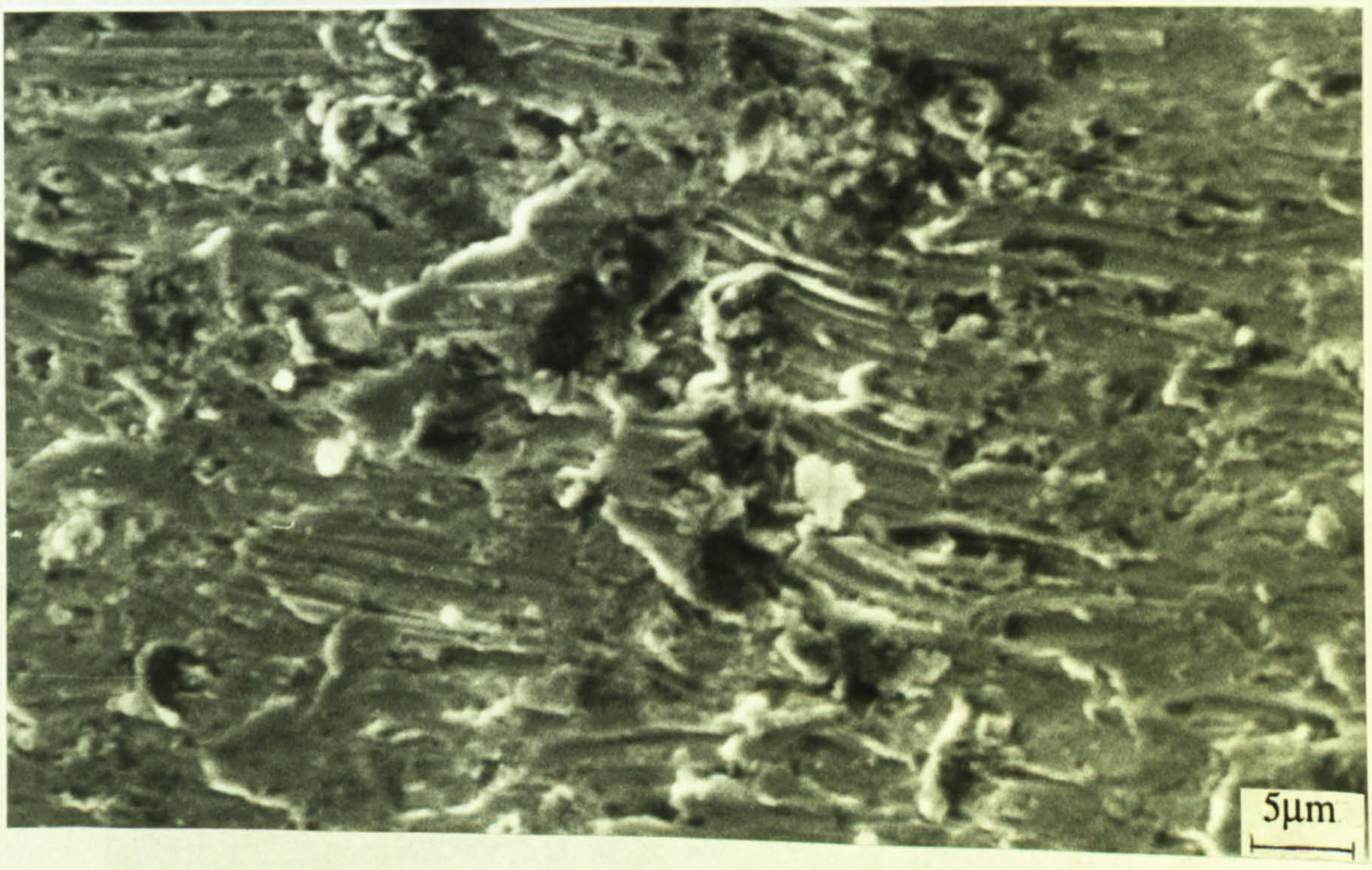


(b) Direction of flow ←

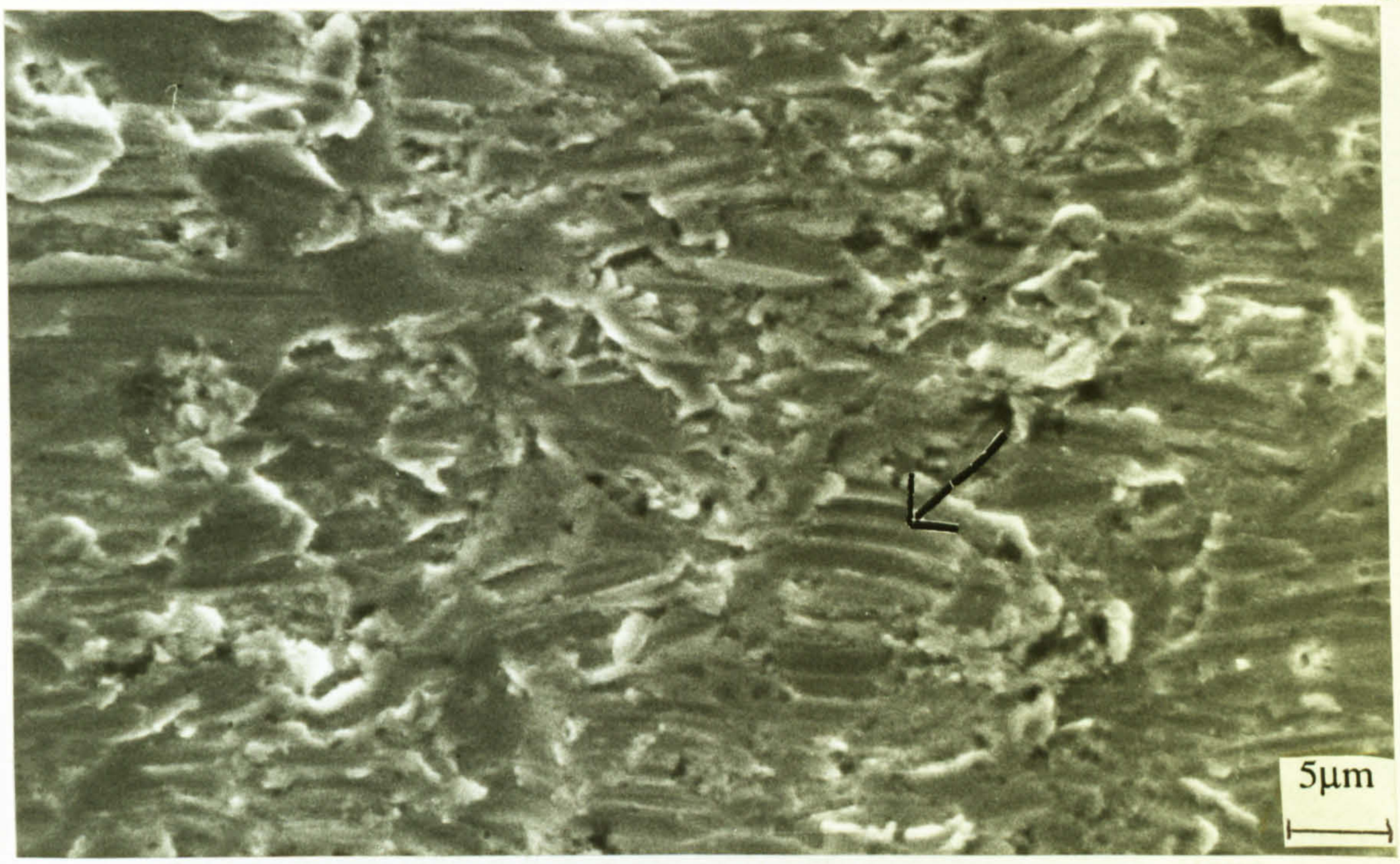


(c) Direction of flow →

Fig. 5.46. Plan view of the deterioration on UNS S31603 after a one hour test in liquid-solid erosion conditions (a) central region, (b) and (c) outward region

The overall form of the wear scar cross section was independent of material and on a smaller scale, it was observed that although the cross section of C-Mn steel and cast iron were significantly rougher than on the other materials, on all the materials a change in the profile was observed on moving outwards from the centre. In the central area the cross section appeared as a relatively smooth surface but in contrast, away from the centre, troughs appeared making the overall cross section seem much rougher. This is shown for the C-Mn steel in Figs. 5.47a and b.

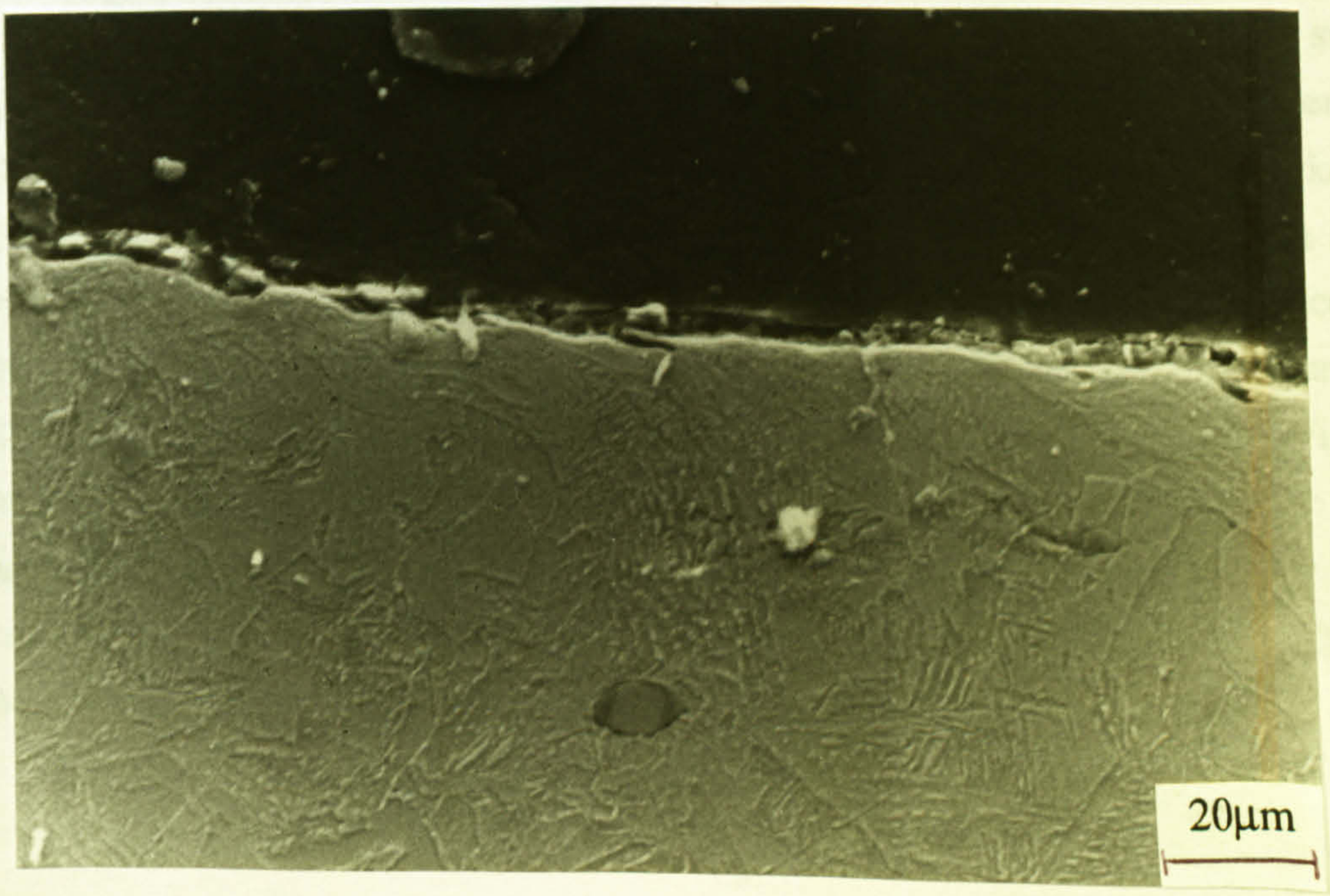


(a)

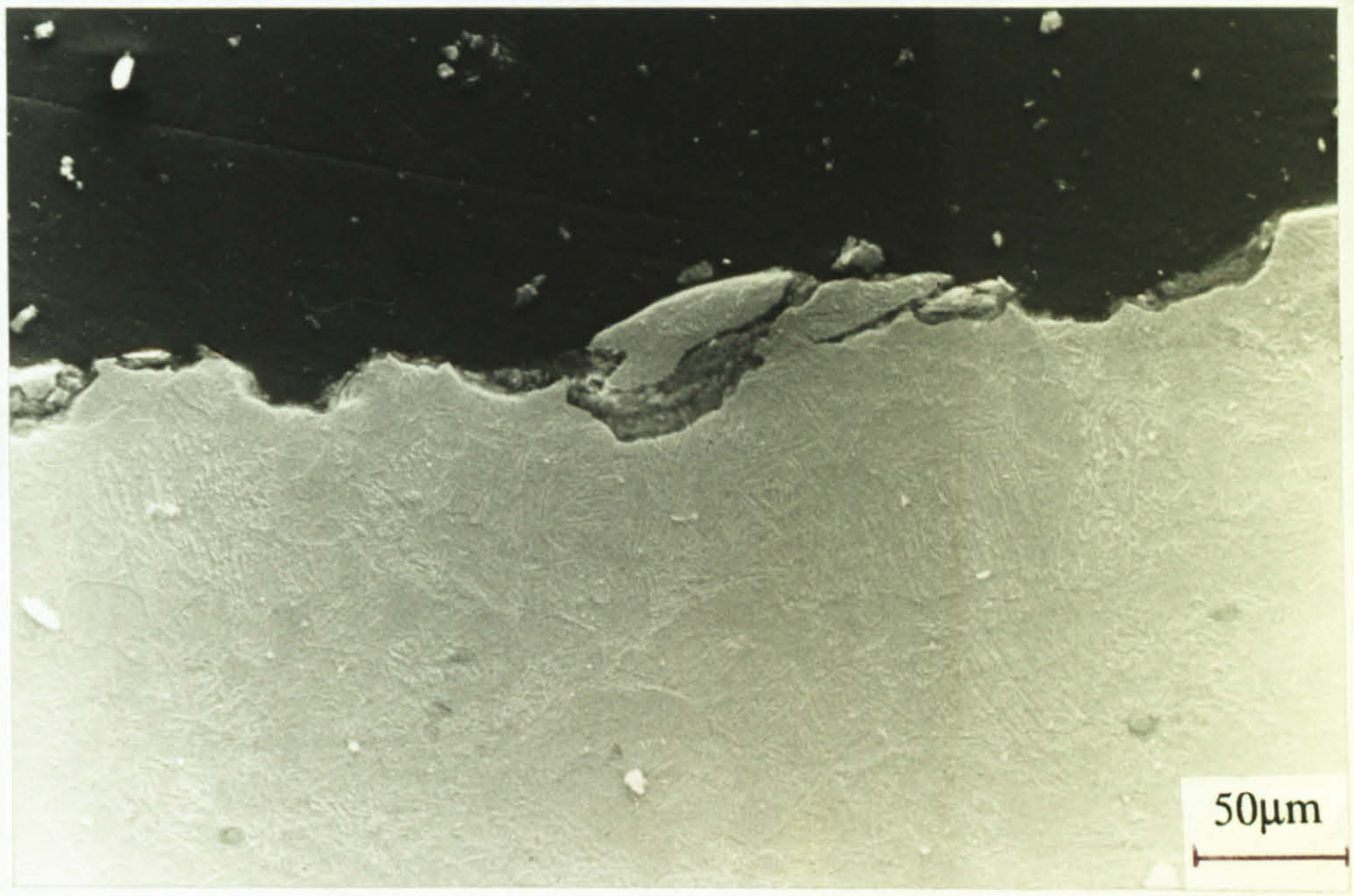


(b)

Fig. 5.47(a) Smooth area inside the wear scar on C-Mn steel and (b) rougher area on the same specimen outward from the central area

In cross section, microhardness values were recorded for each material after a one hour test and it was found that in all cases, there was a significant hardening of the surface, albeit in a very thin layer of <50μm. For example the hardness of UNS S31603, SAF 2205 and C-Mn steel increased by 50, 71 and 88Hv respectively. Hence the repeated bombardment of the surface by solid particles was able to work harden the outer layer. In conjunction with this finding, cracking was often found leading to removal of an outer layer of material. These cracks seemed to initiate perpendicular to the surface, and propagate parallel to the surface until eventual detachment of the material, as shown on 25Cr duplex in Fig. 5.48a. The region corresponds to the region marked **a** in Fig. 5.39b. In Fig. 5.48b, a closer view of the cracked region is shown with a three dimensional network of cracks principally propagating parallel to the surface. No compositional difference could be detected in the region marked 1-5. Similar attack was found on the austenitic stainless steels on a smaller scale as shown in Fig. 5.49 (region represents **b** on Fig. 5.39b) where fragments of material are visible on the surface which have been detached by the propagation of cracks. In addition on the Ni-base alloy Inconel 625, the same effect can be seen in Fig. 5.50 in the area out from the stagnation point marked **a** in Fig. 5.39b.

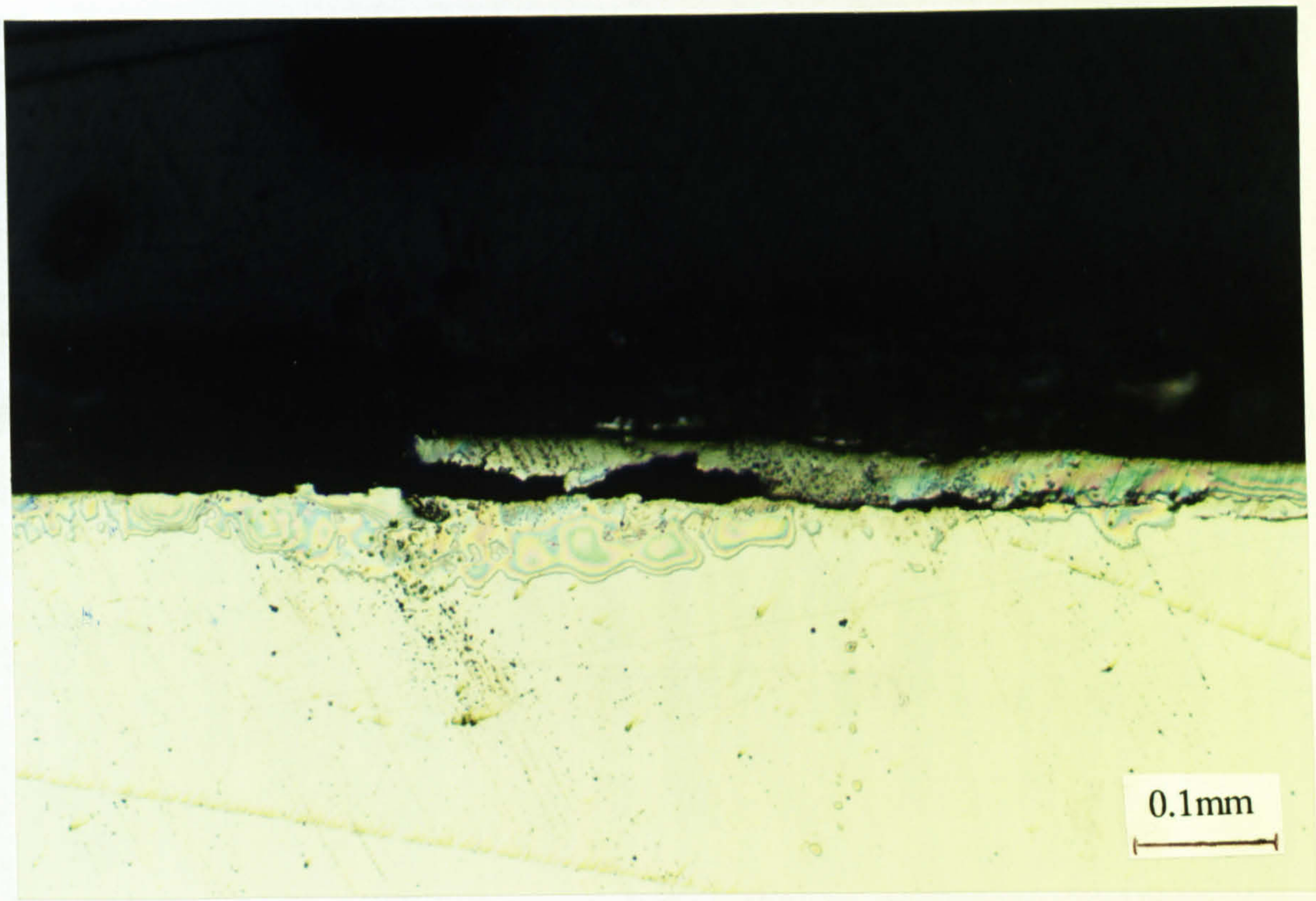


(a)


(b)

Fig. 5.48. Propagating cracks leading to material removal on 25Cr duplex (a) light micrograph (b) same specimen SEM micrograph showing the EPMA analysis area

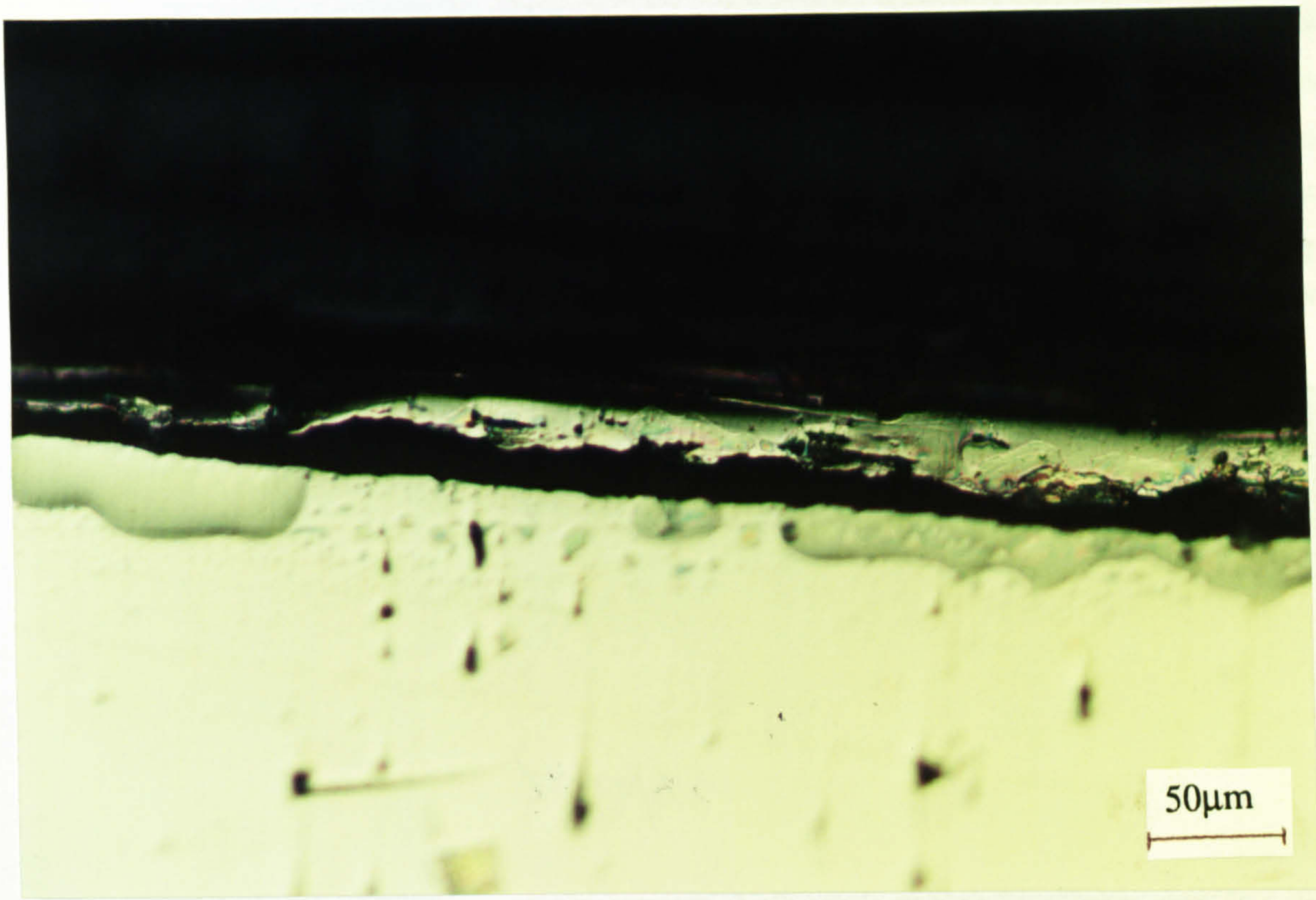


Fig. 5.49. Removal of material from the surface of Inconel 625 by crack propagation


Fig. 5.50. Fragments of material detaching from the surface of an eroded sample of UNS S31603

Under liquid-solid erosion, no difference could be seen on examination of the specimens between those anodically polarised or held at the potential 50mV positive

from $E_{corr}$. Also, in line with the calculations which indicated an enhanced weight loss in the coupling experiments, no difference could be detected in the weight loss between coupled cast iron or Stellite 6 specimens and the freely corroding specimens under the same conditions. However on the specimen held at +600mV for the duration of the experiment, enhanced deterioration was obvious from the wear scar as in Fig. 5.51 in which the top two specimens were exposed at $E_{corr}$ and the lower specimen was potentiostatically controlled at +600mV. A much deeper wear scar is obvious.


Fig. 5.51. Deeper wear scar on specimen under potentiostatic control at 600mV (SCE)

**Effect of Reduced Temperature - in 3.5%NaCl**

In static conditions and in liquid impingement, the effect of increased temperature has been shown to be significant in enhancing corrosion propagation and initiation on the stainless steel and related alloys. Part of the study in liquid-solid erosion involved investigating the effect of reduced temperature on the wear rate and in particular, the proportions of weight loss attributed to corrosion, erosion and any synergy. Preliminary tests showed that on each material, the weight loss was reduced in lower temperature NaCl. The reduction was consistent for each of the stainless steels and Ni-base alloy at between 10 and 12% as shown in Fig. 5.52. A larger reduction of 14% was recorded on the Co-base Stellite 6. The study then focused on five materials to investigate the distribution of weight loss : Stellite 6, UNS S32760, UNS S31603, cast iron and C-Mn steel.

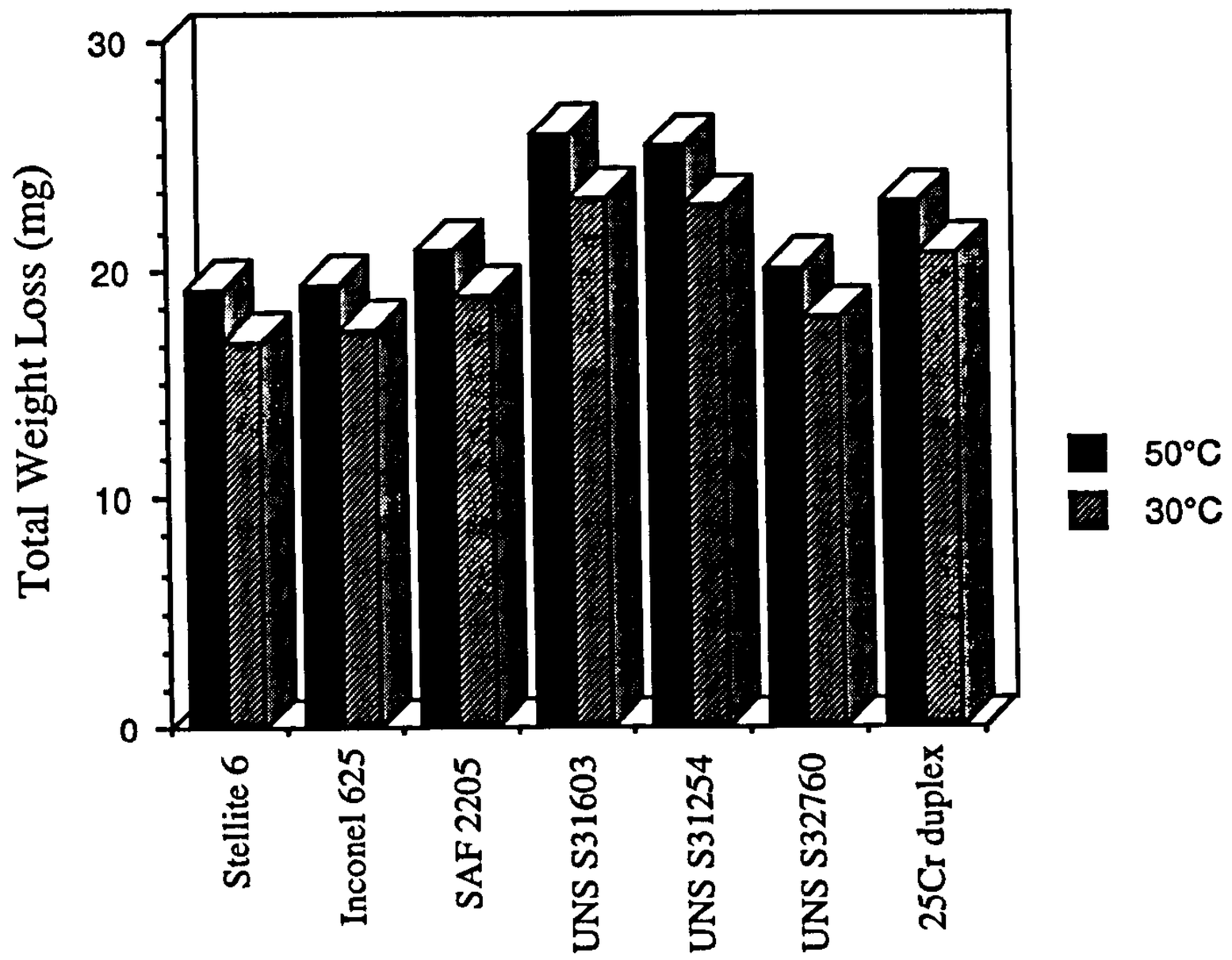


Fig. 5.52. Reduction in TWL for all materials on reducing the temperature to 30°C. For each material, the reported weight loss is an average of 12 specimens, recorded over three test periods

Reduction of the temperature still produced a weight loss which was heavily dominated by erosion and in which pure corrosion represented a small factor. Table 5.4 shows for the 30°C the relative proportions of weight loss as were tabulated for 50°C in Table 5.1. Whilst there was very little change in the pure corrosion component of deterioration on any of the materials tested, it was evident that on the Stellite 6 and more so on the C-Mn steel and cast iron, the synergistic effect became less in the lower temperature fluid thus reducing the overall component directly and indirectly due to corrosion (C+S) and hence increasing the proportion of weight loss due to mechanical erosion. Figure 5.53 shows the change in C+S as a percentage of the total weight loss for the five materials tested.

Comparison of the rate of current decrease on UNS S31603 when the liquid-solid erosion is stopped was made and it was found that there was very little difference at the lower temperature of 30°C as shown in Fig. 5.54. It should be noted though that the current magnitude at the lower temperature while under potentiostatic control was smaller.

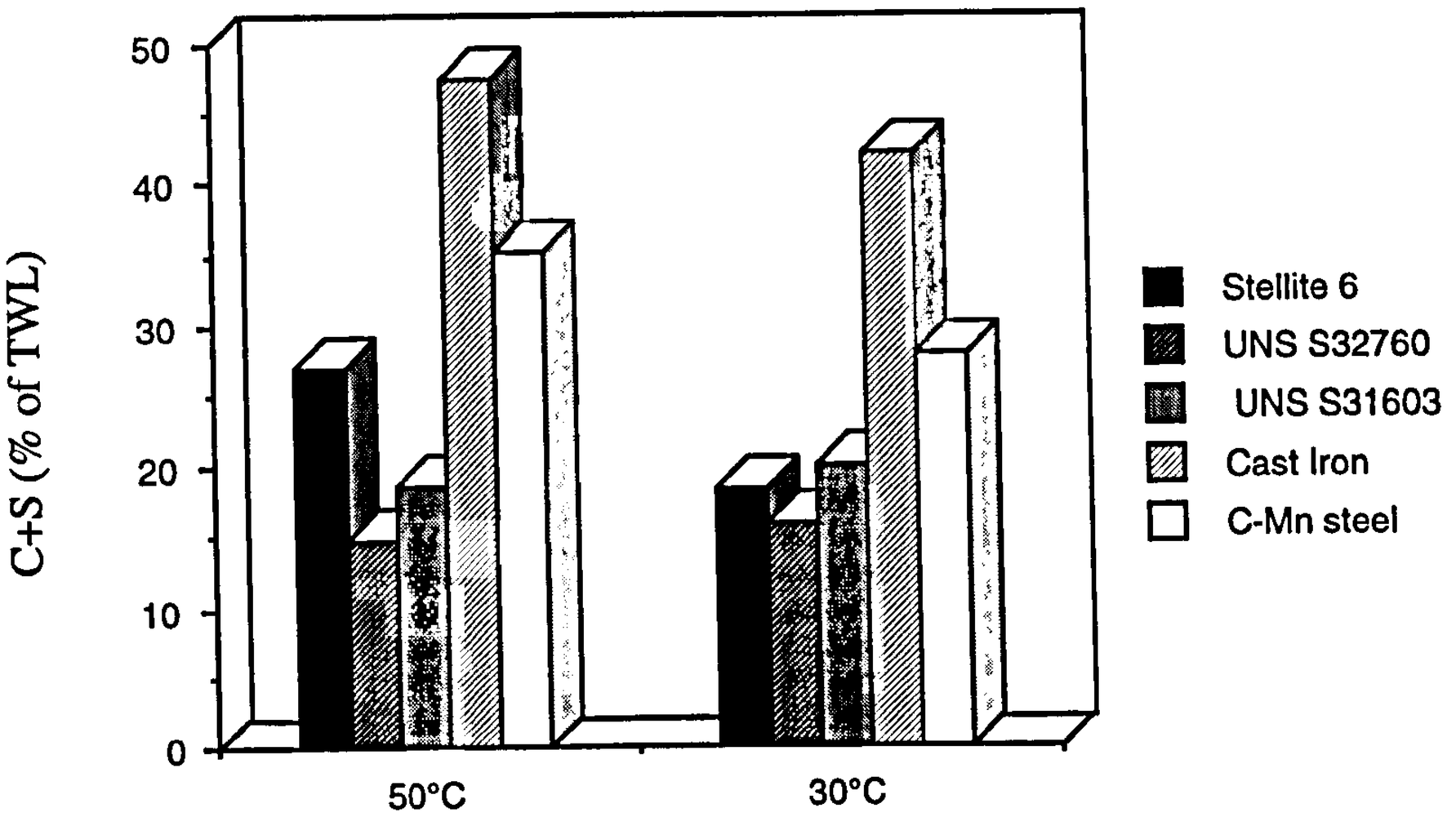


Fig. 5.53. Proportion of weight loss directly and indirectly attributed to corrosion at 30°C and at 50°C in liquid-solid erosion.

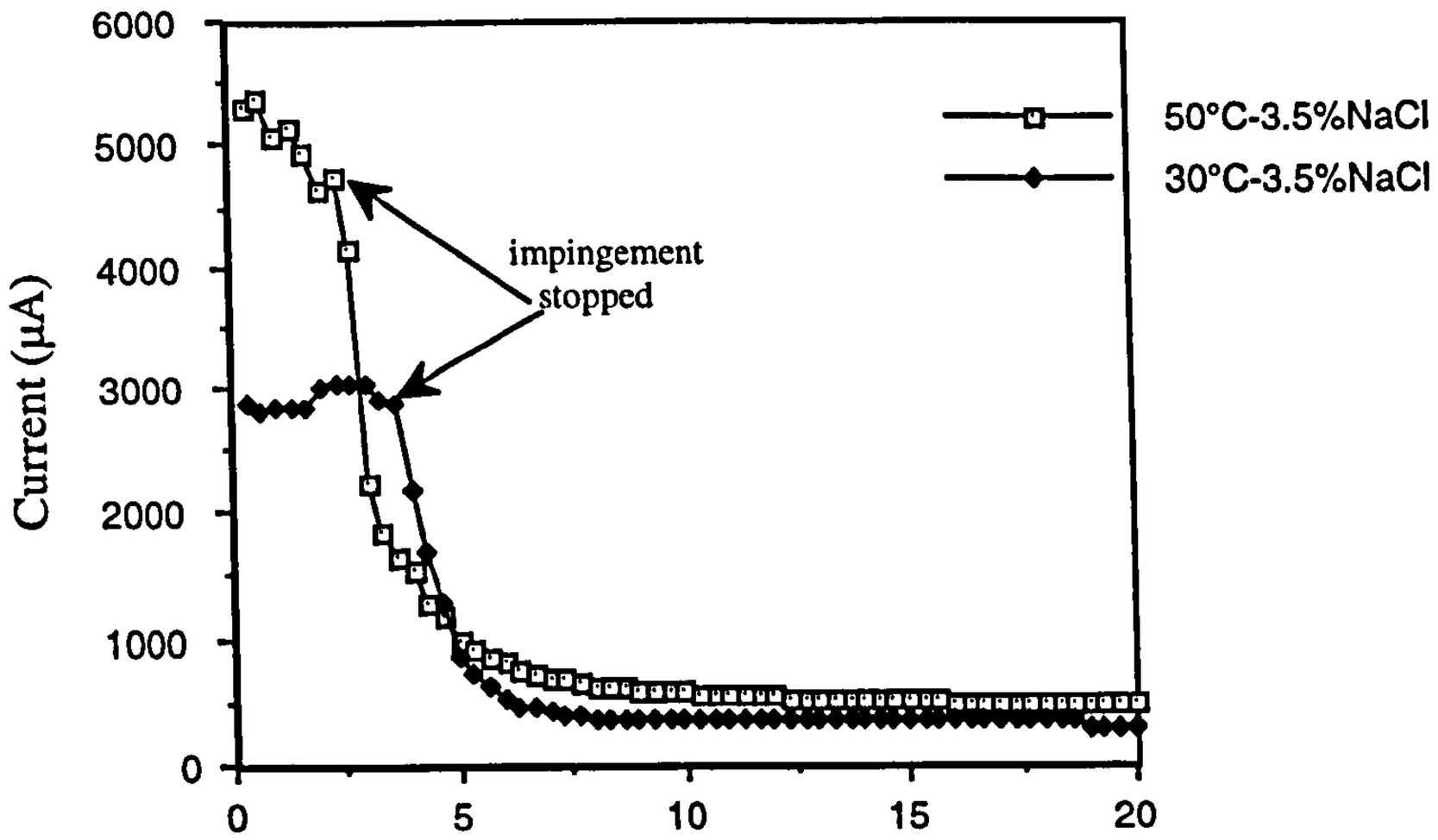


Fig. 5.54. Current decrease rate under potentiostatic control on UNS S31603 at 30°C and at 50°C when the impingement stops

**Effect of Reduced TDS - in 500ppm impinging flow at 50°C**

The intention of this part of the study was to assess the effect of reduced salinity on the parameters controlling the material degradation during liquid-solid impingement. The

work so far has addressed situations which are of practical importance in marine pumping conditions and in contrast the tests in this section of the work were focused on a pumping application which involved the movement of a slurry flow of river water which contained a high level of suspended solids. The materials under study here were only the austenitic stainless steel UNS S31603 and cast iron. The aqueous stream consisted of 1000ppm solids and the TDS was constant at 500ppm.

Small differences in the TWL were recorded for each material over the one hour test period in the 500ppm TDS solution compared to the 3.5%NaCl. On cast iron, a decrease of 2.6% in the TWL was recorded and the corresponding figure on UNS S31603 stainless steel was 7.3%. However much more significant changes in the breakdown of the components of the TWL were observed between the two solutions. The effect of reducing the TDS of the solution was to drastically reduce the pure corrosion component of the deterioration, denoted (C) in the TWL calculation. Table 5.5 illustrates the changes in the breakdown of the total weight loss and Fig. 5.55 shows the changes in $I_{corr}$ in the lower TDS solution.

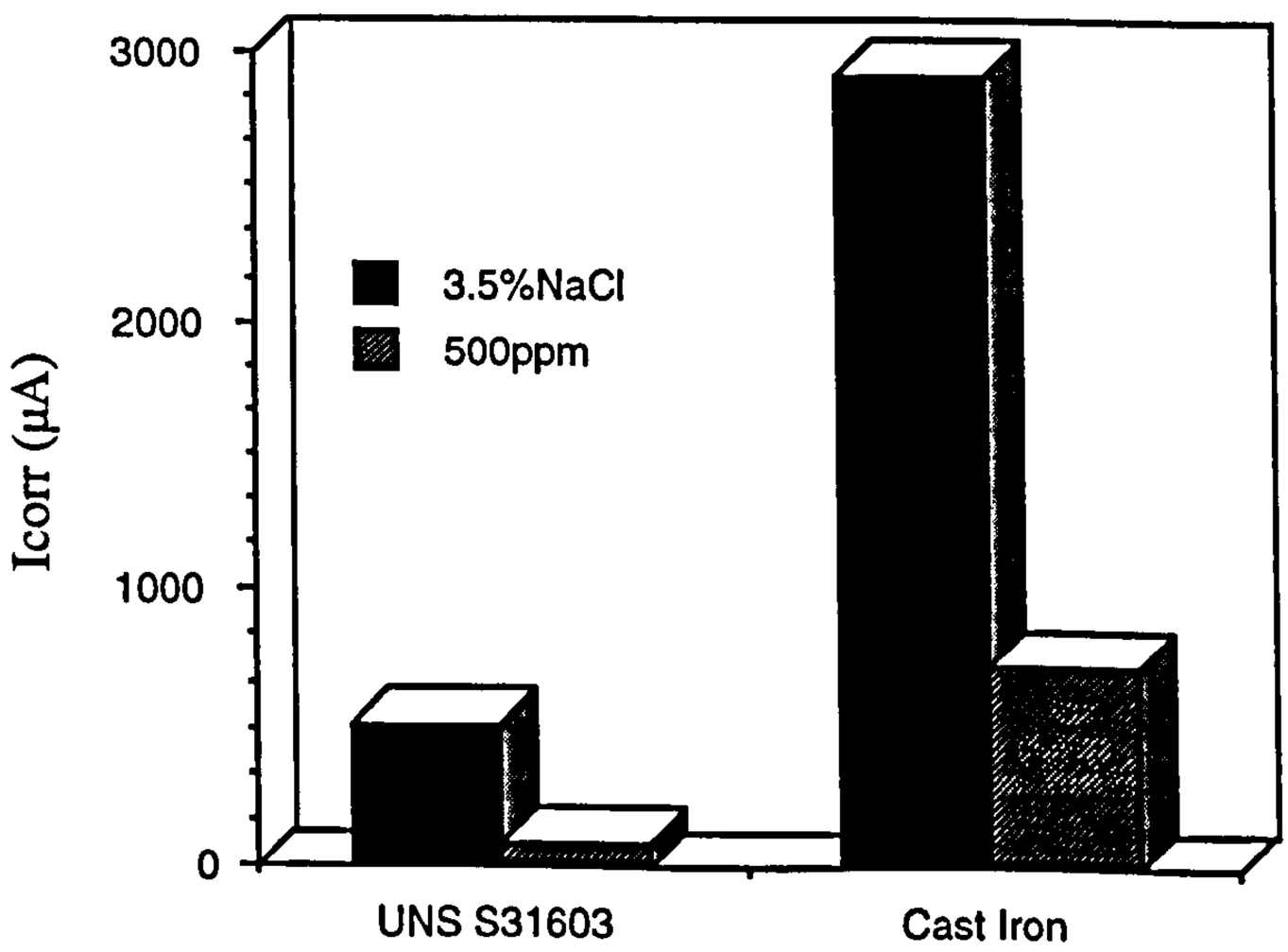


Fig. 5.55. Substantial reduction in the corrosion current in the lower TDS solution on UNS S31603 and cast iron in liquid-solid erosion.

These figures might be considered to indicate that the contribution of corrosion to material loss, the corrosion component (C), under conditions of liquid-solid impingement, in a low TDS liquid, is negligible. However this would be an inaccurate representation, particularly in the case of the cast iron, when we consider the complex interactions between erosion and corrosion. Thus measurement of the TWL in the

absence of corrosion i.e. under the influence of cathodic protection provides a means to quantify the synergistic component of deterioration, S, and thereby demonstrates the important indirect effect of corrosion on degradation under liquid solid impact. The sum of the components of pure corrosion and synergy (C+S) is a measure of how much of the total weight loss is influenced by corrosion and is therefore a more effective measure of the effect of fluid corrosivity. From Table 5.5, it is clear that on reducing the TDS, the contribution to total weight loss of corrosion (C+S) on the UNS S31603 stainless steel drastically reduces to 1% compared to 18.8% in the 3.5% NaCl. On the cast iron, in the low TDS solution, more than 12% of the total metal loss could be attributed to the effect of corrosion which is still a significant proportion even if it is much reduced from the corresponding figure of 47.6% in 3.5%NaCl.

Considering the pure corrosion rate in terms of metal thickness loss per year, on UNS S31603, at the lower TDS, it is equivalent to 0.74mm/year which is of only academic interest since the corrosion component is heavily overshadowed by the mechanical erosion effects in the low TDS impinging liquid solid particle flow. On the cast iron a corrosion rate of 7.2mm/year in low TDS solution was recorded which represents a significant rate of deterioration. A decrease of 4 times was observed on the pure corrosion rate of cast iron in the slurry impingement conditions when the TDS was reduced from 3.5%NaCl to 500ppm. This is in contrast to the more modest decrease of almost 2 times recorded in static solutions for the same decrease in TDS. Hence the effect of the increase in TDS is more pronounced in slurry conditions even on a material such as cast iron which is known to corrode actively and, as such, the impacting particles are not responsible for changing a passive surface into an active one.

Strangely, in low TDS conditions, the effect was to increase the actual weight loss due to pure erosion, in comparison to that measured in 3.5%NaCl as well as the weight loss as a proportion of the total weight loss. The mechanisms by which this can occur are not clear but possible explanations will be discussed later.

It is interesting to point out that the corrosion rate on a pre-eroded specimen in 500ppm TDS water was comparable to that in static conditions on a non-eroded sample, in contrast to the increased corrosion current measured on cast iron after liquid-solid erosion in 3.5%NaCl.

On reducing the TDS of the liquid media, the CP currents on both materials were significantly reduced as shown in Fig. 5.56. Such a large increase in current on directing the jet onto the specimen (i.e. the start of the repeated bombardment) was not

in the low TDS water, thus further evidence of the significantly reduced corrosion rate in the lower TDS solution.

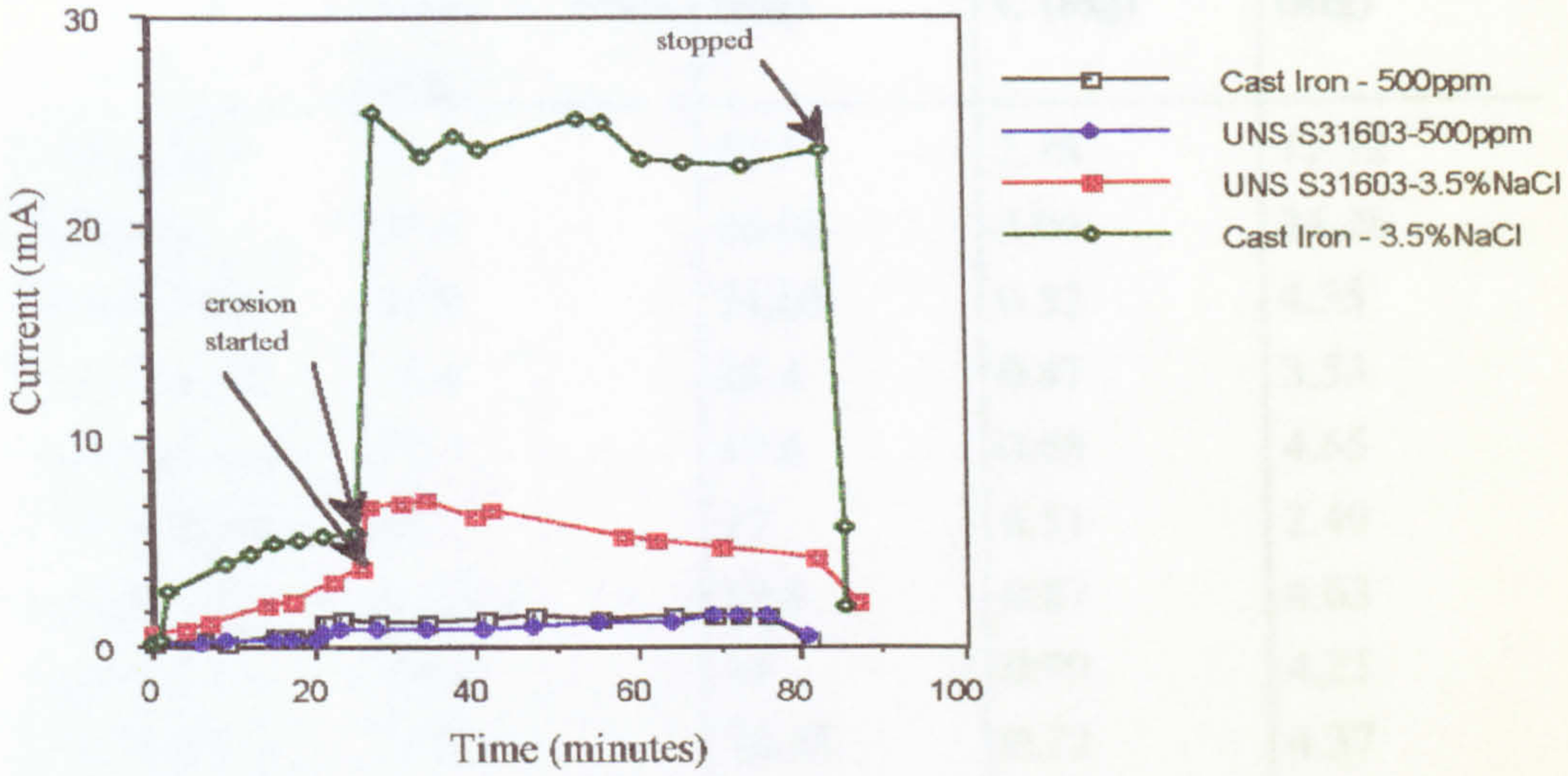


Fig. 5.56. CP currents on cast iron and UNS S31603 in 3.5%NaCl and 500ppm TDS solution at 50°C

Specimen Examination

In the low TDS solution, there were still corrosion products visible on the surface of the cast iron after a one hour test in liquid erosion at 50°C. However, the extent of the attack, as expected was visibly less than in 3.5%NaCl. Microscopy revealed the presence of attack, again seemingly at the graphite/matrix interface).

| Material | Total Weight Loss, TWL (mg) | Erosion, E (mg) | Corrosion, C (mg) | Synergy, S (mg) |
|---|---|---|---|---|
| **C-Mn steel** | 42.5 | 27.6 | 2.18 | 12.72 |
| **Cast Iron** | 57.4 | 30.08 | 3.04 | 24.28 |
| **UNS S31603** | 25.9 | 21.03 | 0.52 | 4.35 |
| **UNS S31254** | 25.4 | 21.4 | 0.47 | 3.53 |
| **25Cr duplex** | 22.9 | 17.6 | 0.65 | 4.65 |
| **UNS S32760** | 20 | 17 | 0.51 | 2.49 |
| **Inconel 625** | 19.3 | 13.8 | 0.87 | 4.63 |
| **Stellite 6** | 19.2 | 14 | 0.99 | 4.21 |
| **SAF 2205** | 20.8 | 16.35 | 0.72 | 4.37 |
| **Ultimet** | 19 | | | |

Table 5.1. Proportions of the total weight loss in mg under liquid-solid erosion at 50°C in 3.5%NaCl

| | Total Weight Loss, mg | Erosion, mg | Corrosion, mg | Synergy, mg |
|---|---|---|---|---|
| **18°C** | 2.9 | 0.183 | 0.402 | 2.315 |
| **50°C** | 4.9 | 0.6 | 0.503 | 3.797 |

Table 5.2. Proportions of the total weight loss given in mg/hour from a 24 hour experiment under liquid erosion at 18°C and at 50°C

| Material | Maximum Cathodic Protection Current, mA |
|---|---|
| C-Mn steel | 19 |
| Cast Iron | 28.2 |
| UNS S31603 | 6.3 |
| UNS S31254 | 4.7 |
| 25Cr duplex | 9.8 |
| UNS S32760 | 5 |
| Inconel 625 | 14.1 |
| Stellite 6 | 16.8 |
| SAF 2205 | 9 |

Table 5.3. Maximum cathodic protection current measured under liquid-solid erosion at 50°C

| Material | Total Weight Loss, TWL (mg) | Erosion, E (mg) | Corrosion, C (mg) | Synergy, S (mg) |
|---|---|---|---|---|
| C-Mn steel | 40.1 | 29 | 1.92 | 9.18 |
| Cast Iron | 50.8 | 29.5 | 2.4 | 18.9 |
| UNS S31603 | 23.1 | 18.48 | 0.51 | 4.11 |
| UNS S32760 | 17.8 | 14.9 | 0.41 | 13.7 |
| Stellite 6 | 16.8 | 13.7 | 0.82 | 13.6 |

Table 5.4. Weight losses in mg attributed to erosion, corrosion and a synergistic factor.

at 30°C

| | Cast Iron | | UNS S31603 | |
|---|---|---|---|---|
| | 3.5% NaCl | 500ppm TDS | 3.5% NaCl | 500ppm TDS |
| TWL (mg) | 57.4 | 55.9 | 25.9 | 24.0 |
| Erosion | 52.4% | 87.2% | 81.2% | 99% |
| Corrosion | 5.3% | 1.4% | 2% | 0.4% |
| Synergy | 42.3% | 11.4% | 16.8% | 0.6% |

Table 5.5. Total weight loss distribution under liquid-solid impingement at 50°C after 1 hour

**Discussion**

This work was undertaken to provide a detailed appreciation of the erosion-corrosion behaviour of a range of ferrous and non-ferrous materials and has demonstrated large differences in the extent and mechanisms of deterioration of the materials investigated. In liquid-solid impingement conditions, all materials suffer severe attack. However, the study has illustrated some significant variations of both practical and fundamental interest between the range of materials investigated. The combination of electrochemical, weight loss and visual/microscopical investigations has quantified the three basic features of deterioration, pure corrosion, pure erosion and synergism, in erosion-corrosion conditions. In particular, it has been shown that the contributions of these processes to the overall material loss varies substantially between the different classes of material.

Recent extensive laboratory studies [41] have succeeded in demonstrating that, contrary to the view held by some material selectors, the resistance of a material to degradation by wear is not solely dependent on the relative hardnesses of the eroding particles and the eroded surface. While the hardness correlation to wear resistance may have some use in predicting relative behaviour of pure metals and single phase alloys, it has been shown to be of little practical use in prediction of multiphase material behaviour. Particularly when the mechanical effects of particle bombardment act in conjunction with the electrochemical corrosion effect due to the corrosive carrier liquid, there are complex interdependent processes which dictate the rate and modes of material degradation. This present study has shown that generally the weight loss due to mechanical erosion decreases as the material hardness increases, although the

relationship is not linear. Also, there is no general correlation when the weight loss due to corrosion and synergy are considered.

There is still a need therefore to identify, on given materials and under defined operating conditions, the factors which dictate the relative deterioration rates and the components of the deterioration. For complex processes such as the simultaneous actions of erosion by an impinging liquid-solid two phase jet and corrosion, there are obviously a number of parameters to dictate the material loss. It has been one of the aims of this work to isolate the corrosivity as a variable parameter and investigate it's effect (via temperature and TDS changes) on not only the corrosion rate but the wear rate as a whole.

General Comments on Erosion-Corrosion Behaviour

From weight loss data, the materials in this study could be broadly divided into 4 categories. Superior resistance to erosion-corrosion was exhibited by the Co-base and Ni-base alloys, confirming the concept of previous authors of a hardness/weight loss correlation. The stainless steels resistance to weight loss related to their metallurgical structure, the duplex and in particular the superduplex stainless steels showing better resistance than the austenitic stainless steels which is in agreement with the work of Renaud et al. [27]. The two materials which are known to offer poor corrosion resistance in seawater (C-Mn steel and cast iron) showed enhanced rates of metal loss under liquid-solid erosion.

The crucial effect of solid content in the liquid stream has been demonstrated. Comparison with results in solids-free erosion has enabled the important role of solid impact to be elucidated. Even at a much reduced free stream velocity of 25m/s, (compared to 100m/s in liquid erosion), the sand particles are capable of immediately removing material. This situation is more surprising when the work of Clark is considered [30], in which he states that the velocity of a impacting particle can be a factor of 10 times less than the free stream liquid velocity due to the diversion of the particles in the squeeze film.

Corrosion Aspects

Significant differences have been shown to exist within the broad classes defined above in the contribution of corrosion to the total weight loss. The proportion of weight loss (and the actual weight loss in mg) was greater on the two duplex stainless steels (SAF 2205 and 25Cr duplex) than on the austenitic and superaustenitic stainless steel, even

though the total weight loss on the duplex stainless steel was significantly lower. This points to important influences of metallurgical structure and alloying content in determining the resistance to corrosion attack under the severe conditions. When considering the weight loss due to corrosion, there is no weight loss/hardness correlation, as indicated by the recorded high corrosion rates of the Co and Ni-base alloys under liquid-solid erosion.

In the presence of sand, the anodic metal dissolution reaction has been shown to be severely depolarised on each material but especially on the stainless steels, Co-base and Ni-base alloys (normally regarded as 'passive' alloys in seawater) and therefore contributes to the more active $E_{corr}$ recorded. Hence, under liquid-solid erosion, the anodic reaction assumes a dominant role in determining the $E_{corr}$ value, whereas in liquid erosion, where the materials are still in the passive domain, there is no significant change in the anodic reaction in the region near to $E_{corr}$ and, as such, the determining factor for the free corrosion potential is the cathodic reaction which has been shown to be depolarised by the enhanced turbulence and fluid mixing.

The situation on the stainless steels, Co-base and Ni-base alloys in this study, once sand was added to the liquid stream, was one where mechanical effects were sufficient to destroy the passivity of the materials via impact by hard silica sand particles which removed areas of the passive film on a repeated basis, revealing unprotected metal on which degradation by corrosion could easily proceed. However, it must be stated that on Stellite 6, the mechanical effect of an impinging solids free jet at 50°C was capable of rendering the surface active. From the moment the sand in the system reached the surface, the effect was to dramatically increase the anodic current and general corrosion prevailed over the entire surface. Nevertheless, the higher corrosion rates of C-Mn steel and cast iron under sand erosion compared to the stainless steels, Co-base and Ni-base alloys confirmed that a level of alloying confers, to a great extent, increased protection even under severe conditions. This indicates that there are mechanisms of reducing somewhat the severity of corrosion attack which can be effective even when the protective oxide film is mechanically removed. Comparison of the behaviour of UNS S31603 with that of SAF 2205 and 25Cr duplex stainless steels in this work provides indications that the well established [42,43] benefits of Cr, Mo and N in enhancing localised corrosion resistance in static conditions may not pertain under more severe environmental conditions of elevated temperature [44] and especially erosion impingement. Perhaps this is not surprising since under liquid-solid erosion the repeated bombardment of the surface prevents the establishment of the passive film so that the corrosion resistance will depend on the behaviour of the material in the active state and will not be dictated by the structure and composition of a passive film.

Notwithstanding the overall active behaviour discussed above of the stainless steels under liquid-solid erosion, the oscilloscope monitoring, Fig. 5.34, yielded relatively large current fluctuations. These might be indicative of a process of rapid sequences of repassivation of the passive film in phase with repetitive impact by individual sand particles, repassivation being aided by an abundance of oxygen at the specimen surface due to the highly turbulent hydrodynamic conditions. This notion is given some support by the much smaller current fluctuations in the corresponding tests with C-Mn steel in which case the tiny fluctuations (on a much higher current value) might have been due to extremely minor influences of corrosion products formed and removed under impact.

Although it has been shown that the pure corrosion element of weight loss on every material represents a very small proportion of the total weight loss, it would be misleading to assume therefore that the effect of corrosion in severe liquid-solid erosion is negligible. The corrosion currents associated with liquid-solid impingement in themselves represent a significant rate of material loss but more importantly, the effect of corrosion on the erosion process, quantified by measurement of the synergistic component must be considered. Of significance in this work is the finding that under severe liquid-solid impingement, the direct and indirect effects of corrosion (C+S) can account for a large proportion of the weight loss and by reducing the corrosion, the actual mechanical wear component of weight loss can reduce. Approximately 25% of the total weight loss can be attributed to corrosion on the Co and Ni-base alloys, 20% on the stainless steels and 40-55% on the cast iron and C-Mn steel.

In static seawater and in liquid erosion, the effect of increased temperature was to significantly enhance the initiation and propagation of localised corrosion on the stainless steels, and related alloys. On the C-Mn steel and cast iron, the rate of general attack is increased. It was therefore not unexpected to find that by reducing the temperature to 30°C in liquid-solid erosion, there was a subsequent reduction in the active corrosion rate on all materials. The effect on Stellite 6, cast iron and C-Mn steel was to significantly decrease the proportion of the weight loss attributed to corrosion and also reduce the synergy but on the stainless steels, the proportion remained almost constant. This meant that on Stellite 6, cast iron and C-M steel, the erosion component assumed greater importance as a proportion of the weight loss in lower temperature conditions (although in mg, E was lower than at 50°C). This finding substantiates the previously found susceptibility of Stellite 6 to liquid erosion once a critical temperature is achieved (see chapter 4).

The effect of lowering the TDS was more pronounced than the effect of temperature thus indicating for practical purposes the relative influences of environmental factors. Indeed the pure corrosion component on the stainless steels became almost negligible (<1%). However, on cast iron, the corrosion component (C) and indeed the total effect of corrosion on erosion (C+S) was still significant. These findings combined with weight loss and microscopy observations posed several questions regarding the mechanistic changes in a low TDS solution. The mechanism by which the high chloride content in the liquid-solid impinging stream of 3.5%NaCl can substantially increase the corrosion rate and synergistic component of the TWL is not fully understood but consideration is given to the rate of oxide film formation and the nature of these oxides.

It has been postulated by previous workers in this field [45] that the important determining factors of wear rates in an aqueous liquid are the formation of oxide films which are subsequently removed by abrasion, erosion or by other mechanical processes. These and other corrosion products could be involved in the large synergy factor which, as argued in the 'Results' section represents, in this study, the influence of corrosion in increasing the mechanical wear rates. Using this argument, the higher 'C' component for cast iron could in turn account for the enhanced 'S' component. On stainless steels, passive behaviour is exhibited at 50°C in static 3.5%NaCl and the importance of the chloride ions is in facilitating localised breakdown of the passive film to promote pitting and crevice attack. The behaviour of stainless steels under erosion-corrosion conditions is very much different and although the chloride content of the liquid could be responsible for a weakening of the protective oxide, it is the mechanical effect of the bombarding particles which can easily remove this film and the question then is how the chloride ions affect this surface which is active shortly after particle bombardment. Where the chloride content of the liquid seems to play an important role is in the period where the oxide film has been removed by solid impact and the rate of repassivation of the oxide is crucial in determining how much electrochemical corrosion can occur. It is not unreasonable to envisage the situation which follows rupture to be the diffusion of chloride ions to the surface at a high rate which prevents the almost immediate reformation of the oxide which would occur in the case where there are few chloride ions and an abundance of oxygen. The chloride ions could have the additional effect of assuming a position within the oxide layer which disrupts its adherence and integrity facilitating easier rupture by subsequent impacts.

The nature of oxides formed on cast iron are inherently different from the thin, closely adherent chromium-rich layers formed on stainless steels. In order to explain the

observed larger increase in corrosion rate in more saline water in erosion conditions compared to static conditions, the different mechanisms of oxide formation can be considered. The trends illustrate that in static conditions, the oxide formation can consist of several phases forming a composite Fe-rich oxide, the rate of growth of which decreases with time due to the semi-protective nature of the underlying oxide and hence forming a barrier to the environment. In the severe erosion-corrosion environment however, the repeated removal of the oxide by the flux of particles means that at all times, the oxide growth is relatively fast since a fresh oxide-free surface is continually exposed. The difference in corrosion rate in static conditions and impingement conditions is due to the fact that the corrosion rate, on the specimen being bombarded by solid particles, does not have the opportunity to reduce in the presence of corrosion products.

Further evidence to suggest that after erosion the cast iron surface is susceptible to a higher corrosion rate due to the initially high rate of oxide formation exists from consideration that a specimen which has under gone erosion-corrosion exhibited a corrosion rate five times greater than on a specimen which had been immersed in static 3.5%NaCl for the same length of time. While this paper was intended to demonstrate the important effects that liquid corrosivity have on the wear modes and components, additionally, it has been shown that the mechanical erosion processes can affect the corrosion behaviour of in this case a cast iron even after the erosion has stopped. Part of this increase in corrosion current could perhaps have been due to the increase in surface area caused by the erosion.

Erosion Aspects

The work involved examination of both the mechanisms by which detachment of eroded material occurs and the resulting morphology of the remaining surface. After testing, examination of specimens cut in cross section revealed a wear scar of the form of Fig. 5.39b. The pattern clearly shows the hydrodynamic features of the flow in the stagnation point where the erosion damage is least and in the severely eroded perimeter area where high shear forces in the flow moving radially outwards induce a greater thickness loss. Also in plan, the wear scar clearly revealed the symmetrical form, showing the central section with lowest metal thickness loss corresponding to where the impinging jet flow separated. At higher magnification the appearance of the eroded area showed clear directionality of metal deterioration defining the flow pattern. In the central area where the jet nominally hits the specimen at 90° incidence, the appearance of the metal loss area is in the form of small indentations, in contrast with the

directional ploughing of the material and long, deep troughs found at the outer areas where the flow would nominally be in the radial direction.

The repeated bombardment produced a significant work-hardening effect on all materials in a very thin outer layer, perhaps contributing to an increase in the susceptibility of the surface to cracking. At the lowest points in the wear scar, cracks initiating perpendicular to the surface were detected. The cracks seemed to propagate parallel to the surface and then finally intersected the surface causing segments of metal to detach.

The overall form of the cross-section was independent of material but on a smaller scale, on each material, the profile roughness increased away from the stagnation point and ploughing deterioration became evident. In the central area suffering the least thickness loss, the profile of the surface did not consist of the troughs evident in the more severely eroded area surrounding the stagnation point. In the radial areas immediately out from the centre of the jet impact region the displaced material formed lips and troughs, also reported to occur in liquid erosion after an initial incubation period [46], which could be easily removed by subsequent impacts. Possibly the increased rotation and angular momentum of the particles, due to increased particle-particle interactions after initially bombarding the surface, enhanced the extent of deterioration.

Consequently, these observations indicate that, under an impinging jet at 90°, mixed modes of material deterioration can exist due to the complex array of incident angles imposed by the hydrodynamic conditions. The effect of impingement angle on material degradation on ductile materials under solid particle erosion is well known and documented [6] and it is suggested that in this work the liquid/solid slurry jet impinging at 90° imposes, on a more localised scale, variations in the type and extent of degradation due to different incident angles. Hence in this one system, analogies can be drawn to the observations under solid particle erosion and the complex flow parameters imply that the extent and form of deterioration is strongly dependent on the local incidence angle. In cases involving an impinging liquid flow containing solid particles, it is therefore necessary to consider these variations in conjunction with overall material deterioration.

Interestingly in the low TDS solution, the actual weight loss due to pure erosion was increased although the total weight loss was significantly decreased compared to 3.5%NaCl. The mechanisms by which this is achieved on both cast iron and on stainless steel are not clear. One possible explanation of this could be the effect of

corrosion products on cast iron and the passive film on stainless steel in acting as a damping barrier which in 3.5%NaCl reduces the mechanical effect of the eroding particle. However, there were reduced corrosion products observed in lower temperature conditions and no subsequent increase in the E component. Examination of the specimens in cross section yielded, in low TDS and in 3.5%NaCl, severe attack down the areas adjacent to graphite flakes leading to material removal. Although this was not detected on specimens which were cathodically protected, it is possible that in localised areas there exists an IR drop which means that during the experiments with applied cathodic protection, there are still localised areas of corrosive attack which enable the material to be more easily mechanically removed. This would therefore slightly complicate calculation of the synergistic effect since under cathodic protection in the low TDS solution there would still be a small localised corrosion effect.

Points of Practical Interest

In this study the information amenable from weight loss considerations has been extended to include detailed information on the mechanisms of attack and interactions between modes of attack occurring in an erosion-corrosion environment. The results have indicated that the process of material selection for a severe erosive-corrosive environment is immensely complicated and several parameters relating to conditions and material properties must be considered.

An important point from this work is the narrowing of the gap between the performance of the low grade materials (C-Mn steel and cast iron) and the advanced alloys under severe erosion-corrosion. In static conditions, the corrosion rate of cast iron is much greater than on stainless steels due to passivity of the latter. However, it has been shown that in applications where joint erosion and corrosion occur, both types of materials are active and as such the corrosion rate of stainless steels more closely relate to the dissolution rate of cast iron.

The effective reduction of weight loss by application of cathodic protection can be of both practical importance and of fundamental importance as a tool for separating the deterioration components. There could be potential in some instances for the successful use of CP as a means of reducing not only corrosion but the erosion component of material deterioration, particularly in the case of a C-Mn steel or cast iron on which a 50% reduction can be achieved in the total weight loss.

Galvanic interactions assume an important role in erosion-corrosion situation between materials which in static conditions would not present a problem. It has been shown

that the galvanic current can increase the corrosion on an eroding specimen significantly and the practical implications from this are obvious.

Importantly it has been shown on cast iron that the effect of solid particle erosion is to enhance the corrosion rate even after the erosion has ceased. There is therefore an important message here in that the situation of intermittent erosion/static periods could be more detrimental to the corrosion of the material.

**Conclusions**

The main conclusion from this work is that under the severe erosion-corrosion conditions, the behaviour of the so-called passive alloys is no longer determined by the stability and the integrity of the passive film and as such high deterioration rates ensue. The presence of sand, even at much lower velocities than the impinging solids free flow in chapter 4, can remove the passivity immediately on contact with the surface, illustrating the aggressiveness of liquid-solid two phase flow.

The rate of metal loss has been shown to accelerate by galvanic coupling thus illustrating the important point that electrical contact of components in severe impinging and erosion-corrosion environments can prove to be significant.

In agreement with the findings in chapter 4 in which the mechanisms of attack n Stellite 6 were shown to change under liquid impingement compared to static conditions at 50°C, this present study has demonstrated an analogous effect on cast iron in the presence of an impinging stream of liquid (containing solids or solids free).

In practical terms, the superiority of the stainless steels and related alloys to C-Mn steel in normal seawater conditions is much reduced. Although there is some difference between the erosion-corrosion resistance of the high-grade materials, high rates of metal dissolution prevail under liquid-solid erosion and as such, it is becoming increasingly recognised that there is a requirement in severe impingng conditions for materials such as ceramics and ceramic/cermet coatings to combat wear problems.

## References

1. G. Silva, Wear generation in hydraulic pumps, SAE Technical Series, *International Off-Highway and Powerplant Congress and Exposition*, Milwaukee, September 1990.

2. J. Madadnia, I. Owen, Accelerated surface erosion by cavitating particle-laden flows, *Wear*, 165, (1993), 113-116

3. M. M. Stack, F. H. Stott, G. C. Wood, Characterisation of erosion-corrosion regimes, Surface Engineering Volume II : Engineering Applications, *Royal Society of Chemistry*, p31-41

4. M. M. Stack, J. Chacon-Nova, F. H. Stott, Relationship between the effects of velocity and alloy corrosion resistance in erosion-corrosion environments at elevated temperatures, *Wear*, 180, (1995), 91-99

5. I. Finnie, Erosion of surface by solid particles, *Wear*, 3, (1960) 87-103

6. I. M. Hutchings, *Tribology : Friction and wear of engineering materials*, Edward Arnold, 1992

7. G.T. Burnstein, I. M. Hutchings, Comparative study of the slurry erosion and free-fall erosion of aluminium, *Wear*, 149 (1991) p73

8. A. Levy, G. Hickey, Erosion of corrosion-resistant surface treatments on alloy steels, *Proceedings of the Int. Conf. on Wear of Materials*, Ed. K. C. Ludema, Vancouver, 1985

9. M. M. Stack, R. C. Newman, Identification of transitions in erosion-corrosion regimes in aqueous environments, *Presented at the 8th Int. Conf. on Erosion by Liquid and Solid Impact*, Cambridge, September 1994

10. A. Karime, R. K. Schmid, Ripple formation in solid-liquid erosion, *Wear*, 156, (1992) 33-37

11. R. I. Hughes, Surface-chemical aspects of the rusting of steel surfaces in oil containing an entrained aqueous phase, *Corrosion Science*, 9, 535, (1969)

12. I. Iwasaki, S. C. Riemer, J. N. Orlich, K. A. Natarajan, Corrosive and abrasive wear in ore grinding,*Wear*, 103, (1985) 253-267

13. G. R. Hoey J. S. Bednar, Erosion-corrosion of selected metals in coal washing plant environments, *Materials Performance*, April 1983, 9-

14. G. Silva, SAE Technical Paper Series, *International Off-Highway & Powerplant Congress and Exposition*, Milwaukee, Wisconsin, September 1990

15. K. Bremhorst, P. J. Flint, The effect of flow patterns on the erosion-corrosion of shell and tube heat exchangers, *Wear*, 145 (1991), 123-125

16. D. H. Graham, A. Ball, Particle erosion of candidate materials for hydraulic valves, *Wear*, 133 (1989), 125-132

17. F. E. Kennedy, B. M. Espinza, S. M. Pepper, Thermocracking and wear of ceramic-coated face seals for seawater applications, *Journal of the Society of Tribologists and Lubrication Engineers*, 46, 10, 1990, 663-671

18. F. Feicht, Failures influencing service life and failure of hydraulic components, *Olhydralik and Pneumatik*, 20, 1976, 804-806

19. Anon, Wear in slurry pumps, *Warman Technical Bulletin*, No. 9, May 1991

20. H. McI. Clark, The influence of flow field in slurry erosion, *Wear*, 152, (1992), 223-240

21. C. H. Pitt, Y. M. Chang, Electrochemical determination of erosive wear of high carbon steel grinding balls, *Mi. Metall. Process.*, August 1985 (166-173)

22. C. H. Pitt, Y. M. Chang, Corrosive-erosive wear of grinding ball metals at high jet velocities, NACE, *Corrosion '86, Symp. on Corrosion and Wear in the Mining and Metal Processing Industries*, Houston, TX, March, 1986

23. D. K. Spencer, A. A. Sagues, Erosion by sand and coal slurries, *3rd Berkeley Conf. on Corrosion-Erosion-Wear at Elevated Temperatures*, Berkeley, CA, January 1986

24. J. Postlethwaite, E. B. Tinker, M. W. Hawrylark, Erosion-corrosion in slurry pipelines, *Corrosion* , Vol. 30, No. 8, 1974, p285-290

25. J. Postlethwaite, Direct measurement of the corrosion current for oxygen reduction corrosion. In F. Mansfeld and U. Bertocci (eds), *Electrochemical Corrosion Testing*, ASTM Spec. Tech. Publ. 727, 1981, 290-302

26. E. Heitz. Chemo-mechanical effects of flow on corrosion, *Corrosion*, Vol. 47, No. 2. 1991

27 L. Renaud, B. Chapey, J. C. Bosson, R. Oltra, J. Charles, Erosion-corrosion properties of austenitic and duplex stainless steels, *Proc. Conf. on Duplex Stainless Steels '91*, eds. J. Charles, S. Bernhardsson, Bourgogne 1991

28. R. J. K. Wood, S. P. Hutton, The synergistic effect of erosion and corrosion : trends in published results, *Wear,* 140 (1990) 387-394

29. J. A. C. Humphrey, Fundamentals of fluid motion in erosion by solid particle impact, *Int. J. Heat and Fluid Flow*, Vol. 11, No. 3, September 1990

30. H. McI. Clark, L. C. Burmeister, The influence of the squeeze film on particle impact velocities in erosion, *Int. J. Impact Engng*. Vol.12, No.3, 415-426, 1992

31 H. McI. Clark, On the impact rate and impact energy of particles in a slurry pot tester, *Wear*, 147, (1991), 165-183

32. A. Neville, T. Hodgkiess, J. T. Dallas, A study of the erosion-corrosion behaviour of engineering steels for marine pumping applications, *Wear*, in press

33. M. Bjordal, E. Bardal, T. Rogne, T. G. Eggen, Erosion and corrosion properties of WC-coatings and duplex stainless steels in sand-containing synthetic seawater, *Presented at the 8th Int. Conf. on Erosion by Liquid and Solid Impact*, Cambridge, September 1994

34. X. X. Jiang, S. Z. Li, D. D. Tao, J. X. Yang, Accelerative effect of wear on corrosion of high-alloy stainless steels, *Corrosion*, Vol. 49, No. 10, 1993

35. M. Abuzriba, R. A. Dodd, T. J. Worzala, J. R. Conrad, Wear corrosion : separation of the components of corrosion and wear, *Corrosion*, Vol. 48, No. 1, 1992

36. J. Weber, Flow induced corrosion : 25 years of industrial research, *Brit. Corros. J.*, 27 (3), 1992, p193

37. L. L. Shrier, *Corrosion*, Vol I, Goerge Newnes, London 1963

38. T. Hodgkiess, A. MacIver, P. Y. Chong, Galvanic studies related to the use in desalination plant of corrosion resistant materials, *Desalination*, Vol. 66, 1987, 147-170

39. F. H. Stott, J. E. Breakall, R. C. Newman, *Corros. Sci.*, Vol. 30, No. 8/9, 813-830

40. U. Meyer, C. C. Bronnan, K. Bremhorst, R. Tomlin, A. Atrens, *Wear*, 176 (1994)

41. J. H. Brunton, in C. M. Preece (ed.), *Erosion : treatise on material science and technology*, Vol.16, Academic Press, 1979, p185

42. E. Alfonnson, R. Qvarfort, Investigation of the applicability of some PRE expressions for austenitic stainless steels, *presented at the Int. Conf. on Electrochemical Methods in Corrosion Research*, EMCR '91, Helsinki, Finland, July 1991

43. T. J. Glover, Recent developments in corrosion resistant metallic alloys for construction of seawater pumps, *Mater. Perf.*, Vol. 7, 1988

44. A. Neville, T. Hodgkiess, An assessment of the corrosion behaviour of high-grade alloys in seawater at elevated temperature and under a high velocity impinging flow, *Corros. Sci.*, accepted for publication

45. H. Ahb-El-Kader, S. M. El Rachy, *Corros. Sci.*, Vol. 26, No. 8, 1986, p647-653

46. F. G. Hammitt, E. J. Heymann, Liquid erosion failures, *in ASM Metals Handbook*, Vol. 10, 8th ed. p160-167